Swansea University
Prifysgol Abertawe

Characterisation and Performance Evaluation of Calcium Treatment in Automotive Steels

James Edward Russell

Presented to Swansea University in Fulfilment of the Requirements for
the Degree of Doctor of Engineering

College of Engineering
Swansea University

2019

“If you can’t have zero inclusions, then at least make them friendly”

M. S. Millman [1]

ABSTRACT

Advanced High Strength Steels (AHSS) are seeing a dramatic usage increase in order to achieve the reduction in weight required for automotive vehicles to adhere to new legislation on emissions. This has resulted in the increase of use of Calcium (Ca), as a means of both oxide and sulphide-based inclusion control. However, this process is not well understood, with no definitive answer on the level of Ca required to obtain adequate modification of the inclusion population within the steel.

As a result, this thesis studied the level of Ca addition applied to the dual-phase steel grade, FB590, by analysing its Calcium Sulphur Ratio (Ca:S). This allowed for the level of modification needed to obtain the required mechanical properties to be studied. It was discovered that even at the low Ca:S of 0.23, sufficient modification of the inclusions was achieved to obtain these properties. Samples across the entire Ca:S range obtained a substantial increase in the number of 'globular' inclusions when compared to non-Calcium treated samples.

The second aspect of this project was to automate the process of analysing the inclusion populations within the steel. Typically, this is done manually and is very time consuming. The resulting automated process analysed a stitched image of the entire sample surface ($200mm^2$) taken at a typical magnification (100x) and was conducted as closely as possible to the BS EN 10247 and ASTM E45 standards. A custom macro was written that allowed this image to be broken up into fields, each of which were analysed individually, for both inclusion population and size. This method proved significantly less time consuming while generating a vast amount of data that would be unavailable utilising standard analysis techniques.

The key problem with the technique, however, is that it did not include the 'grouped' inclusions stated in the standards. Nevertheless, EDS analysis proved that a significant proportion of these inclusions were in fact distinct globular inclusions and therefore not the inclusions separated by the polishing process that the standard assumes. A suggestion has been made to conduct all future inclusion analysis on FB590 at 500x magnification so as to reduce the negative effects of pixel size. A series of different regions would then be analysed to better ensure the accuracy of the results.

DECLARATIONS

I declare that the work presented in this thesis has not previously been accepted in substance for any degree and is not being concurrently submitted in candidature for any degree.

Signed _________________ (candidate)

Date _________________

I declare that the work presented in this thesis is the result of my own investigations, except where otherwise stated and that other sources are acknowledged by footnotes giving explicit references and that a bibliography is appended.

Signed _________________ (candidate)

Date _________________

I declare consent for this thesis, if accepted, to be available for photocopying and for inter-library loan, and for the title and summary to be made available to outside organisations.

Signed _________________ (candidate)

Date _________________

ACKNOWLEDGEMENTS

Firstly, I would like to thank both my sponsoring company, Tata Steel UK, and funding body, EPSRC through the MATTER scheme, without which this research would not have been possible.

To my academic supervisor, Prof. Cameron Pleydell-Pearce, for both his guidance after becoming my primary supervisor very late in the game, but also because of his actions as my secondary. Without which, aspects of my project would have been completely stuck in limbo.

To the AIM department within the College of Engineering for allowing me to become one of the first people trained on some of their new equipment/techniques and permitting me what seemed like endless hours of EDS analysis. But also, to their fantastic facilities manager, ‘Smiley Pete’ Davies, for his never-ending guidance and patience.

My Industrial Supervisor, Dr Richard Underhill, thank you for always answering my emails quickly and pointing me in the right direction. To Brownie and Geraint in the Harbourside workshop, for not only cutting and testing my tensile samples but also delving into the Tata stores in the hope of finding my missing samples. Jeff and Rhian from the main PT Tata site, thank you for being able to battle the computer systems to be able to obtain my PDA data.

To John, James and Tito from my original office in the dark basement of Talbot, for not only your advice and guidance, but also the laughs that not only helped get my project off the ground at the beginning but got me enjoying it.

A massive thank you to my awesome parents for their continued support in what cannot have been an easy job being my parents at times. To my amazing sister for putting up with me through all these years.

And lastly, to Claire, my incredible girlfriend, without you I do not think I would have been able to survive and actually finish this thesis.

Table of Contents

List of Figures

Chapter 1

Introduction

With the ever increasing demands to reduce CO_2 and other emissions, the automotive industry is becoming ever more reliant on Advanced High Strength Steels (AHSS) and Ultra High Strength Steels (UHSS) in order to facilitate the mass reduction required to conform to stringent EU regulations [2]. This has led to an increase in the use and variety of secondary steelmaking practices due to:

1. A demand for higher quality steel products that have lower levels of impurity elements (e.g. hydrogen, carbon, nitrogen, sulphur and phosphorus.)
2. A need for improved cleanliness with lower levels of segregation.
3. The need for a closer control over composition and temperature [3].

The presence of non-metallic inclusions is one of the main reasons why manufacturers struggle to reach the desired level of cleanliness in many grades of commercial steel. Generally, inclusions have significantly different properties to the steel and form weak interfaces with the surrounding matrix. This causes a negative effect on the mechanical properties of the steel, resulting in the reduced ductility of the wrought and cast metal, increasing the risk of mechanical failure of the final product. Among the various types of non-metallic inclusions in steels, it is the oxide and sulphide inclusions that are thought to be the most numerous and therefore of the highest concern.

Alumina (Al_2O_3) inclusions occur mainly as the by-product of the aluminium-based deoxidation (killing) of steel. However, they can also be caused by exothermic reheating of the melt. Due to pure Al_2O_3 have a melting point above 2000°C, it is present in a solid state in liquid steel. These solid inclusions tend to clog the

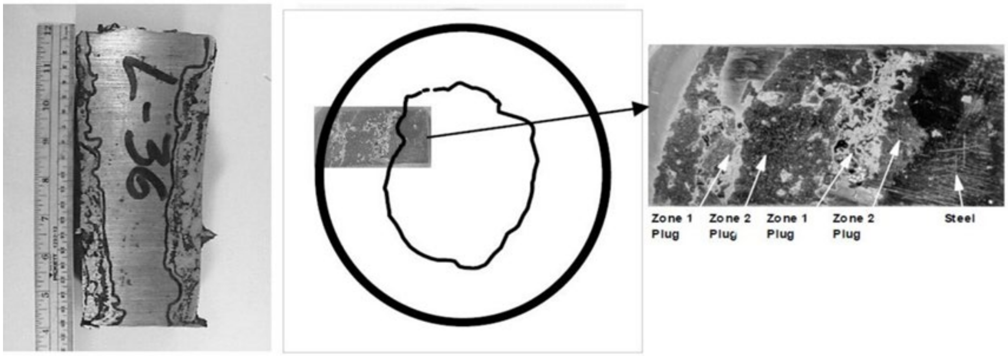

Figure 1-1. Blocked tundish nozzle from Al-killed steel highlighting the effects of alumina agglomeration [4].

submerged-entry nozzle in the continuous caster [4] (Figure 1-1). Following Calcium (Ca) addition to steel, these inclusions modify their composition from pure Al_2O_3 to calcium aluminates. Up until a point, the melting temperature of these calcium aluminates decreases with increasing Calcium Oxide (CaO) content. This enables the inclusions to be liquid during casting temperature of 1550-1560°C. The liquidus approaches the casting temperature when the Al_2O_3 percentage is roughly 42-58wt.% [5], any higher than this and the melting temperatures will rise resulting in solid inclusions during casting.

As well as Al_2O_3, it is important to control the dissolved sulphur. This is because Manganese Sulphide (MnS) inclusions tend to elongate during rolling, lowering the through thickness strength of the steel [6]. The Ca reacts with these MnS inclusions, forming the globular calcium sulphide (CaS) particles shown in Figure 1-2. Even though these small globular particles are not able to float out of the steel, they have been shown to be far less detrimental to both the physical and mechanical properties of the steel than pure Al_2O_3 [7].

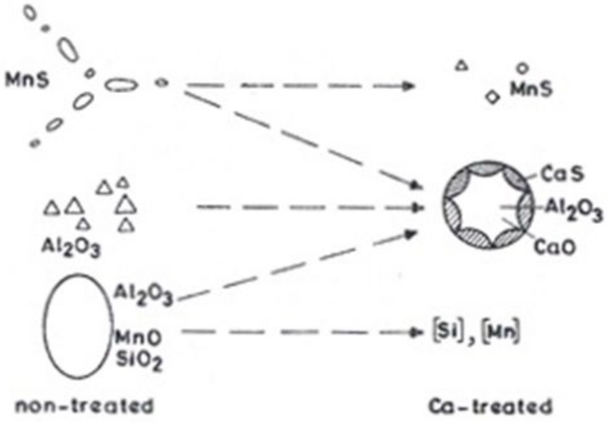

Figure 1-2. Schematic representation showing modification of inclusions with Ca treatment [8].

As a result, the injection of Ca and its alloys into liquid steel has become very important for sulphur, oxygen and inclusion control. However, while the Ca modification process itself is broadly known, it tends to be employed as a result of past practice, with no definitive level of Calcium Sulphur ratio (Ca:S) agreed. In fact, previous studies have this this ratio anywhere between 0.7 [9, 10] and 3 [11] in order to obtain complete modification of the inclusions.

As a result, a key objective of this study is to determine the Ca:S for the automotive AHSS grade, FB590, where complete modification of the sulphide-based inclusions is achieved. There will also be a specific focus on calculating the required Ca:S needed to obtain the level of inclusion modification that achieves the desired mechanical properties. This will allow the steel to be designed more efficiently and on the basis of this information, it may be possible to specify the required Ca that needs to be added to obtain the required inclusion modification as a function of batch composition, instead of using a set quantity. The key impact of this is that if too much Ca is added, it can ultimately lead to clogging and further cleanness issues within the steel.

The second aim of this study relates to the acquisition and processing of characterisation data. Ultimately, if this inclusion analysis is not conducted accurately, and in a time-efficient manner, it will be impossible to determine the Ca:S required to achieve the mechanical properties. Currently, inclusion analysis tends to be conducted manually, using a standard optical microscope and a graticule to measure each individual inclusion. As a result, this method is extremely time consuming, potentially taking several months to complete an in-depth study, the results of which can vary depending on the person completing the analysis [12].

Whilst there is software available that is capable of completing this analysis automatically and therefore at a much quicker rate, they are proprietary, with the analysis procedure less available for auditing. As a result, work was carried out to automate this process as much as possible, and in such a way that it could be employed using standard equipment, whilst also making suggestions on how to further improve this analysis to yield more accurate results in the future.

2.

Chapter 2

Literature Review

2.1. Calcium Modification of Steel

2.1.1. Inclusions

There are 2 main groups of inclusions that form during secondary steelmaking. These 2 groups are determined by their route of origin within the steel, naturally classifying them as either ‘indigenous’ or ‘exogenous’.

The indigenous inclusions, according to Sims’s definition [13], are those that precipitate through homogenous reactions within the steel melt. They largely comprise of oxide and sulphide-based inclusions that form from either alloying addition to the steel melt, or by changes in solubility as the steel solidifies. Within the indigenous inclusion family, there are two main subsets, ‘primary’ and ‘secondary’.

Primary indigenous inclusions are non-metallic compounds that precipitate in the molten steel and as such, tend to have a negative effect on the final material properties. Their tendency to nucleate early on during steelmaking can also make this process more difficult. A typical example of this type of inclusion would be aluminium oxide or alumina (Al_2O_3).

Secondary inclusions, on the other hand, incorporate compounds that precipitate as a result of the decreased solubility within the solidifying steel. As a result, they tend be much smaller in size than the primary inclusions and can commonly be found nucleating upon them during formation [14]. Unlike primary inclusions however, this inclusion type is commonly used to improve the steels final properties. They have been exploited in the past to control both a grains growth rate and its final size. Another common use case for secondary inclusions is to alleviate the influence that certain elements have on the final steels properties [15].

In contrast, exogenous inclusions appear in the steel melt from external sources such as refinery lining fragments or entrapped slag [15, 16]. However, it is rare that exogeneous inclusions remain in the melt in large quantities unless that is, they extensively react with melt and change significantly. While in the past this type of inclusion used to play an important part in the overall population [17], modern steelmaking practices have greatly reduced their impact [15]. It should be made clear, however, that while their impact has been reduced, it does not mean it has become negligible [18].

Exogenous inclusions tend to be easily distinguishable from their indigenous counterparts due to a number of characteristic features [19]:

1. Generally larger size
2. A favoured location within the steel (either a physical position or a position that is relative to the time of its entrapment)
3. Irregular shape
4. Complex structures
5. Sporadic occurrence – usually in association with an identifiable production event.

If, as proposed by Ruby-Meyer *et al* [20], this exogenous inclusion definition was expanded to include, for example, inclusions that form through interacting with air or the entrained slag, the range of inclusions classified as exogenous increases dramatically. While this is possibly a more suitable definition of exogeneous inclusions, it can be argued that these interactions are 'part of the process', therefore it must be asked to what extent this exogenous-indigenous classification actually helps. Irrespective of its origin, from the moment an inclusion enters the steel melt, it influences, and is influenced by, the entire life of the steel. This results in non-metallic inclusions that can change both their phase and composition continuously, until the diffusion rate becomes negligible. This can even occur in solidified steel.

The composition of the inclusion alone tends to not be enough to fully determine its origin, with its shape, size, morphology and position also being contributing factors to an accurate determination. This has led to the development of a number of standards to help in this identification which are made up of a series of comparative-chart inspection systems [21]. While these standards provide useful information that can help quickly identify inclusions and supply a general analysis of a steel's cleanliness levels, these charts are based upon dimensions that are no longer common in modern steelmaking. As a result, whilst these can be useful as a guide for initial analysis, equipment such as scanning electron microscopes or image analysis should be used to conduct proper investigations.

2.1.2. Oxide Inclusions

Oxide inclusions are commonplace within the steel industry due to the large number of circumstances which can lead to their formation. This is especially evident in the heavy use of oxides within Basic Oxygen Steelmaking (BOS) which provide plenty of routes for exogenous inclusions to form. Primary indigenous inclusions on the other hand, tend to form via deoxidisation treatments during the manufacture of strip-products.

The solubility of Oxygen (O) in Iron (Fe) is 0.185% at 1550°C and increases to >0.4% at 1800°C [19]. However, at room temperature, this solubility level is virtually reduced to zero with any remaining O therefore precipitating as inclusions. Because of the obviously large quantity of iron within steel, these inclusions tend to form a substantial volume fraction of FeO. However, the more stable oxides, e.g. Manganese Oxide (MnO) and Alumina (Al_2O_3) are also found. If this concentration of O is increased further, it combines with Carbon (C) forming a gas that is rapidly released from the ladle. This rapid gas expulsion forms a 'mushroom-like' foamy structure in the solidified 'unkilled' steel [22]. As a result, the comprehensive removal of O from the melt has become commonplace in strip-steel manufacture. The acceptable remaining level of O is dependent on the final products application [23].

Figure 2-1 shows the free energy of formation ($\Delta G°$) for various oxides. The more negative the value, the more stable the compound and, therefore, the more likely it is to precipitate. As can be seen, Al_2O_3 has one of lowest $\Delta G°$ values, this has resulted in it becoming the deoxidisation element of choice within the steel industry. The resulting indigenous oxide precipitates are split into the 3 classifications:

1. The Aluminium Oxide system
2. The Spinel system
3. The Calcium Aluminate system

In addition to Al use as a deoxidisation agent within steel, the reaction that forms the oxide is also highly exothermic producing roughly 1.01MJ per mole of alumina [24]. This has resulted in the use of Al to chemically reheat the steel. Any reaction product that then forms tends to be so close to the steel/slag interface, that it easily floats out of the melt, reducing any potential impact on final material properties.

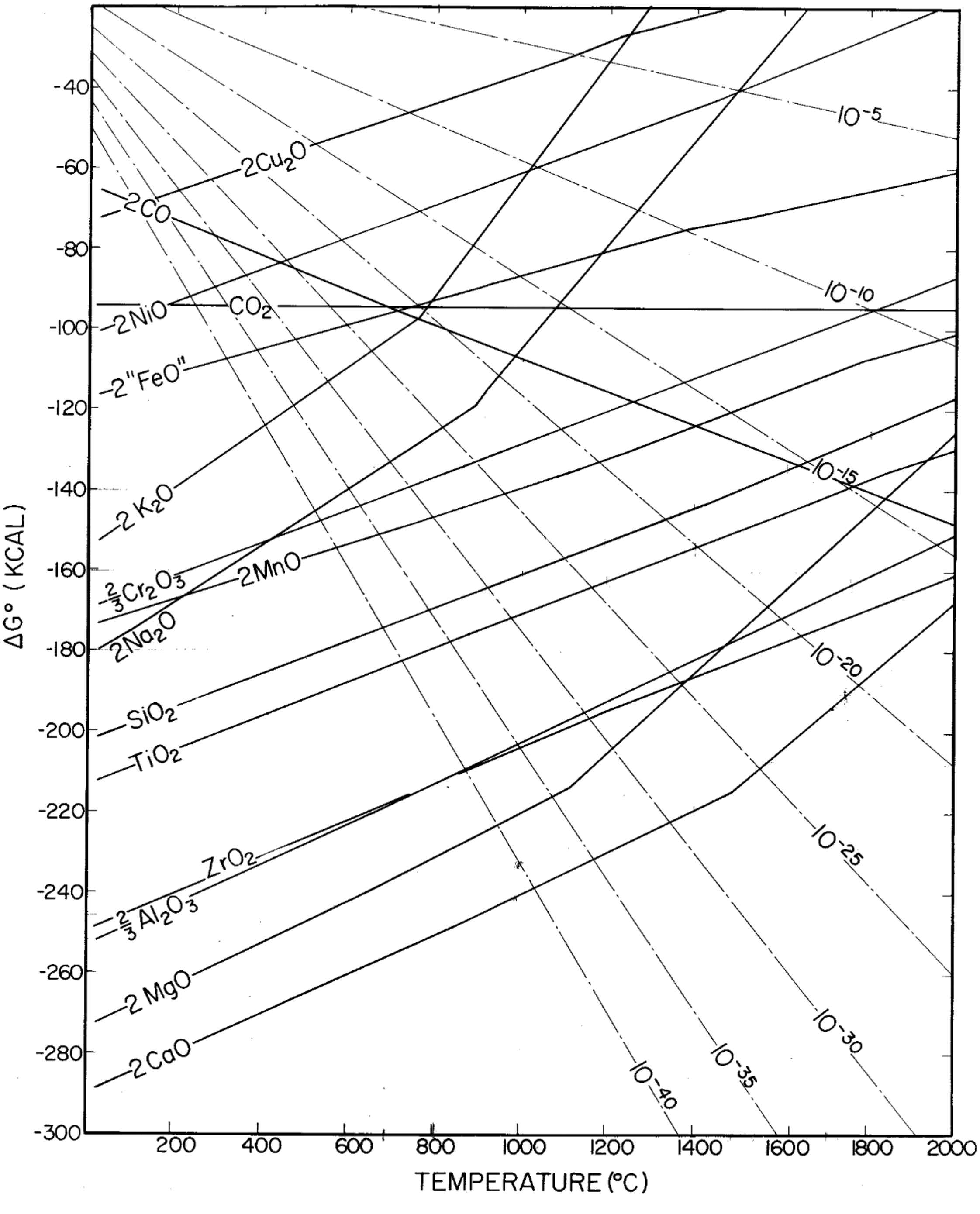

Figure 2-1. Standard free energies of formation ΔG°(kcal) for various oxides from the elements as a function of temperature. The light dash-dot curves are lines of equal oxygen pressure (atm) of the gas phase, as labelled on each curve [25].

2.1.2.1. The Aluminium Oxide (Al_2O_3) System

Three stable forms of Al_2O_3 have been known to exist; α, β and γ. However, as the other forms of alumina transform into α-Al_2O_3 at steelmaking temperatures, α-Al_2O_3 will be the primary focus of this literature review and from now on will simply be referred to as Al_2O_3. Al_2O_3 forms either by reducing FeO and $FeO \cdot Al_2O_3$ or through direct precipitation from the melt [26] with structures varying from small and facetted to large dendrites [27]. The structure that develops depends on the point in the production route where they were analysed [28]. Both these morphologies, however, have the same melting temperature of 2050°C and therefore remain solid throughout the entire steelmaking process.

Because of Al_2O_3 inclusions 'non-wetting' with liquid steel, a high interfacial free energy variation forms at the inclusions interface. Their effort to minimise this interfacial energy encourages particle agglomeration, resulting in the formation of large clustered inclusions [29]. Yin *et al* [30] calculated that any Al_2O_3 inclusions within 50μm of each other, induced an attractive force of 10^{-16}N due to a combination of surface energy and capillary effects. Subsequent deformation of the steel can then lead to the mechanical fracture of these inclusions resulting in the formation of a string of discrete Al_2O_3 particles that can significantly reduce the materials isotropy and therefore its ability to be formed into parts [31, 32]. This affinity for agglomeration can also lead to the blockage of both the ladle shroud and the SEN of the continuous caster resulting in the loss of mould-control and entrapment of exogenous inclusions [31].

2.1.2.2. The Spinel ($MgO \cdot Al_2O_3$) System

Spinel's are crystalline oxides that have a high structural flexibility that gives them their characteristic chemical and thermal stability [33]. While the true spinel phase has the composition $MgO \cdot Al_2O_3$, either the Mg and the Al oxides can be substituted for several II-valence (A) or III-valence (B) elements. This has resulted in the spinel name being applied to a family of double oxides that possess the same chemical structure and therefore general formula $AO \cdot B_2O_3$ [34]. Common members of this family include $FeO \cdot Al_2O_3$ (Hercynite) and $MnO \cdot Al_2O_3$ (Galaxite).

$MgO\cdot Al_2O_3$ forms via the reaction of Al_2O_3 with MgO through a number of different routes [35]:

1. Contamination on the Al to be used for deoxidation of the steel with Magnesium (Mg).
2. Reactions between the liquid steel and the refractory lining of the ladle.
3. Vaporisation of Mg from slags during arc-heating.
4. Steel melt reacting with the slag during the refining process.

Irrespective of the type of spinel that forms, they all conform to a cubic lattice. The $MgO\cdot Al_2O_3$ spinel, specifically, shares a lot of similarities with Al_2O_3, in that they both exhibit similar dendritic/facetted structures [28], they both exhibit high melting temperatures (2135°C for $MgO\cdot Al_2O_3$) so remain solid during the steelmaking process and, also similar to Al_2O_3, they are 'not-wetting' with steel and, as such, have a tendency to accumulate on the SEN resulting in clogging of the continuous caster [36].

2.1.2.3. The Calcium Aluminate ($XCaO\cdot YAl_2O_3$) System

As can be seen in Figure 2-1, Ca displays the lowest $\Delta G°$ for all the oxides. As a result, it is particularly adept at controlling the formation of detrimental alumina inclusions within the steel.

5 stable phases of calcium aluminate ($CaO\cdot Al_2O_3$) have been observed. While there has been a sixth phase ($5CaO\cdot 3Al_2O_3$) identified, it most likely exists as a ternary phase that contains Fe [34] and as such is not included in the pseudobinary phase diagram shown in figure 2-2. In the diagram, the oxides have been written in the standard convention of $C_3A = 3CaO\cdot Al_2O_3$, $C_{12}A_7 = 12CaO\cdot 7Al_2O_3$, $CA = CaO\cdot Al_2O_3$, $CA_2 = CaO\cdot 2Al_2O_3$ and $CA_6 = CaO\cdot 6Al_2O_3$.

While $CaO\cdot Al_2O_3$ can occur accidentally by the reduction of basic slags, it tends to be engineered via a Ca addition process. In terms of oxide control, this is because they typically have a lower melting temperature than Al_2O_3 – e.g. $12CaO\cdot 7Al_2O_3$ at $\simeq$1455°C – which means these modified inclusions would be liquid in the ladle and, as such, do not have the clogging tendencies of either Al_2O_3 or $MgO\cdot Al_2O_3$ [15]. However, if the Ca content of the steel is either too high or too low, higher melting temperature inclusions can form (e.g. $CaO\cdot 6Al_2O_3$ at $\simeq$1850°C). While these inclusions do not have the tendency to move towards each other in the melt, they can still agglomerate if they come into contact. As such, they can still present the nozzle clogging propensities of Al_2O_3 [37].

Another impact of $CaO{\cdot}Al_2O_3$ and the fact that they tend to remain liquid in the molten metal, is that the inclusions that form are globular in nature due the effect of surface tension on the liquid inclusion [38]. As a result, these inclusions do not suffer from the stress raising effects of the facetted/dendritic structures of Al_2O_3 and $MgO{\cdot}Al_2O_3$.

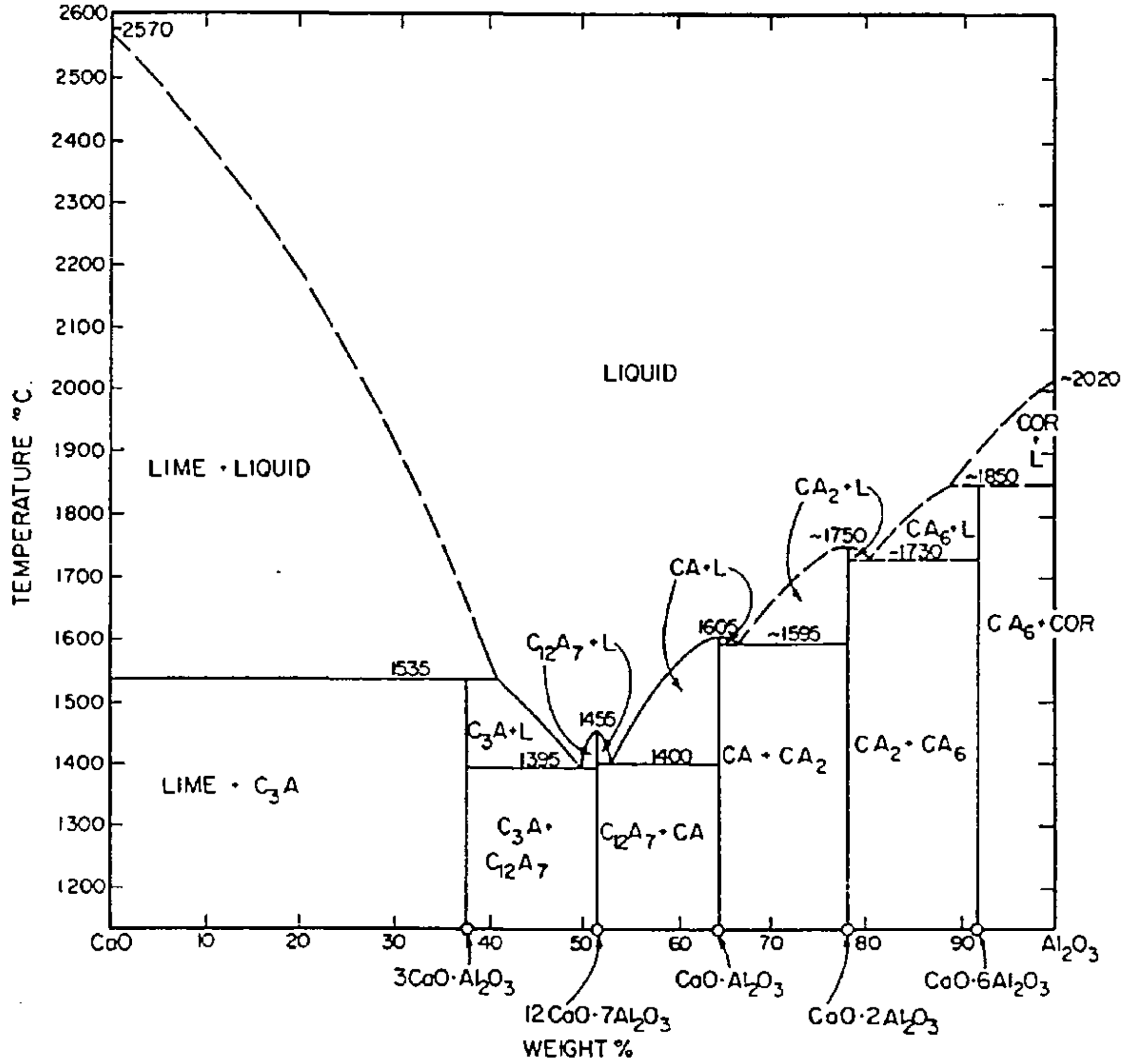

Figure 2-2. A $CaO{\cdot}Al_2O_3$ Equilibrium Phase Diagram that shows the five stable calcium aluminate phase [39].

2.1.3. Sulphide Inclusions

A graph showing the ΔG° for a range of sulphides important in steelmaking is shown in Figure 2-3. From this, Kiessling [34] was able to approximate that the preferential formation of sulphide inclusions within a pure metal, conforms to the following sequence:

$$\mathbf{Ni \rightarrow Fe, Cu \rightarrow Mn, Ti \rightarrow Al \rightarrow Mg, Na, K \rightarrow Ca}$$

Out of these potential sulphide systems, the most commonly found in modern steelmaking practices are Iron Sulphide (FeS), Manganese Sulphide (MnS) and Calcium Sulphide (CaS). As a result, these are the ones that will be investigated further within this literature review.

2.1.3.1. Iron Sulphur System

Within the Iron-Sulphur system, there are 2 main intermediate phases, FeS and FeS_2. Of these two phases, FeS is the most common and as such will be the focus here. Because FeS has a large stability range if the Iron Sulphur ratio (Fe:S) is less than or equal to 1, a more accurate representation of the nomenclature would be $Fe_{1-x}S$. Within this, the x-value varies between zero and roughly 0.125 [28]. This molar variation must be attributed to the Fe since it has been known for this inclusion type to exhibit metal vacancies [40].

Because S is soluble in liquid Fe but has very low solubility when the Fe is solid, any S that is present within the steel precipitates as FeS. This takes the form of either a primary sulphide dendrite (melting point of 1190°C) or as part of an Fe eutectic [34]. While this eutectic already has a low melting point (988°C), any addition of O would further lower this. This means that when the steel solidifies, the S segregates to the regions of the steel that are last to solidify, the grain boundaries. If the steel is then reheated to anywhere between 900 and 1200°C, in order to conduct any hot working, the FeS then re-melts resulting in voids appearing on the grain boundaries of the steel. These voids can then coalesce during plastic deformation leading to rapid crack propagation through the steel. This phenomenon is known as ‘Hot Shortness’ [41].

In modern steels, the formation of FeS and the resulting ‘hot shortness’ is avoided through the addition of Manganese (Mn) [42]. This is because the resulting MnS that form have a lower ΔG° and therefore form a more stable inclusion than FeS.

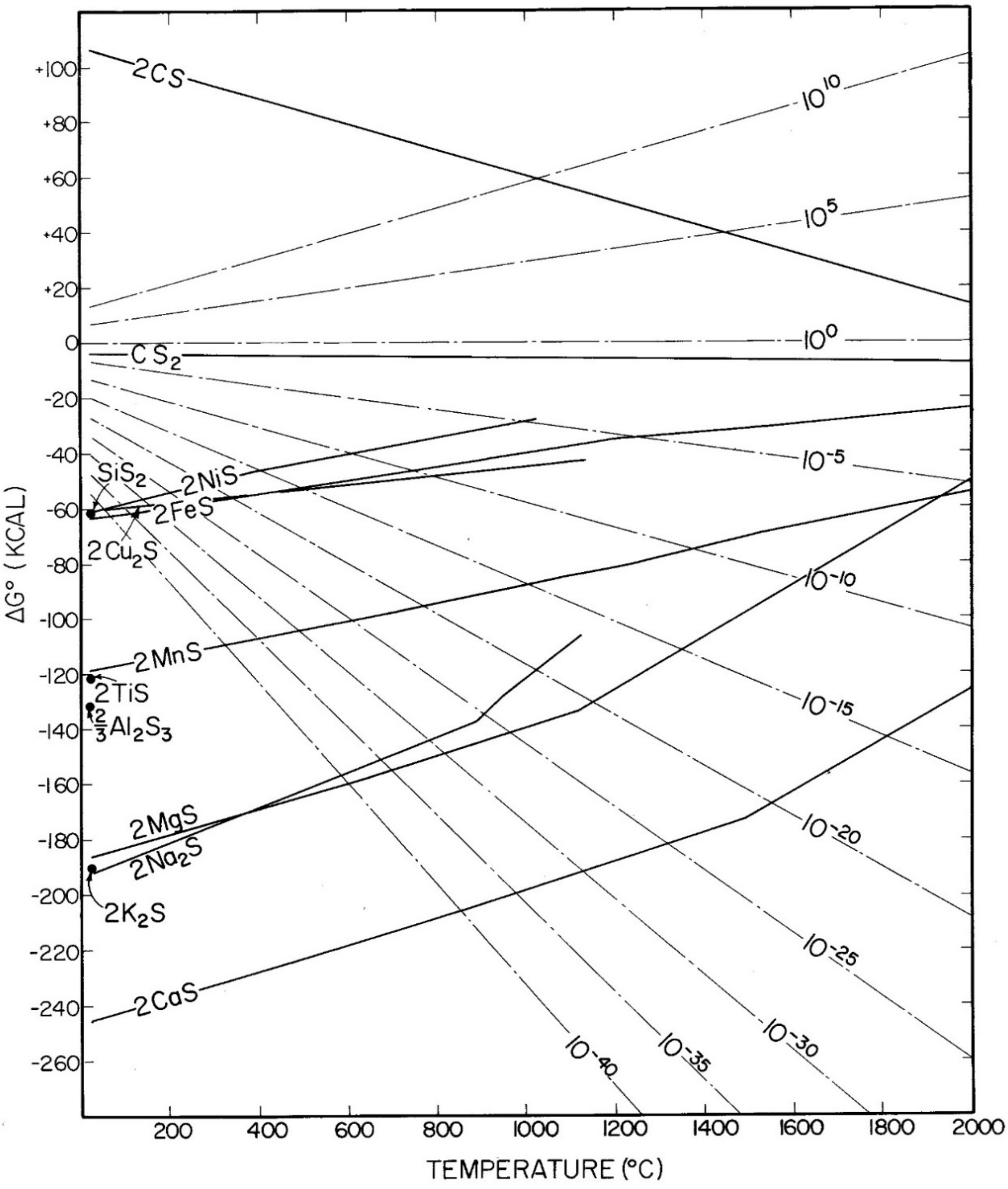

Figure 2-3. Standard free energies of formation ΔG°(kcal) for various sulphides from the elements as a function of temperature. The light dash-dot curves are lines of equal sulphur pressure (atm) of the gas phase, as labelled on each curve [25].

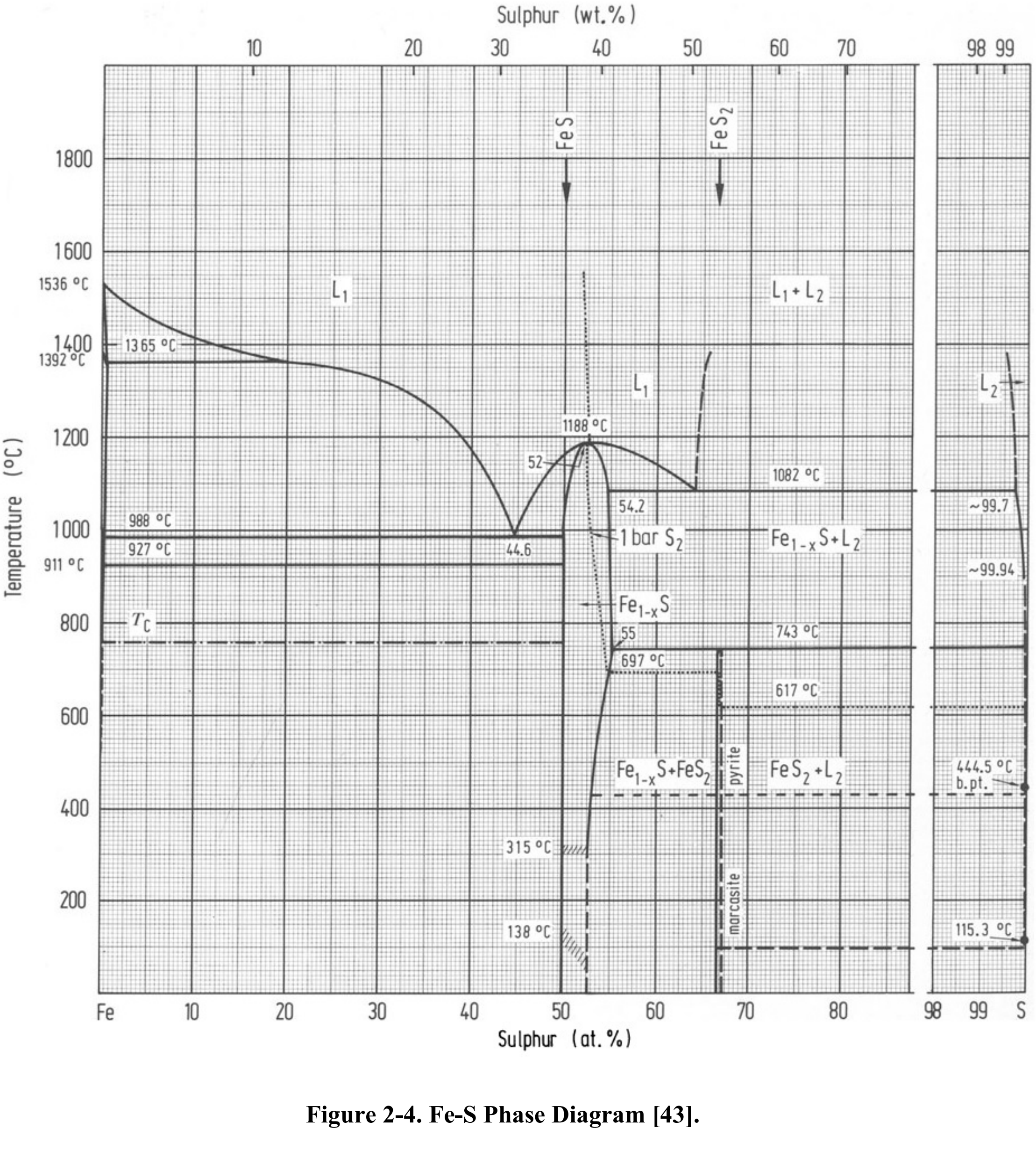

Figure 2-4. Fe-S Phase Diagram [43].

The reason the aforementioned ‘hot shortness’ is prevented is because this inclusion type has a significantly higher melting temperature (1610°C) and is therefore a solid during hot working. While it is generally accepted that a minimum Manganese Sulphur Ratio (Mn:S) must be obtained to allow for the modification of all the FeS inclusions, there are a few opposing views on what this ratio should be.

Kiessling & Lang [34] suggested that due to the peculiar metal affinities that exist in the Fe-Mn-S system, the Mn/S ratio must be higher than 4 for complete modification of FeS. Mann & Vlack [41] put this value to be closer to 20 if the sulphur level is not too high, while Brimacombe [44] argues that the Mn/S ratio should in fact be between 25 and 30 to reduce crack formation and improve hot-ductility in steel billets.

2.1.3.2. The Manganese Sulphur System

Similar to the iron-sulphide system, MnS also shows two intermediate phases, MnS and MnS_2. While the MnS_2 phase shares a common structure with Pyrite (FeS_2), it is not of great interest in steelmaking. MnS, on the other hand, is both the most common and most important sulphide inclusion in modern steelmaking. While MnS forms three different modifications (α, β and β’ (otherwise known as γ)) only the α-MnS phase has been regularly encountered as a steelmaking inclusion [34] and as such, will simply be referred to as MnS from now on.

MnS shows greater stability than its iron counterpart and is identifiable by its light-grey colour, although it is usually slightly transparent. As MnS is softer than FeS, it is plastically deformed if subjected to rolling loads. This leaves extended inclusion stringers that are parallel to the rolling direction. This elongation gives rise to stress concentrations on the tips of the MnS inclusions which act as sites of crack initiation as well as causing anisotropy within the steel. As such, the MnS inclusions are usually considered to be harmful and to be reduced wherever possible [41, 45].

Since 1938, MnS has been classified into the 3 forms employed by Sims and Dahle [46]. The form that develops within the steel is entirely dependent on the steelmaking practice that is used to develop the steel.

Type I MnS

Type I MnS (figure 2-5) precipitates as duplex, globular inclusions, with an oxide phase of either alumina or silicate. It also commonly exhibits a variety of different elements held in solid solution (e.g. Cr). This type of MnS can form in a variety of different sizes and tends to be randomly distributed through the entire steel thickness. The formation of its characteristic duplex structure is because it precipitates while the deoxidisation process is still on-going. As a result, it nucleates at higher temperatures than would be expected given sulphurs low solubility in steel.

Because this type of MnS tends to form in semi-killed steels that possess a reasonably high soluble-O content, they are rarely found in modern steels. This is because modern steelmaking tends to demand O content that is below 5ppm. However, they have been found in free-cutting steels due to their ability to cause internal stress concentrations that chip the steel at the cutting edge. These micro-cracks in the shear deformation zone, decrease the size of the shear area and therefore reduce the overall cutting stress on the material [47].

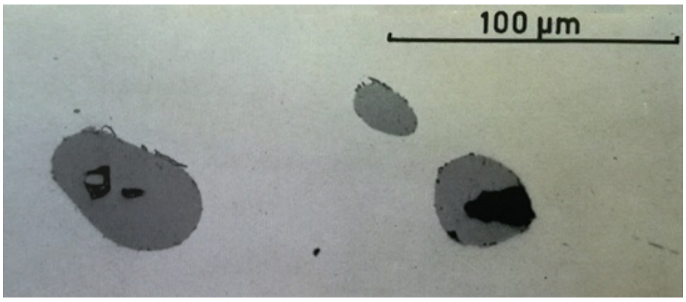

Figure 2-5. A photomicrograph depicting an example of a Type I MnS Inclusion taken from an Si-killed Electrical Steel [34].

Type II MnS

Type II MnS are traditionally referred to as ‘Eutectic MnS’ and tend to form within fully-killed steel grades. Because these steel grades undergo a significant level of deoxidation, they tend to show a high-level of S solubility. As a result, they form within the regions that are last to solidify, precipitating as the dendritic shape seen in figure 2-6 on primary grain boundaries. In Al-killed steels, the Al_2O_3 which are present often act as nucleation sites for the MnS inclusions [3].

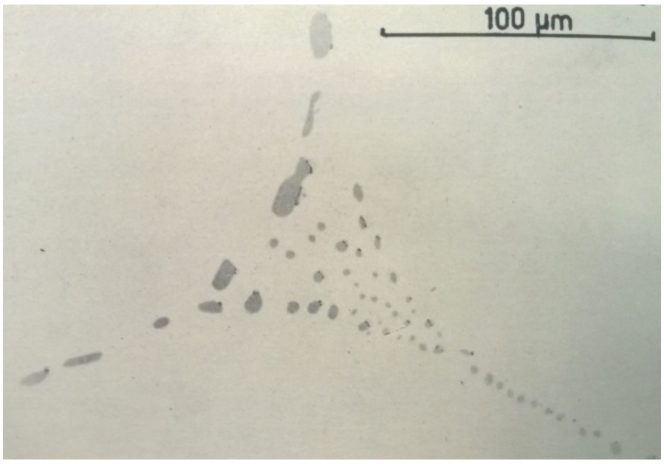

Figure 2-6. A photomicrograph depicting an example of a Type II MnS Inclusion taken from an Al-killed Steel [34].

Type III MnS

It is believed that this type of MnS inclusion forms directly from the melt as a solid particle which is what causes its irregular and often angular shape (Figure 2-7). They tend to form in fully killed steels that have been treated with an excessive amount of deoxidising agent which, as mentioned earlier, is normally Al. This high degree of deoxidisation prevents the formation of oxide inclusions that can act as a nucleus or form a duplex inclusion with the MnS. This results in the formation of a monophase particle that is generally considered to be the purest form of MnS that can precipitate [34]. The high level of Al, which is present to act as a deoxidising agent, suppresses the S solubility. This is similar to how O content favours the precipitation of Type I MnS. As a result, they share significantly more in common with each other than Type II MnS. For example, both types precipitate much earlier in the solidification process and are therefore randomly distributed throughout the steel.

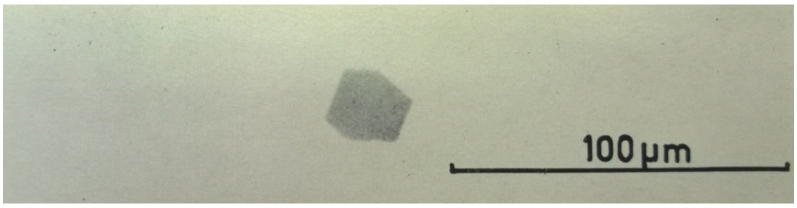

Figure 2-7. A photomicrograph depicting an example of a Type III MnS Inclusion taken from an Al-killed Steel [34].

2.1.3.3. The Calcium Sulphur System

There are 2 common sulphide inclusions that precipitate from Group II metals, these are CaS and Magnesium Sulphide (MgS). However, as can be seen in Figure 2-3, out of these 2 sulphides, CaS preferentially forms due to its lower level of $\Delta G°$. This, combined with the fact that Ca still has a strong tendency to form sulphides even if O is also present [34], means Calcium (Ca) is the one most commonly used to reduce the S content to low levels ($\leq$0.005% S) [14]. CaS has a high melting point (in excess of 2500°C) and often appears as a 'shell' precipitated around an oxide inclusion, typically Calcium Oxide (CaO) or alumina [9, 48, 49]. Its key discerning property over MnS, other than its higher affinity to S, is that it is hard and therefore does not deform upon rolling [50].

2.1.3.4. The CaS – MnS System

CaS and MnS are both cubic isostructures of NaCl, forming the continuous sulphide solid solution (Ca,Mn)S at high temperatures. When reduced to room temperature however they tend to split into 2 phases, (Ca,Mn)S and (Mn,Ca)S [51] - Figure 2-8. Because CaS has a larger lattice constant than MnS – 5.683 Å compared to 5.226 Å – it hardens the solid solution by cation substitution of Mn^{2+} and Ca^{2+}, paralleling the mechanism of hardening found in simple metal systems, e.g. Copper hardening of Nickel and vice versa. This means the odd sized atoms stop dislocation movement by locally reducing strain energy therefore requiring a higher shear stress to induce slip. In addition, Ca^{2+} is more ionic than Mn^{2+} and therefore increases the hardness further. This all results in only a few percent of CaS in solid solution successfully hardening the MnS [52] - Figure 2-9.

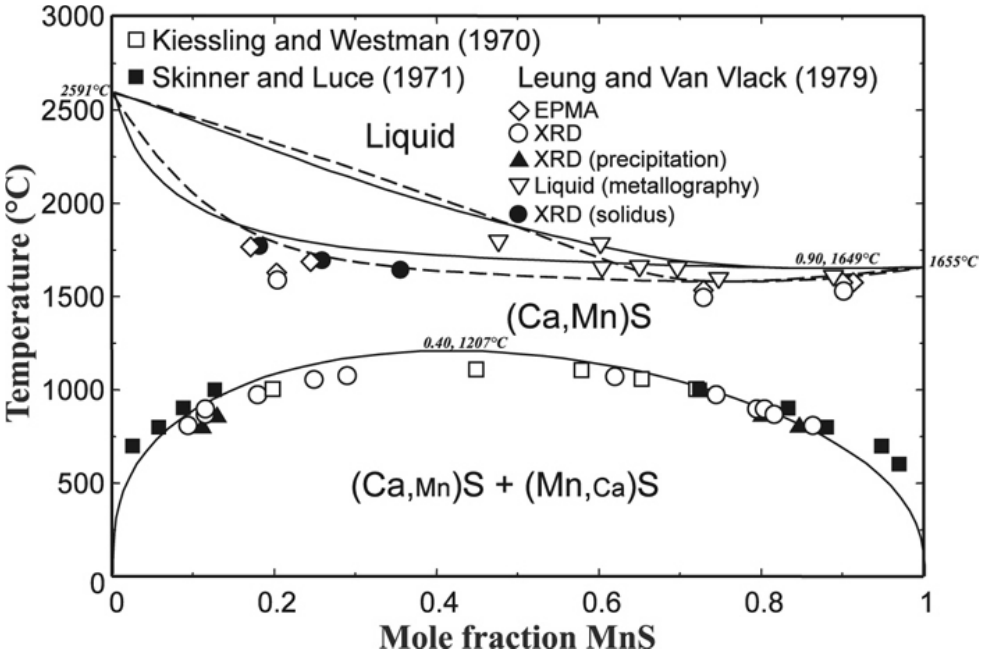

Figure 2-8. Phase Diagram of the CaS-MnS system [53].

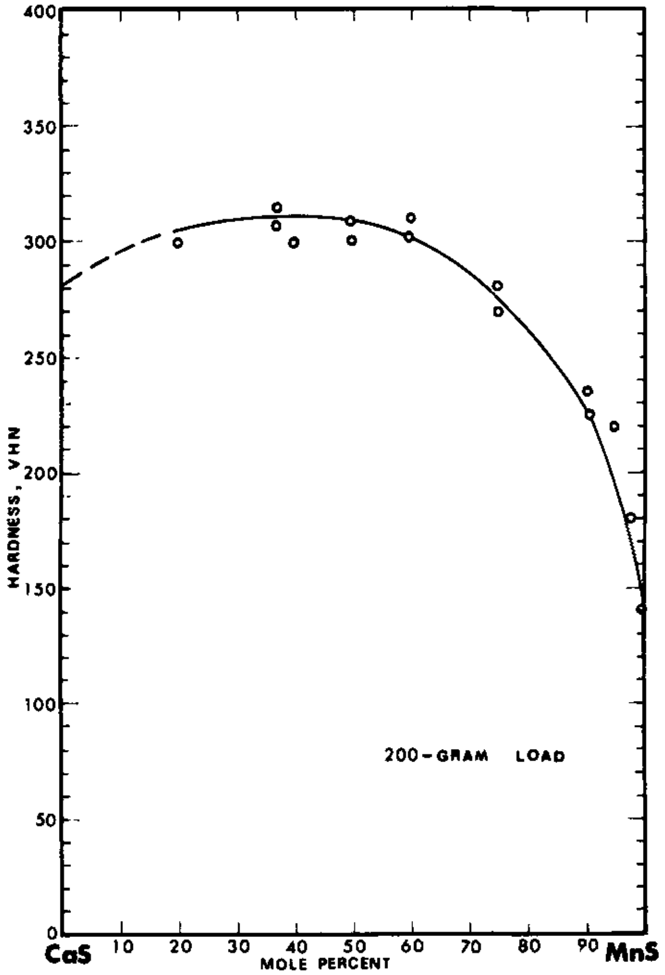

Figure 2-9. Vickers Hardness of (Ca,Mn)S vs Composition [52]

2.1.4. Calcium Treatment

The addition of Ca to steel comes with its own list of distinct advantages, some of which have been touched on before:

1. Improves the steel's castability during continuous casting by modifying the alumina into calcium aluminates thus helping to minimise the effects on nozzle blockage [31, 54–59].
2. Modifies the detrimental MnS stringers into CaS, increasing the level of isotropy of the steel [60–62].
3. Reduces the overall O and S levels therefore improving the cleanliness of the steel [63].

As a result, Ca treatment is applied whenever any of these properties are required. Enough Ca must then be applied to react with the alumina and ensure that the calcium aluminates that form are liquid at steelmaking temperatures.

If the system is simplified to its 4 components (Al, Ca, O and S), the most essential reactions that control the formation and transformation of the inclusions are [59]:

$$2[Al] + 3[O] = (Al_2O_3)_{inc} \tag{2-1}$$

$$[Ca] + [O] = (CaO)_{inc} \tag{2-2}$$

$$[Ca] + [S] = (CaS)_{inc} \tag{2-3}$$

$$[S] + (CaO) = (CaS)_{inc} + [O] \tag{2-4}$$

$$[Ca] + 6\tfrac{1}{3}(Al_2O_3)_{inc} = CaO \cdot 6Al_2O_{3\,solid\ inc} + \tfrac{2}{3}[Al] \tag{2-5}$$

$$[Ca] + 2\tfrac{1}{3}(Al_2O_3)_{inc} = CaO \cdot 2Al_2O_{3\,solid\ inc} + \tfrac{2}{3}[Al] \tag{2-6}$$

$$[Ca] + \tfrac{4}{3}(Al_2O_3)_{inc} = CaO \cdot 2Al_2O_{3\,solid\ inc} + \tfrac{2}{3}[Al] \tag{2-7}$$

$$3[Ca] + (Al_2O_3)_{inc} = 2[Al] + 3(CaO)_{inc} \tag{2-8}$$

$$3(CaO)_{inc} + 2[Al] + 3[S] = 3(CaS)_{inc} + (Al_2O_3)_{inc} \tag{2-9}$$

$$(CaS)_{inc} = CaS_{solid\ inc} \tag{2-10}$$

In these equations, a square bracket represents an element that is dissolved in the steel melt, round brackets indicate components that are dissolved in liquid slag inclusions and the subscript 'solid inc' represents a solid (saturation) phase. Beyond this; (2-1) – (2-4) shows the deoxidisation and desulphurisation reactions by Ca and Al, (2-5) – (2-7) are the reactions in which the alumina inclusions are modified by Ca to form solid calcium aluminates; (2-8) is simply the general reaction for this modification; and (2-9) - (2-10) shows sulphurs interaction between the steel and the inclusions including the precipitation/dissolution of sulphides. It should be noted that if the transformation proceeds by reaction (2-7), liquid aluminates are formed. Also, while these are only some of the reactions that take place, they still aid in the overall understanding of the Ca modification process.

As a result of this there are 3 key classes of inclusions which form that can result in the efficiency of the Ca treatment being evaluated [38]:

Class 1. Non-metallic inclusions consisting of intermingled sulphide and aluminate phases indicating that the inclusions have been liquid through the whole process, and they have solidified at the same time. The sulphide phase tends to be CaS with a calcium aluminate of either $CaO \cdot Al_2O_3$ or $12CaO \cdot 7Al_2O_3$. This suggests high levels of Ca due to formation of the lowest melting calcium aluminates.

Class 2. These are the most prevalent in Ca treated steels and consist of a 'core' that consists of $CaO \cdot Al_2O_3$ or $CaO \cdot 2Al_2O_3$ that has solidified first, surrounded by a sulphide 'shell'. In this instance the sulphide tends to be a solid solution of (Ca,Mn)S.

Class 3. This is indicative of incomplete Ca treatment and consist of an unmodified MnS phase and a central calcium aluminate which tends to be $CaO \cdot 6Al_2O_3$.

If $CaO \cdot 6Al_2O_3$ precipitates during casting it can result in a severe blockage in the SEN that can be even worse than the clogging caused by alumina. This is due to the fact that the volume of the $CaO \cdot 6Al_2O_3$ phase unit cell is practically seven times the size of alumina – 579.25 A^3 compared to 84.50 A^3 [54]. As a result, the possible benefits which can be obtained from Ca modification can be overshadowed by the limitations faced in the liquid steel.

The increase in the use of Ca within the ladle also provides the chance for additional solute interactions and therefore increases the appearance of previously unknown precipitation patterns. This has been shown in the observations of Boussard *et al* [64] which highlight the significance of the relative sulphur (S), aluminium (Al) and oxide concentrations during attempts to modify oxide inclusions.

If any of these elements were present at unusually high levels it resulted in a non-equilibrium relationship as well as the prolific and unwanted precipitation of high melting temperature CaS. This means that it will be solid throughout the majority of the steelmaking process and can actually accelerate nozzle clogging [58].

The equilibrium diagram of the Fe-Al-Ca-O-S system at 1600°C, that was developed by IRSID [65, 66], is shown in Figure 2-10. If a steel contains 0.05% wt. Al, when Ca is added, the amount of dissolved Ca is minimal because of its general low level of solubility in Fe. This means it reacts with Al_2O_3 forming calcium aluminates and the percentage amount of CaO in these inclusions increases along with the amount of Ca. When these newly formed calcium aluminates reach 40% CaO, they become liquid at 1600°C. At this point, if the S content of the steel is too high (≥0.035%), it will result in the formation of solid CaS inclusions. When the S content is low (≤0.006%), it allows for the formation of calcium aluminates with atleast 50% CaO.

Figure 2-11 then breaks this down further for a specific grade of steel, showing the impact of different Al contents. For both these diagrams, the solid lines indicate the boundaries in which various oxides form. The dotted line on the other hand shows

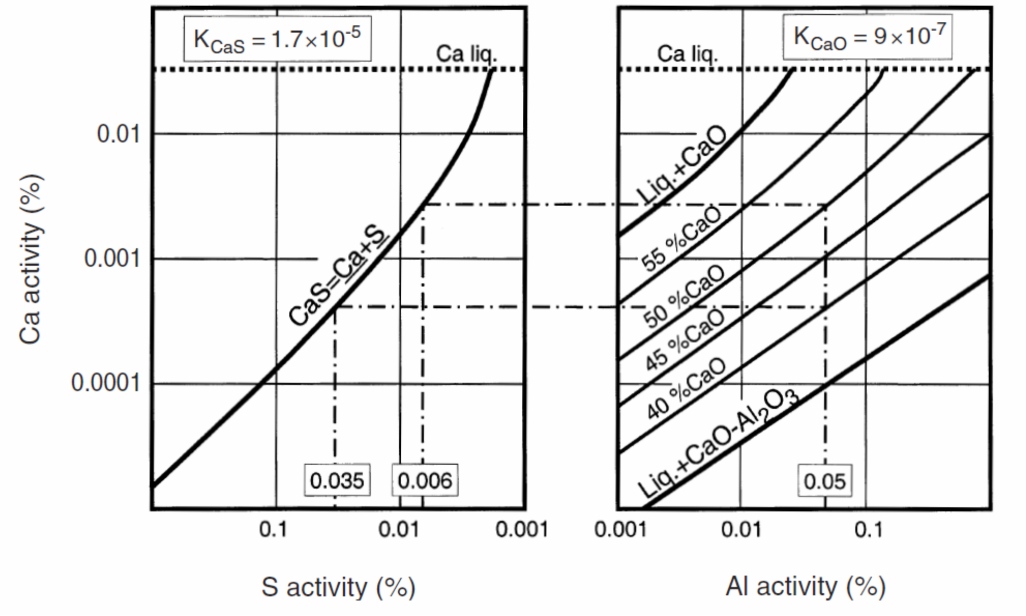

Figure 2-10. Equilibrium Diagram for the System Fe-Al-Ca-O-S at 1600°C [67].

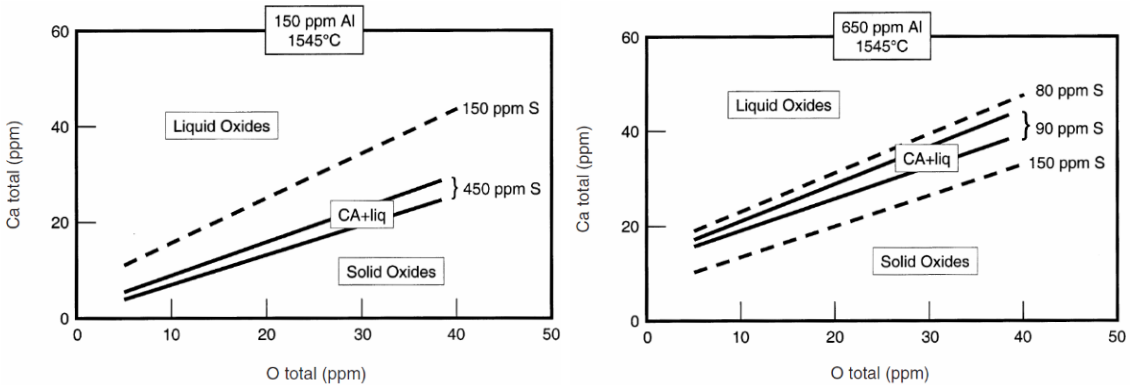

(a) **(b)**

Figure 2-11. Stability Regions for Solid & Liquid Oxides at CaS Precipitation during Ca Treatment for a Steel (0.8%C, 0.65%Mn, 0.2% Si, 0.13%Cr) where: (a) 0.015%Al; (b) 0.065%Al [68].

the points at which CaS saturation occurs for the associated S contents. When both the Al and the S content are low, CaS can only form after high levels of Ca addition leaving a wide window in which calcium aluminate inclusions can form. However, if the Al levels in the steel are high, it completely closes this “liquid window” for S levels as low as 0.009%. As a result, the level of Ca addition needs to be carefully controlled depending on the general S and Al content of the steel.

However, what is important to note is that as the CaO content of these inclusions increases beyond 40%, it becomes more and more difficult to ensure the formation of these liquid aluminates without the accompanying precipitation of CaS. Figure 2-12 shows this phenomenon, as well as indicating regions (A-D) that correspond to ever more stringent manufacturing conditions. As a result, it is important to ensure that the CaO content of these aluminates is a maximum of 50% - preferably between 40-45% [64, 69].

Steel composition alone is not the only factor in the successful modification of Al_2O_3 inclusions without the formation of detrimental CaS. As shown by the invariant equilibrium diagram in Figure 2-13, temperature also plays a major role in the quality of S that can present in the steel while still preventing potential nozzle blockage. As can be seen, the higher the temperature, the higher the amount of S that can be present and vice versa.

Due to advances in modern steelmaking, steels with a maximum 0.002% S can be easily achieved if required [39]. This value is however closer to 0.0025% in Tata Steel Port Talbot’s best practices. What this does show, however, is that these calcium

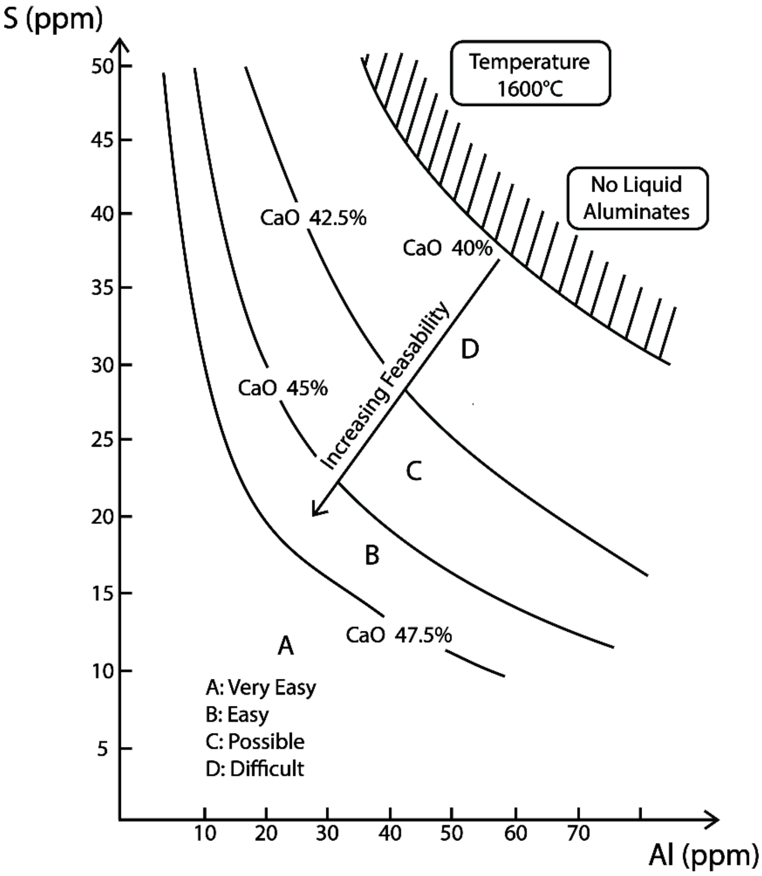

Figure 2-12. Likelihood of Casting Without Clogging in Relation to S and Al Level for Different Constant CaO Contents of the Aluminates [64].

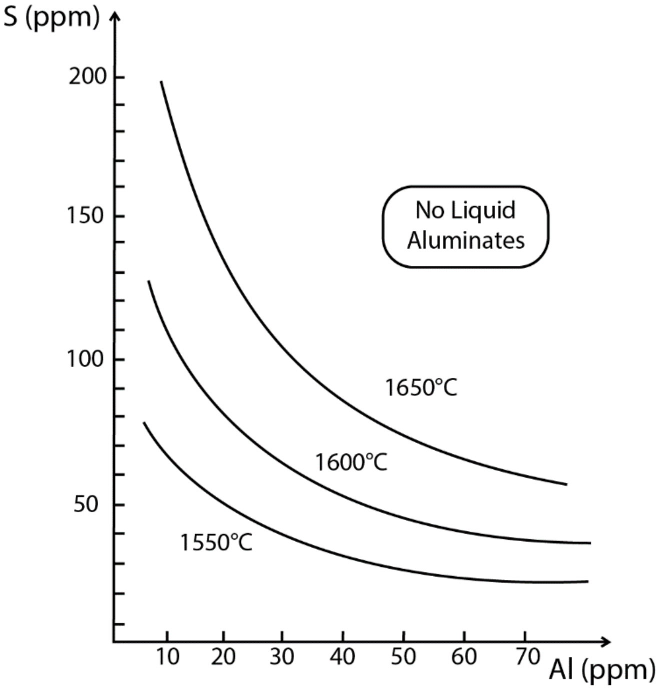

Figure 2-13. Maximum S Content Where No Solid Aluminates Form in the Steel in Relation to Both Al Content and Casting Temperature [64].

aluminates with >40% CaO can be achieved over a wide range of Al content and Ca addition levels. What is less obvious, is what happens to the sulphur itself if it does not form the detrimental CaS early in the steelmaking process.

Research by Gatellier *et al* [70] and Wang *et al* [71] has shown that as the metal cools, the calcium aluminates act as nuclei for the precipitation of MnS-rich inclusions. This MnS then reacts with the Ca in the oxide core, resulting in a globular Al_2O_3-rich core and an outer layer of (Ca,Mn)S or potentially pure CaS. This reaction is according to (2-9) where [S] corresponds to MnS.

What is less obvious however, is the specific levels of Ca and S that need to be within the steel for this reaction to occur to such an extent that there is little to no detrimental elongated inclusions after rolling. From previous research, the indicator of successful modification of these “soft” MnS inclusions into “hard” (Ca,Mn)S/CaS is the Ca:S. However, this research does not agree on a definitive ratio.

Turkdogan [39] calculated that, should the S level of the steel be less than 30 ppm, the Ca:S should be at least 1 but would preferably be somewhat higher. Ototani [10] states that this value should be at least 0.7 which was corroborated by Lis [9] who also calculated this value to be 0.7, as long as the Ca:Al was above 0.14.

This is further backed up by work by Jehan [72] during testing conducted at Lackenby Steel works (Figure 2-14 (b)). This shows that significant modification occurs when the Ca:S is between 0.7 and 1, with full modification occurring if the ratio is greater than 2. Figure 2-14 (a) on the other hand shows complete

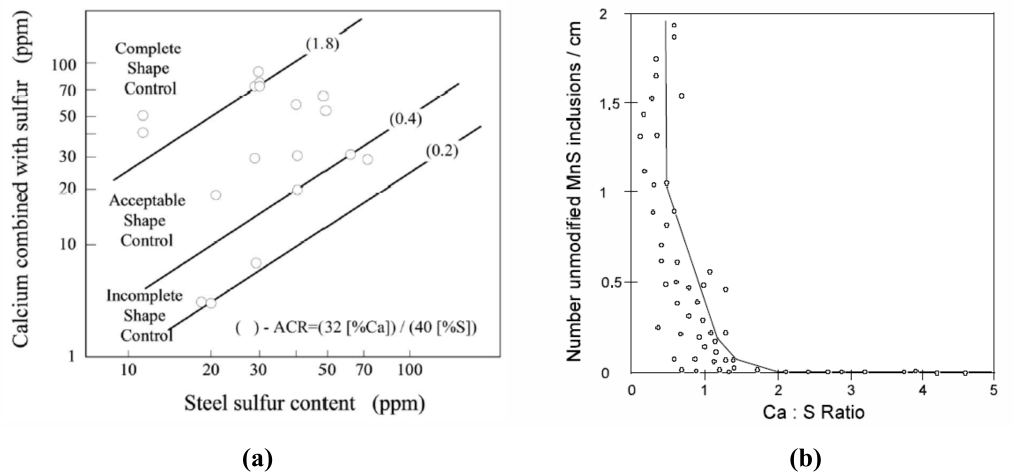

(a) **(b)**

Figure 2-14. (a) Calcium Addition’s Effect on the Shape of Sulphides in HSLA Steel [72] (b) Ca:S Compared to the Number of Unmodified MnS Inclusions per cm in Low Sulphur Carbon Steel [73].

modification at roughly Ca:S of 1.44 (corresponds to an Atomic Concentration Ratio (ACR) of 1.8), with acceptable levels at 0.32 (ACR 0.4).

$$ACR = \frac{32[\%\,Ca]}{40\,[\%\,Si]} \qquad (2\text{-}11)$$

However, these results cannot be generalised for all levels of S, with the acceptable level of Ca:S in low S steels possibly being several times higher than that of steel with higher levels of S [38]. At these higher S levels, Ca:S of approximately 3 have been seen [74] to be needed for compete modification. This variation in chemistry could be one of the potential causes for the differences in required Ca:S. In the case of Turkdogan, it could also be the fact that it is based on calculations that assume a need to have more CaS than MnS in solid solution to achieve hardness values that are high enough to prevent elongation, when in fact it could be lower. It could also be the fact that general improvements in steelmaking have resulted in the size of the inclusions being analysed by Jehan at Lackenby Steel works no longer being regularly encountered.

In addition to this, there appears to be very limited research that directly connects a specific Ca:S to the required mechanical properties for a steel grade. The only research that could be found that directly links Ca:S (and the resulting level of detrimental elongated inclusions) to mechanical properties indicated that, for a low temperature Si-Mn steel, a Ca:S > 0.7 was required to eliminate anisotropy within the steel. It was also found that this value should be no higher than 1.3 because this led to the agglomeration of spherical inclusions that seemed to deteriorate the steels properties (Taken from [10] which covers a study conducted in 1979 by Okamura *et al*, unfortunately the original study could not be found).

This specific Ca:S is important because even without complete modification, a steel may still obtain its required properties if the level of detrimental stringers has been reduced to a sufficiently low level. As a result, both the Ca:S needed for complete modification of the sulphide inclusions and the effect of Ca:S on mechanical properties will be significant aspects of this research.

The fundamental thermodynamic properties of Ca also add some limitations to its use. The low solubility of Ca in liquid steel is the principle of these limitations, with Sponseller and Flinn [75] reporting the solubility of Ca to be as low as 0.032%

at 1607°C. At these conditions, the Ca-vapour was measured to be 1.69 atm. This means that at atmospheric pressure, the solubility of Ca is just 189ppm. However, as Ca evaporates at 1440°C, achieving even these levels of solubility can be difficult since the Ca will evaporate almost immediately at working-steel temperatures (1600-1650°C). This rapid evaporation results in a high-pressure vapour (1.69 atm) that rapidly ejects from the ladle.

This high-pressure vapour also promotes the collision and coalescence of alumina inclusions. This means that, with a combination of intense bath stirring, the alumina inclusions are aided in their removal from the melt when compared to small non-buoyant alumina inclusions which must cluster on their own without forced convection [38].

Fortunately, Ca can be engineered to increase its level of dissolution within steel. By alloying the Ca powder with elements of nickel, carbon, silicon and Al, its solubility has shown a marked improvement, to the extent that some products report yields of up to 30% [76]. Ferro-static pressure can also be used to help slow down Ca evaporation, therefore extending the ladle residence time.

The boiling point of a liquid is defined as the temperature at which the vapour pressure of the liquid and the atmospheric pressure are equal. This means, at a certain depth in the ladle, the pressure exerted by the weight of the steel (the ferro-static pressure) combined with the atmospheric pressure equals the Ca vapours pressure (i.e. 1.69 atm). As a result, the Ca evaporation would be suppressed if it can be transported to depth that is greater than this point. In modern secondary-steelmaking facilities, this is usually between 1.8 - 2m from the surface of the melt.

While the powder injection method is effective, it does have the following weaknesses that have resulted in it being rapidly replaced by Ca cored wired injection. The principle of these being [10]:

1. There is an increase in nitrogen content if the melt comes into contact with air at any point.
2. As CaC_2 decomposes in the melt, the leftover C remains within the molten steel.
3. Because of the gas injection of powder, hydrogen pickup is inevitable.
4. There is a danger of powder explosions due to excessive reactivity.

2.1.4.1. Wire Feeding Method (WF Process)

The method of adding Al wire to a steel melt has been widely used in the adjustment of soluble Al content, largely due to its ability to produce a high and controlled yield. This has developed into a technique for the addition of Ca to the melt via a continuous feed directly into the ladle. During this process, the melt is normally stirred by channelling a gas through a porous brick at the base of the ladle. Figure 2-15 shows the outline of this feeding process.

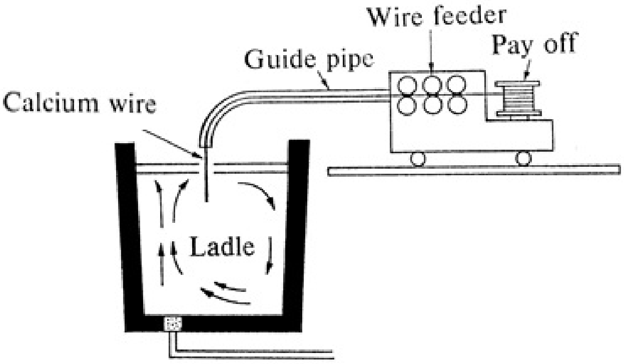

Figure 2-15. Schematic of the wire feeding process [10].

The wire itself consists of a core containing either pure Ca, a Ca/Al mixture or a calcium silicide (CaSi) powder that is sheathed in steel and placed on a pay-off reel. The wire is designed with this outer steel sheath as a means of delaying the release of the highly reactive cored materials which have a significantly lower melting temperature and density than steel. As a result, it delays the wire from melting completely, allowing the cored materials to fuse before being released deep in the steel melt, and therefore making the Ca treatment more effective. The existence of the aluminium or silicon in the wire core provides the following advantages [10]:

1. The combined action of the Ca plus either aluminium or silicon results in an improved deoxidisation and desulphurisation rate.
2. The solubility of Ca in the steel bath increase which in turn leads to a better distribution and quieter reaction of the added Ca.

A feeding machine pulls this wire through a series of pinch rolls until it is finally drawn through a guide pipe and into the steel melt. The wire pulling speed can be varied from 0.05 to 5.1 m/s depending on the volume of the melt to be treated. Unwanted smoke development and excess Ca evaporation at the melt surface can also be prevented by varying this pulling speed. This results in a much more stable addition process with a higher percentage of Ca which is either retained in the melt or bonds with residual elements (e.g. O and S).

In industry, general Ca yields of 15-25% can be obtained during the steel refining processes which is 2-3 times higher than those achieved through powder injection methods. Additionally, these high yield levels are stable and are easily reproduced between different melt charges [10]. As a result, this is the method of Ca treatment that is utilised within Tata Steel, Port Talbot where they use a CaSi powder core.

2.2. Effect of Inclusions on Mechanical Properties

In general, inclusions are detrimental to the properties of steel, even more so for high strength steels in critical applications. These properties include [14, 19, 77]:

- Mechanical properties (e.g. strength and fatigue)
- Ductile and Brittle Fracture
- Hot Shortness and Tearing
- Weldability
- Machinability
- Surface Finish
- Corrosion

The key factors that can cause these effects are inclusion geometry (i.e. size and shape), distribution and quantity of inclusions as well as the properties of the inclusions themselves. These properties include plasticity/hardness in relation to temperature, thermal expansion coefficient, crystallisation behaviour (in relation to "glassy" inclusions) and, less significantly, the solubility of any metallic components [78].

2.2.1. Influence on Ductile Fracture of Steel

Ductile fracture is an important characteristic in the structural and mechanical application of steel as it directly influences, not just the steels ductility, but also its formability and toughness [78]. This is of course dependent on the deformation occurring at temperatures where the ductile deformation is still a predominant part of the fracture process – i.e. above the ductile-brittle transition temperature. In most

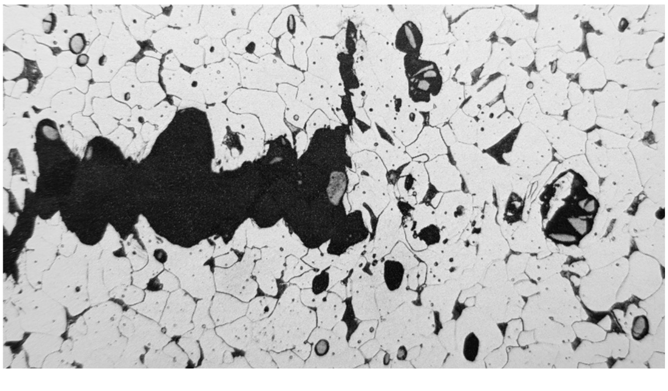

Figure 2-16. Longitudinal Section Taken from a Tensile Specimen in Necking Region that Shows the Nucleation and Coalescence of Microvoids Around Inclusions [79].

cases, ductile fracture occurs through the nucleation of microvoids within the steel, which then grow and coalesce, potentially resulting in the ultimate failure of the material. It has been shown [80] that this nucleation of microvoids preferentially occurs around inclusions, with the coalescence then proceeding as the result of necking developing between the microvoids which surround separate inclusions. A good example of this is shown in Figure 2-16.

When deforming the steel, these voids can form due to the difference in plasticity between the inclusion and the surrounding steel. This "relative plasticity" – as shown by the deformability index (ν) - is the ratio between the true deformation of inclusions to the true deformation in the steel and was summarised by Kiessling [81] in the graph shown in Figure 2-17.

Because inclusions are made up of ionic, covalent and mixed bonding, they are generally brittle at room temperature and do not have strong bonding to the surrounding metallic matrix. This means that when the steel is deformed, inclusions can either elongate in line with the deformation, fracture or show a combination of the two (Figure 2-18). For inclusions that are too hard to deform to the same extent as the surrounding steel matrix ($0 \leq \nu < 0.5$), the combination of low bonding strength to the matrix and the deformation of the matrix itself leads to the formation of a void between the inclusion and the surrounding matrix [78]. The size of the void is then proportional to the amount of deformation the inclusion has undergone - i.e. the lower the ν.

Inclusions with $\sim 0.5 < \nu < 1$, usually deform plastically with the steel and as such, the deformation of the steel alone is not expected to cause voids. However, the inclusions themselves can act as stress raisers in the slip planes of the steel causing anisotropy [19]. This anisotropy cannot be eliminated by further heat treatment [78].

The size and distribution of these inclusions also plays a vital role in void nucleation, growth and coalescence. The size of the inclusion is important because the larger the inclusion, the smaller the strain needed to nucleate a void [80]. As for the distribution of these inclusions, if the inclusions are close enough together, the stress concentrations surrounding the inclusions can interact, allowing voids to coalesce more easily. In fact, if the distance separating the inclusions is small enough, it can actually increase the stress concentration to the point that a micro-crack forms in between the inclusions [77].

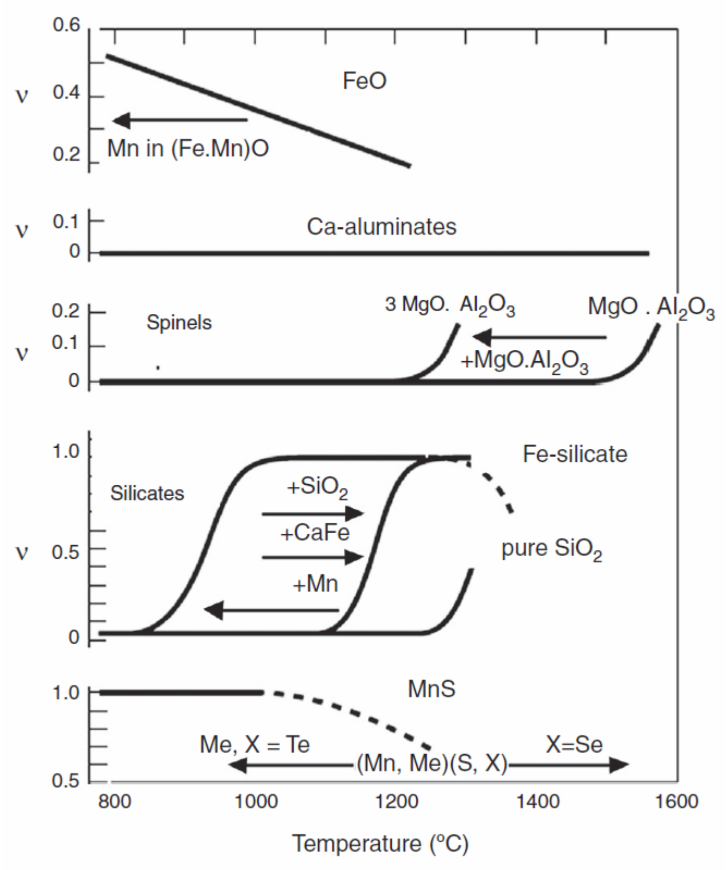

Figure 2-17. How Changing Temperature Affects the Relative Plasticity of Different Inclusions. Please Note That the Curves are Semi-Quantitative in Nature. (Taken from [78] which in turn was adapted from [81])

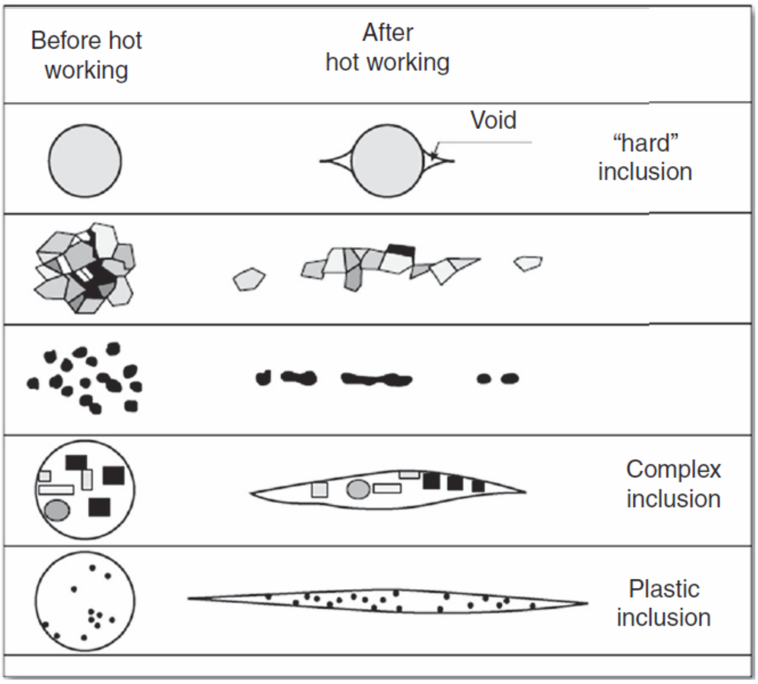

Figure 2-18. Representation of Different Inclusion Types and their Morphologies Before and After Hot Working [78].

Of the two however, it has been shown that the number of inclusions has a greater impact on the properties of the steel. Research conducted by Roesch *et al* [82] on alumina particles within sintered compacts of iron with inclusion volume fractions ranging from pure iron (i.e. 0%) to 7% and particle sizes between 15-35µm can be seen in Figure 2-19. While they concluded that the volume fraction of inclusions was more important than particle size, the research also showed that as the quantity of inclusions increased it resulted in:

1. The disappearance of the upper yield point.
2. Both the yield stress and ultimate tensile stress (UTS) decreasing.
3. A decrease in ductility.

The shape of inclusions themselves also plays a key role. Spherical inclusions by their very nature have no effect on the isotropy of a material. If, however, the inclusion was plastic at working temperature, as mentioned previously, this inclusion would elongate in line with the working direction, resulting in anisotropy in the material.

An example of this is seen on the effect of MnS on tensile properties. In the longitudinal direction, MnS have little to no effect on yield strength, UTS, work hardening exponent or work hardening rate. However, when a 3” bar of AISI 1144

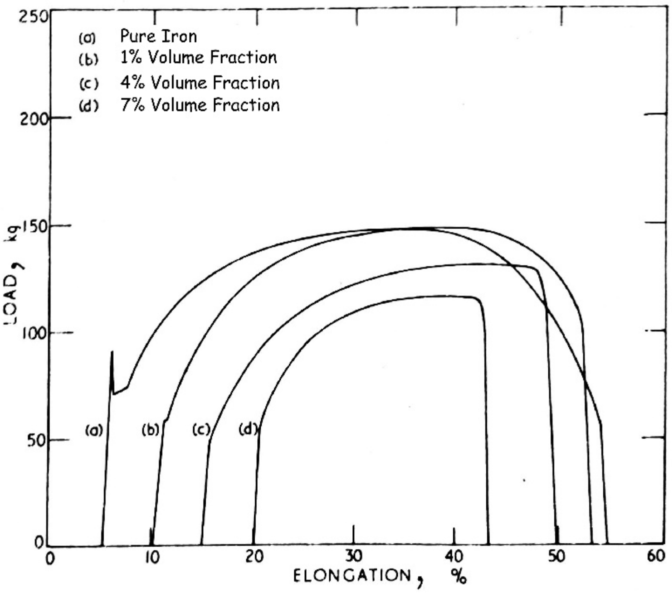

Figure 2-19. Graph Illustrating How the Amount of Alumina Influences the Tensile Properties of Sintered Compacts of Iron [82].

was tested in both the longitudinal and transverse directions, the average UTS dropped by 23.8%, the average yield strength dropped by 24.6% and the elongation dropped by 77% [61].

The key reason for this is that, even though MnS is plastic at the elevated temperatures of hot rolling, when returned to cold working conditions the inclusions become harder than the surrounding ferrite. Instead of deforming with the surrounding matrix, Wu *et al* [83] observed 4 typical variations during the load process (Figure 2-20):

1. Decohesion of the MnS from the surrounding matrix
2. Fragmentation of the bulk MnS inclusions
3. Microvoids forming along the line connecting two MnS inclusions if the void surrounding the inclusion had become rounded, blunting the crack tip.
4. Cracks caused by the sharp tips of the MnS inclusions themselves.

It was found that no cracks that were caused by decohesion of the matrix propagated because the crack tip rounded under the low stress. As the tensile load increased however, stress concentrations formed at the MnS that could not be abated by elastic deformation. This meant that the stress was higher in the regions of the matrix that were perpendicular to the load. As a result, microvoids nucleated in a line which in turn coalesced to form cracks. It was also found that if the inclusions themselves are relatively evenly distributed (Type C in Figure 2-21), the cracks are blunt and quasi-one dimensional and may not propagate until the specimen fractures.

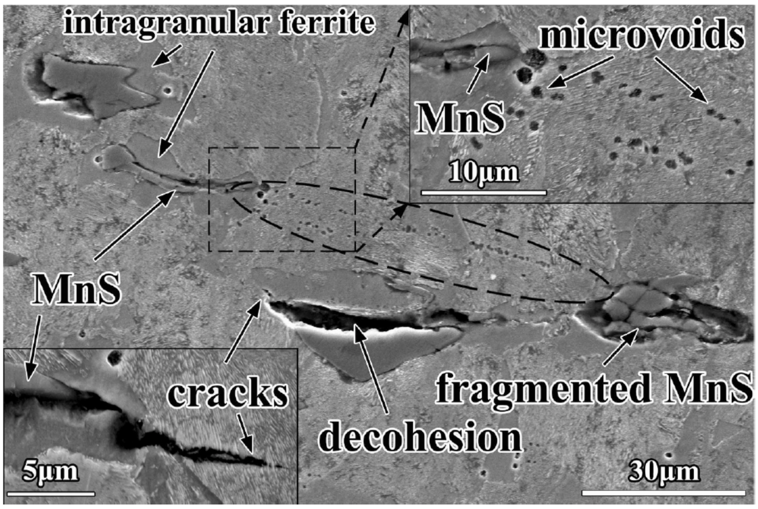

Figure 2-20. Image Taken of the Surface Perpendicular to Necking of a Specimen that was Unloaded at a Strain of 0.1 [83].

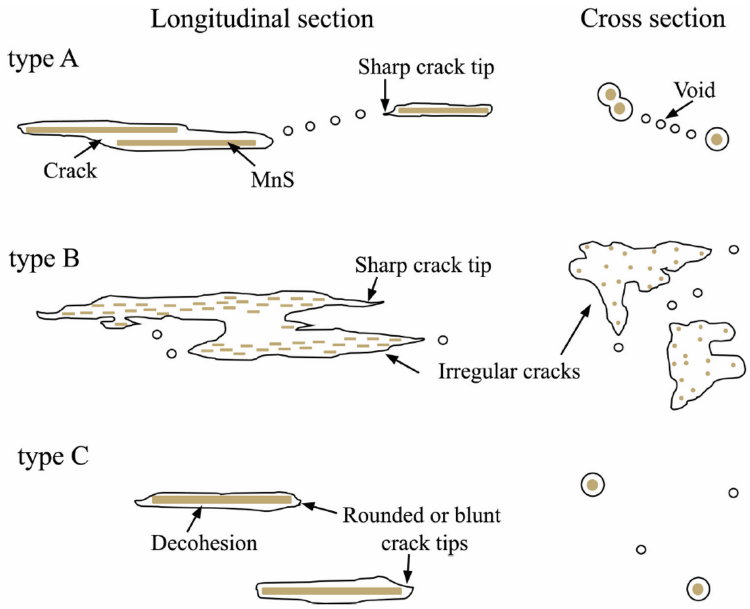

Figure 2-21. Void and Crack Behaviour at Different Types of MnS Inclusions During Deformation [83].

This is because the void coalescence is caused by localised shear and necking between the inclusion. However, at a certain distance, this internal necking of the matrix between two voids becomes inconsequential. At this point the mechanism of failure in samples with MnS Type C is just random void nucleation, growth and coalescence. As this distance decreases so does the strength of the matrix between them leading to the premature end of the necking process and preferential void nucleation and coalescence.

Wu also found that for MnS inclusions that had sharp tips, the increase in stress concentrations at these points causes microcracks to form regardless of the process of void nucleation & coalescence, as shown in Figure 2-20. While not captured in this image, Wu believed that the small radius of the void caused by the decohesion at these tips might be responsible for the cracks. This implies that the more an inclusion has elongated, and thus the higher the inclusions length/width (L/W) ratio , the more likely it is that that inclusion will form a microcrack on the tip that could coalesce, potentially resulting in the earlier failure of the material under transverse loads. The other logical impact would be that, the higher the L/W ratio, the larger the void that would form through decohesion of the matrix and the inclusion, if the load is applied transverse to the rolling direction compared to longitudinally. While it would be preferable to be more quantitative about the impact of the shape of the inclusion, currently there is no literature available that can provide this information.

2.3. Assessment of Inclusion Analysis

With increasingly cleaner steels becoming ever more important to the steel industry, the demand for analysis techniques that can characterise the inclusion population within the steel has only increased. This characterisation consists of evaluating the inclusions' size, distribution, morphology and chemical composition [84, 85]. While there are various techniques and preparation methods that can evaluate one or more of these parameters at the same time [86, 87], the way they accomplish this varies from direct to indirect methods. Direct methods, while typically accurate, tend to have a high cost associated with the analysis. Indirect methods, on the other hand, are fast and inexpensive but as they rely on indicators for inclusions' content, can be unreliable [23].

There are numerous types of direct methods including Sulphur prints, Laser Microprobe Mass Spectrometry (LAMMS), X-ray Photoelectron Spectroscopy (XPS), Mannesmann Inclusion Detection by Analysis Surfboards (MIDAS) [23]. However, the most widely used are optical and scanning electron microscopy [88]. Both these techniques tend to analyse steel cross-sections and, as such, only offer a 2-dimensional representation of a 3-dimensional structure. As such, they are often not a true representation of the inclusion (Figure 2-22).

While optical microscopy offer no chemical-composition of the inclusions unlike EDS-based SEM analysis [89], it is still the most commonly used inspection method in the industry [90]. This is likely due to it being a relatively cheap technique, that does not require extensive training to complete to a high standard. If conducted manually, however, it is not only both incredibly time consuming and tedious [23, 89]. In addition to this, a study by Vander Voort [12] in 2017 found that not only were there misclassification problems associated with manual assessment, there was also a poor level of reproducibility when the experienced metallographers, employed within the study, examined the same samples.

As a result, an effort needs to be made to not only automate this procedure, so it is not only as reproducible and accurate as possible, but also cost/time effective. While commercial software/hardware is available to automate this analysis, they tend to be proprietary and expensive. This proprietary nature therefore means that the method used to assess the inclusions is not fully auditable.

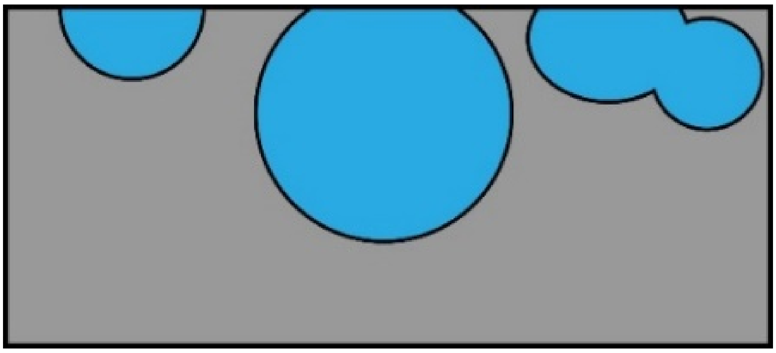

Figure 2-22. Example of 3 Different Inclusions That Would Appear Identical After Cross-Section Analysis.

As the standard method of determining the size and shape of inclusions is by using a microscope, it is too time consuming to implement as a means of quality control during the steel making process [91]. This has led to the development of Optical Emission Spectrometry with Pulse Discrimination Analysis (OES-PDA) for the on-line bulk analysis of steel samples [91, 92]. During OES-PDA analysis, most of the signals are generated by the bulk material, with only a few percent caused by the actual inclusions themselves. In order to identify these inclusions signals, the outliers in the dataset will have to be isolated [93]. Because OES-PDA data is not normally distributed, the peaks at the higher intensities are not only being associated with inclusions themselves, but also incorporates data from the bulk material (Figure 2-23). As a result, existing algorithms that have been developed to detect outliers in normally distributed datasets, have to be modified [93].

After work using OES-PDA to characterise deoxidation inclusions was conducted at IRSID, Tata Steel (then CORUS(UK)) collaborated with SPECTRO to develop a commercial tool [92]. However, while initial work analysing low sulphur Nissan steels yielded both statistical and qualitative identification of inclusions, it was decided to broaden the data interpretation to also include a quantitative component by factoring in the relative emission of each of the elements in the inclusion. This led to an ECSC funded project by Whiteside *et al* [94]. The project had the principal aim of developing both instrumentation and data interpretation algorithms that could predict the final steel products physical properties based off the size and composition of the inclusion population and therefore enable more effective inclusion engineering. This projects model, however, is still in need of validation [95].

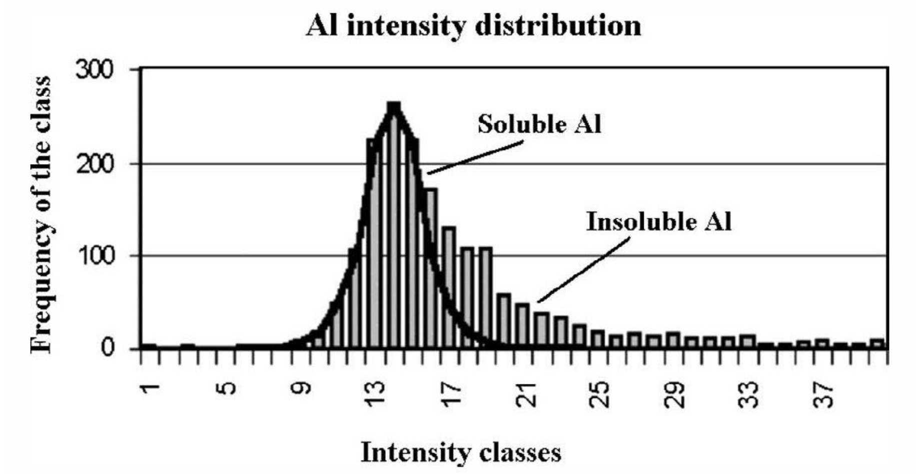

Figure 2-23. Separation of Aluminium that is Associated to Al_2O_3 and the Aluminium that is Dissolved in the Steel Matrix [91].

Because of the cost, time requirements and sampling difficulties which are usually associated with direct inclusion measurements, indirect methods of assessing a steels cleanliness levels are generally used in the steel industry [23]. However, due to their very nature, they can only be used to indicate whether inclusions are within the steel and cannot be definitive [96]. A typical example of an indirect method is that of measuring the total O of the steel [20]. Because O is a key component of the harmful inclusions within steel, a decreasing trend of total O is considered a good estimation of the total amount of oxide inclusions in the steel, and thus its overall cleanliness levels [96].

3.

Chapter 3

Experimental Practices

3.1. Investigated Grade

3.1.1. FB590

The grade that will be the focus of this study is a hot rolled FB590 which is a ferrite-bainite high strength steel (AHSS). It is designed to offer high strength, ductility, and formability and is used in automotive chassis and suspension applications, such as; upper and lower control arms, engine sub-frames and road wheels (specifically wheel discs) where a high strength, highly formable material is required. This grade was chosen because it offers a good range of Ca:S ratios while being a widely used grade. As a result, not only is a deeper understanding of its properties vitally important but it also ensures that it is regularly manufactured in Tata Steel Port Talbot, thereby making sample collection more straightforward.

Upon retesting to obtain PDA analysis, it was discovered that these updated chemistries differed from the original chemistries. Some varied in relatively large amounts, including one sample that was originally classified as Ca treated sample (11QS44/7) subsequentially showing no signs of treatment. This was potentially because these chemistries were calculated from lollipops taken from the ladle, instead of from the actual coil strip. As a result, an effort was made to reanalyse as many samples as possible, in order to get both updated and more accurate chemistries, but also to obtain PDA data from a larger sample set. The resulting chemistries for these retested samples can be seen in Table 3-2 and Table 3-3.

Unfortunately, not all samples were available for reanalysis. As a result, to include the mechanical data from these samples in the analysis, some assumptions had to be made about their chemistries. The subsequent chemistries can be seen in Table 3-4 and Table 3-5, with further details on the calculation of these chemistries shown in Appendix B.

Table 3-1. Accepted composition range chemical composition (wt.%) of FB590.

	C	Si	Mn	Sol. Al	Tot. Al	Nb	Ti	Ca
Aim	0.07	0.197	1.33	0.036	0.04	0.045	0.017	0.0023
Min.	0.05	0.150	1.20	0.020	0.02	0.035	0.010	0.001
Max.	0.08	0.220	1.40	0.045	0.05	0.050	0.020	0.003

Table 3-2. Highlighted OES Chemistries from Retested Samples (Part 1).

Sample I.D.	Process Route	Si	Mn	S	Sol. Al	Tot. Al	Ca	Ca:S	Ca:Al
11QS44/7	P&O	0.019	1.322	0.0054	0.033	0.035	0.0003	0.06	0.009
12S43/1	P&O	0.182	1.324	0.0029	0.03	0.032	0.0029	1.00	0.091
12S43/2	P&O	0.204	1.320	0.0045	0.034	0.036	0.0025	0.56	0.069
13S24/18	P&O	0.198	1.314	0.0042	0.038	0.041	0.0023	0.55	0.056
14S17/1	HR	0.194	1.303	0.0056	0.044	0.047	0.0028	0.50	0.060
14S17/2	HR	0.194	1.301	0.0060	0.045	0.048	0.0025	0.42	0.052
14S17/3	P&O	0.198	1.307	0.0032	0.037	0.039	0.0026	0.81	0.067
14S17/4	HR	0.199	1.306	0.0030	0.036	0.039	0.0025	0.83	0.064
14S17/5	HR	0.243	1.335	0.0059	0.044	0.048	0.0029	0.49	0.060
14S17/6	HR	0.187	1.298	0.0035	0.033	0.036	0.0026	0.74	0.072
14S17/7	HR	0.185	1.293	0.0035	0.032	0.035	0.0024	0.69	0.069
14S17/8	HR	0.179	1.346	0.0050	0.029	0.032	0.0020	0.40	0.063
14S17/9	HR	0.176	1.337	0.0049	0.030	0.033	0.0019	0.39	0.058
14S17/10	HR	0.204	1.340	0.0051	0.039	0.042	0.0028	0.55	0.067
14S17/11	HR	0.201	1.333	0.0051	0.038	0.041	0.0028	0.55	0.068
14S17/12	HR	0.191	1.333	0.0037	0.035	0.038	0.0021	0.57	0.055
14S17/13	HR	0.198	1.364	0.0054	0.034	0.036	0.0020	0.37	0.056
14S21/1	P&O	0.202	1.335	0.0052	0.038	0.040	0.0029	0.56	0.073
14S21/2	P&O	0.164	1.412	0.0079	0.034	0.037	0.0018	0.23	0.049
14S21/4	P&O	0.179	1.345	0.0057	0.025	0.027	0.0015	0.26	0.056
14S21/7	P&O	0.179	1.364	0.0055	0.027	0.029	0.0015	0.27	0.052
14S21/8	P&O	0.179	1.365	0.0052	0.027	0.030	0.0016	0.31	0.053
14S21/9	P&O	0.179	1.369	0.0052	0.027	0.030	0.0016	0.31	0.053
14S21/10	P&O	0.180	1.371	0.0052	0.027	0.029	0.0015	0.29	0.052
14S21/11	P&O	0.181	1.366	0.0054	0.027	0.029	0.0015	0.28	0.052
14S21/12	HR	0.192	1.295	0.0064	0.035	0.038	0.0014	0.22	0.037
14S21/13	HR	0.190	1.286	0.0065	0.034	0.037	0.0015	0.23	0.041
14S21/14	HR	0.193	1.295	0.0066	0.035	0.038	0.0015	0.23	0.039
14S21/15	HR	0.193	1.289	0.0064	0.034	0.037	0.0014	0.22	0.038

HR = Hot Rolled Dry P&O = Hot Rolled Pickled & Oiled

Table 3-3. Highlighted OES Chemistries from Retested Samples (Part 2).

Sample I.D.	Process Route	Si	Mn	S	Sol. Al	Tot. Al	Ca	Ca:S	Ca:Al
14S21/16	HR	0.193	1.292	0.0058	0.031	0.034	0.0014	0.24	0.041
15S24/1	HR	0.202	1.354	0.0023	0.038	0.041	0.0023	1.00	0.056
15S24/2	HR	0.203	1.350	0.0027	0.041	0.044	0.0023	0.85	0.052
15S24/3	HR	0.203	1.350	0.0029	0.041	0.044	0.0025	0.86	0.057
15S24/4	HR	0.199	1.322	0.0029	0.033	0.036	0.0027	0.93	0.075
15S24/5	HR	0.196	1.326	0.0021	0.030	0.033	0.0024	1.14	0.073
15S24/6	HR	0.186	1.341	0.0015	0.032	0.035	0.0021	1.40	0.060
15S24/7	HR	0.190	1.329	0.0022	0.034	0.037	0.0025	1.14	0.068
15S24/8	HR	0.184	1.334	0.0018	0.036	0.038	0.0021	1.17	0.055
15S24/9	HR	0.184	1.323	0.0014	0.032	0.035	0.0021	1.50	0.060
15S24/10	HR	0.191	1.331	0.0020	0.032	0.034	0.0025	1.25	0.074
15S24/11	HR	0.187	1.318	0.0021	0.034	0.037	0.0025	1.19	0.068
15S24/12	HR	0.188	1.317	0.0023	0.035	0.037	0.0027	1.17	0.073
15S24/13	HR	0.187	1.321	0.0023	0.034	0.037	0.0027	1.17	0.073
15S24/14	HR	0.199	1.365	0.0025	0.037	0.040	0.0024	0.96	0.060
15S24/15	HR	0.197	1.362	0.0030	0.040	0.043	0.0025	0.83	0.058
16S18/10	HR	0.018	1.184	0.0041	0.042	0.045	0.0003	0.07	0.007
16S18/14	HR	0.028	0.731	0.0048	0.034	0.037	0.0003	0.06	0.008
16S18/15	HR	0.023	0.739	0.0049	0.039	0.042	0.0003	0.06	0.007
16S18/17	HR	0.027	1.138	0.0042	0.050	0.053	0.0003	0.07	0.006
16S18/21	HR	0.024	1.164	0.0051	0.061	0.065	0.0003	0.06	0.005
16S18/22	HR	0.015	1.098	0.0046	0.026	0.028	0.0003	0.07	0.011
16S18/24	HR	0.025	1.179	0.0051	0.041	0.045	0.0003	0.06	0.007
16S18/25	HR	0.024	1.095	0.0037	0.045	0.048	0.0003	0.08	0.006
16S18/26	HR	0.016	1.106	0.0048	0.026	0.028	0.0003	0.06	0.011
16S18/27	HR	0.016	1.146	0.0046	0.045	0.048	0.0003	0.07	0.006

Table 3-4. Averaged OES Chemistries from Samples that Were not Available for Retesting but Had Samples from the Same Heat Number Retested.

Sample ID.	Process Route	Si	Mn	S	Sol. Al	Tot. Al	Ca	Ca:S	Ca:Al
13S24/4	P&O	0.198	1.314	0.0042	0.038	0.041	0.0023	0.55	0.056
13S24/5	P&O	0.198	1.314	0.0042	0.038	0.041	0.0023	0.55	0.056
13S24/6	P&O	0.198	1.314	0.0042	0.038	0.041	0.0023	0.55	0.056
13S24/13	HR	0.198	1.314	0.0042	0.038	0.041	0.0023	0.55	0.056
13S24/14	HR	0.198	1.314	0.0042	0.038	0.041	0.0023	0.55	0.056
13S24/15	HR	0.198	1.314	0.0042	0.038	0.041	0.0023	0.55	0.056
13S24/16	P&O	0.198	1.314	0.0042	0.038	0.041	0.0023	0.55	0.056
13S24/17	P&O	0.198	1.314	0.0042	0.038	0.041	0.0023	0.55	0.056
14S21/3	P&O	0.184	1.370	0.0057	0.034	0.037	0.0020	0.35	0.054
14S21/5	P&O	0.180	1.363	0.0054	0.027	0.029	0.0015	0.29	0.052
14S21/6	P&O	0.180	1.363	0.0054	0.027	0.029	0.0015	0.29	0.052

Table 3-5. Estimated Chemistries for Samples that Were Neither Available for Retesting nor had Samples from the Same Heat Retested.

Sample ID.	Process Route	Si	Mn	S	Sol Al	Tot Al	Ca	Ca:S	Ca:Al
12S23/13	HR	0.2069	1.3200	0.0024	0.0312	0.0330	0.0024	1.00	0.073
13S24/1	HR	0.1815	1.2802	0.0031	0.0331	N/A	0.0015	0.48	N/A
13S24/2	HR	0.1815	1.2802	0.0031	0.0331	N/A	0.0015	0.48	N/A
13S24/3	HR	0.1815	1.2802	0.0031	0.0331	N/A	0.0015	0.48	N/A
13S24/7	P&O	0.1815	1.2802	0.0031	0.0331	N/A	0.0015	0.48	N/A
13S24/8	P&O	0.1815	1.2802	0.0031	0.0331	N/A	0.0015	0.48	N/A
13S24/9	P&O	0.1815	1.2802	0.0031	0.0331	N/A	0.0015	0.48	N/A
13S24/10	HR	0.1747	1.2563	0.0018	0.0263	N/A	0.0023	1.25	N/A
13S24/11	HR	0.1747	1.2563	0.0018	0.0263	N/A	0.0023	1.25	N/A
13S24/12	HR	0.1747	1.2563	0.0018	0.0263	N/A	0.0023	1.25	N/A
13S3/1	HR	0.1913	1.2882	0.0025	0.0283	N/A	0.0030	1.21	N/A
13S3/2	HR	0.1913	1.2882	0.0025	0.0283	N/A	0.0030	1.21	N/A
13S3/3	P&O	0.1913	1.2882	0.0025	0.0283	N/A	0.0030	1.21	N/A
14S17/14	HR	0.0322	0.4818	0.0040	0.0253	N/A	0.0014	0.35	N/A
14S17/15	HR	0.0322	0.4818	0.0040	0.0253	N/A	0.0014	0.35	N/A
14S17/16	HR	0.0459	0.5077	0.0017	0.0341	N/A	0.0016	0.95	N/A
14S17/17	HR	0.0410	0.5027	0.0048	0.0331	N/A	0.0016	0.33	N/A
14S17/18	HR	0.0410	0.5027	0.0048	0.0331	N/A	0.0016	0.33	N/A
14S17/19	HR	0.1562	1.2056	0.0040	0.0263	0.0282	0.0027	0.67	0.096
14S17/20	HR	0.0586	0.4579	0.0018	0.0370	0.0408	0.0019	1.03	0.047
14S17/21	HR	0.0390	0.4878	0.0032	0.0370	0.0398	0.0021	0.64	0.053
14S17/22	HR	0.0390	0.6869	0.0040	0.0390	0.0427	0.0016	0.40	0.037
14S17/23	HR	0.0488	0.6769	0.0036	0.0312	0.0340	0.0015	0.41	0.044
14S17/37	P&O	0.1601	1.2056	0.0040	0.0263	0.0281	0.0027	0.67	0.096
14S17/38	P&O	0.1601	1.2056	0.0040	0.0263	0.0281	0.0027	0.67	0.096
14S17/39	P&O	0.1601	1.2056	0.0040	0.0263	0.0281	0.0027	0.67	0.096

3.2. Mechanical Testing

3.2.1. Tensile Testing

Tensile testing was conducted in order to calculate the ultimate tensile strength (UTS), elongation and strain to failure of the material. This was then used to compare the differences between steels of varying levels of calcium sulphur ratio.

The tensile testing was completed on a Zwick Roell 1471 (Figure 3-1) under a 100kN load. The analysis was completed at Tata Steel's Harbourside facility in Port Talbot by an on-site technician, due to restrictions regarding access to the equipment. The testing was completed so that it adheres to the BS EN 10002-1:2001 [97] specifications. The instrument works under an electric screw mechanism with serrated wedge grips to hold onto the sample. It is equipped with an extensometer for both gauge length and width.

The samples were taken from the positions shown in Figure 3-2 and cut to the dimensions illustrated in Figure 3-3.The only variable to these dimensions was the sample thickness, which varied depending on the sheet thickness from which the sample was taken from.

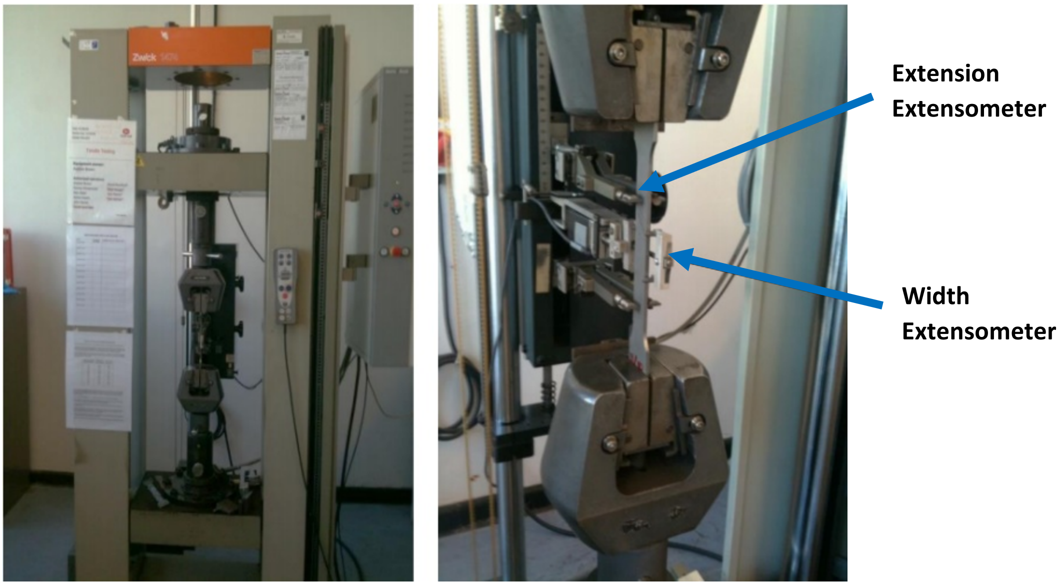

Figure 3-1. Zwick Tensile Tester

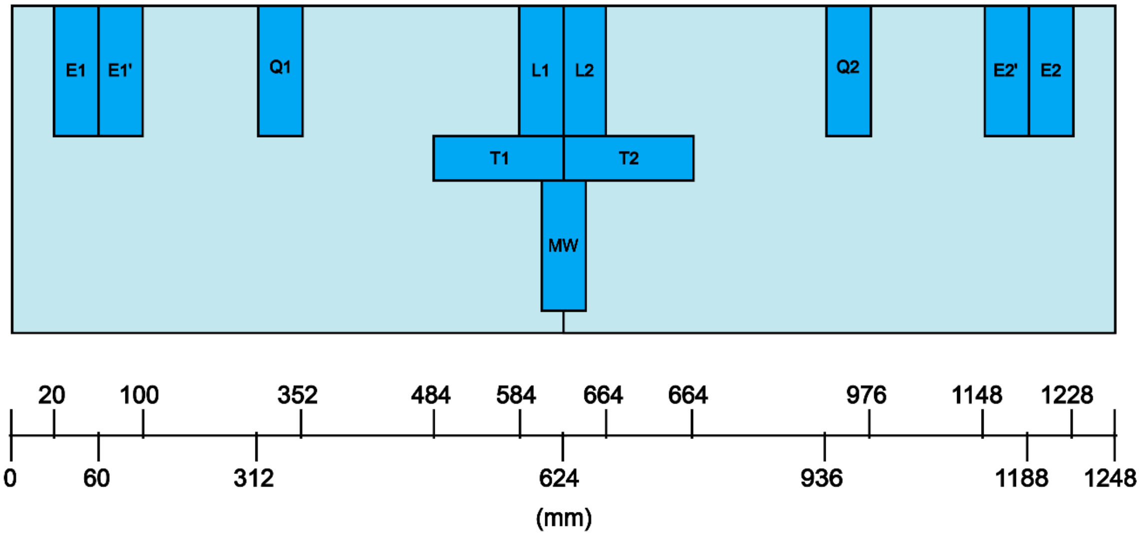

Figure 3-2. Positions of the Samples Through the Width of the Coil.

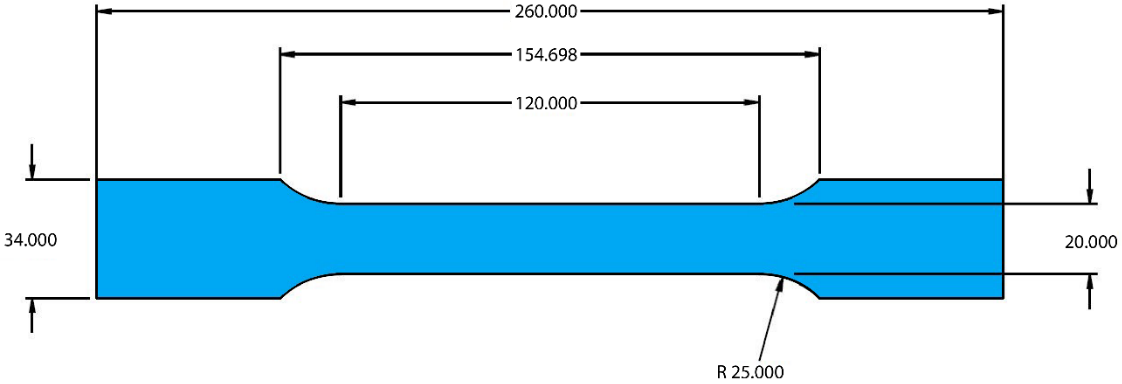

Figure 3-3. Tensile Test Specimen Dimensions

3.2.2. Hole Expansion Testing

Depending on its design, the vast majority of automotive chassis components undergo at least some forming, hole punching and expansion during manufacture. As a result, the Hole Expansion Coefficient (HEC) is an important product property when it comes to HR strip steels as a means of assessing its sheared edge flangeability. This gives a measure of the quality of the steel by showing how much the hole size has increased the moment a crack propagates through the thickness of the material.

The hole expansion testing was performed at Tata Steel's Swindon Technology Centre (STC) in Rotherham. The testing was conducted by an on-site technician in accordance to the ISO 16630 standard [98] due to restrictions on access to the equipment. The sample is cut to a 100mm x 100mm square before a 10mm hole is punched in the centre of each sample. The sample is then clamped firmly, exposing the centre area (70mm diameter) with the burr of the hole facing up. This hole is then expanded using a conical punch with a 40mm diameter and a 60° top angle (Figure 3-4). When a through thickness crack is seen, the punches movement is stopped immediately, and the final diameter of the hole is measured.

The HEC is then calculated using the following equation:

$$\eta = \frac{D_f - D_0}{D_0} \times 100\% \qquad (3\text{-}1)$$

Where D_0 is the average initial diameter of the hole and D_f is the average final diameter of the hole.

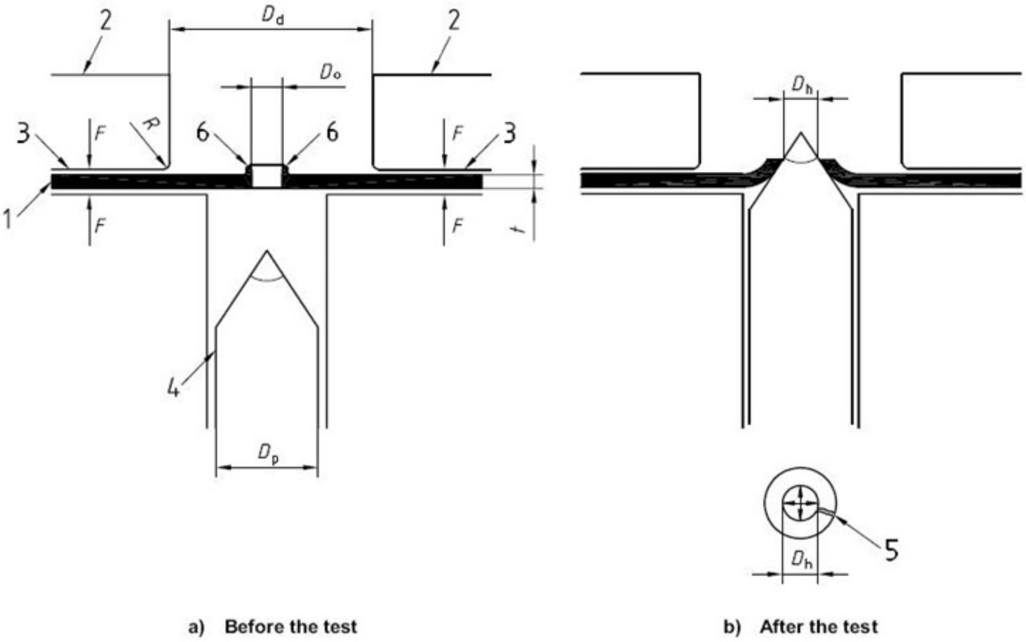

Figure 3-4. Illustration of Hole Expansion Test [98]**.**

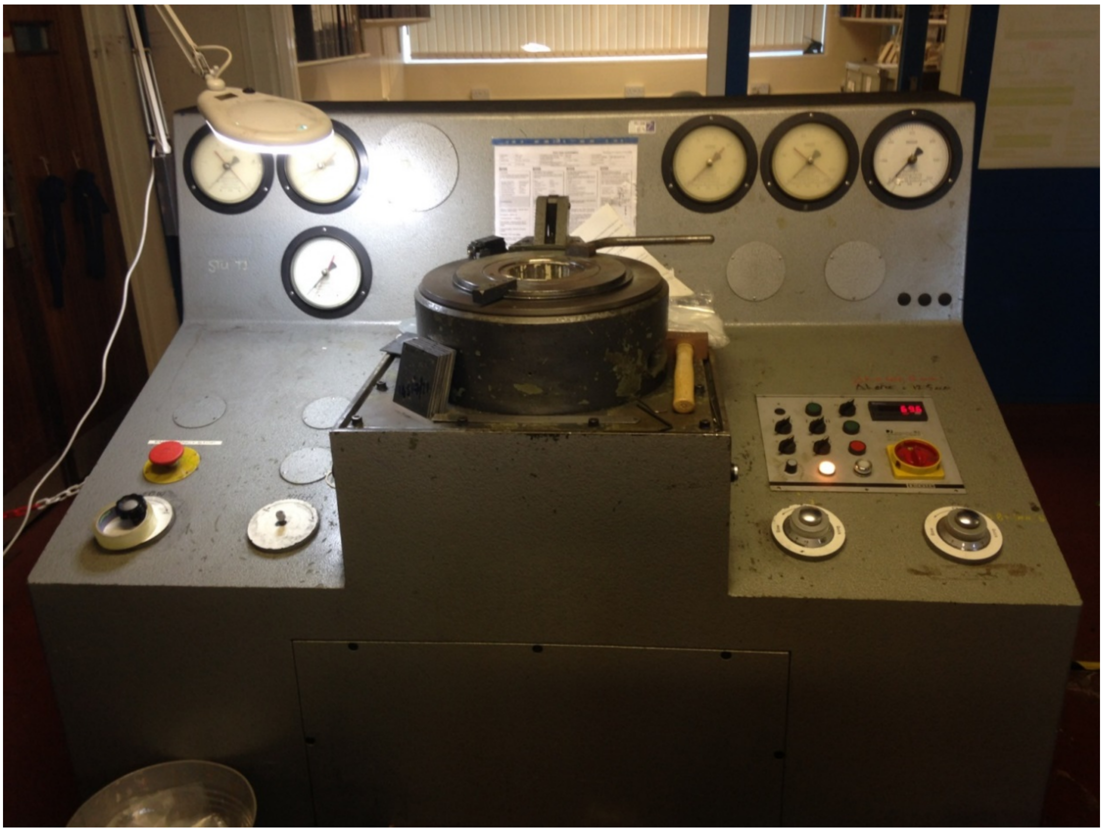

Figure 3-5. Hole Expansion Tester

3.3. Sample Preparation

To conduct the inclusion analysis in line with both ASTM E45 [99] and BS EN 10247 [100], 200mm^2 samples were ground and polished down to a minimum of 0.25µm finish, using the grinding and polishing procedure found in Table 3-6. This ensured that any scratches remaining on the sample did not interfere with the greyscale reading for the automated inclusion assessment discussed in section 3.4.3.

The polishing pads listed in Table 3-6 were chosen specifically as any other type of polishing pad designed for this finish range led to a significant amount of inclusion pull-out. The same was also true for the general polishing parameters.

Table 3-6. Grinding and Polishing Procedure.

Stage	Grit	Cloth	Time (min)	Force (N)	Disk Rotation Speed (U/min)	Head Rotation Speed (U/min)
Grinding	P80	N/A	3:00	12	- 150	- 50
	P360		3:00			
	P600		4:00			
	P2500		6:00			
Polishing	6 µm Monocrystalline Oil Based Diamond Suspension	MetPrep Planocloth	15:00			+ 50
	1 µm Monocrystalline Oil Based Diamond Suspension	MetPrep Alphacloth	15:00			
	0.25 µm Monocrystalline Oil Based Diamond Suspension	MetPrep Alphacloth**/ Buehler Microcloth***	1:00			
	0.05 µm Alumina Powder Micropolish Suspended in Ethanol*	MetPrep Chemicloth	15:00			

\+ = Clockwise - = Counter-Clockwise

* Found to be ineffective as it led to mild etching of the sample but did complete some samples successfully so included for completeness. Quickly replaced with 0.25µm Monocrystalline Oil Based Diamond Suspension

** Used if conducting this stage on the ATM Saphir 550 Autopolisher

*** Used if conducting this stage by hand on the Struers LaboPol-5 also at a disk rotation speed of 150 U/min.

3.4. Inclusion Measurements

3.4.1. Manual Inclusion Measurements

To give the most complete analysis possible for the inclusion population of each sample, which can also be compared to an automated procedure, the Random Scanning technique for Average Field Measurements: Method K – BS EN 10247 [100] was used. This is one of the assessment techniques employed by Tata Steel.

Based on previous analysis (i.e. Reichart Method), an underestimation of the average number of inclusions was employed with 10 inclusions per 1mm^2 predicted. This meant, according to the standard, a minimum number of 80 fields had to be analysed at 100x magnification to obtain a minimum 90% level of confidence in the data. In a further effort to ensure accuracy, these fields were taken at roughly the top, a quarter down and in the middle of the sample to incorporate the variation of inclusion size and shape through the thickness of the steel strip.

The sample was investigated using a bright field inverted optical microscope (Zeiss Axio Observer 7). Using the microscope's "Mosaic" function, an image was obtained of the entire surface area by stitching together a series of images. The entire image was kept in focus by using the 'Focus Correction' tool within the AxioVision software. This tools allows you to set points that change the focus level as the microscope moves around the sample, an example of which is shown in Figure 3-6.

A 710µm^2 region of interest (ROI) was placed over the surface of the sample at 100x magnification. An example is shown in Figure 3-8 of the grid setup on the Reichart microscope. Only inclusions within this area were analysed with any that overlapped with the ROI's boundary were ignored. The ROI was moved around the sample surface, ensuring that there was no overlap of the individual grids, as shown in Figure 3-9. The 'line' of ROI's was taken to try to ensure the key areas of the steel strip (Upper/Lower edge, Middle and Upper/Lower Third) were all analysed.

Each inclusion was measured and any with a length larger than 3µm and a width larger than 2µm was included. The inclusions were then characterised based on their shape, i.e. whether the inclusion classed as an elliptical or globular inclusion. This classification was completed by dividing the height of the inclusion by its width. If the resulting aspect ratio was larger than 1.3, the inclusion would be classified as an elliptical inclusion, if not, it was categorised as globular (Figure 3-10). If 2 or more inclusions were close enough together to satisfy the conditions laid out in Figure 3-11 they were classed as a single inclusion. The resulting data was then input into excel to calculate statistics on the inclusion population.

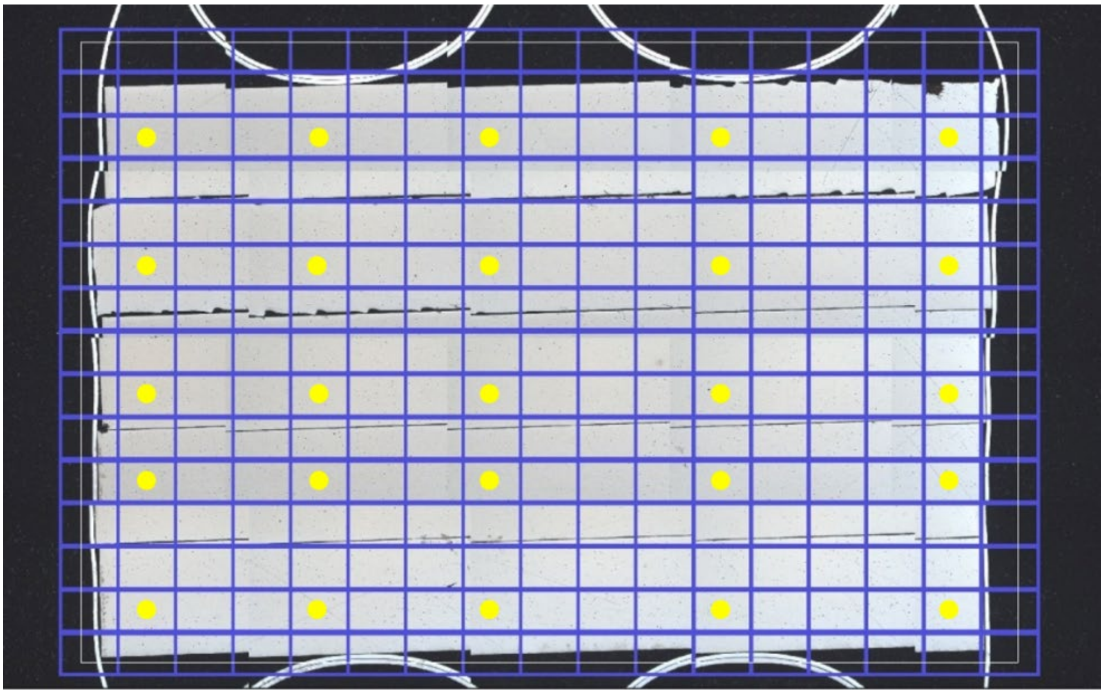

Figure 3-6. Example of image positions plus the Focus Correction points.

Figure 3-7. Final stitched Images

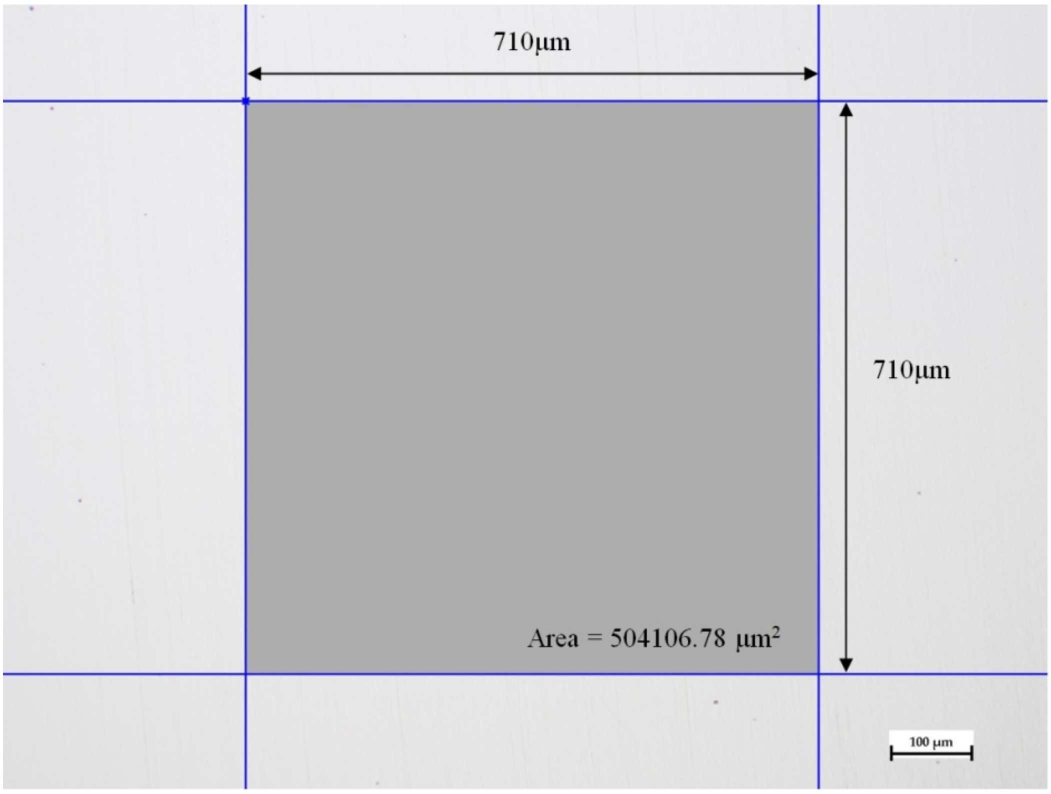

Figure 3-8. Area of examination (710µm^2)

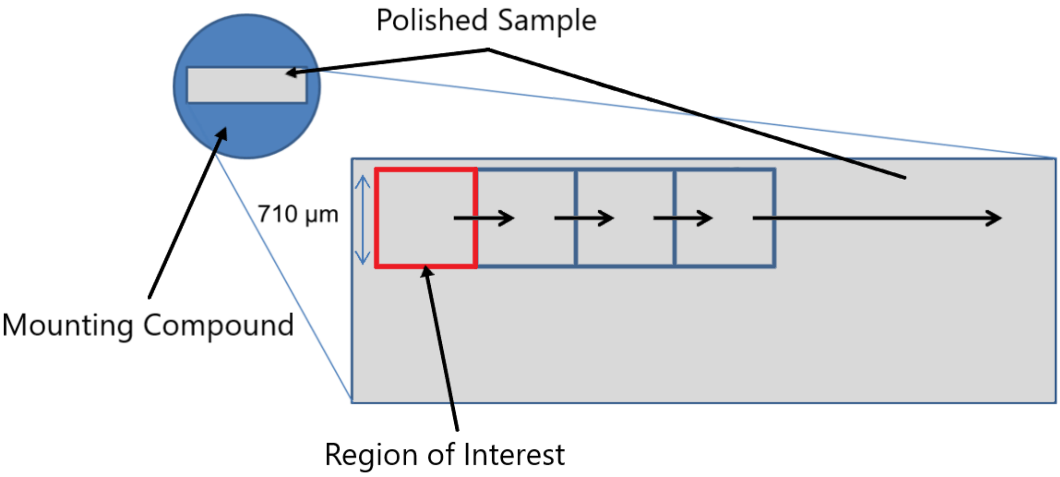

Figure 3-9. Image illustrating movement around the sample (Adapted from [101]).

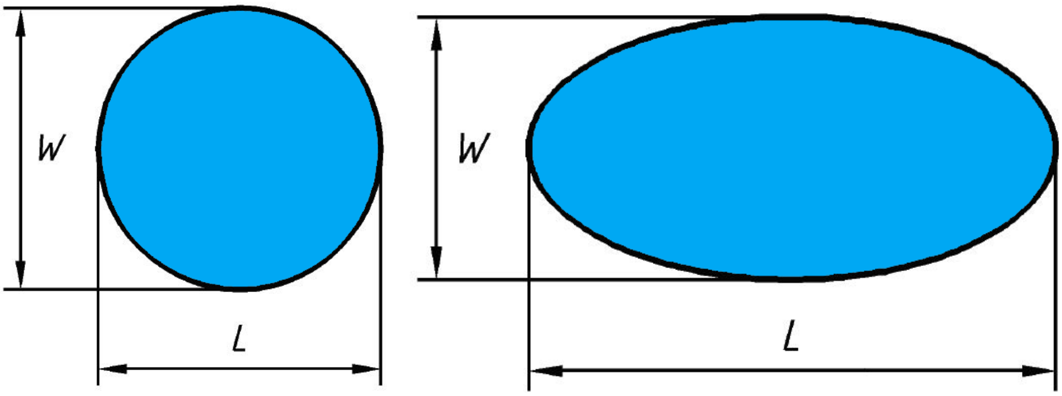

(a) (b)

Figure 3-10. Definition of (a) Globular (b) Stringer inclusion as standard shapes [100].

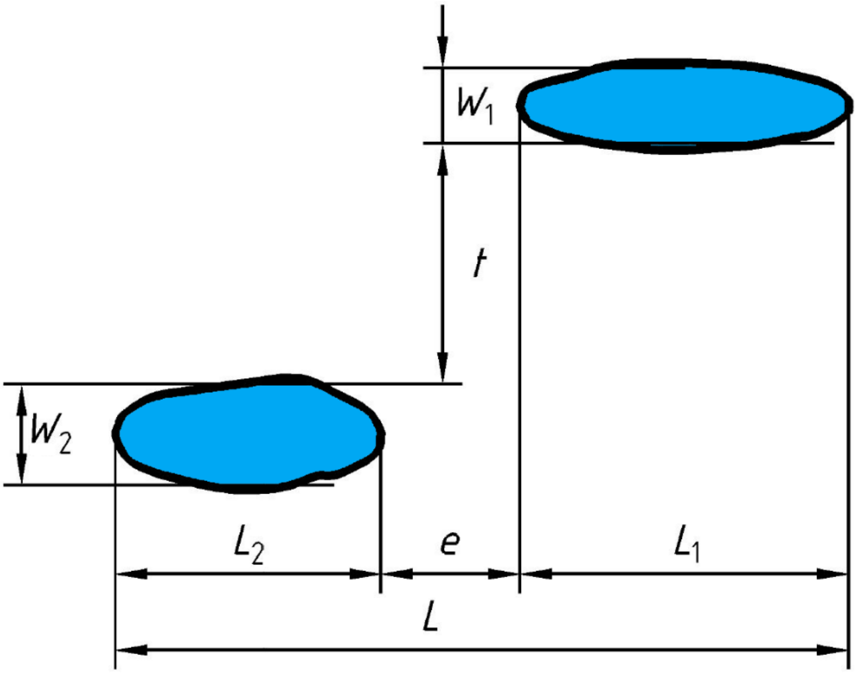

<u>1 Inclusion</u>

If $e \leq 40$ µm and $t \leq 10$ µm
$L = L_1 + e + L_2$
$w_2 > w_1$
$w = w_2$

<u>2 Inclusions</u>

if $e > 40$ µm or $t > 10$ µm
$L_1 = L_1$ $w_1 = w_1$
$L_2 = L_2$ $w_2 = w_2$

Figure 3-11. Definition of inclusion that is composed of single particles [100].

3.4.2. Semi-Automated Inclusion Measurements (Reichart Method)

A 200mm^2 sample was ground and polished before being investigated under a bright field optical microscope (Reichart MeF3), as close to both BS EN 10247 [100] and ASTM E45 [99] as was viable. It was not successfully analysed to the complete standard due to time restraints on accessing the equipment, the volume of images to be analysed (roughly 300 per sample – roughly taking 5 minutes each to capture plus processing time) and image overlap/separation. This overlap/separation was caused by the simplistic nature of the stage, and how it moved around the sample. This would have resulted in some inclusions being counted twice or not at all.

A compromise was made such that 10 randomly placed images were taken per sample. This meant an average inclusion density and average inclusion type could be calculated, per sample, without it being too time consuming, while still giving a good overall view of the sample.

The captured images were then loaded into Photoshop and cropped to the grid size. Using Photoshop's 'Magic Wand' tool - which selects all the pixels that contain a similar colour, within a controllable range, of the selected pixel - the inclusions were isolated, before deleting the unnecessary parts of the image. A manual check was necessary to ensure that only the correct features are included.

These inclusions were then quantified using the 'Record Measurement' tool which counts the number of pixels within the designated area and converts the data into microns. This calculation is based on the measurement taken from the scale bar and the resulting data was exported into Excel for further analysis. Using the method described in Section 3.4.1, the inclusions were then characterised into the globular/stringer shape categories, as well as by inclusion density, average size and area.

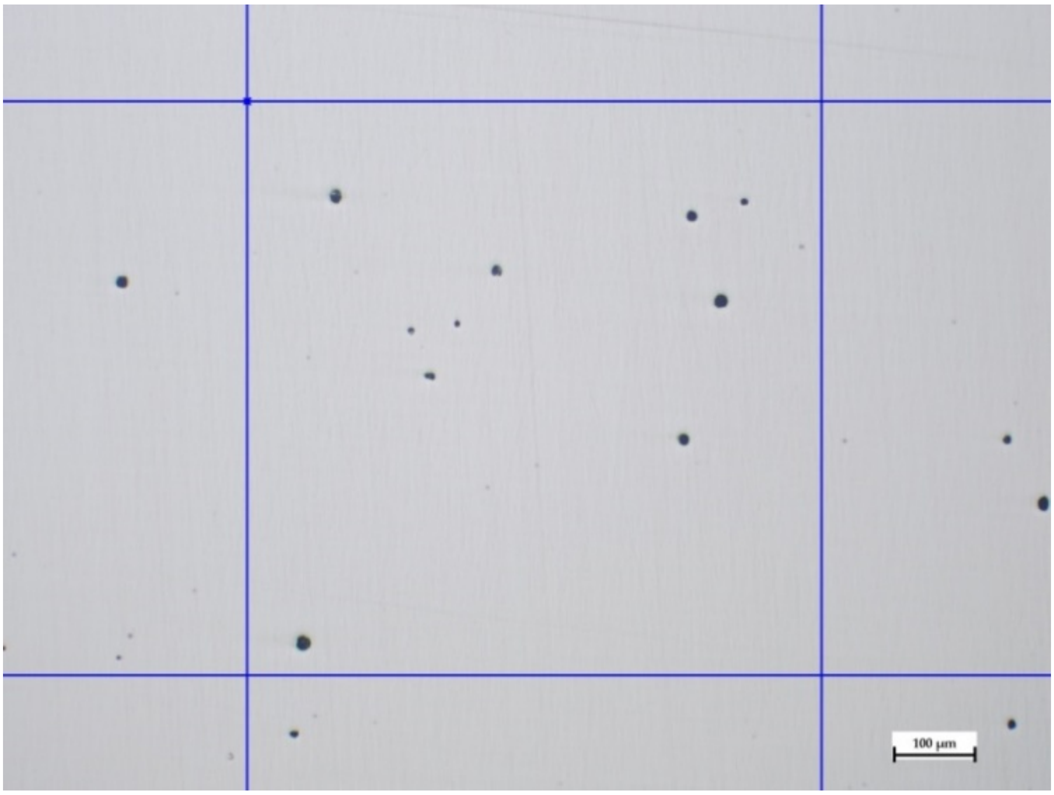

Figure 3-12. Inclusion Cell Pre-Photoshop

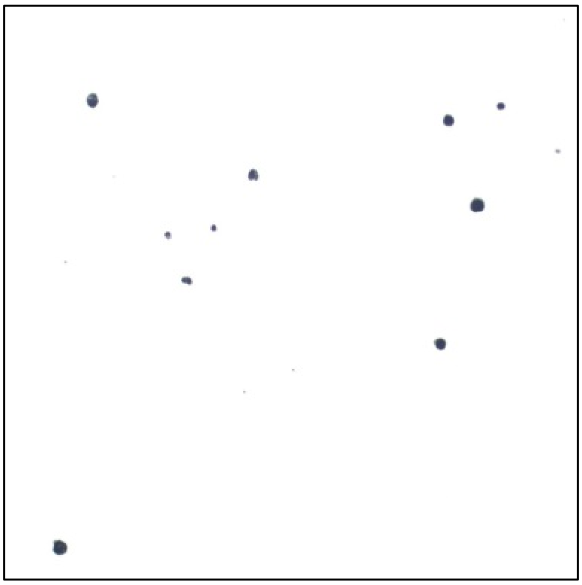

Figure 3-13. Inclusion Cell Post-Photoshop

3.4.3. Automated Inclusion Analysis (Observer Method)

The same images used for the manual inclusion analysis described in Section 3.4.1 were also used for the automated inclusion analysis in an effort to better compare both the results and the assessment method. This also ensured that the procedure/sample was as close to the requirements of the BS EN 10247 [100] and ASTM E45 [99] standards as possible. The main deviation being, any inclusion that was isolated by the software was treated as an individual and not by the standards shown in Figure 3-11. This will be discussed in greater detail in Chapter 5 – Assessment of Automated Inclusion Analysis.

The final stitched image (Figure 3-7) was then loaded into ImageJ where it was cropped and repositioned to create a single image of just the metal surface that is as close to 200mm^2 as possible, ensuring that the image was aligned with the rolling direction. The image was then converted to an RGB stack so as to allow for its threshold to be adjusted in order to highlight the inclusions as effectively as possible (Figure 3-14). These features were then quantified using the ‘Analyse Particle’ tool, which counts the number of pixels within the inclusions on the ‘thresholded’ image and converts that data into microns using calibration from the scale bar.

After using the ‘Analyse Particle’ tool, a data file for the entire inclusion population was created, plus an image of the ‘masked’ inclusions (Figure 3-15). The macro shown in Appendix B was then applied, separating the image into the designated 710µm^2 region of interests (ROI) required by the standards, before measuring the size of each inclusion within each ROI. While this was occurring, any inclusion that crossed the boundary of the ROI, and any ROI that did not satisfy the 710µm^2 area requirement were disregarded, just as the standards dictate. As described in Section 3.4.1, not all the data produced by ImageJ could be used. As a result, IF functions and filters were used to discard the unwanted data and to characterise the inclusions based on their shape.

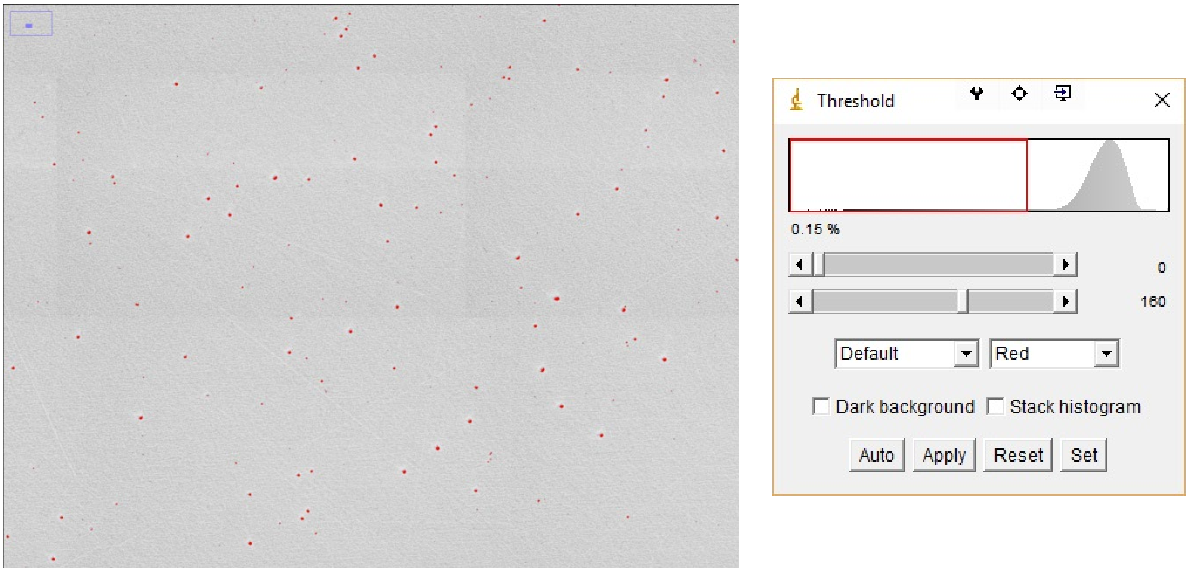

Threshold

0.15 %

0

160

Default

Red

☐ Dark background ☐ Stack histogram

[a] [b]

Figure 3-14 [a] Sample after ‘thresholding’ [b] Thresholding Scale

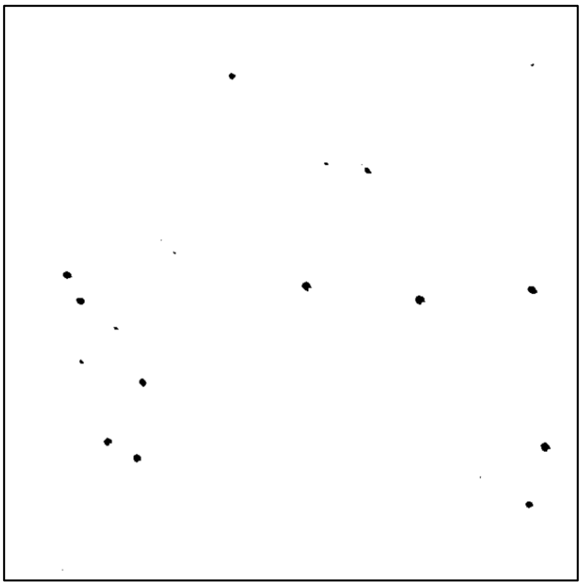

Figure 3-15. Example of the ‘Masked’ inclusions after using ‘Analyse Particle’ Tool.

3.4.4. Correlated Inclusion Analysis (EDS)

Without moving the sample from the correlative stage (CorrMic MAT Universal B) (Figure 3-16.), it was then placed in the Zeiss EVO LS 25 scanning electron microscope (SEM) (Figure 3-17). The stage itself has 3 calibration points which allow for the location of inclusions within the image obtained from the light microscope, so that the SEM can accurately navigate to them. This enables the easy evaluation of a range of inclusion types and sizes using energy-dispersive X-ray spectroscopy (EDS) through Oxford Instruments Aztec Software and Detector (XMax50n).

For the EDS analysis to function, the SEM must first stimulate the emission of 'characteristic' X-Rays from the sample. For this to occur, a beam of high-energy electrons is focused onto the sample surface. Upon interaction with atoms within the material's structure, electrons in their inner shell can become excited. If the energy of the interacting electron is greater than the ionisation energies of the inner-shell electrons (i.e. critical ionisation energy), the electron will be ejected from the shell, creating a hole where the electron used to be. This causes an electron from a higher-energy shell to 'drop in' to fill this hole. To facilitate this energy loss, the excess energy is released as an X-Ray which is 'characteristic' of the atomic structure of the emitting element and can be measured to allow quantification of the specimen composition.

The EDS analysis parameters shown in Table 3-7 were applied to generate either a spectrum from a specific point or a layered elemental map of an inclusion.

A process time of 6 was chosen for analysing spots to limit the effect of overlapping peaks in the resulting spectrum, that might limit the accuracy of the elemental measurement. At this processing time, the effect of 'dead time' is limited because the measurement will be averaged only for that spot.

For creating the elemental maps, a process time of 4 was chosen to both increase the number of counts and to limit the effect of 'dead time' which would be higher in some areas than others. A frame rate of 180 with a pixel dwell time of 100 was chosen to also maximise the amount of counts in these areas.

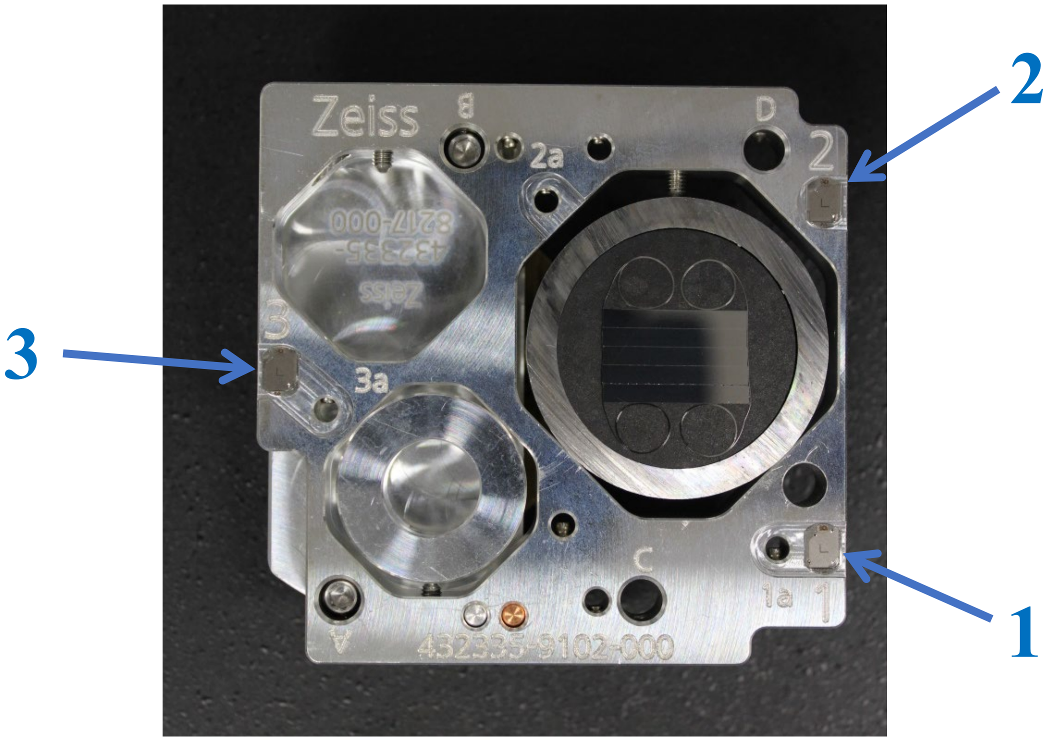

Figure 3-16. CorrMic MAT Universal B Correlative Stage

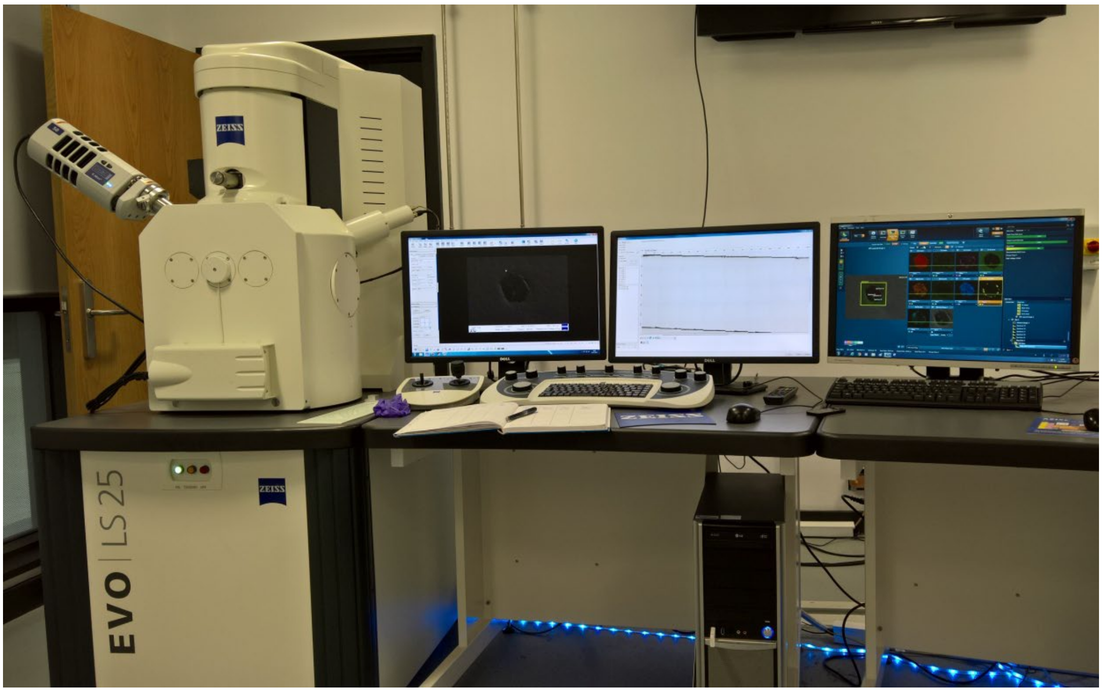

Figure 3-17. Zeiss EVO LS 25 with AZtec EDS Software.

Table 3-7. EDS Acquisition Parameters.

Scan Image Settings	**Image Scan Size**	**1024**
	Dwell Time (μs)	70
	Input Signal	SE
	Number of Frames	1
	Frame Time (secs)	55.05
	Auto Lock	Auto
EDS Acquire Spectrum Settings	Energy Range (keV)	20
	Number of Channels	1024
	Process Time	6
	Acquisition Mode	Counts
	Count Limit	300,000
	Pulse Pile Up Correction	Yes
Map Data Settings	Resolution	1024
	Fixed Duration → Frame Count	180*
	Energy Range (keV)	20
	Number of Channels	1024
	Process Time	4
	Pixel Dwell Time (μs)	100
	Frame Live Time (s)	0:01:19

* If this leads to an excessive scan time, the scan was manually stopped after 1 hour to ensure a maximum throughput of inclusion analysis in the allotted time on the instrument while still maintaining accurate measurements and maps.

3.4.5. Inclusion Analysis (Automated SEM)

Analysis was carried out using the ‘Particle Analysis’ module within the EDAX Genesis software on a FEI Quanta 600 Field Emission Gun Scanning Electron Microscope (FEG-SEM) with an EDAX 132-10 EDS Detector. For each of the samples, it was the centre region that was analysed.

Initially attempts were made to adhere to the BS EN 10247 standard, in order to aid in comparison. However, the large 710 μm^2 field size dwarfed the finer particles, making them difficult to identify. A significant amount of de-focussing was also encountered due to the large scan area, resulting in particle identification being very unreliable. This, combined with the number of particles found in the first sample, resulted in both the scan area and the field size being reduced.

For the final analysis, the scans consisted of 400 adjacent fields in a 20x20 matrix. This meant that the field size was limited to 250 μm x 196 μm with an individual scan area of ~19.6 mm^2. This lowered the de-focussing significantly while still enabling a good sample size of the total inclusions analysed in each of the samples. Because finer particles can be difficult to determine using the SEM, the minimum inclusion size was also set to 0.49 μm. The data obtained was then exported into Excel for analysis in a similar manner to the methods described in Section 3.1.

3.5. Grain Size Analysis

The samples were ground and polished down to a 1μm finish and then etched using 2% Nital. This caused preferential attack on the grain boundaries within the steel sample which enables them to be visible under white light microscopy (Zeiss Axio Observer 7). The grain size was calculated using the 'Grain Size Measurement' tool within the AxioVision software in accordance to the BS EN ISO 643 standard [102].

The two phases present within the steel were first separated using the phases' differing grey scales (Figure 3-18). Various parameters were then adjusted, enabling the software to trace over the grain boundaries as accurately as possible (Figure 3-19). Any obvious errors in tracing were then manually corrected. This was repeated at 5 different locations through the thickness of the steel strip, thus ensuring a sample size of over 1000 grains were analysed. The software is able to output this data in the format of the standard, as well as the raw data. This raw data was then analysed in Excel in order to obtain an average grain size in μm^2.

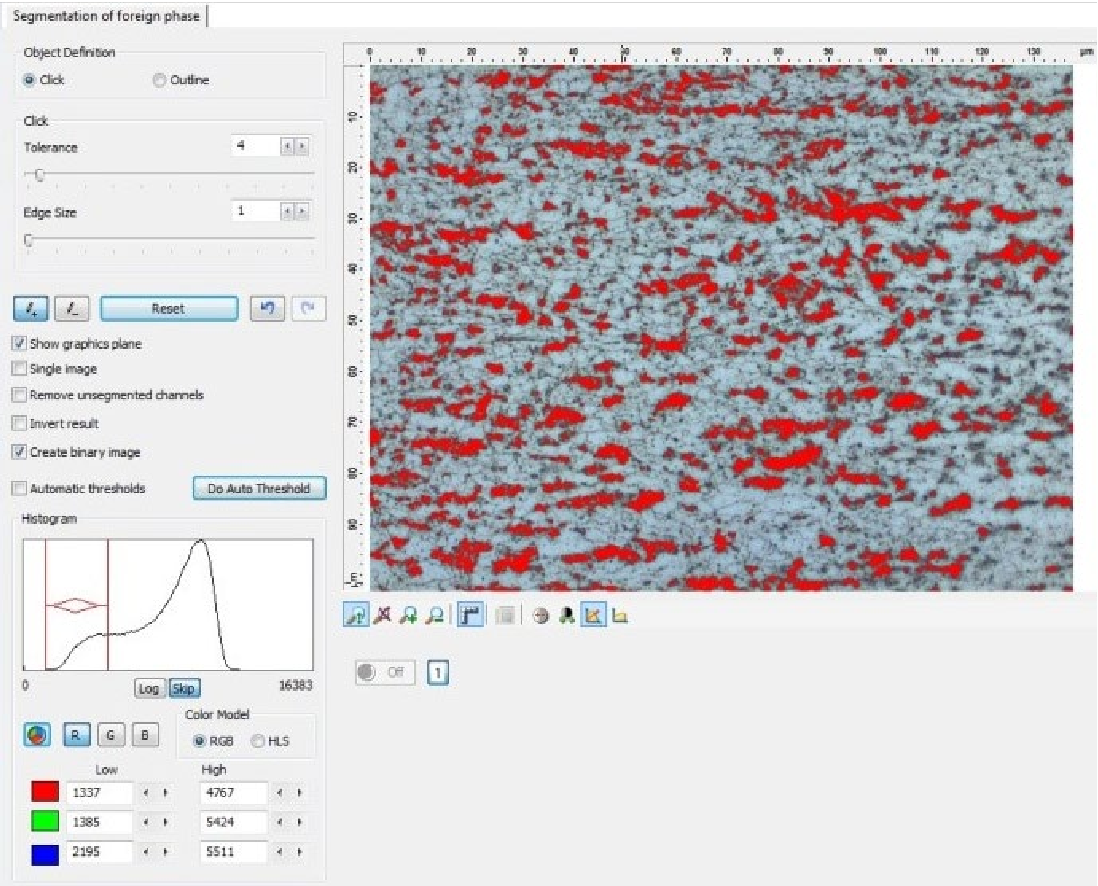

Segmentation of foreign phase

Object Definition

● Click ○ Outline

Click

Tolerance 4

Edge Size 1

☑ Show graphics plane

☐ Single image

☐ Remove unsegmented channels

☐ Invert result

☑ Create binary image

☐ Automatic thresholds

Color Model ● RGB ○ HLS

	Low	High
🟥	1337	4767
🟩	1385	5424
🟦	2195	5511

Figure 3-18. Threshold the Image to Isolate the 2 phases.

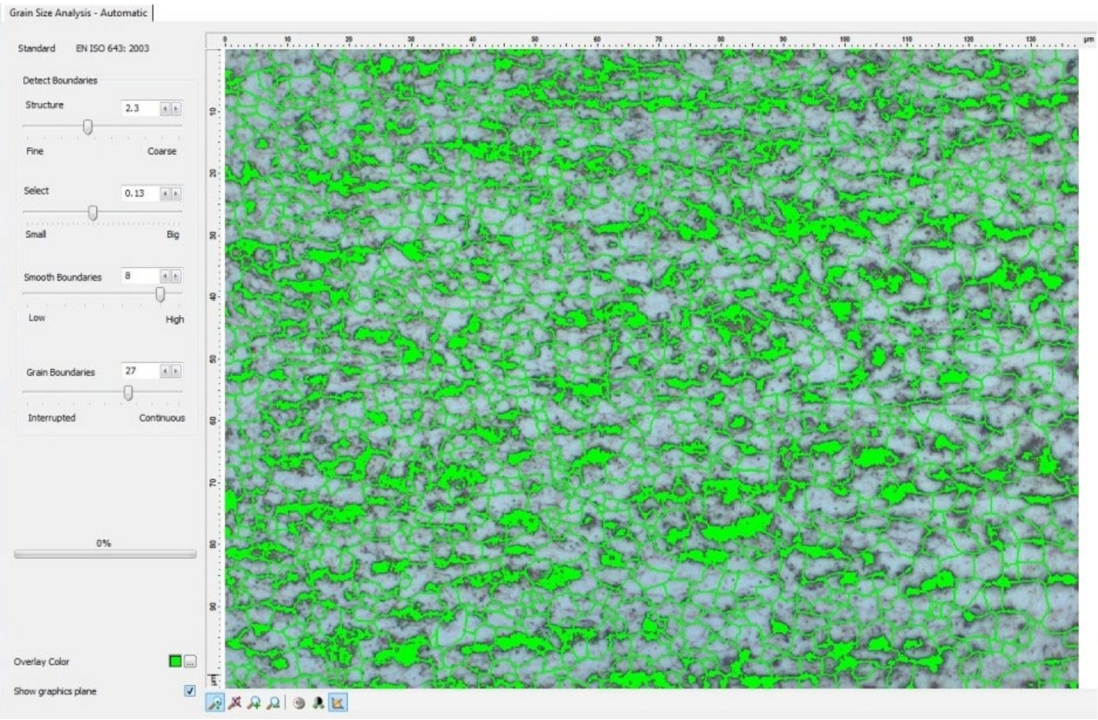

Grain Size Analysis - Automatic

Standard EN ISO 643: 2003

Detect Boundaries

Structure 2.3 (Fine – Coarse)

Select 0.13 (Small – Big)

Smooth Boundaries 8 (Low – High)

Grain Boundaries 27 (Interrupted – Continuous)

0%

Overlay Color 🟩

Show graphics plane ☑

Figure 3-19. Software Tracers Over Grain Boundaries

3.6. Surface Roughness Measurements

The Veeco NT9300 Wide Area White Light Interferometer is a non-contact optical method that was used to measure the surface profiles of the steel samples using its vertical scanning mode. This works on the basis of wave superposition theory. During analysis, the interferometric lens scanned the varying heights of the sample surface by moving the focus vertically and capturing interference data at fixed intervals. At each point on the sample's surface, the interference signal was recorded. This provides information about the fringe modulation which the Wyko Vision 32 software uses to calculate a height profile of the surface.

The arithmetical mean deviation of the roughness profile (Ra) is calculated using the following equation:

$$Ra = \frac{1}{l}\int_0^l |Z(x)|dx \qquad (3\text{-}2)$$

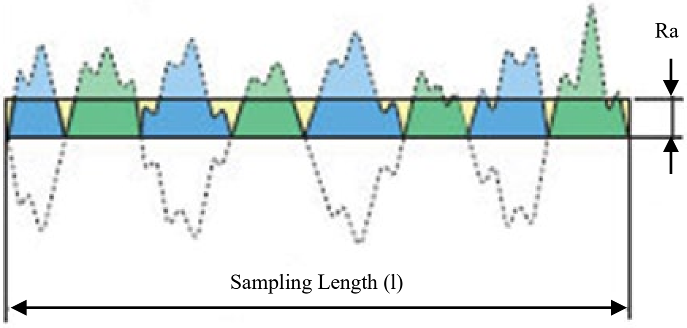

Figure 3-20. Diagram Illustrating the Arithmetical Mean Deviation of the Roughness Profile [103].

Figure 3-21. Veeco NT9300 Wide Area White Light Interferometer.

3.7. Optical Emission Spectroscopy

Optical Emission Spectroscopy (OES) was carried out on the samples using the OBLF QSG 750 in order to calculate each sample's chemistry. While an effort was made to conduct all the specimen's measurements on the same piece of equipment, unfortunately 8 of the samples had to be analysed on a separate OBLF QSG 750 due to time constraints. However, the same standard was used in both cases, with the standards being rechecked at roughly 6-hour intervals in an attempt to ensure accuracy.

During analysis, a minimum of 2 sparks were taken, with each generating up to 2000 individual sparks from the ablated steel surface. A number of these sparks will hit inclusions within the sample, which in turn led to individual spark intensities that are significantly higher than those for the surrounding steel (Figure 3-22 (a)). A Pulse Discrimination Analysis (PDA) algorithm identifies these inclusions and by treating them separately to surrounding steel matrix, was able to calculate the number of sulphide/oxide-based inclusions that contain enough calcium to be successfully modified.

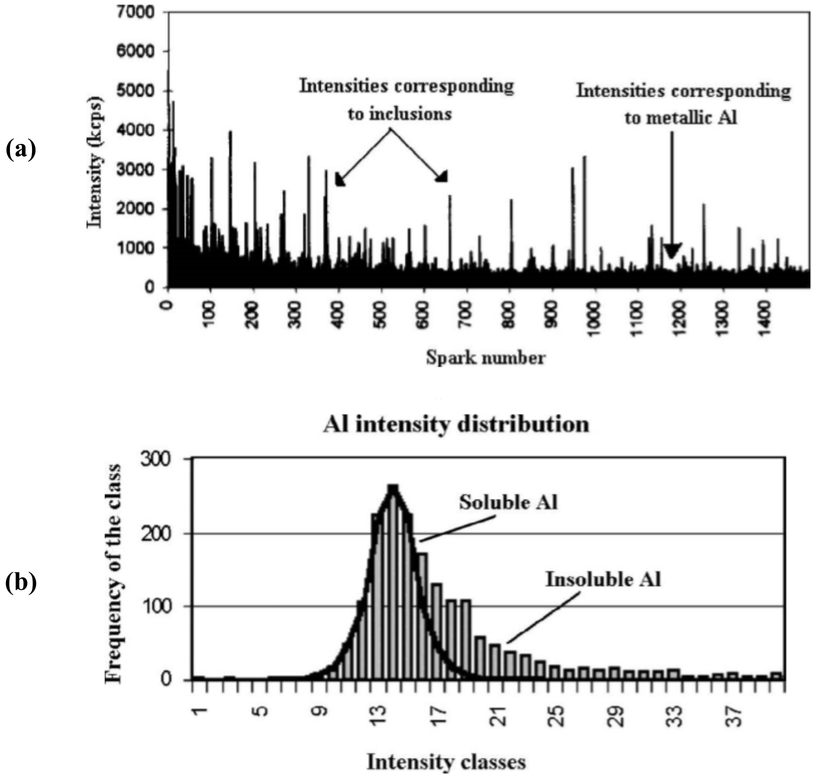

Figure 3-22. Diagram Illustrating the Soluble and Insoluble Aluminium Concentrations of a Steel Sample (a) Lower Signal Intensities Indicate Dissolved Aluminium While Each of the Individual Intensity Peaks Indicate Inclusions [104].

Chapter 4

Mechanical &
Microstructural Analysis of
AHSS Automotive Steel

4.1. Introduction

This sections first presents the mechanical data from all the samples that have been obtained from both the Hot Rolled Dry (HR Dry) and the Hot Rolled Pickled and Oiled (HR P&O) process routes. A non-calcium (Ca) treated HR P&O sample was also analysed to help give an understanding of the mechanical properties if the Ca modification of inclusions does not take place. This sample set was then broken down into 19 samples that covered as large a range of Calcium Sulphur ratios (Ca:S) as possible, in an effort to analyse how the resulting microstructure affects the mechanical properties. These 19 samples microstructures were then compared to 9 non-Ca treated samples to compare their inclusion populations.

All graphs within this chapter show averaged results, with any resulting error bars indicating ± 1 standard deviations (σ) from this average. All results are also to 0 decimal places (dp) simply because the pixel size for the microscopy and testing error range associated with the mechanical testing meant quoting to a larger level of significant figures would be impossible. Both these statements are true unless otherwise stated, with further analysis supporting these results presented in Appendix C.

4.2. Mechanical Properties of FB590

4.2.1. Tensile Testing Results

For each steel sample, if the sample section allowed it, 8 longitudinal samples across the coil width were taken and 2 transverse sample were taken at the centre of the section that correspond to the L1 and L2 sample positions. This allowed for the comparison of the longitudinal and transverse properties. First the entire sample set is analysed to see if there is a general effect of Ca treatment level on tensile properties, before analysing the transverse direction specifically – i.e. the direction that will be most affected by the detrimental MnS – and, finally, comparing them directly with the equivalent longitudinal samples.

Because these samples were taken from industrially produced material, they showed a range of thicknesses. For the entire sample range, this varied from 1.718mm (14S17/13E1) to 5.817mm (12S23/13L2). While this range is large, the average sample thickness was 2.989mm ± 0.777mm (1σ) (3dp).

To generate these results, any Uniform Elongation (UE) result lower than 4% has been discounted as machine error or defective sample preparation. Any Total Elongation (TE) value that has a difference of less than 3% when compared with the UE result has also been ignored as it was most likely caused when the sample had broken outside of the calibrated gauge length (BOGL). These values have been chosen in accordance with the 2% error margin of the extensometer and the experience of operators who work on the equipment in the laboratory.

4.2.1.1. Entire Sample Range

An example of the stress-strain curves exhibited by the samples is shown in Figure 4-1 and highlights samples taken at a range of sample thicknesses and Ca:S. Unfortunately, not all tensile curves were available, so this presents samples with as much of a range in both sample thickness and Ca:S as possible. As can be seen, the biggest variation between the different samples stress-curves is the degree in which the sample undergoes Yield Point Elongation (YPE).

A comparison of UE and TE is shown in Figure 4-2. It shows a positive trend between UE and TE for both the HR Dry (1) and the HR P&O (2) with the following equations indicating their line of best fits. These lines of best fit were chosen with the assumption that it would have to go through the origin which a linear line does not.

$$y = 4.3781x^{0.6092} \quad R^2 = 0.36\ (2dp) \quad \text{Student T-Ratio} = 13.34\ (2dp) \tag{1}$$

$$y = 4.6628x^{0.5989} \quad R^2 = 0.33\ (2dp) \quad \text{Student T-Ratio} = 8.39\ (2dp) \tag{2}$$

While neither of the sample sets exhibit the R^2 values that would indicate small variation in the sample population from the line of best fit, they both show student T-ratio's considerably higher than 2, indicating that this trend is significant. Following this, it can be seen that for equivalent TE values, HR Dry samples on average have higher levels of UE indicating the earlier onset of necking in HR P&O samples but they both suffer ultimate failure at similar levels of overall elongation.

Also highlighted is the fact that the non-Ca treated samples, while generally in the lower range of the results for both UE and TE, sit within the rest of the results for the Ca treated samples and neither data sets (longitudinal or transverse) are significant outliers.

While the HR P&O samples also exhibit UTS & 0.2% Proof Stress (PS) results that sit within the same range of results exhibited by the HR Dry, they tend to sit in the lower region of the results, resulting in the average shown for the entire data set being slightly lower (Table 4-1). The UTS and 0.2% PS values for the non-Ca treated samples also fall within the range of results shown for the Ca treated samples, with a slightly higher average. Of course, with significantly fewer non-Ca treated samples tested compared to Ca treated ones, this is not unexpected.

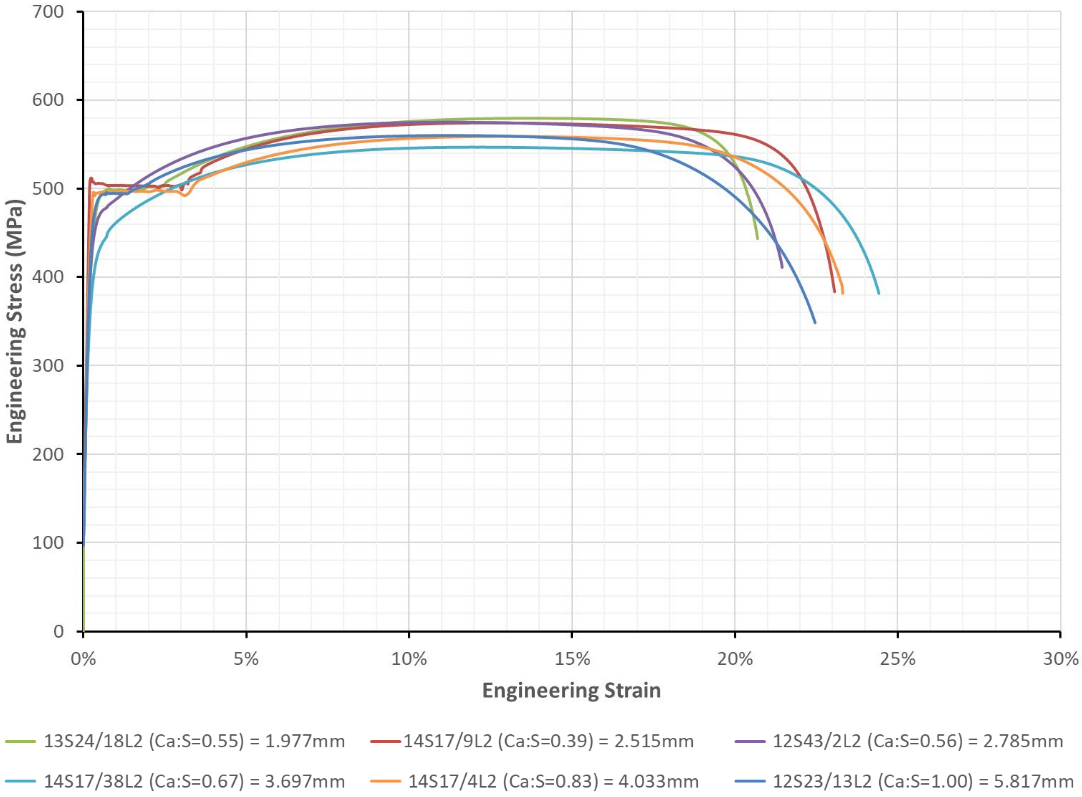

Figure 4-1. Example of Stress-Strain Curves Taken at a Range of Sample Thicknesses

Table 4-1. Average UTS & 0.2% PS Results.

Sample Type	UTS (MPa)	σ (MPa)	0.2% PS (MPa)	σ (MPa)
HR Dry	610	27	530	25
HR P&O	595	21	508	31
Non-Ca Treated HR P&O	635	12	507	27

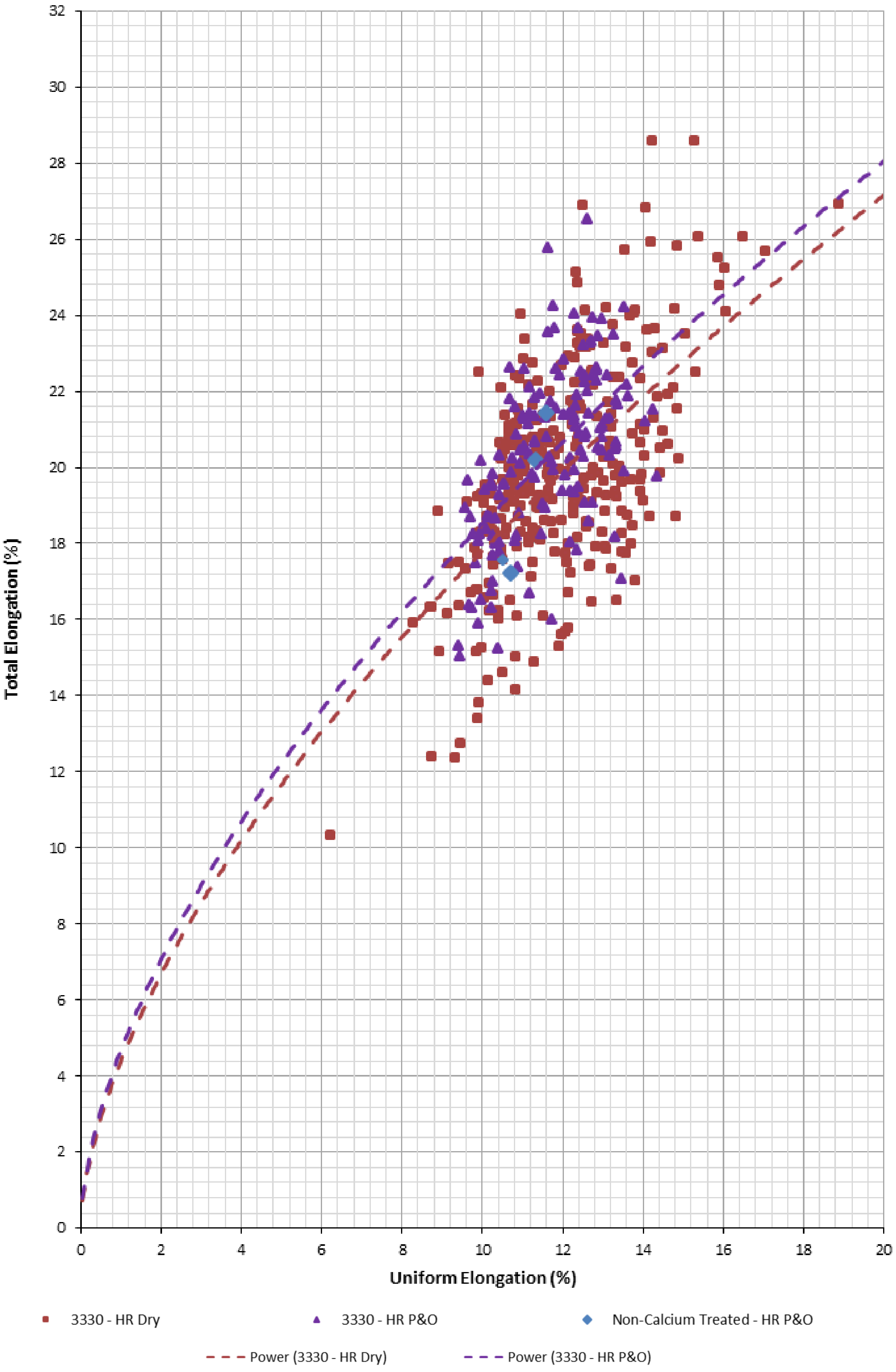

Figure 4-2. Comparison of UE and TE Values in FB590 and a Non-Calcium treated grade.

UE, UTS and 0.2% PS were all compared against both Ca:S and S level as these were determined to be properties that would be most affected by changes in inclusion population. Ca:S was chosen because samples with a higher Ca:S theoretically undergo an increase in Ca modification and thus less elongated inclusions to negatively impact properties, and S level based on the simple theory that the higher the S content of the steel, the higher the number of Sulphide-based inclusions.

As highlighted in the comparisons of UE against Ca:S (Figure 4-3) and S level (Figure 4-4), all the graphs show a flat trend as both the Ca:S ratio and S level increases. UE exhibits the largest variation in both results and error when compared to both UTS and 0.2% PS. However, this variation also has no relation to either the Ca:S ratio or the S level.

Figure 4-3 & Figure 4-4 illustrate that most of the samples achieve a UE value of between 10-14%. Samples also achieved average UTS values of 550-650MPa and 0.2% PS values of 500-550 MPa respectively.

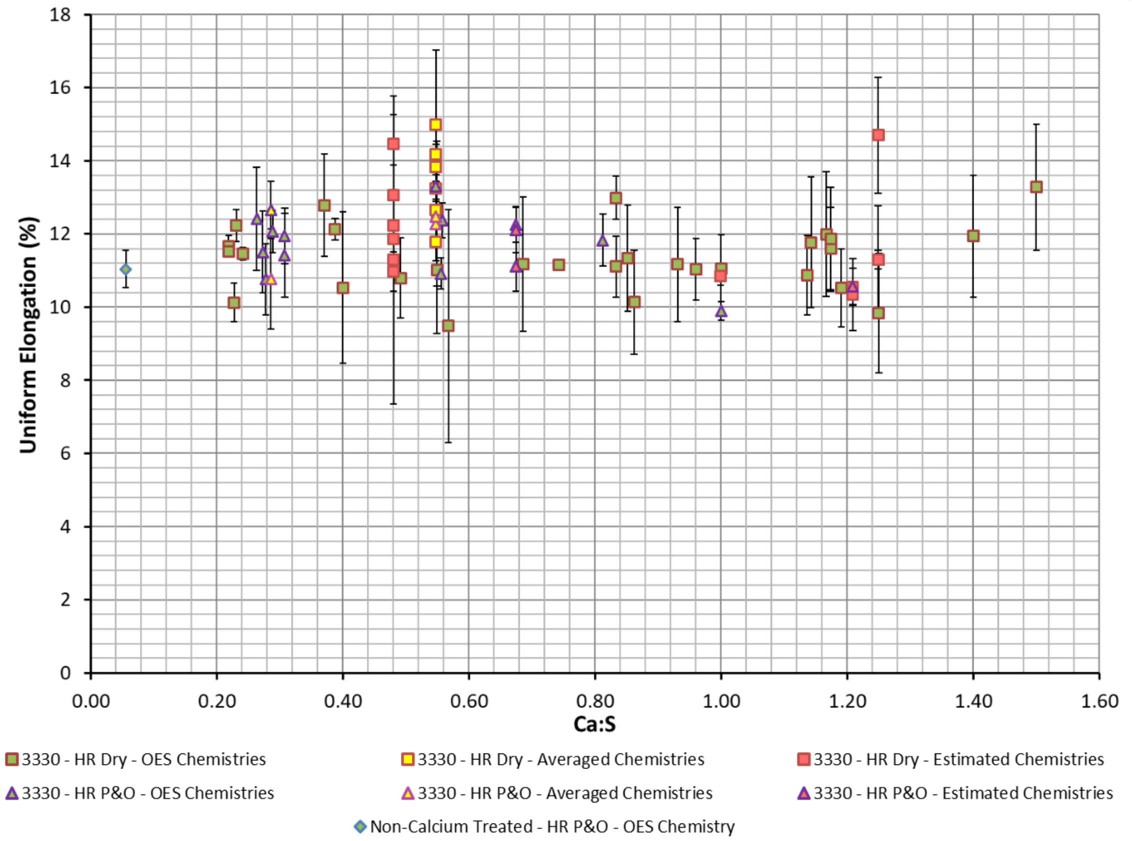

Figure 4-3. Comparison of UE and Ca:S in FB590 and a Non-Calcium treated grade.

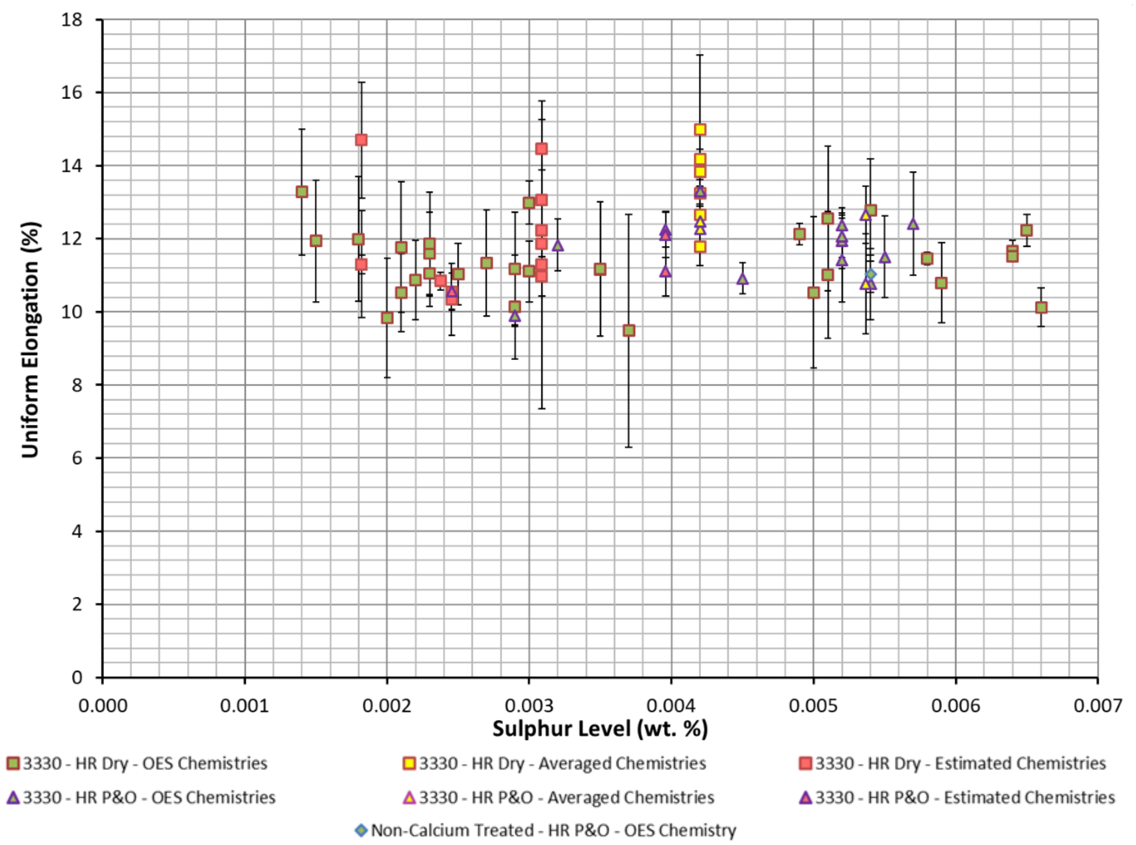

Figure 4-4. Comparison of UE and Sulphur Level in FB590 and a Non-Calcium treated grade.

4.2.1.2. Transverse Samples Only

Because samples taken in the transverse direction are going to be most affected by the quantity of stringers within a sample, they were isolated to better analyse the resulting impact on mechanical properties. As most of the sample sets were only made up of 2 samples, this meant that the resulting average and error would be more affected by any variation. It also meant that if the results did not fit the constraints on UE described in Section 4.2.1 then the average may only consist of 1 sample and therefore will not have a subsequent error bar.

As highlighted in Figure 4-5, there was no variation in either the values or error of UE, UTS and 0.2% PS respectively as either the Ca:S or S level changes, instead showing the same flat trend that can be seen in the full sample set. The Transverse samples achieve similar overall values for UE, UTS and 0.2% PS on average when compared to the full sample set in general.

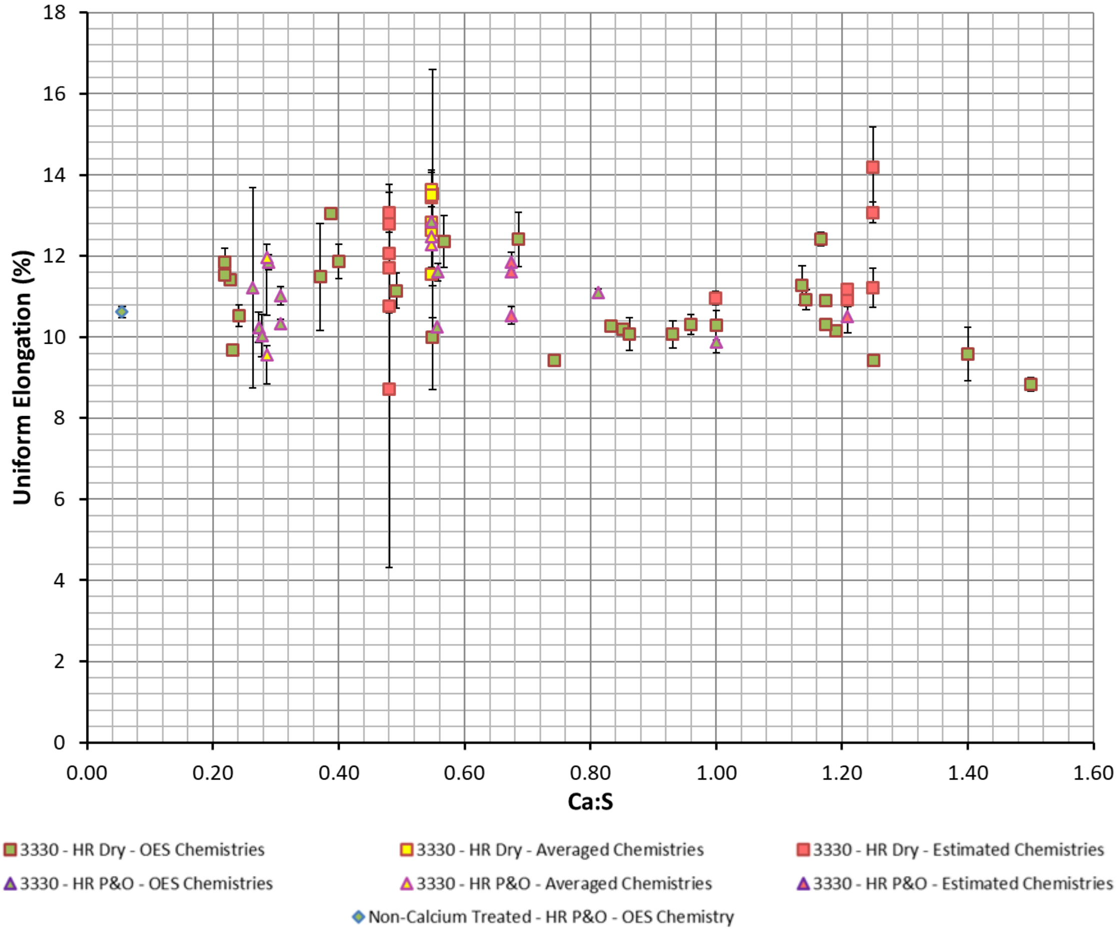

Figure 4-5. Comparison of UE and Ca:S in FB590 and a Non-Calcium treated grade only in the transverse direction.

4.2.1.3. Transverse vs Longitudinal Direction

As has been mentioned previously, the level of Ca modification and therefore the level of Ca:S is meant to have the most effect on samples taken from the transverse of the rolling direction of the steel. As a result, the percentage difference between the transverse sample and its equivalent longitudinal has been calculated, with any negative results indicating lower values in the transverse direction and vice versa. However, unlike in the previous sections, each individual result has been plotted, instead of an average, to get a better understanding of the direct impact on comparable samples, as well as limit the impact of anomalous results.

Figure 4-6 shows that samples typically showed a difference between 0% and 10% indicating that most samples exhibit a lower UE value in the transverse direction. If this was not the case however, they difference tended to be smaller, roughly <5%.

Figure 4-7 is indicative of the remaining key properties, in that it shows that most of the samples exhibit an increase in the UTS in the transverse direction. For a significant proportion of the samples, this increase was roughly 1-4% and <10% for UTS and 0.2% PS respectively. If the samples did exhibit a higher 0.2% PS in the longitudinal direction, this difference was generally markedly small, roughly <2%.

As highlighted in both Figure 4-6 & Figure 4-7, there is no trend in the percentage differences that can be associated with either a change in Ca:S or S level. It can also be seen that the HR Dry and the HR P&O samples, as well as the non-Ca treated sample, all exhibited similar differences in properties between the longitudinal and transverse directions.

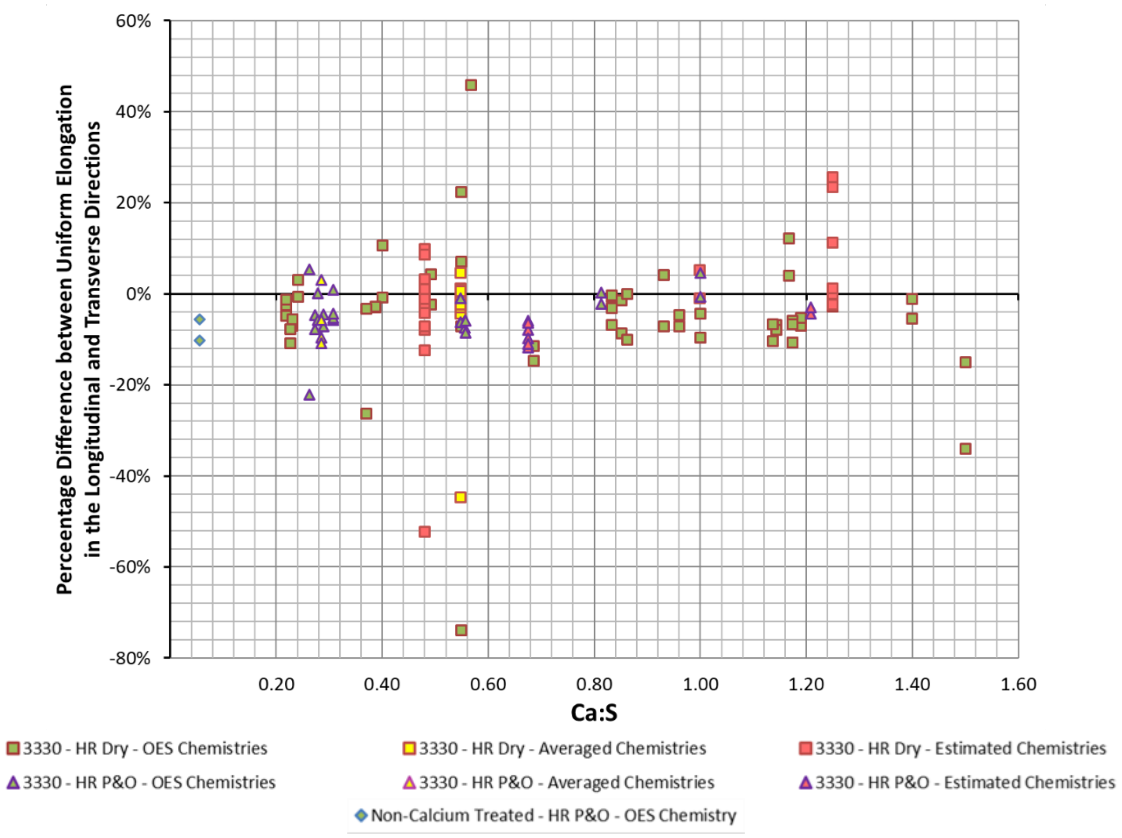

Figure 4-6. Comparison of UE and Ca:S in FB590 and a Non-Calcium treated grade showing the percentage differences between the transverse and longitudinal directions

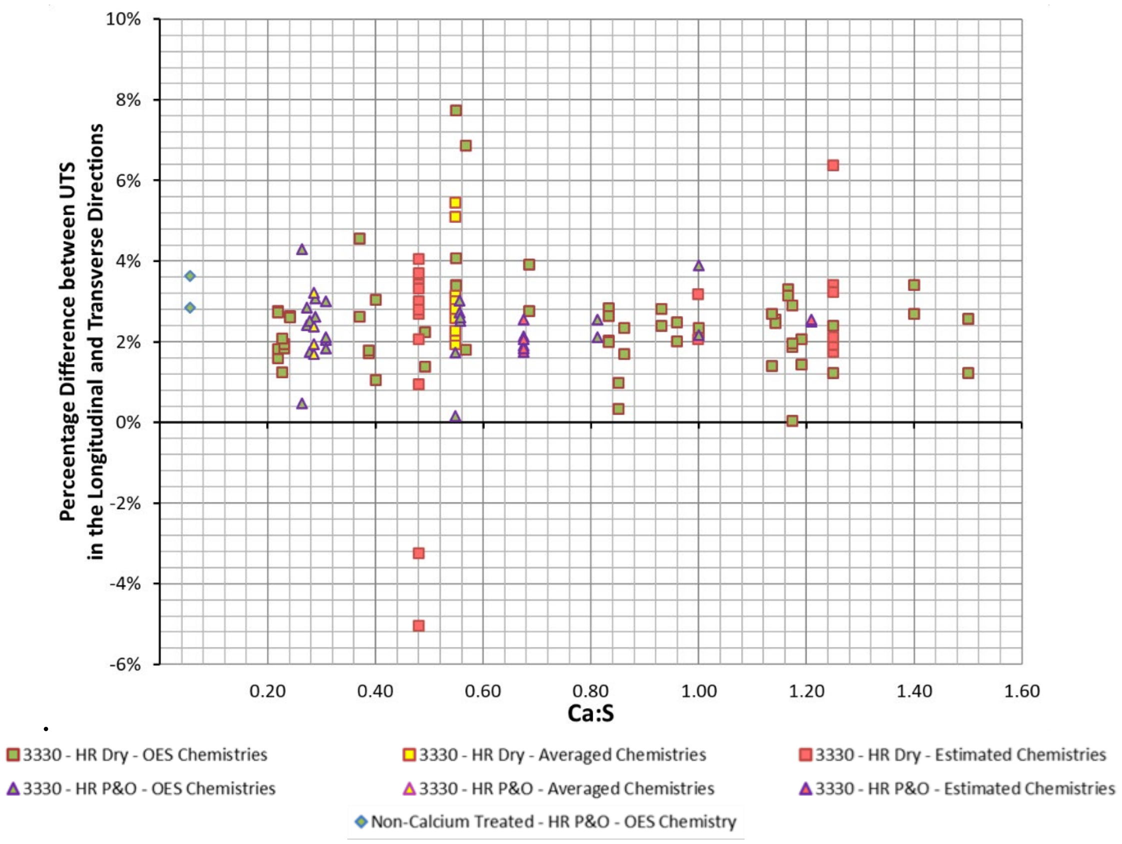

Figure 4-7. Comparison of UTS and Ca:S in FB590 and a Non-Calcium treated grade showing the percentage differences between the transverse and longitudinal directions.

4.2.2. Hole Expansion Results

Hole expansion was chosen to test the material in a ‘worst case’ scenario compared to the bulk response during tensile test. This is because different areas of the material will be under different stresses so will respond differently to failure under uniaxial load. For each sample, an effort was made to cut 4 test pieces from each section. However, depending on the width of the section, this was not always possible so occasionally 3 samples from each coil position were able to be obtained.

As the HEC for a given strength level increases with gauge thickness, for a direct comparison to be made between samples, it is first necessary to normalise the results to a standard gauge thickness. This is extremely important as the samples tested show a large range of gauges, from 1.75mm (14S21/3) to 5.79mm (12S23/13). In-house investigations at Tata Steel [105] show that there is an approximate gain of 10% in HEC for each additional mm of steel thickness. Using this relationship, all the HEC were normalised to 2.75mm, an example of which can be seen in Table 4-2.

Figure 4-8 & Figure 4-9 show these normalised results plotted against Ca:S and S level respectively. Most of the samples have HEC roughly between 40% and 80% with no distinct change of HEC that can be associated with an increase in either Ca:S or S level, instead showing a generally flat trend. It should also be noted that there is no distinct difference between the data sets for the HR Dry and HR P&O samples. It can also be seen that while the non-Ca treated sample exhibits a very low HEC with small resulting error bars, 2 of the Ca treated samples also exhibit a similarly low HEC. While these samples have similar S contents to the non-Ca treated sample, it should be noted that there are other Ca treated samples that have higher levels of S, without exhibiting the same poor level of HEC.

Table 4-2. Example of HEC Results before and after they have been normalised to 2.75mm.

Sample ID		**Key Chemistries**		**Gauge (mm)**	**HEC (%)**	**Averaged HEC (%)**	**Normalised HEC (%)**	**Averaged Normalised HEC (%)**
		S	Ca:S					
14S17/4	1	0.0030	0.83	4.02	48	62	35	49
	2	0.0030	0.83	4.01	71		58	
	3	0.0030	0.83	4.00	54		41	
	4	0.0030	0.83	4.00	75		62	
14S17/5	1	0.0059	0.49	3.44	95	81	88	74
	2	0.0059	0.49	3.46	65		58	
	3	0.0059	0.49	3.45	97		90	
	4	0.0059	0.49	3.45	68		60	

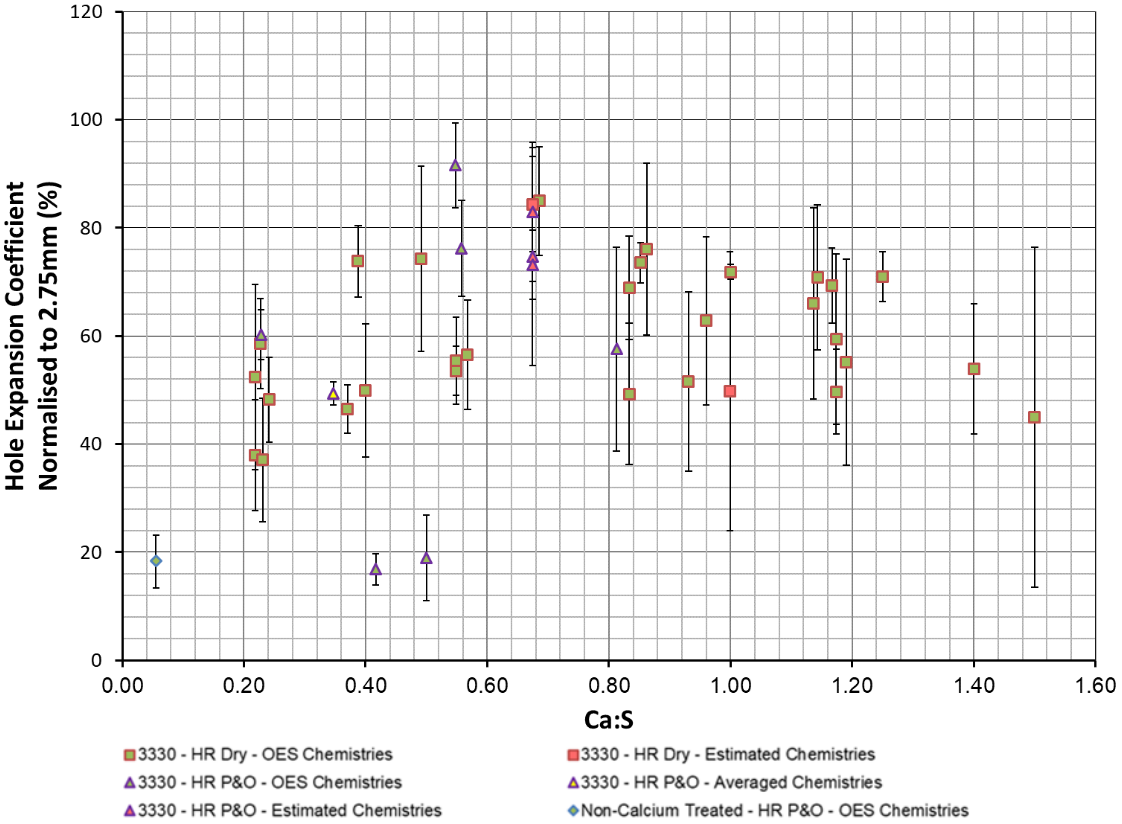

Figure 4-8. Calcium Sulphur Ratio Versus Average HEC Normalised to 2.75mm in FB590 and a Non-Calcium Treated Sample.

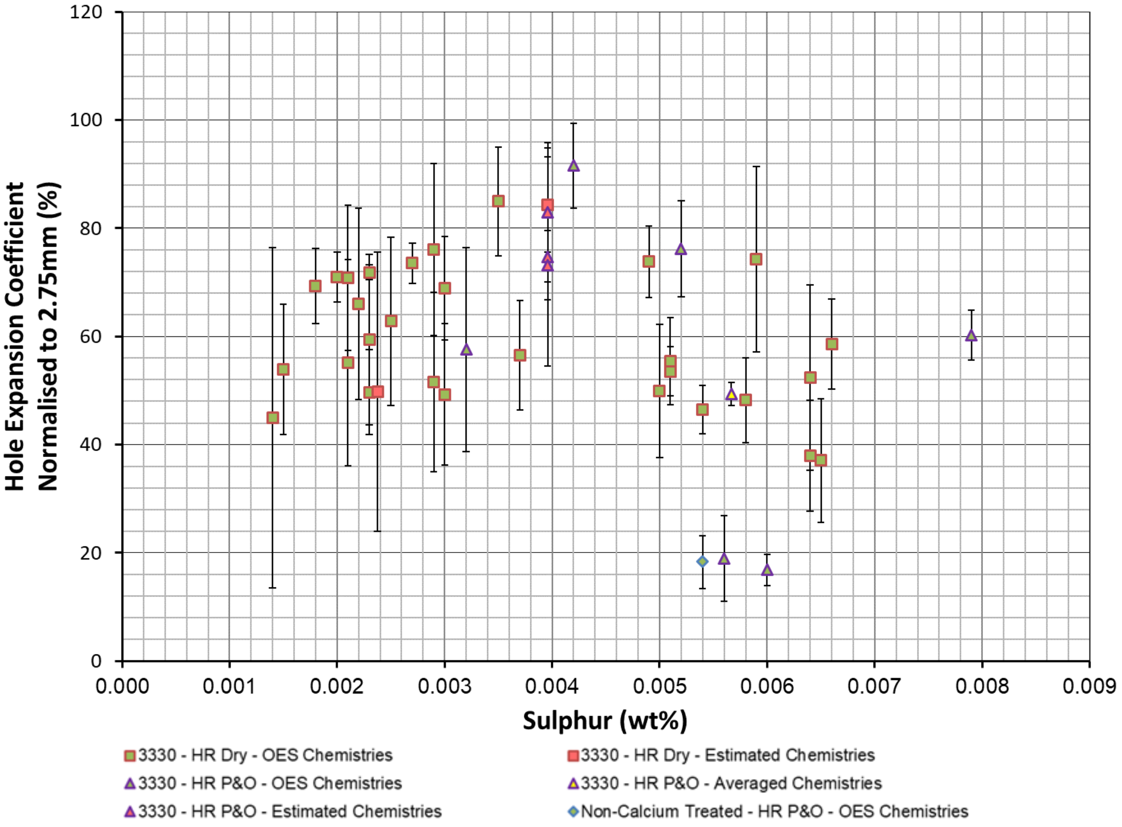

Figure 4-9. Sulphur Level Versus Average HEC Normalised to 2.75mm in FB590 and a Non-Calcium Treated Sample.

4.3. Microscopic Analysis

Optical microscopy and white light interferometry were utilised as a means to eliminate any outside factors (i.e. other than chemistry) that could impact mechanical properties. After which a large-scale inclusion analysis was conducted in an attempt to investigate the full inclusion population to a high degree of accuracy. A Scanning Electron Microscope (SEM) was then used to analyse a wide range of these inclusions in order to get a fundamental understanding of their chemical compositions and structure.

4.3.1. Surface Roughness Analysis

White light interferometry was used to analyse the surface roughness for 20 samples from the 2 differing process routes; 13 HR Dry and 7 HR P&O. For each sample, 5 scans were taken on the tensile coupons in areas that were unaffected by either the elongation caused by testing or the indents caused by the grips of the tensile tester. All of measurements were taken at a magnification of 5.1x, with a sampling size of 1.96μm. Each sample's average arithmetical mean height (Sa) were averaged to create an overall average for each process route (Figure 4-10).

While the HR Dry has a lower Sa value than HR P&O, the large error bars for both data sets indicate that this result should be taken with a level scepticism. This could be down to the fact that these samples were quite old when analysed and as a result could, have mildly oxidised or suffered scratches from manhandling resulting in the large error bars. However, as an effort was made to take a significant amount of measurements, over as large an area as possible, the averages themselves should still be indicative of the sample sets as a whole.

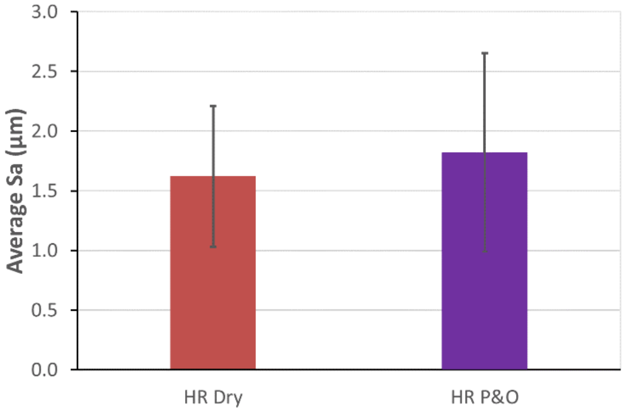

Figure 4-10. Average Arithmetical Mean Height of the Surface for the 2 Process Routes

4.3.2. Grain Structure Analysis

Grain size analysis was first carried out on 9 Ca treated FB590 grades – 3 HR Dry & 6 HR P&O – in addition to the non-Ca treated HR P&O sample that was also mechanically tested. For each sample, a minimum of 5 images were taken through the thickness of the material in effort to capture a true representation of the whole of the samples, while also ensuring that a sufficiently large number of grains were measured to obtain an accurate average.

The general microstructure that was seen across the Ca treated grades is shown in Figure 4-11. The optical micrograph shows there is a high degree of homogeneity within FB590 that consists of a fine ferritic matrix with relatively evenly distributed bainitic islands – the dark regions in the image. The grains also show some elongation in the rolling direction. Figure 4-12 shows that the non-Ca treated grade exhibits a similar microstructure with a similar level of Bainite, grain size and comparable elongation in the rolling direction. There is a slight difference in the appearance of the Bainite between the 2 samples, however this is most likely due to a variation in the amount of etching that has occurred to these regions.

This is emphasised in Figure's 4-13 to 4-15 which show the average grain size, average Feret ratio of these grains and the average amount of bainite in the steel grades. In an effort to eliminate any incorrect data, any grain that had a height or width lower than 0.2μm was ignored, as any value smaller than that was smaller than the pixel size and therefore could not be accurate. This small pixel size is also the reason why the values are quoted to 1dp instead of the standard 0dp.

Figure 4-13 shows that on average, all the samples have very fine microstructures. While there is some variation between the samples, there are no drastic changes with all samples combined showing an average grain size of 2.8μm ± 0.4μm. This is in line with the FB590 data obtained through Electron Backscattered Diffraction (EBSD) analysis by McCulloch [106] which is generally accepted as being a more accurate technique.

Figure 4-14 shows that all the samples have grains that are elongated in the rolling direction, with only a small variation between each of the samples. If the average Feret ratios for all the samples are combined and averaged it results in a Feret ratio of 0.63 ± 0.03 (2dp). This is slightly higher than the aspect ratio of 0.47 (2dp)

Rolling Direction

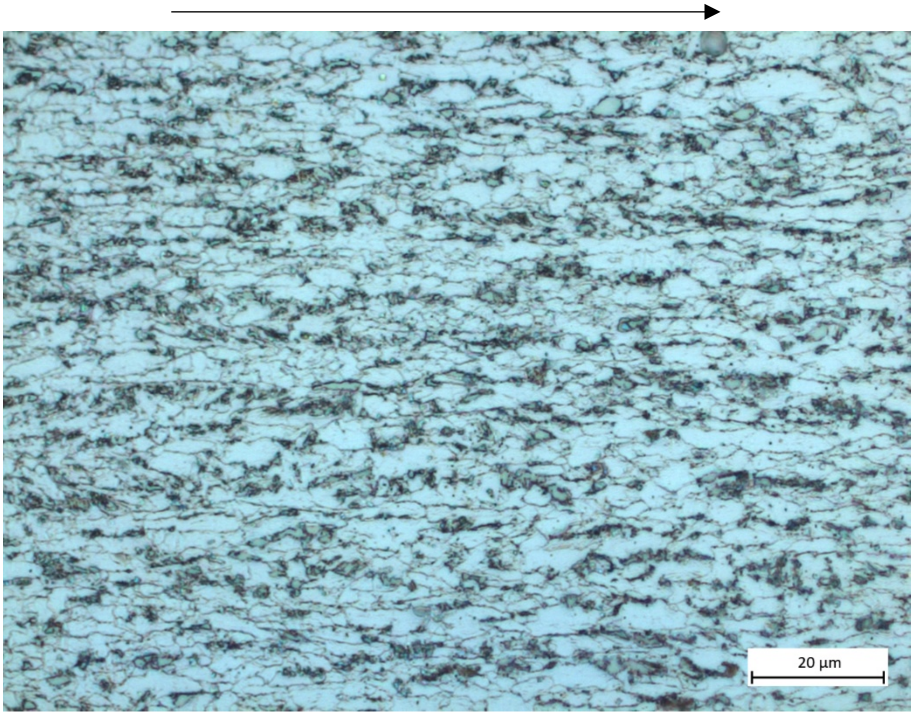

Figure 4-11. Optical Micrograph of Calcium treated FB590 (14S17-8MW) exposed by 2% Nital etch.

Rolling Direction

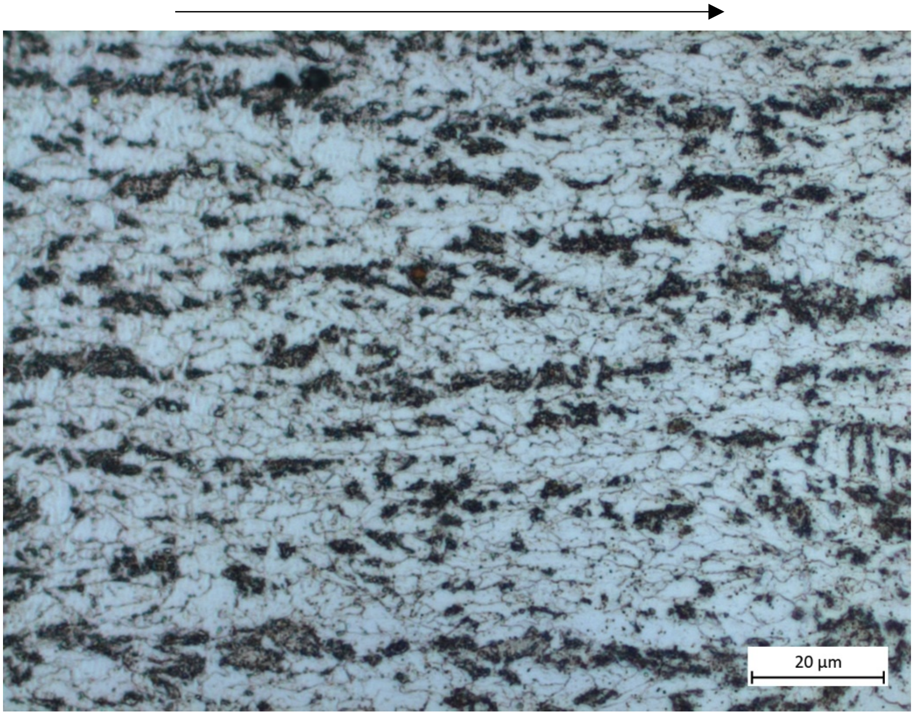

Figure 4-12. Optical Micrograph of non-Calcium treated grade (11QS44-7L1) exposed by 2% Nital etch.

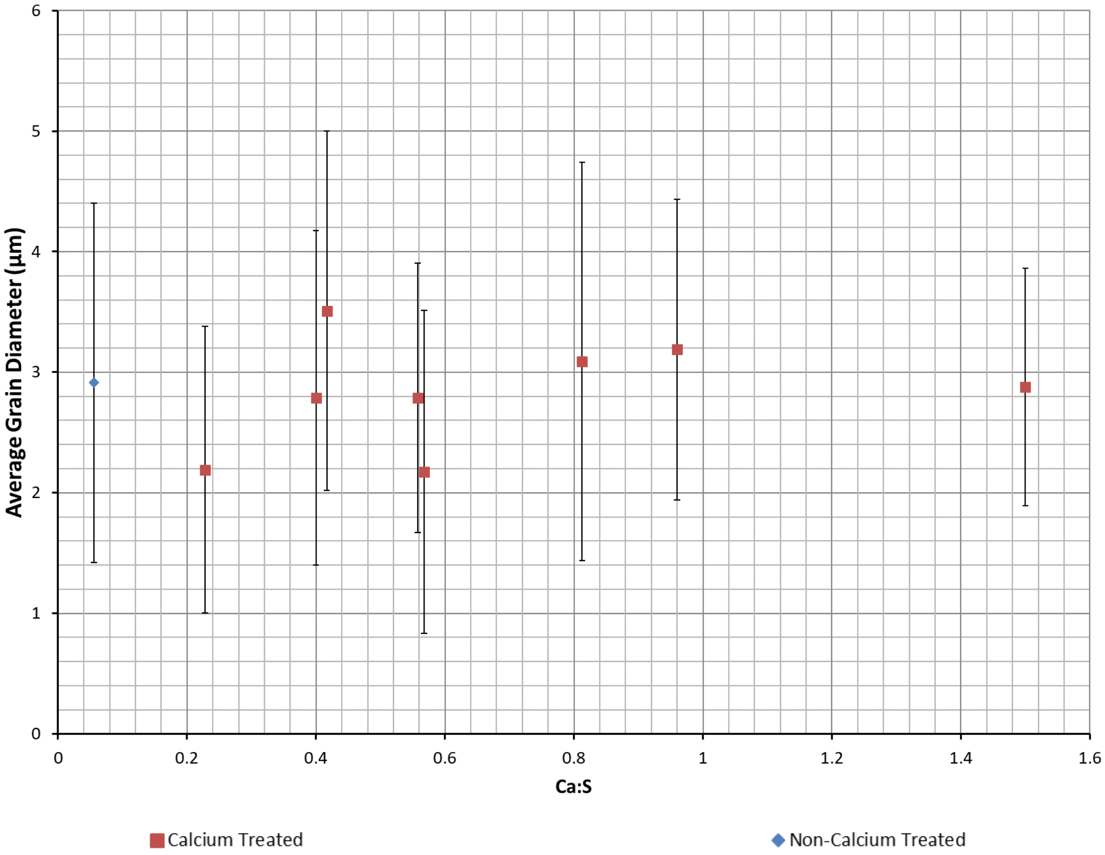

Figure 4-13. Average Grain Size Across the Calcium-Sulphur Range.

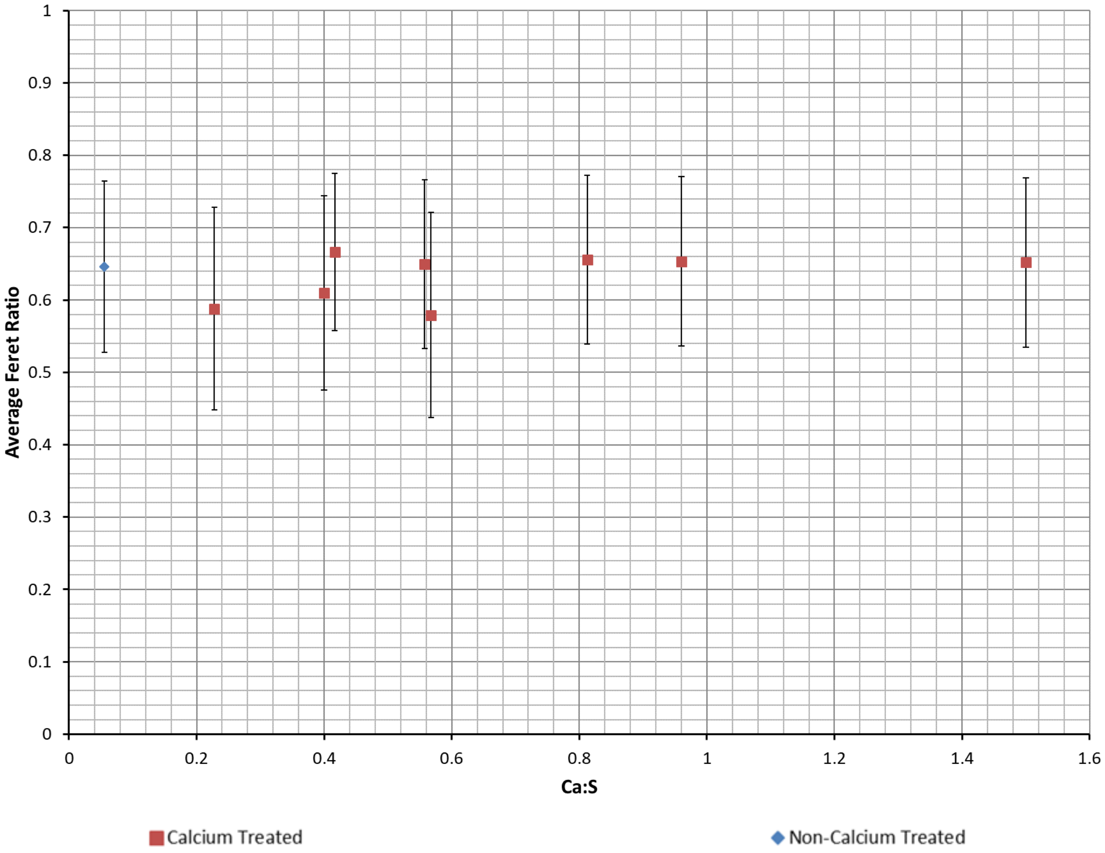

Figure 4-14. Average Feret Ratio of the Grains Across the Calcium-Sulphur Range.

seen in McCulloch's EBSD analysis. This difference could be down to the fact that optical microscopy is not subject to either the trapezium or tilt correction distortions associated with the 70° tilt needed for EBSD [107].

The average volume fraction ferrite is calculated, rather crudely, by the amount of the image that has not been removed through the greyscale segregation at the first stage of the grain size measurement described in the Experimental Section. Whilst not as accurate as data obtained through EBSD, it will give a good picture of any large variations between samples, whilst also indicating the amount of bainite over a much larger area within the sample. As Figure 4-15 shows, there is a slight variation in the amount of ferrite between the samples with the overall combined average being 65.5 % ± 5.0 %. Whilst this is quite significantly below McCulloch's calculated value of 86.7 % ferrite [106], if the micrographs obtained from the samples in this study are visually compared to the FB590 micrograph in McCullough's thesis, it can be seen that his sample contains a significantly higher level of ferrite.

It should be noted that the standard deviation value quoted in the above averages does not consider the original variation in the samples and are simply meant to indicate the variation in the averages themselves.

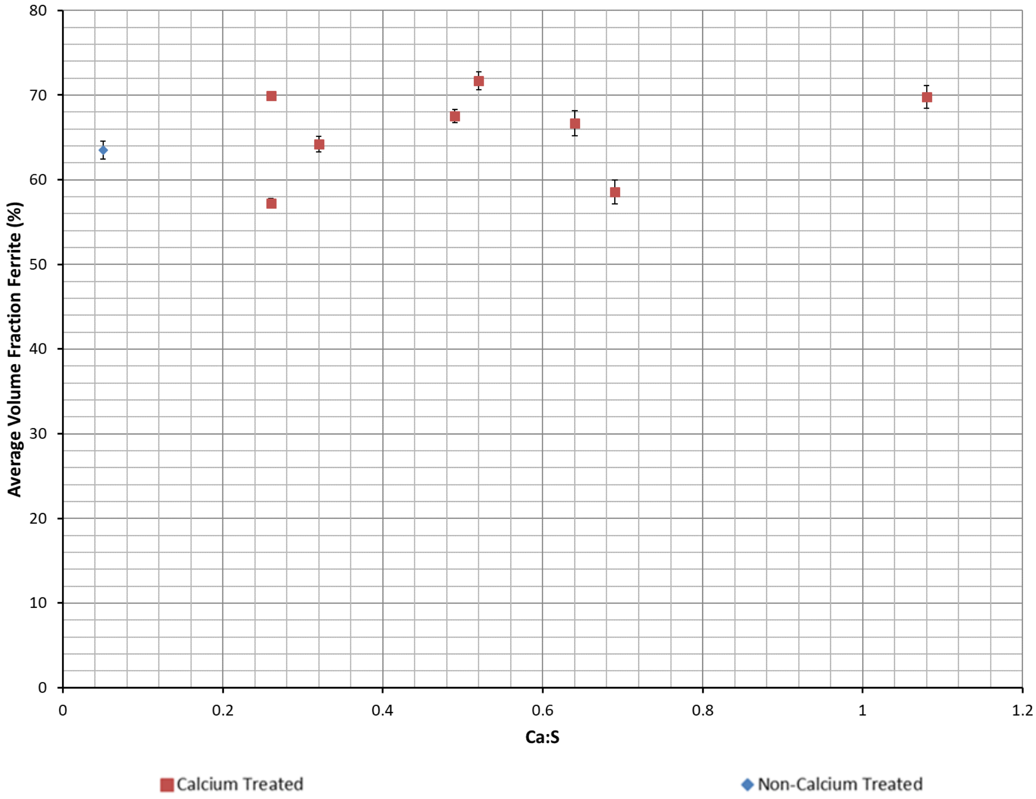

Figure 4-15. Average Volume Fraction Ferrite Across the Calcium-Sulphur Range.

4.3.3. Inclusion Analysis of FB590

From the entire sample set, a total of 19 Ca treated samples were analysed, using both optical and scanning electron microscopy. These samples were selected to give a good representation of the entire Ca:S range that was obtained from Tata Steel Port Talbot. As any significant differences between the 2 different process routes used during this analysis have no direct impact on the inclusion population/structure, this was a secondary factor when selecting samples. However, an effort was made to ensure that a reasonable amount of sample was selected from both routes.

4.3.3.1. Optical Microscopy

In order to conduct the analysis as close to the 200mm^2 area that the standards required, the samples - depending on the original gauge thickness - were made up of between 3 and 6 sections, taken from the grip ends of fractured tensile coupons. The samples were always taken from the centre of the coil width, from either the MW or L1/L2 positions, to ensure that an accurate representation of inclusion population was gathered. This area was then analysed at 100x magnification and in 710µm^2 fields, as described in Chapter 3.

4.3.3.1.1. Percentage Globular

The resultant average amount of globular inclusions as a percentage of the overall inclusion population, is presented in Figure 4-16 and Figure 4-17, graphed against its corresponding Ca:S and S level respectively. It can be seen that most samples exhibit above 50% globular inclusions, with only 2 samples not showing a majority of globular inclusions. Instead, both these samples demonstrate 49% globular if rounded to a whole number. In actuality however, most samples exhibit >60% globular inclusions or very near to it. Figure's 4-16 and 4-17 also demonstrate that there is no real change in the percentage amount of globular inclusions that can be directly associated with an increase in either Ca:S or S level respectively.

However, all of the samples show large error bars indicating a large range of results within the sample set. This is most likely because some grids will have very low quantities of inclusions, sometimes only 1, and if this inclusion is a stringer, it will lead to a result of 0% globular inclusions and while not being indicative of the sample at large, would result in a larger than normal σ.

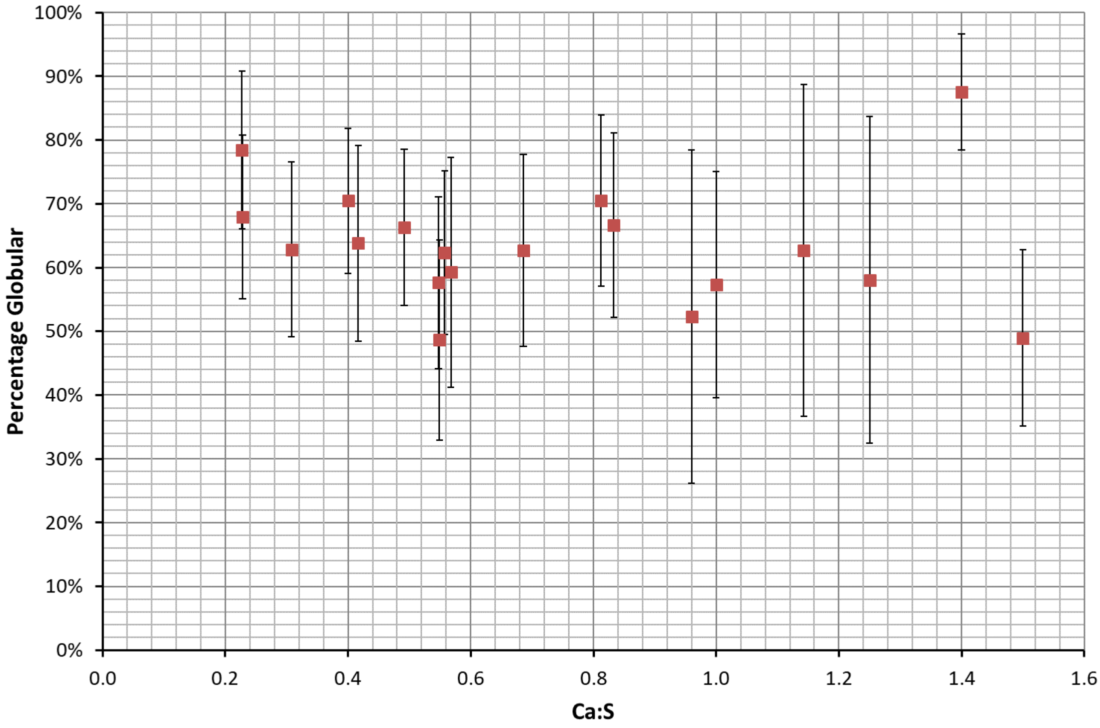

Figure 4-16. Percentage Globular vs Calcium Sulphur Ratio for the Calcium Treated FB590.

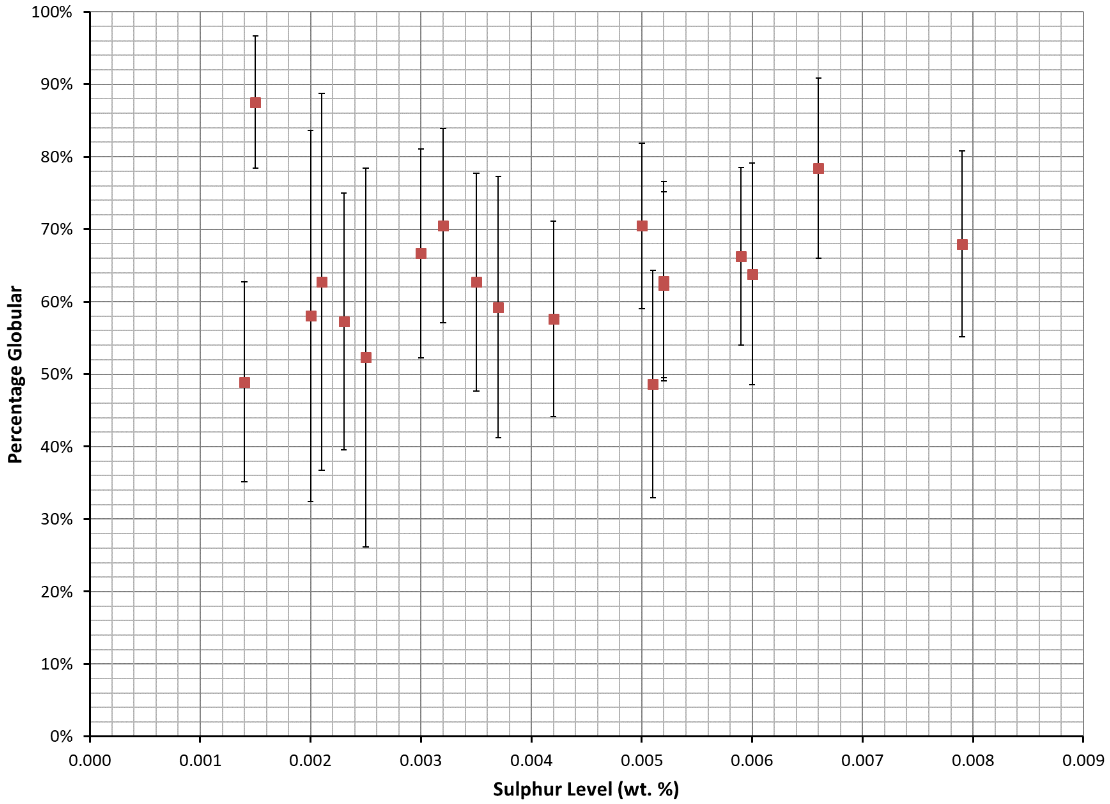

Figure 4-17. Percentage Globular vs Sulphur Level for the Calcium Treated FB590.

4.3.3.1.2. Inclusion Population Density

Figure 4-18 shows the average total number of inclusions in each 710µm^2 field against the sample's corresponding S level. As can be seen there is a general increase in the number of inclusions as the S level increases. Figure 4-19 then splits these results to show the average number of globular and stringer inclusions in each 710µm^2 field, also against its S level. It shows that there is an increase in the amount of globular inclusions as S level increases. There is also an increase in the number of stringer inclusions as the S level increases up until a S level of roughly 0.004 wt.% after which it levels off.

Whilst there is also a decrease in the number of inclusions as the Ca:S level increases, the variation around the mean is less. The relationship associated with S level shows an increased R^2 value of 0.41 (2dp) over the R^2 value of 0.35 (2dp) for a linear trend. This implies that the relationship is more strongly associated with a change in S level than a change in Ca:S.

Similarly, the relationship is stronger for both globular and stringer inclusion levels when plotted against S level (Figure 4-19) than against Ca:S. The relationship relating to globular inclusions show an R^2 value of 0.37 (2dp) and stringers an R^2 value of 0.32 (2dp) for S level, compared to 0.31 (2dp) and 0.27 (2dp) if compared to Ca:S. It should be noted that while the globular trendlines are linear, the stringer has a 'power' trendline in an effect to better represent the relationships that have been previously described.

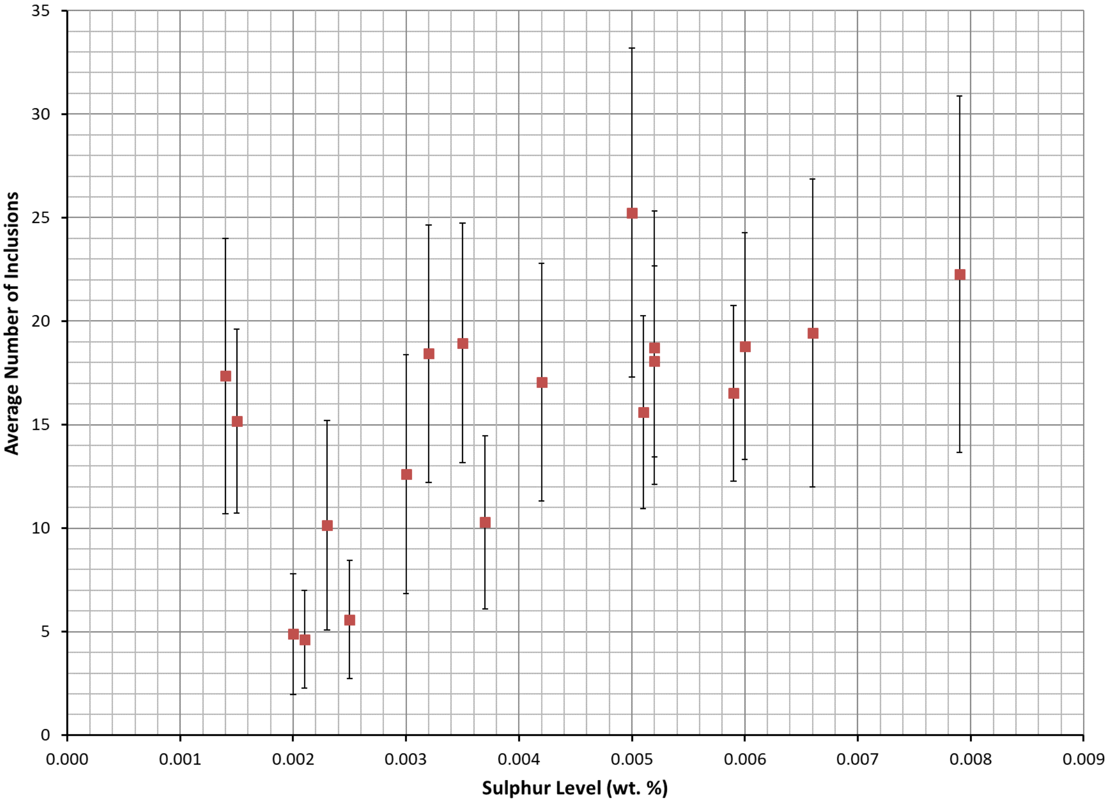

Figure 4-18. Average Number of Inclusions vs Sulphur Level for the Calcium Treated FB590.

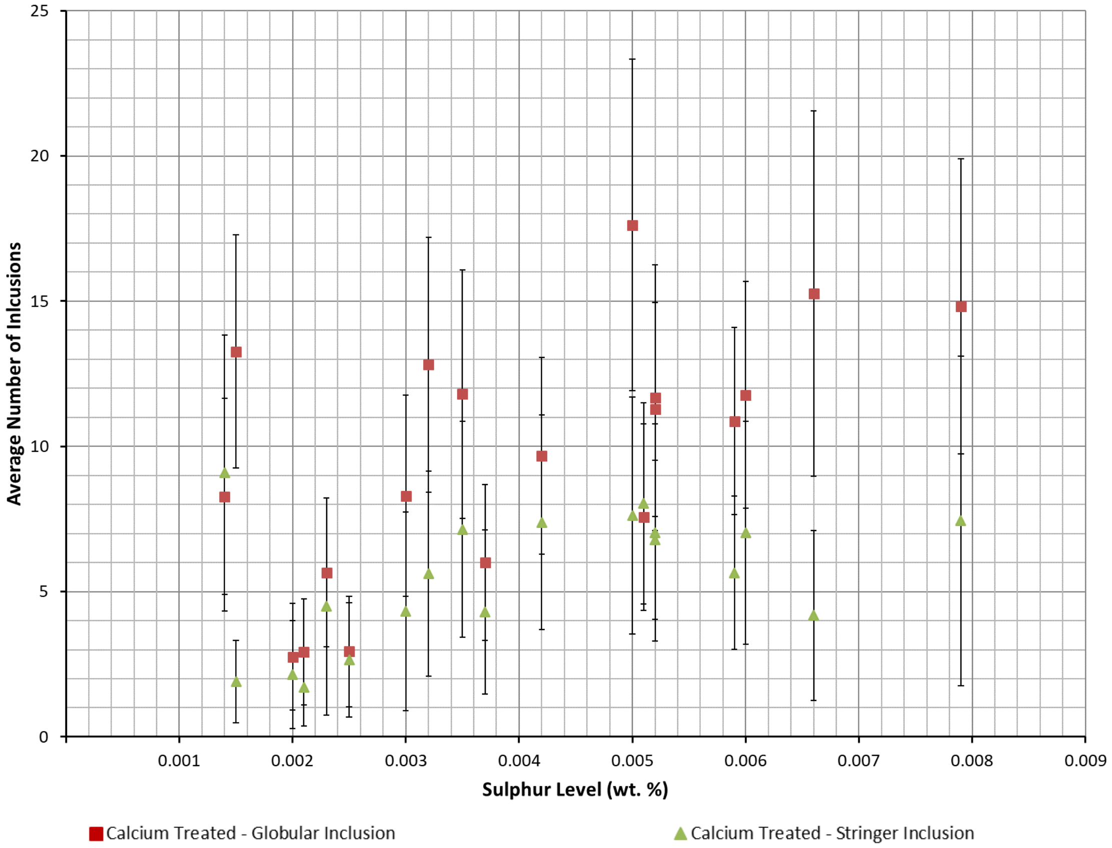

Figure 4-19. Average Number of Globular and Stringer Inclusions vs Sulphur Level for the Calcium Treated FB590.

4.3.3.1.3. Size of Inclusions

For each 710μm^2 field, the average inclusion size is shown plotted against the sample's S level in Figure 4-20. In a similar fashion to Ca:S, there is a large size distribution when plotted against the entire S level range, with roughly half of the samples having an average inclusion size between 10 and 20μm^2. Some of the sample's averages, however, reach up to almost 60μm^2. There is also an indication of more samples exhibiting lower average inclusion sizes at lower S levels with the inclusion size generally increasing as the S level increases. Similar to the average number of inclusions, this trend is more defined when compared to S level than Ca:S.

Figure 4-21 shows the results split instead into the two inclusion types, globular and stringer demonstrating that the globular inclusions show a large variation in average size with average inclusion sizes of up to 72μm^2. The stringer inclusion however shows a lower size range with the largest average size being 37μm^2. Furthermore, every sample shows a larger average globular inclusion size than the average stringer inclusion size. It should also be noted that the trend mentioned previously is also seen here, with the globular or stringer inclusions average size generally increasing as the S level increase. Once again this is significantly less distinct if compared against Ca:S. There are however a few anomalies that do not fit in with either of these trends making it appear less defined.

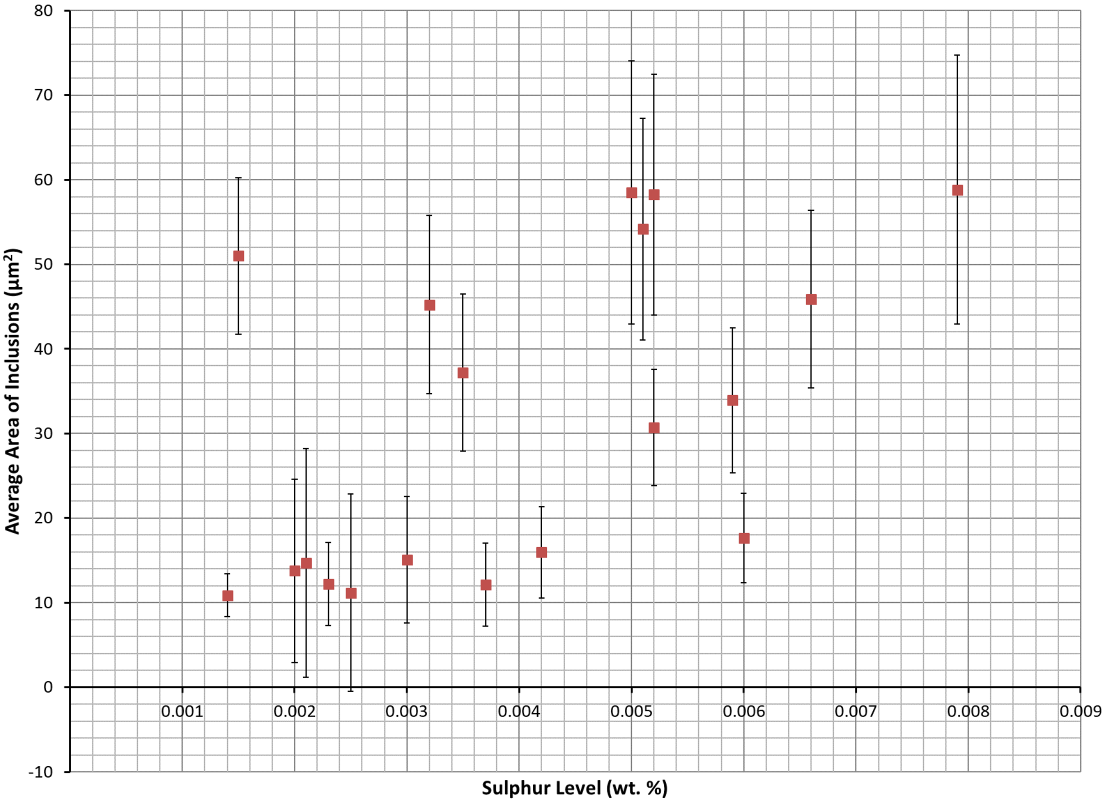

Figure 4-20. Average Area of Inclusions vs Sulphur Level for Calcium Treated FB590.

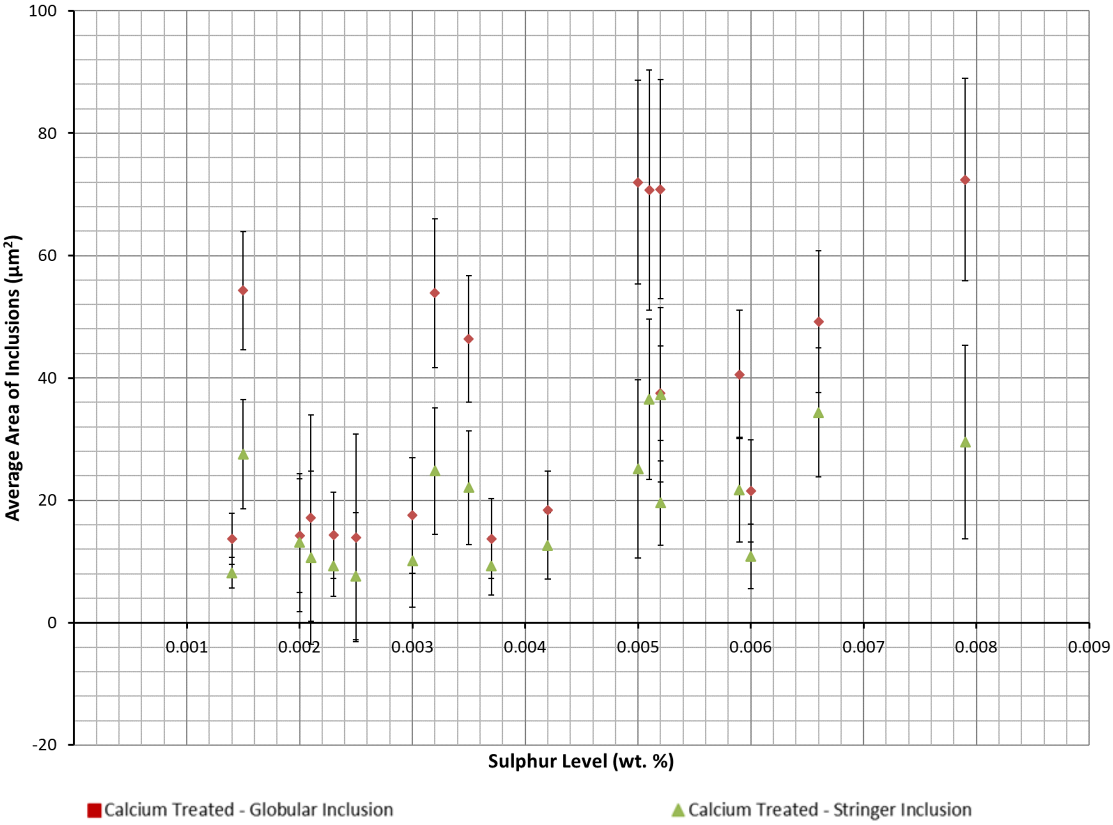

Figure 4-21. Average Area of Globular and Stringer Inclusions vs Sulphur Level for Calcium Treated FB590.

4.3.3.1.4. Inclusion Position and Size Distribution

Figure's 4-23 and 4-24 show an example of 8 of the samples that were analysed in total. For each sample there is two graphs, one demonstrating the average number of inclusions (left) for each individual row of the sample and one showing the average size of the inclusions for the given row (right). Each row marker indicates a row of 710µm^2 fields, therefore indicating the average number/size of inclusions in these distance bands (710µm^2 from surface, 1420µm^2 from surface, etc). The vertical lines (including the 2 vertical axes) on the graph demonstrate where the sample edges are. The number of lines then depends on how many sample sections the area to be analysed is built up of. For each sample the averaged results are then split into 3 categories: stringer, globular and the total inclusion population (Figure 4-22).

Figure 4-23 (a), (b), (d) and unpredictably Figure 4-24 (c) demonstrate typical examples that can be seen at lower Ca:S/higher S level. For these samples there is an increased number of inclusions near the surface of the sample. However, towards the centre of the sample, as the number of inclusions lowers, the average size of these inclusions increases. This difference tends to be more exaggerated in samples that have both larger numbers of inclusions and a larger average size of these inclusions, as can be seen in Figure 4-23 (b).

As the Ca:S increases/S level decreases, the trend reduces to a point where there is not much variation in inclusion density across the sample thickness with no subsequent build-up of larger inclusions in the centre of the sample. This only seems to happen if the sample has a low average size of the inclusions (< 20µm^2) which explains why this overall trend appears with decreasing S level. Examples of this can be seen in Figure 4-23 (c) and Figure 4-24 (a) and (b). Figure 4-24 (d) however does show that it can be possible to see a slight increase of inclusions on the centre-line even if the average inclusion size is below <20µm^2. In this case it is an increase of roughly 5 inclusions in the centre of the sample compared to the near surface.

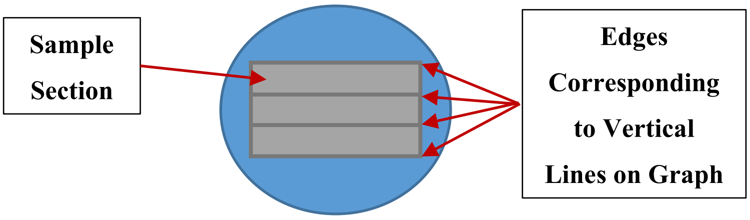

Figure 4-22. Example of Edge Positions on 3 Section Sample.

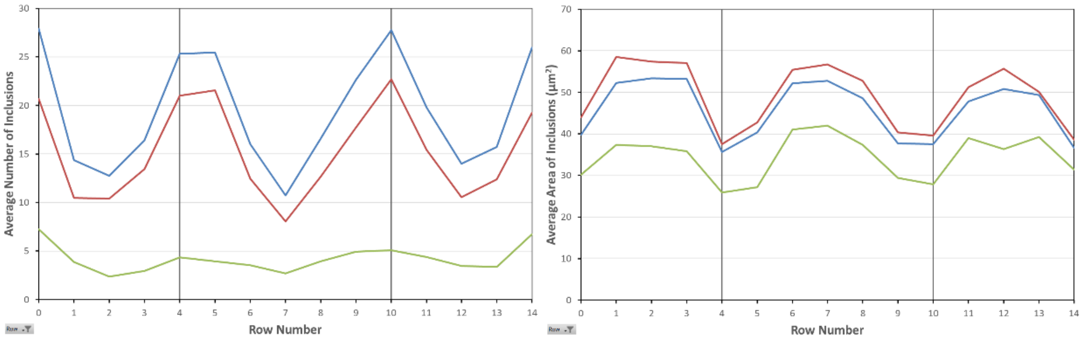

(a) 14S21-14L2 (Ca:S – 0.23, S – 0.0052 wt.%)

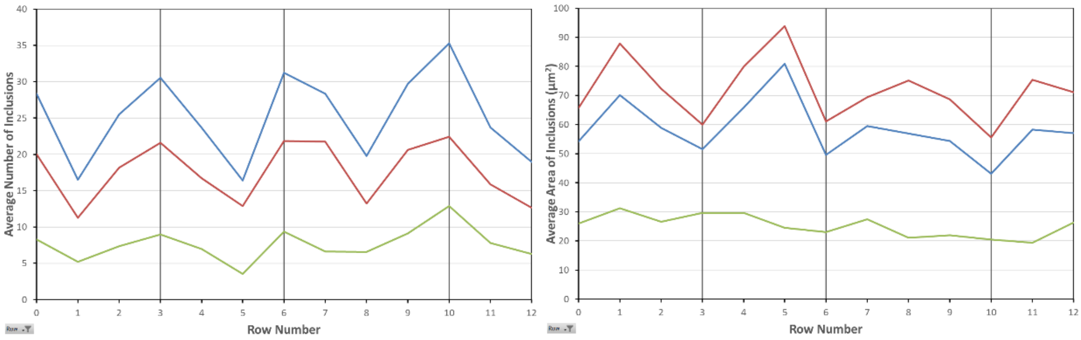

(b) 14S17-8MW (Ca:S – 0.40, S – 0.0050 wt.%)

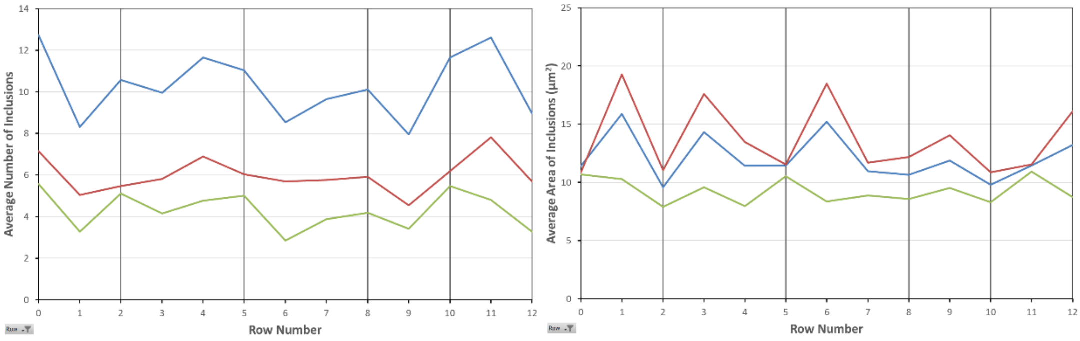

(c) 14S17-12MW (Ca:S – 0.57, S – 0.0037 wt.%)

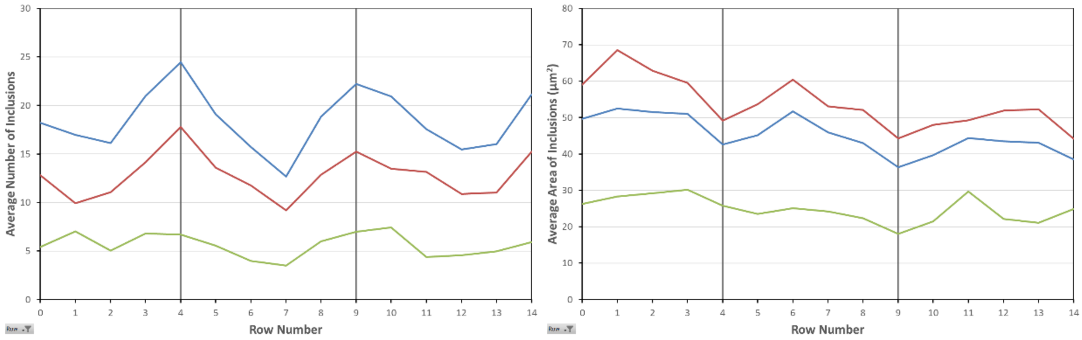

(d) 14S17-3MW (Ca:S – 0.81, S – 0.0032 wt.%)

— Total Inclusions — Globular Inclusions — Stringer Inclusions — Position of Edge

Figure 4-23 (a)-(d). Average Number of Inclusions and the Average Area of Inclusions for Each Individual Row of the Samples Labelled.

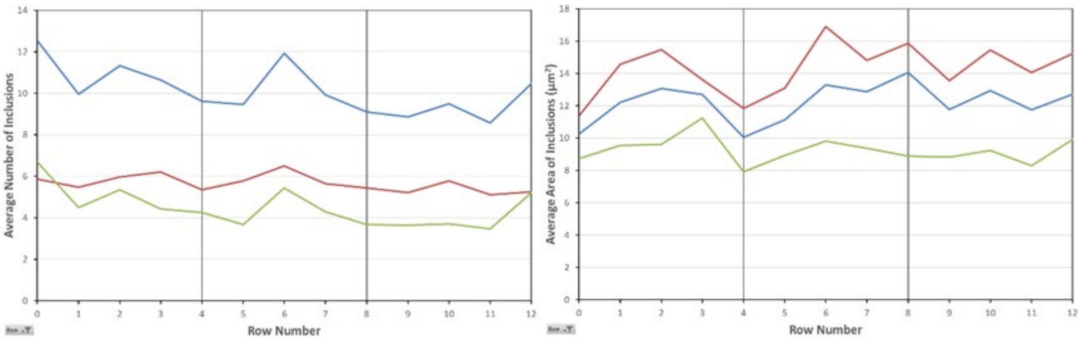

(a) 15S21-1L1 (Ca:S – 1.00, S – 0.0023 wt.%)

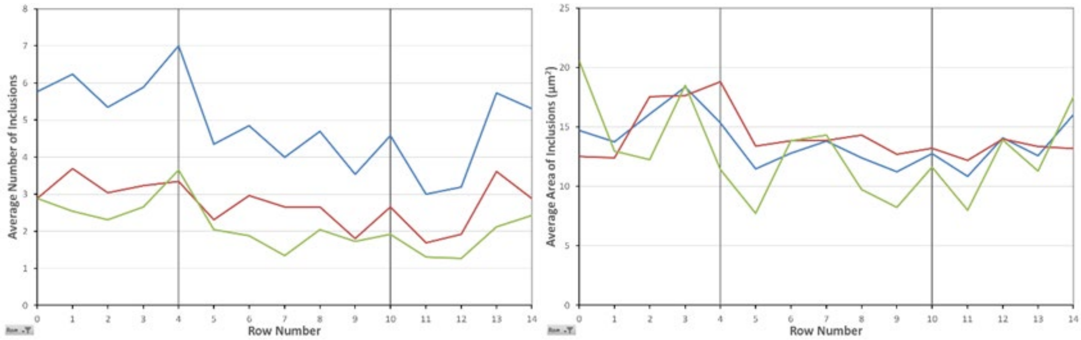

(b) 15S24-10L1 (Ca:S - 1.25, S – 0.0020 wt.%)

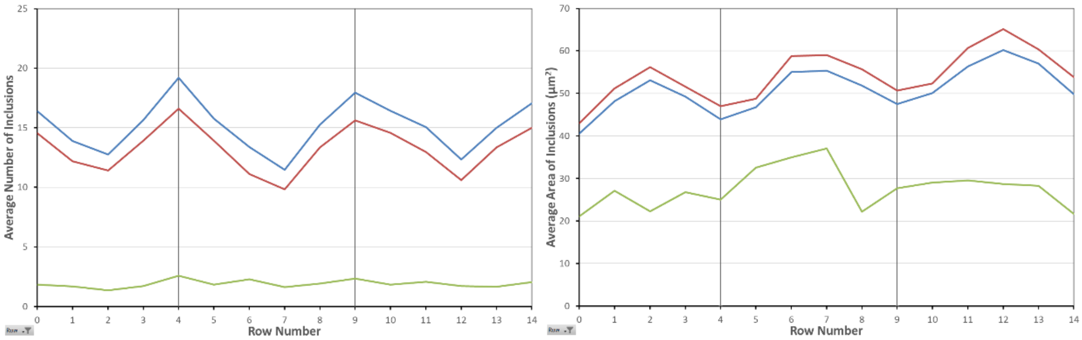

(c) 15S24-6L1 (Ca:S - 1.40, S – 0.0015 wt.%)

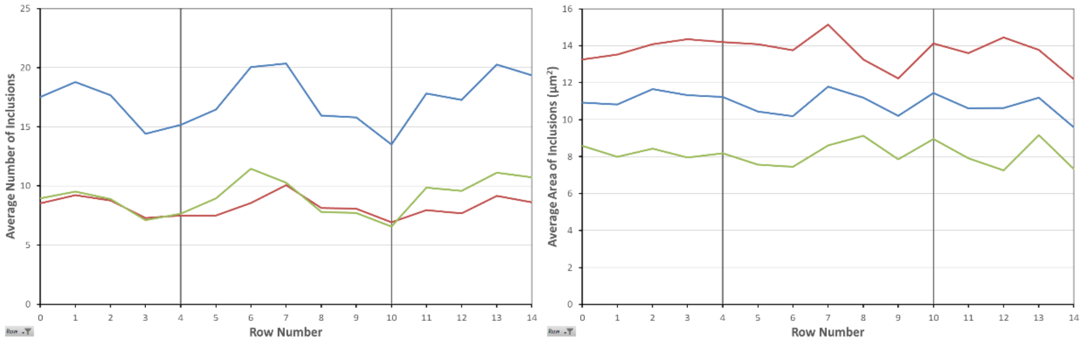

(d) 15S24-9L1 (Ca:S - 1.50, S – 0.0014 wt.%)

▬ Total Inclusions ▬ Globular Inclusions ▬ Stringer Inclusions ▬ Position of Edge

Figure 4-24 (a)-(d). Average Number of Inclusions and the Average Area of Inclusions for Each Individual Row of the Calcium Treated Samples Labelled.

4.3.3.2. Scanning Electron Microscopy (EDS Analysis)

Energy-Dispersive X-Ray Spectroscopy (EDS) was carried out on all 19 of the samples used in the large-scale inclusion analysis with the optical microscope. For each of the samples, a minimum of 8 inclusions were analysed using the correlative technique described in Chapter 3. These were selected based of their appearance in the LM image (i.e. size and shape) in an effort to ensure a complete range of the inclusion types were analysed. A small selection of the images that demonstrate the types encountered across the entire Ca:S range can be seen in Figure's 4-25 to 4-34.

The inclusions tend to be made up of a combination of a sulphide and alumina or one of its alloys. Of these, there were 3 key types of globular inclusion that were seen across the entire sample range.

The first and most common type of inclusion (Figure's 4-25 & 4-26) are generally made up of an alumina-based **'core'** consisting of phases of pure alumina (Al_2O_3), calcium aluminate ($CaO \cdot Al_2O_3$), magnesium aluminate ($MgO \cdot Al_2O_3$) or the ternary system Al_2O_3-MgO-CaO. The 'core' can either exist as a single phase (Figure's 4-25 & 4-27) or as a combinations of distinct phases (Figure 4-26). It should be noted that while it may appear that the combination of distinct phases only appears in large inclusions and vice versa, this is not always the case and just happened to occur in the examples presented here.

This 'core' is surrounded by a 'shell' of either pure Calcium Sulphide (CaS) - especially at higher Ca:S - or a solid solution of CaS and Manganese Sulphide (MnS) – (Ca,Mn)S. The 'shell' tends to be ~1µm in thickness and if it surrounds a facetted alumina 'core', turns the 'cores' angular shape into a more rounded, globular shape.

As a result of this, the overall size of this inclusion type is largely determined by the size of this alumina-based 'core'. An example of this can be seen in Figure 4-26, where even though the inclusion has a diameter of roughly 25µm, the actual proportion of the sulphide shell is actually very small. If these are compared to the a much smaller inclusions with <2.5µm diameter (Figure 4-25), the sulphide 'shell' takes up are much larger proportion while still maintaining a thickness of ~1µm.

The second type is made up of almost a **'Ying Yang'** shape, with one side being predominantly alumina-based and the other being a sulphide (Figure 4-27).

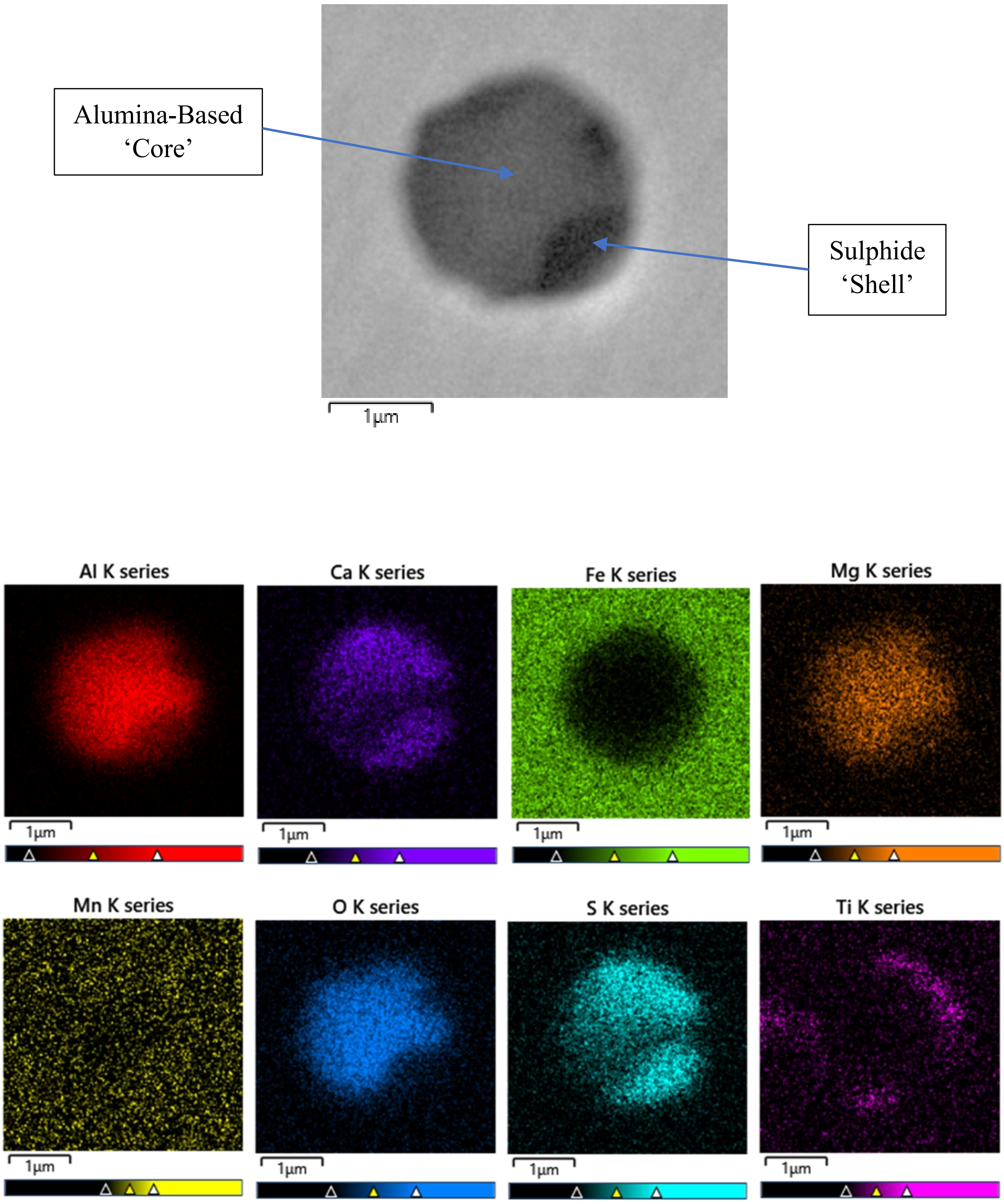

Figure 4-25. Example of a "Small" 'Cored' Globular Inclusions (i.e. <2.5µm Diameter) from 15S24/1L1 that Identifies the Different Components of the Inclusion.

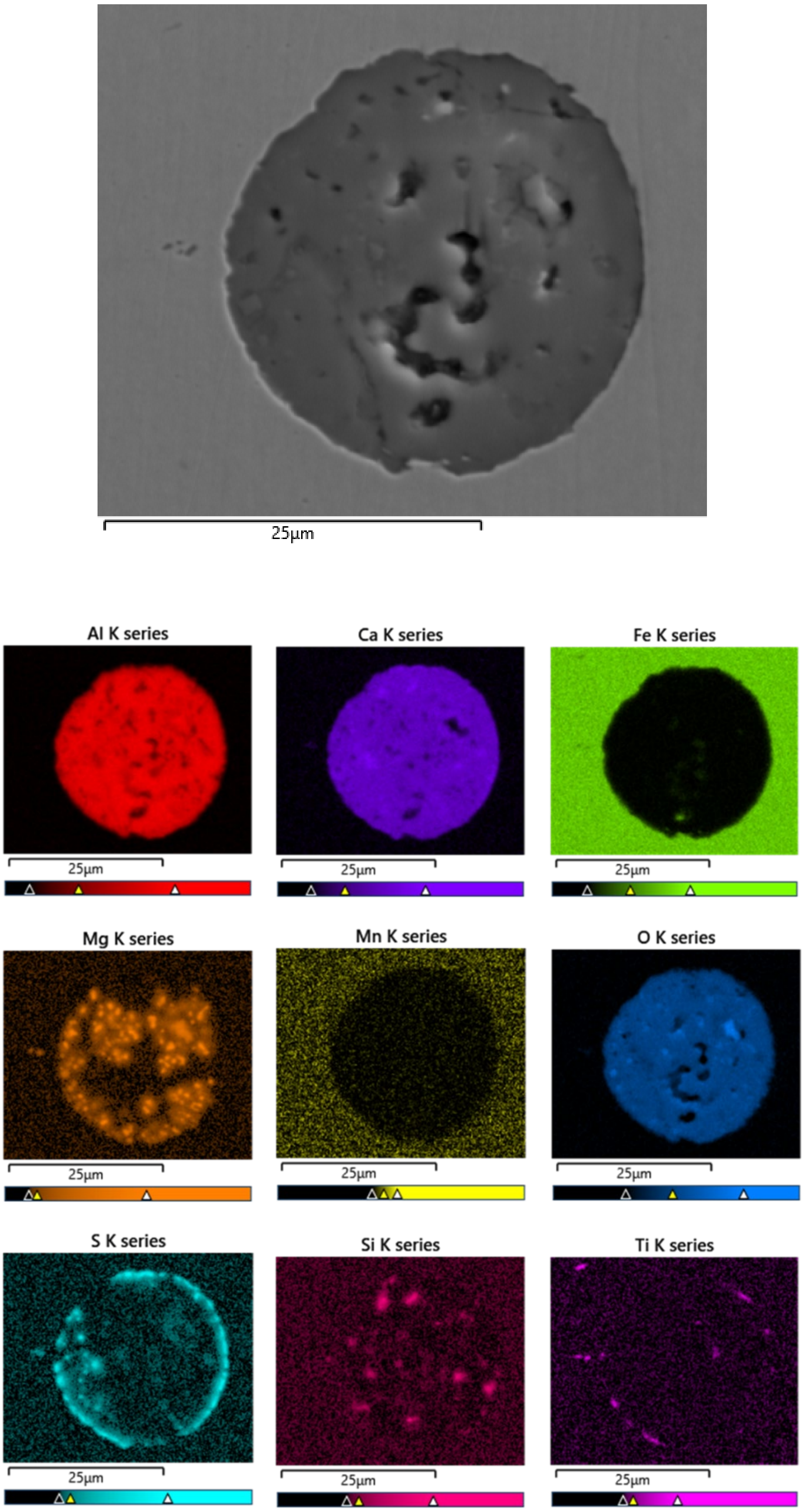

Figure 4-26. Example of a "Large" 'Cored' Globular Inclusion (i.e. >25µm Diameter) from 14S17/4MW.

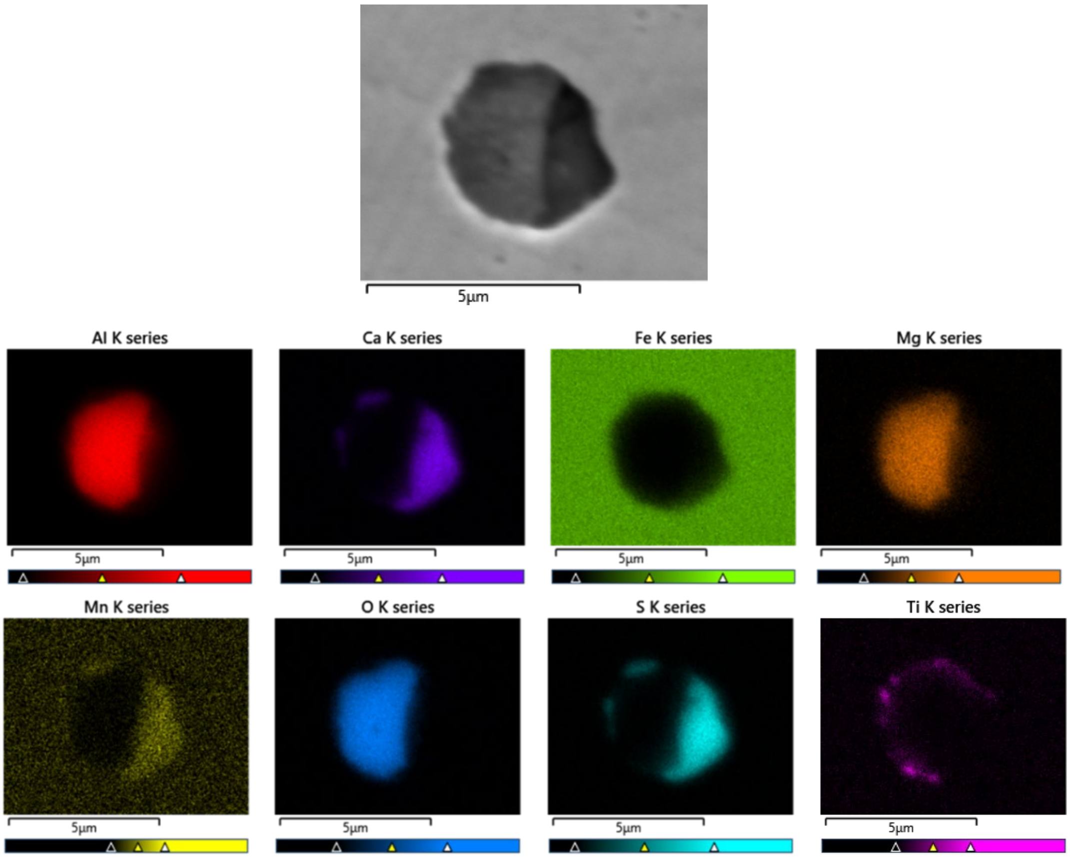

Figure 4-27. Example of a 'Ying-Yang' Globular Inclusions from 15S24/1L1

While rare, this inclusion type can also be comprised of one-side alumina/sulphide-based and the other a 'Cored' inclusion, similar to those described previously. It has been also been seen that this type of inclusion can agglomerate in such a way as to classify itself as a stringer. However, this formation was so uncommon that it cannot be described in its own category.

Unlike globular inclusions, there several different types of stringer that were encountered across the Ca:S range. These consisted of 7 different forms with a large variety of L/W ratios, most of which exhibited a very similar 'core'/'shell'-based structure to their globular counterparts.

The first is the **'classic'** elongated stringer that is seen in Figure 4-28. This consists of a purely MnS 'shell' surrounding an alumina-based 'core'. As can be seen, this type of inclusion undergoes a significant amount of deformation resulting in only 2 examples seen in all the non-Ca treated samples.

The second type of inclusion consists of a 'shell' that has only been **'partially-modified'** with Ca. As a result, this 'shell' has partially elongated upon rolling but to nowhere near the same degree seen in the 'classic' stringer (Figure 4-29).

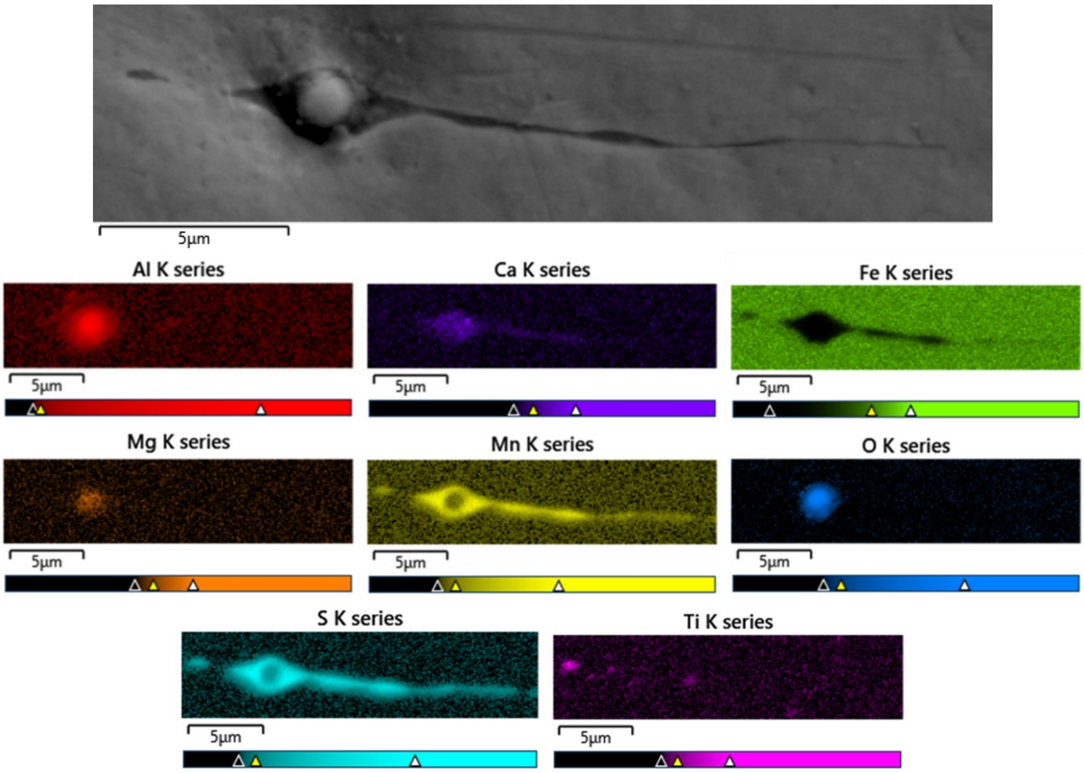

Figure 4-28. Example of a ‘Classic’ Stringer Inclusion from 14S21/2L1

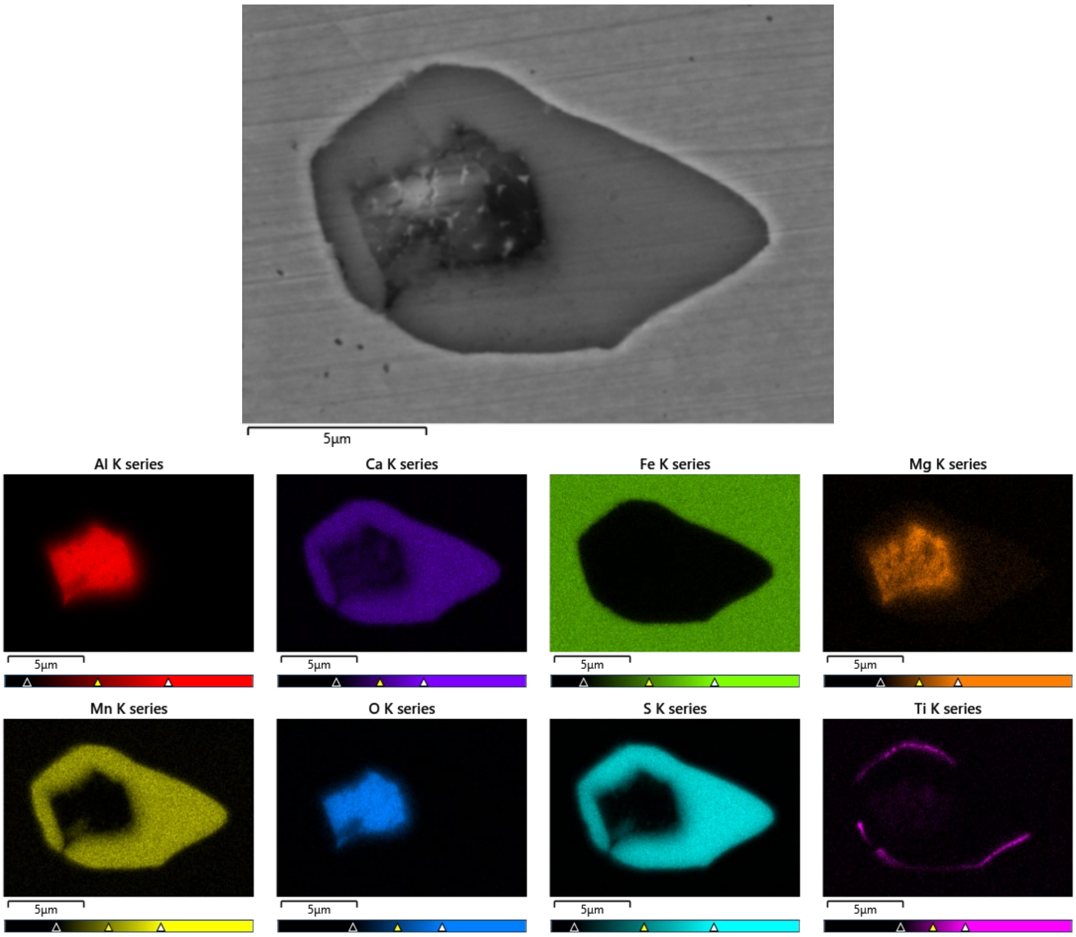

Figure 4-29. Example of a ‘Partially Modified’ Stringer Inclusion from 13S24/18MW.

The third type of stringer encountered consists of a purely **'sulphide-based'** inclusion, without any associated alumina. While the example in Figure 4-30 consists solely of (Ca,Mn)S there were other examples that consisted purely of MnS. As can be seen, this particular inclusion is very slightly elongated in rolling direction but is still relatively globular in appearance and is only ~1µm thick.

The fourth type of stringer is a stringer simply because the alumina-based core is so **'facetted'** that the sulphide 'shell' cannot grow large enough to turn the inclusion into a globular inclusion. Because overall shape of the inclusion is largely determined by the shape of the alumina 'core', the L/W ratio of this stringer type varies quite dramatically, from just above the 1.3 ratio described in the standard to the 'worst-case' ratio seen in Figure 4-31.

The fifth, and most common type of stringer inclusion that was encountered consisted of a normal globular inclusion that had **'fractured'** upon rolling. This resulted in the formation of a cluster of inclusions in the rolling direction and happened to varying degrees. This could be anything from a small amount of the sulphide 'shell' fracturing off (Figure 4-32) to where inclusion has completely disintegrated, forming a long clustered stringer (Figure 4-33). This fracture, however, only occurred in large inclusions that contained a large alumina 'core' with the smallest inclusion having an estimated diameter of 5.18μm^2 (2dp) before fracturing. Most of the time however the inclusions that fractured were significantly larger with the average estimated diameter of these inclusions prior to fracture being 17.85μm^2 (2dp). This diameter was calculated by first assuming the inclusion was perfectly globular, combining the areas of the fragmented pieces and calculating the diameter from this summed value.

The final type of stringer inclusion observed was categorised as a stringer solely because of the classification found in BS EN 10247:2007. This type exists when 2 or more separate inclusions have **'nucleated'** within 40µm of each other in the rolling direction and 10µm in the perpendicular direction (Figure 4-34).

It can also be seen that an amount of Silicon (Si) and Titanium (Ti) also appears with the inclusions. In this situation, the Ti invariably forms on the surface of the inclusion (Figure's 4-25 and 4-29). If Si is found it is usually bonded to the alumina core (Figure 4-32), most likely in the form of SiO_2-CaO-Al_2O_3. However, these are not always found and if they are it is in much smaller quantities.

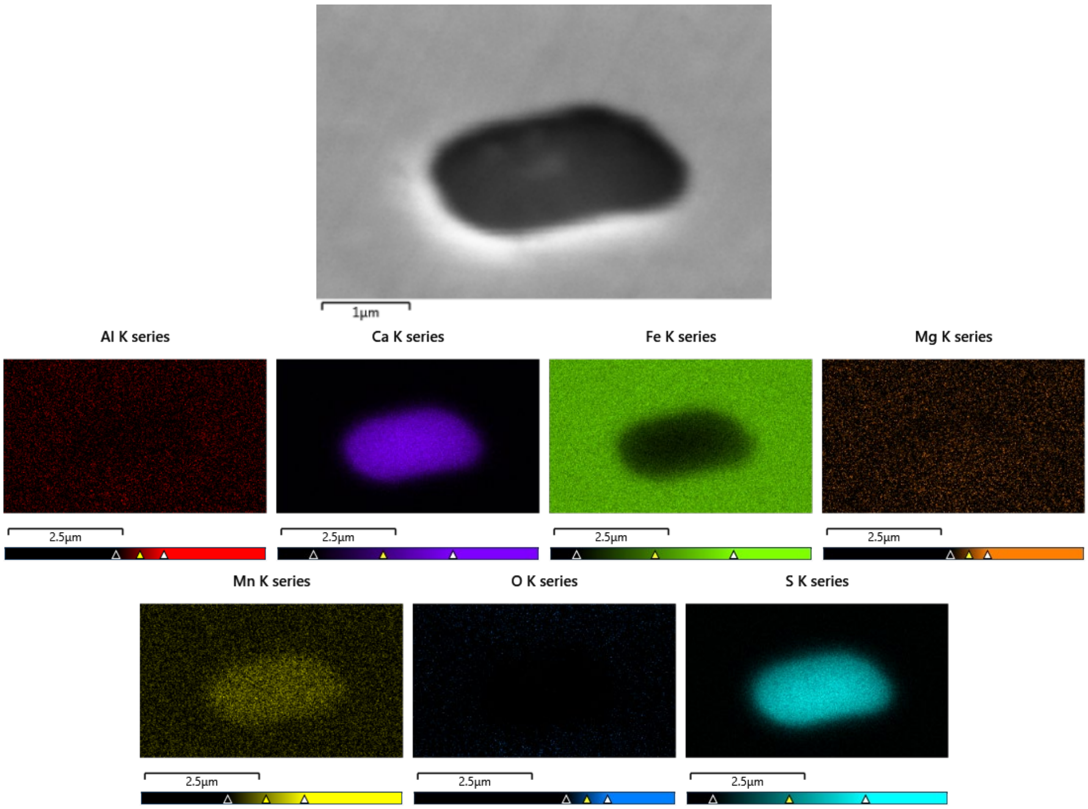

Figure 4-30. Example of a Purely 'Sulphide-based' Stringer Inclusions from 15S24/1L1

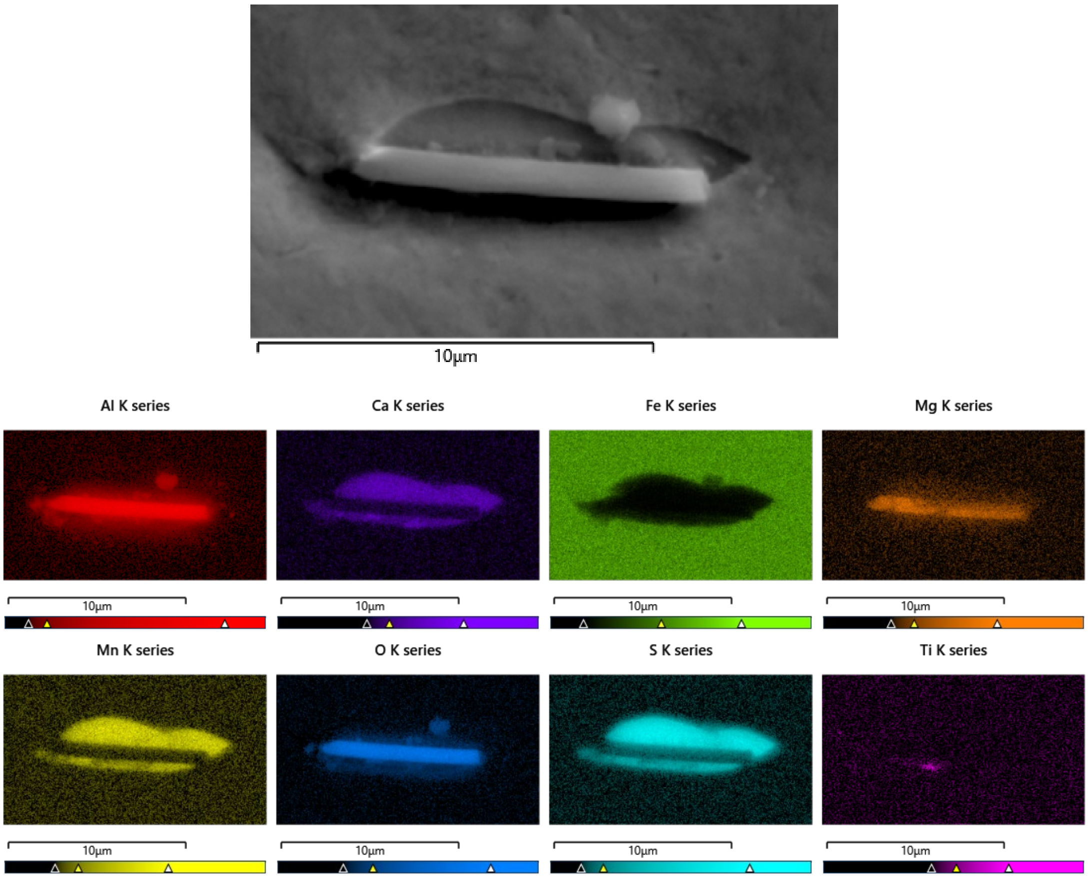

Figure 4-31. Example of a 'Facetted' Stringer Inclusion from 14S21/2L1.

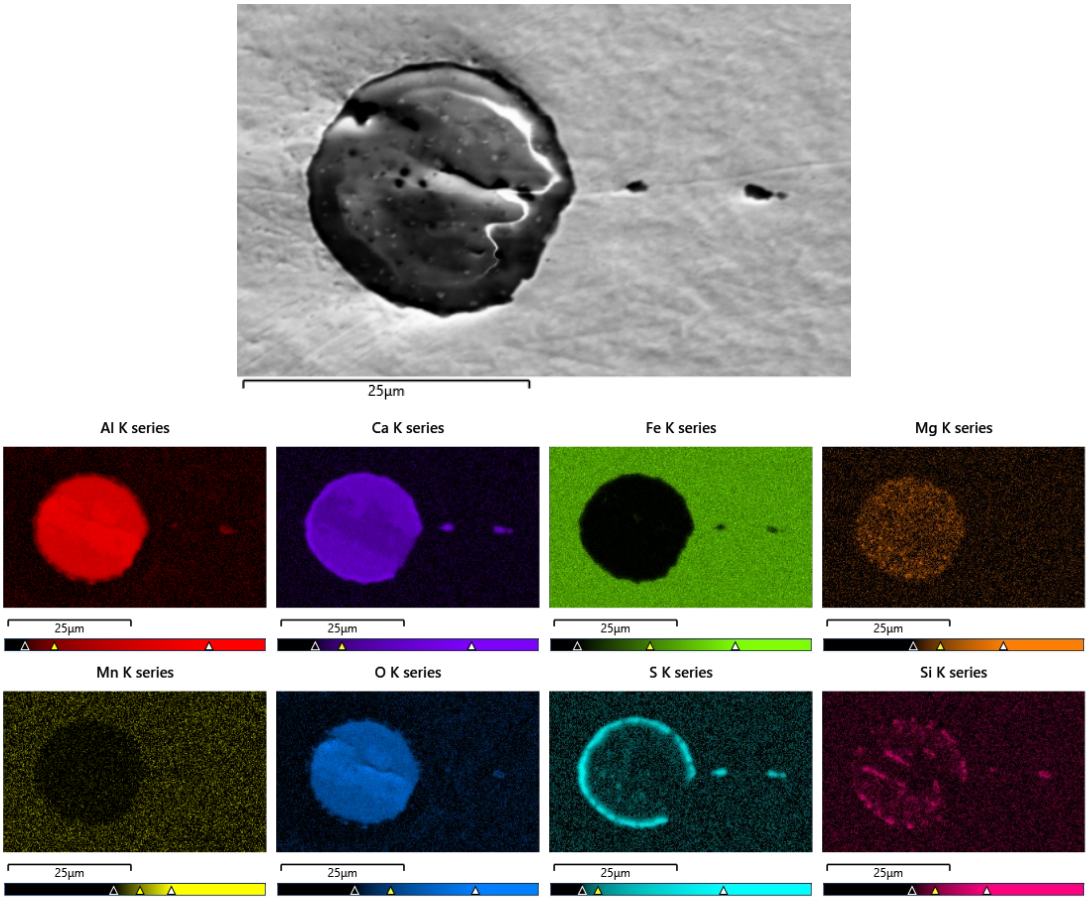

Figure 4-32. Example of a Partially 'Fractured' Stringer Inclusion from 14S17/2MW.

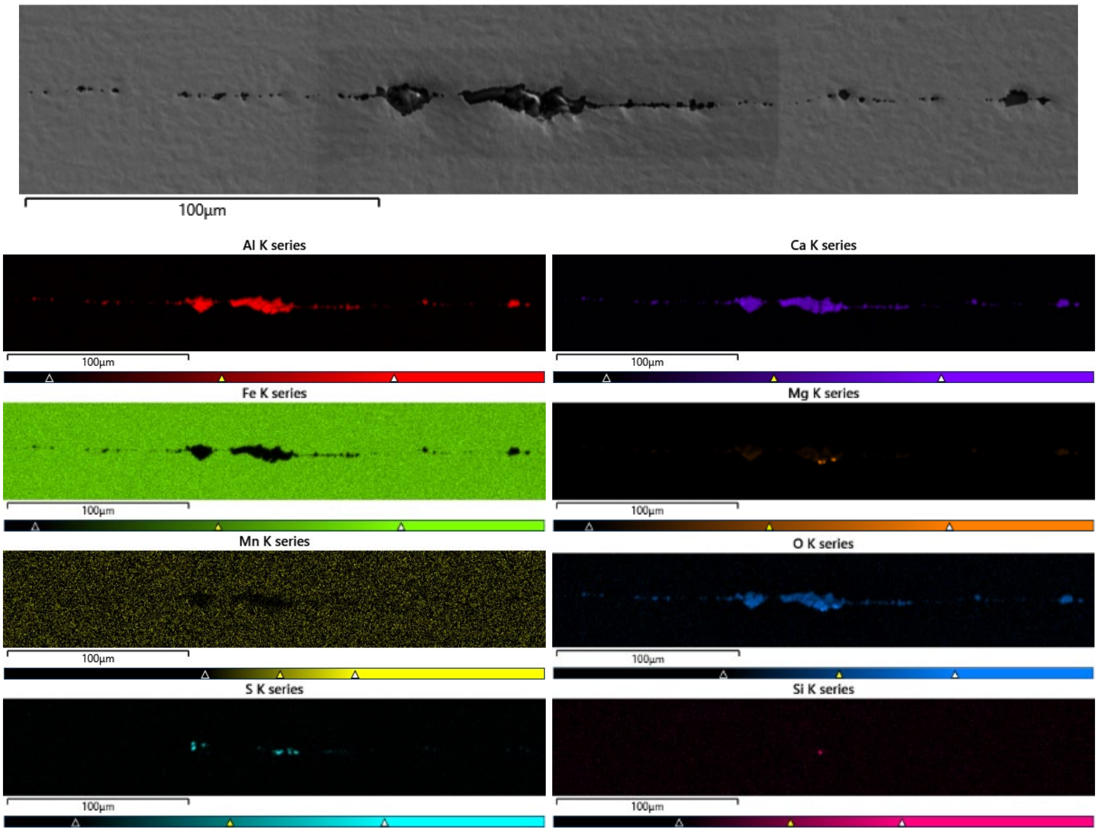

Figure 4-33. Example of a Completely 'Fractured' Stringer Inclusions from 15S24/6L1.

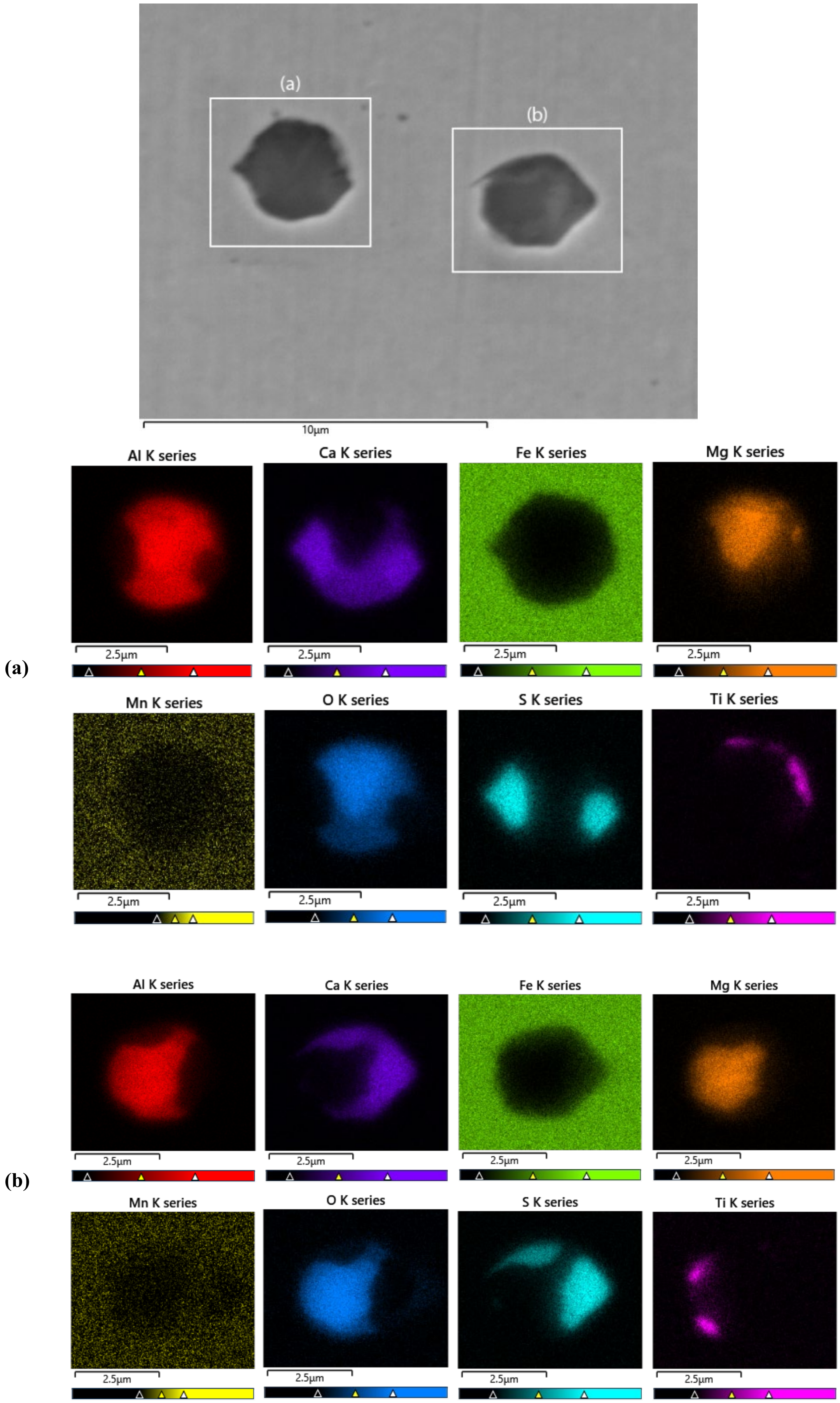

Figure 4-34. Example of a ‘Nucleated’ Stringer Inclusions from 15S24/9L1

4.3.4. Inclusion Analysis of Non-Calcium Treated Grade

4.3.4.1. Optical Microscopy

To obtain a better understanding of how Ca treatment affects the inclusion population of the steel, a similar study, albeit of a smaller number of samples, was carried out on 9 non-Ca treated samples. Whilst 8 of these samples underwent a significantly different rolling procedure than the Ca treated samples that would make them unsuitable for mechanical result comparison, they would still give a baseline to compare the microstructures. As with the Ca treated samples, $200mm^2$ examples were taken from the centre of the coil in the L1 position and analysed in $710\mu m^2$ areas at 100x magnification.

4.3.4.1.1. Percentage Globular

The average percentage of globular inclusions that were encountered can be seen Figure 4-35. For this, both the non-Ca and Ca treated samples were compared against their relative levels of S in weight percent, because at this point comparing them against Ca:S would be redundant.

It can be seen that the non-Ca treated samples exhibit significantly lower levels of globular inclusions than their Ca treated equivalents. The entire data set displays, on average, between 20 & 30% globular inclusions. There also does not seem to be any sort of change in the percentage amount of globular inclusions that can be associated with an increase/decrease in S level. Instead the amount of globular inclusions shows a flat trend with increasing S level.

All the samples show large error bars similar to those seen in the Ca treated samples. Therefore, as mentioned for the Ca treated samples, this will most likely be due to the fact that some grids only incorporate one or a few inclusions. If these are classified as globular it will lead to an overall extension of the error range.

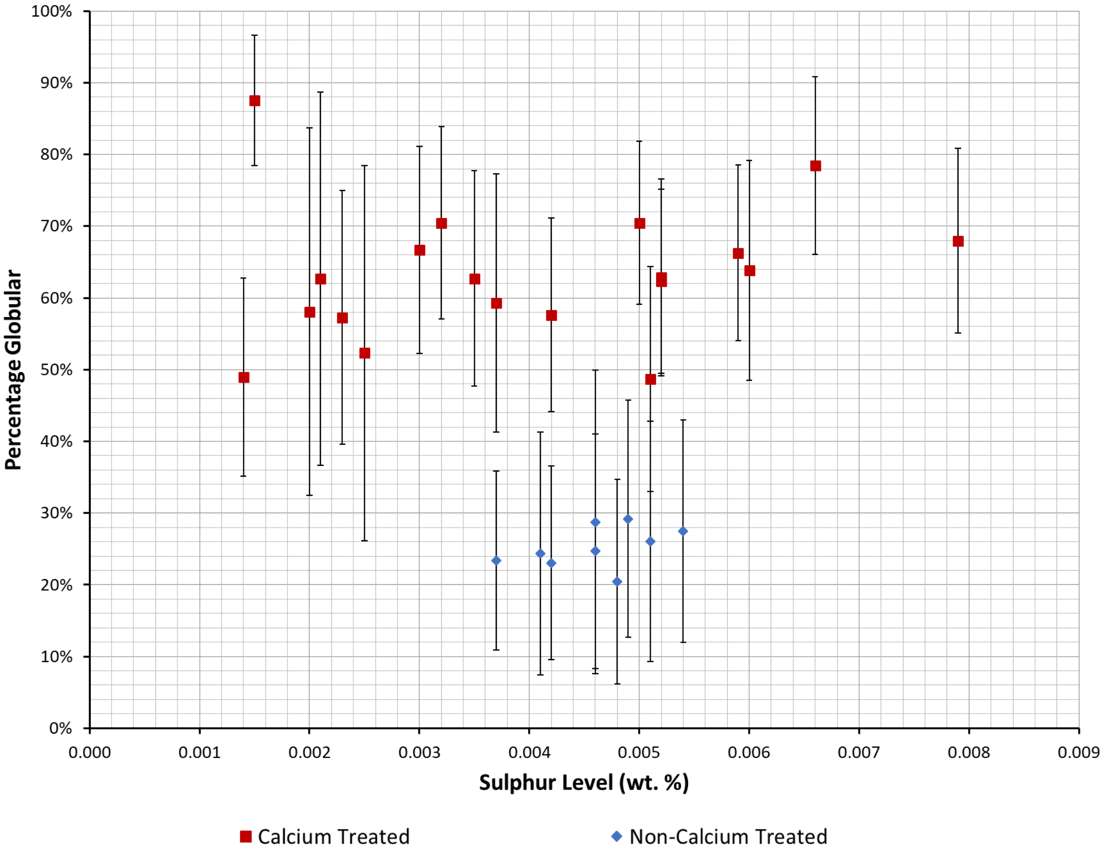

Figure 4-35. A Comparison of the Amount of Globular Inclusions in Calcium Treated FB590 and Non-Calcium Treated Steel when Compared to Sulphur Level.

4.3.4.1.2. Inclusion Population Density

Figure 4-36 shows the average number of inclusions per 710µm^2 grid area for both the Ca and non-Ca treated grades. It can be seen that the results for non-Ca treated grades fits within the trend seen in the Ca treated grades, where the average number of inclusions increases as the S level increases within the sample. However, while they do fit with the trend seen in the Ca treated samples, they do appear to have slightly lower numbers of inclusions on average.

Figure 4-37 then splits these results into the 2 inclusion types, showing the average amount of globular and stringer inclusions for both the non-Ca and Ca treated grades against their respective S levels. The graph shows that the number of stringer inclusions for the non-Ca treated steels corresponds to the amount and trend for globular inclusions in the Ca treated steels. The globular inclusions for the non-Ca treated grades do not show a trend, instead remaining at a constant level of ~3 inclusions per 710µm^2 as the S level increases.

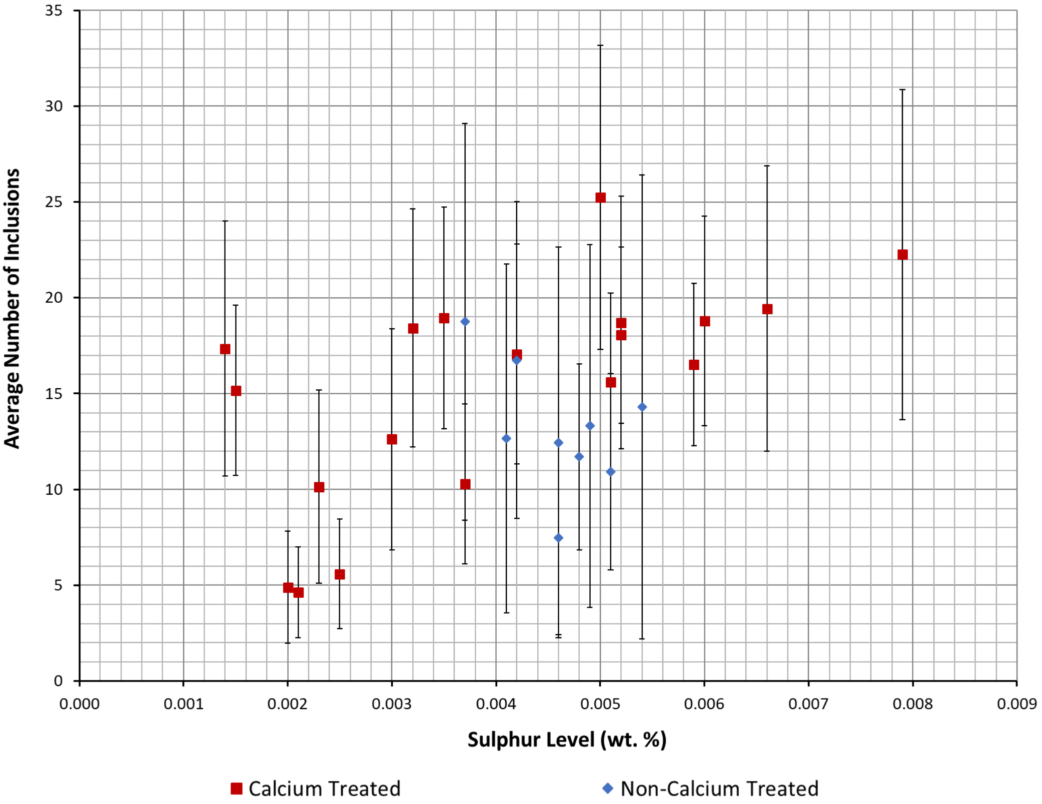

Figure 4-36. A Comparison of the Average Number of Inclusions in Calcium Treated FB590 and Non-Calcium Treated Steel when Compared to Sulphur Level.

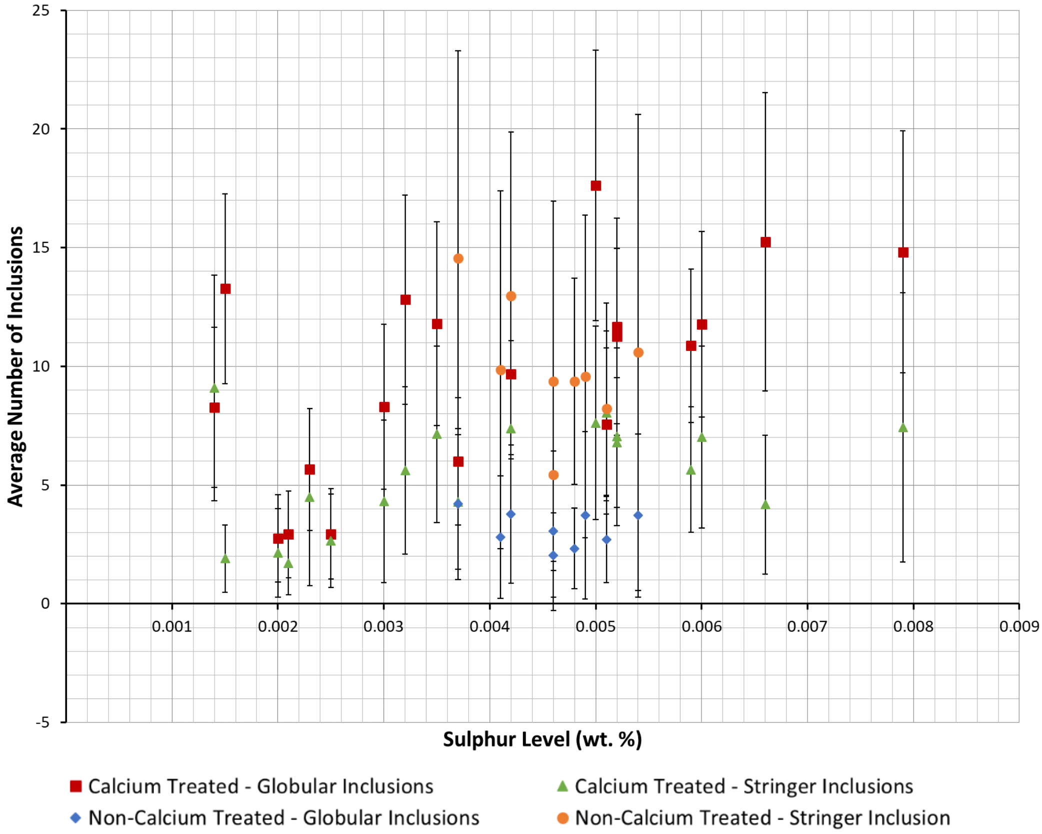

Figure 4-37. A Comparison of the Average Number of Stringer and Globular Inclusions in Calcium Treated FB590 and Non-Calcium Treated Steel when Compared to Sulphur Level.

4.3.4.1.3. Size of Inclusions

Figure 4-38 compares the average size of inclusions of the non-Ca treated samples against the Ca treated samples, in relation to both their S levels. It can be seen that the average area of the inclusions in the non-Ca treated grades is smaller than the equivalent Ca treated samples at the same sulphur levels. In fact, the non-Ca treated samples have some of the smallest size inclusions across the entire sulphur range, with all samples exhibiting inclusions with an area of roughly 12μm^2.

These results are then split into the two inclusion types and compared against the Ca treated grades in relation to their S level in Figure 4-39. Both the globular inclusions and the stringer inclusions have very similar sizes. However, in every case the globular inclusions have a slightly larger area than their stringer counterparts. Both inclusion types are smaller on average than their counterparts in the Ca treated grades at the same S levels. They are, however, similar in area to stringer inclusions in the Ca treated samples at lower sulphur levels.

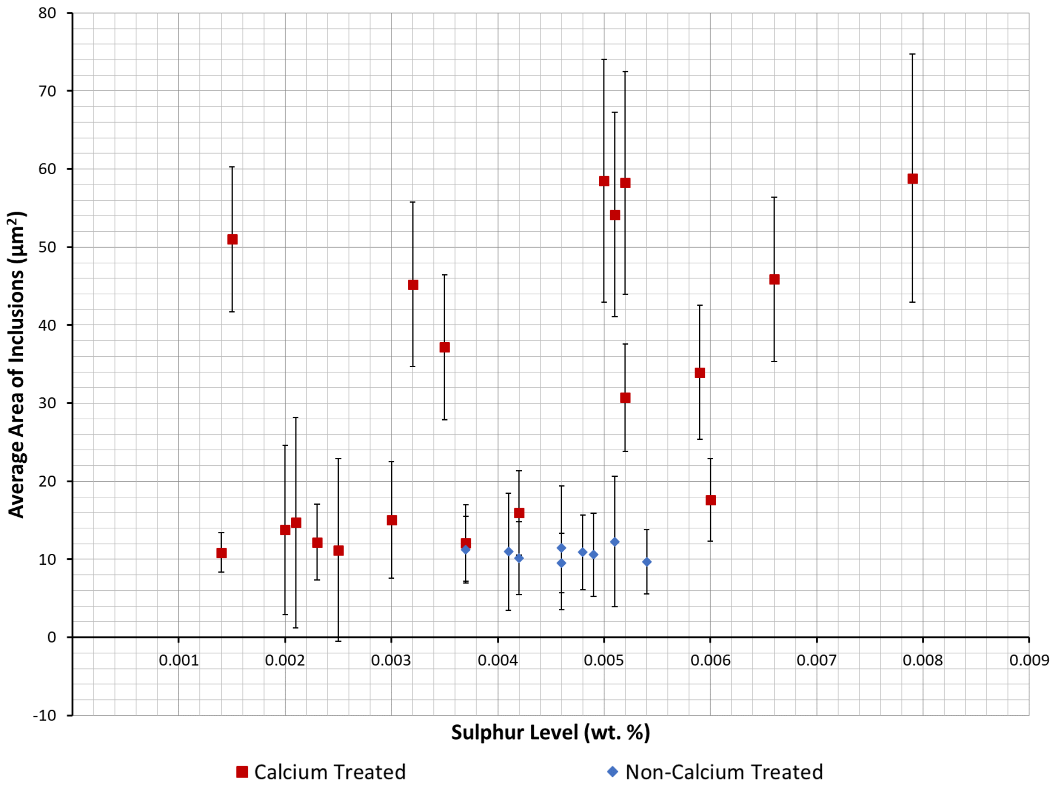

Figure 4-38. A Comparison of the Average Size of Inclusions in Calcium Treated FB590 and Non-Calcium Treated Steel when Compared to Sulphur Level.

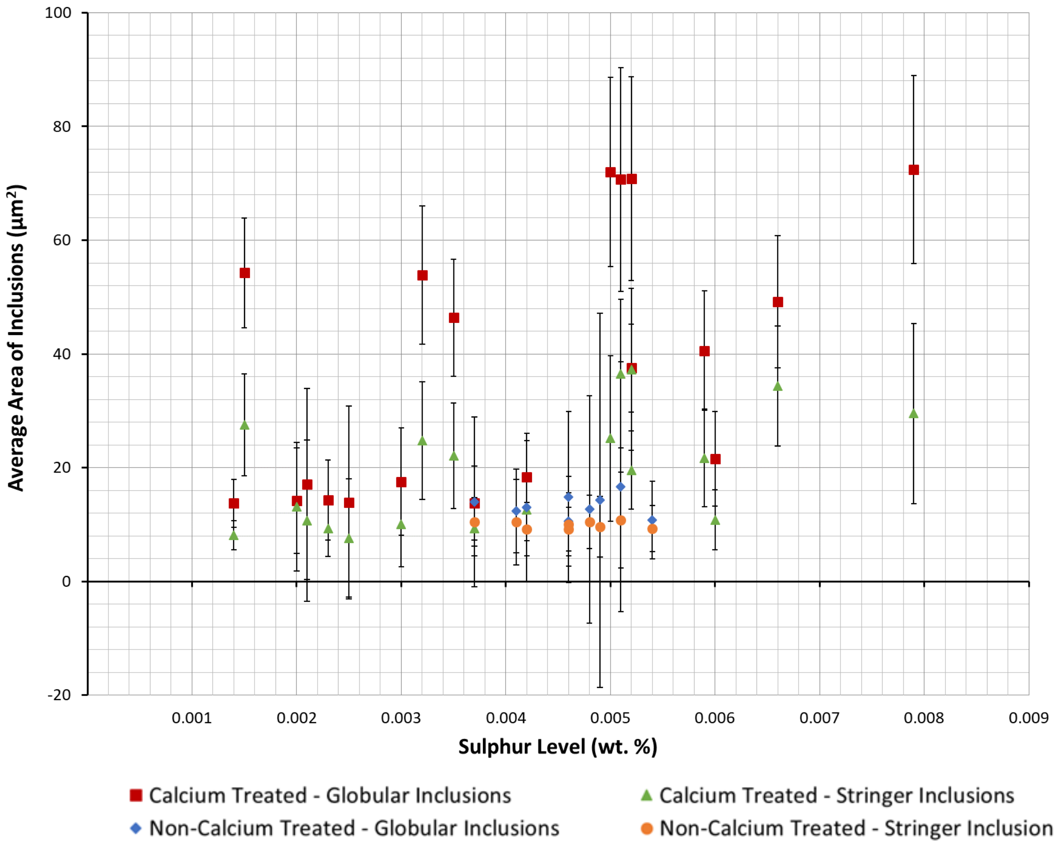

Figure 4-39. A Comparison of the Average Size of Stringer and Globular Inclusions in Calcium Treated FB590 and Non-Calcium Treated Steel when Compared to Sulphur Level.

4.3.4.1.4. Inclusion Position and Size Distribution

As with the Ca treated samples, an example of 4 of the non-Ca treated samples have been chosen that are representative of all the samples, with the average size and number of inclusions shown in Figure 4-40 and split into total, stringer and globular inclusions. The through thickness averages for the inclusions, are then split into rows consisting of 710 μm^2 fields in the same way as the Ca treated samples in Figure's 4-23 to 4-24. While the vertical lines in Figure 4-40 (d) represent the edges of each section, (a) – (c) do not have these lines because the sample is made from a single section of steel.

Figure 4-40 (a) and (b) show quite clearly an increase in inclusions near the edge of the sample. This is shown in (c) and (d) as well, but to a much lesser extent. It is, however, more difficult to clearly see these in (d), as the sections of the steel were significantly thinner. Figure 4-40 (a) and (b) also show a slight increase in the number of globular inclusions towards the edges. The number of globular inclusions in (c) and (d) however, have roughly the same number of inclusions through the full thickness of the steel.

Figure 4-40 (a) and (c) show a large increase in the number of inclusions towards the centre of the centre of the sample. This is also shown in (d) and to a much lesser extent in (b). However, unlike their Ca treated equivalents, the samples did not show a resulting change in inclusion size, as the number of inclusions varied with the size of stringer and ‘total’ inclusions remaining relatively flat through the thickness of the steel. The average size of globular inclusions varies to a much larger amount, but this is most likely due to small number of inclusions being more affected by 1 or 2 large/small inclusions.

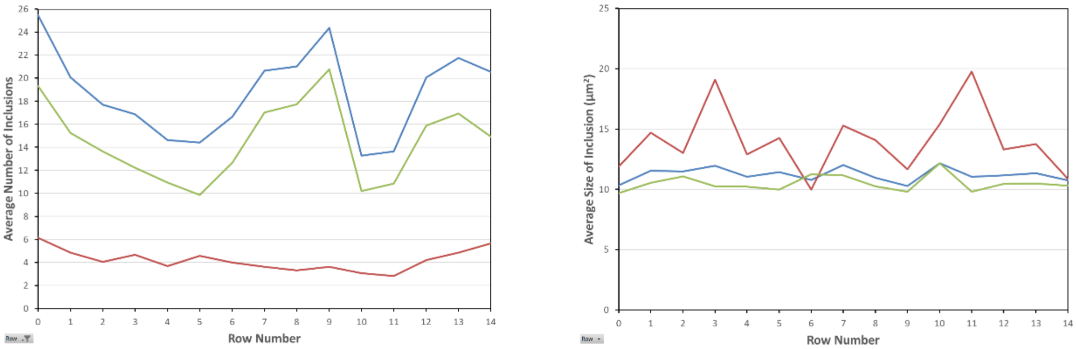

(a) 16S18-25L1 (S – 0.0037 wt.%)

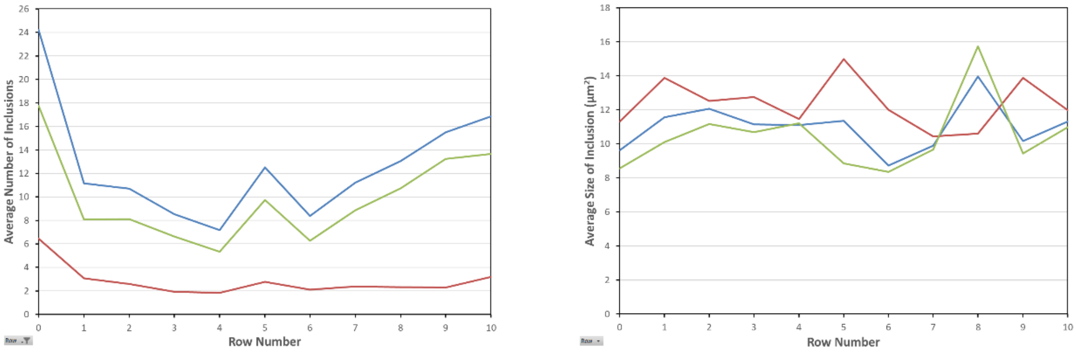

(b) 16S18-10L1 (S – 0.0041 wt.%)

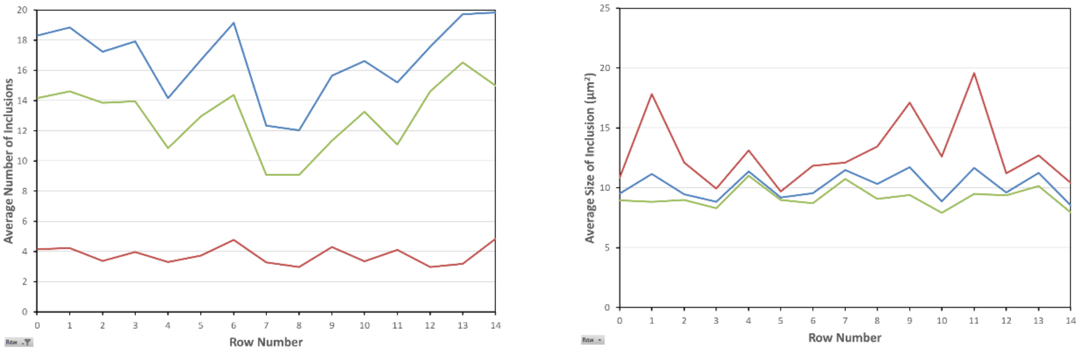

(c) 16S18-17L1 (S – 0.0042 wt.%)

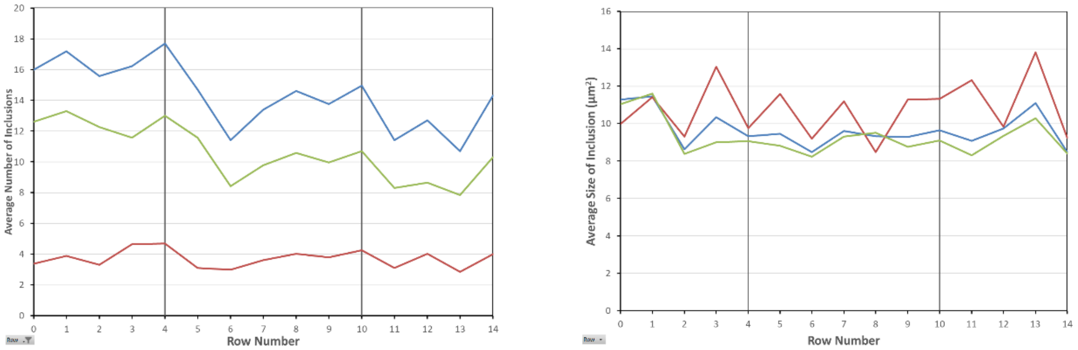

(d) 11QS44-7L1 (S – 0.0054 wt.%)

Figure 4-40 (a)-(d). Average Number of Inclusions and the Average Area of Inclusions for Each Individual Row of the Non-Calcium Treated Samples Labelled.

4.3.4.2. Scanning Electron Microscopy (EDS Analysis)

EDS Analysis was carried out on the one non-Ca treated sample that was mechanically tested to gain a greater understanding of how the inclusions is structured through its constituent elements. For this sample, a total of 14 scans were taken, using the correlative technique to ensure that a good range of sizes/shapes were analysed. A selection of these inclusions is shown in Figure's 4-41 to 4-44.

As with the Ca treated inclusions, the inclusions are generally made up of a ‘core’ of either Al_2O_3, $MgO{\cdot}Al_2O_3$ or very small amounts of $CaO{\cdot}Al_2O_3$. This ‘core’ is a key component in determining the overall shape of the inclusion. However, unlike the Ca treated inclusions this alumina ‘core’ is always surrounded by a ‘shell’ of pure MnS. This has the added effect of, if the alumina ‘core’ is particularly angular in nature, the MnS will ‘round’ these corners off, creating a much smoother overall inclusion. This ‘shell’ of MnS is always elongated in the rolling direction, sometimes in both directions, and can be extremely long. For example, the inclusion in Figure 4-41 has ‘tail’ that is visible to roughly 50µm in length. It is however, less than 1µm thick.

Unlike the Ca treated samples, there was not such a variety in either globular or stinger inclusions, with only 1 of the 3 globular and 3 of the 4 stinger inclusions types being analysed. This was the standard ‘cored’ globular inclusion seen in Figure 4-44 as well as the ‘classic’ elongated stringer (Figure 4-41), the fractured stringer (Figure 4-42) and the purely ‘sulphide-based’ stringer seen in Figure 4-43. Of these 4 total inclusion types, the ‘classic’ and the ‘sulphide-based’ inclusions were the most common.

The ‘sulphide-based’ inclusions, unlike the ones in the Ca treated samples, tended to appear in small clusters of a few stringer inclusions that were significantly elongated in the rolling direction, with the typical example in Figure 4-43 showing a visible length of over 50µm. However, as with the inclusion seen in Figure 4-41, this elongated inclusion still has a thickness of less than 1µm. Also like the Ca treated samples, there are also examples of Ti bonded to the MnS ‘Shell’ (Figure 4-41) and Si bonded to the alumina core (Figure 4-42).

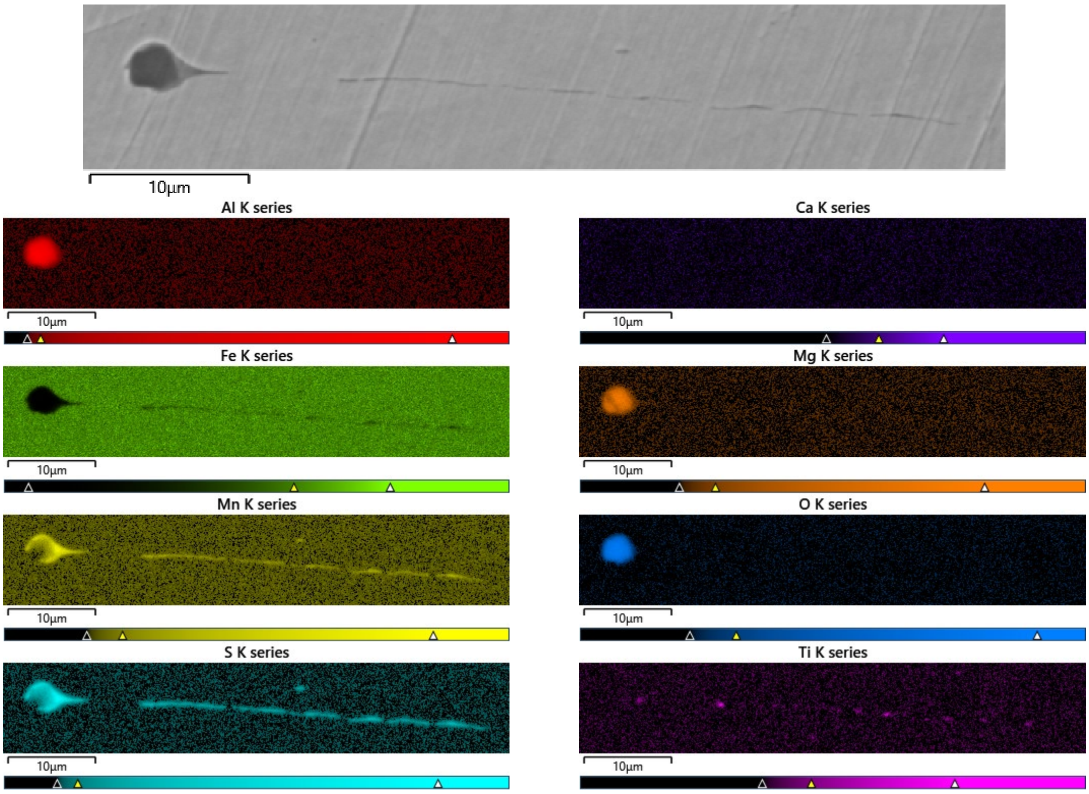

Figure 4-41. Example of a ‘Classic’ Stringer Inclusion found in 11QS44/7L1.

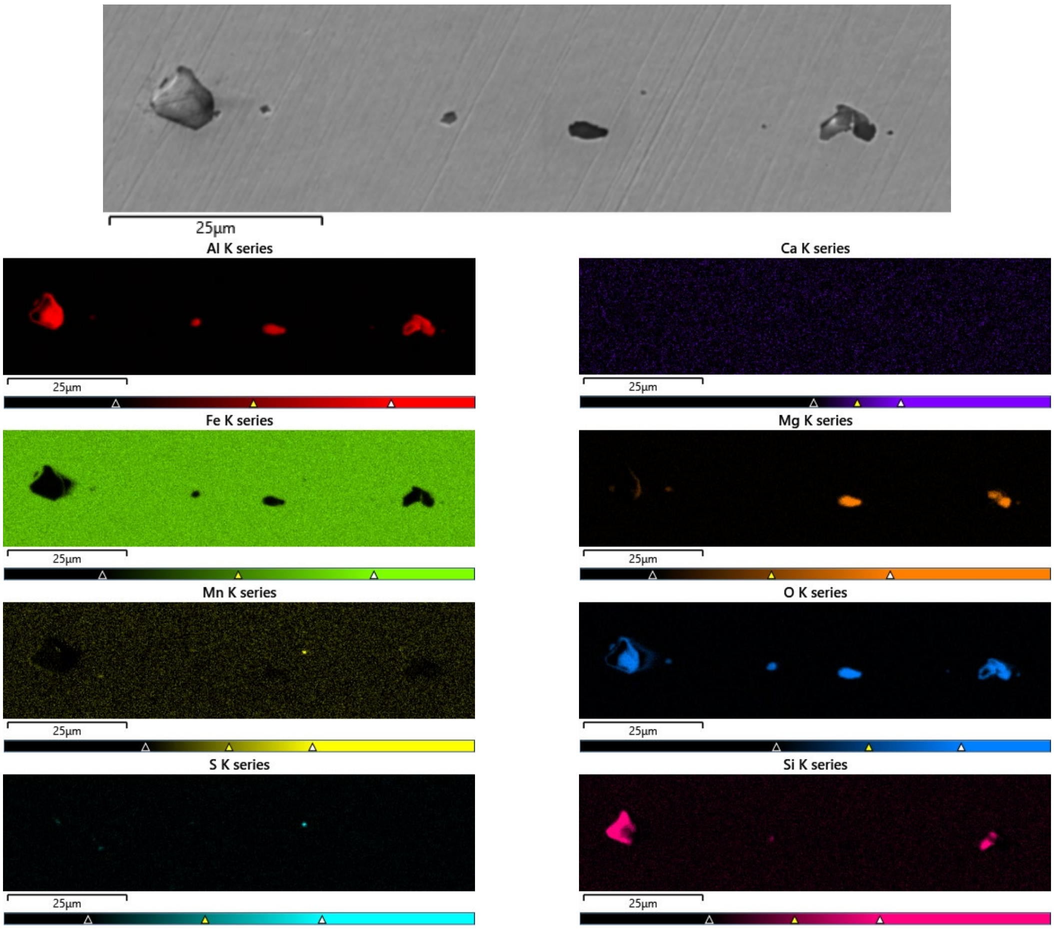

Figure 4-42. Example of a Completely ‘Fractured’ Stringer Inclusion found in 11QS44/7L1

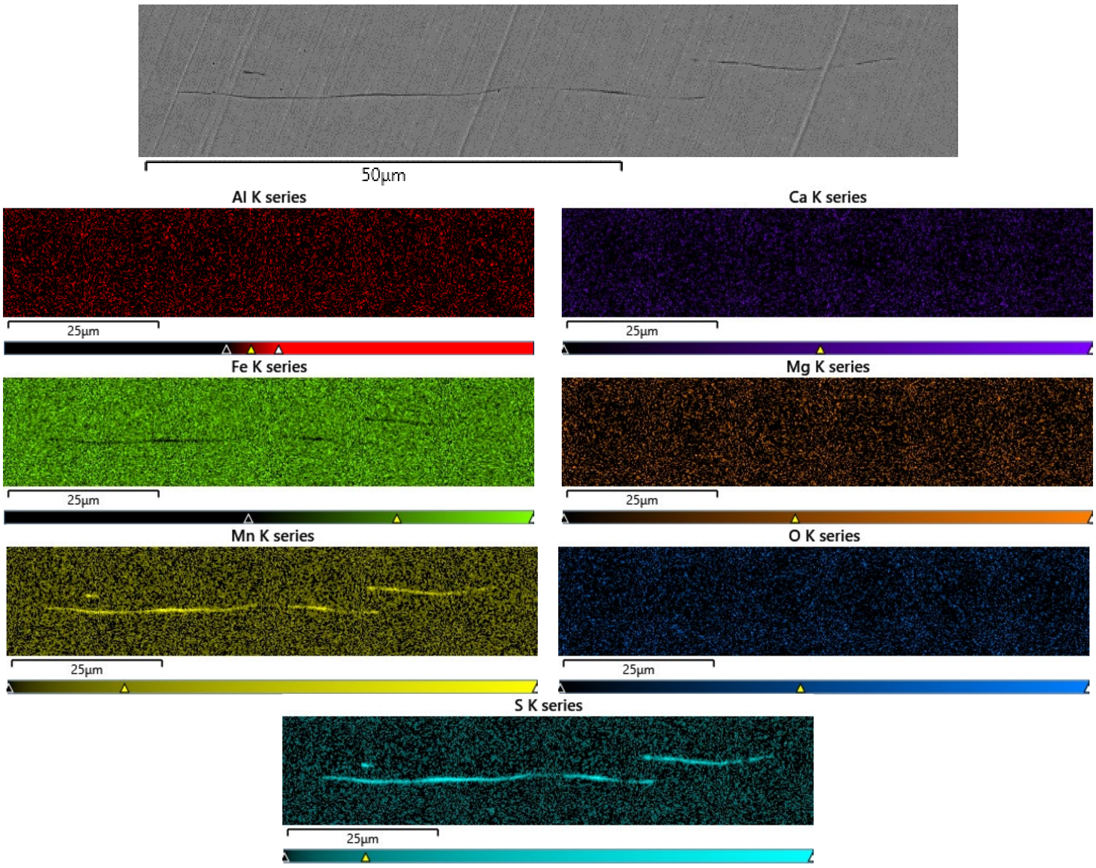

Figure 4-43. Example of a Purely ‘Sulphide-Based’ Stringer Inclusion found in 11QS44/7L1

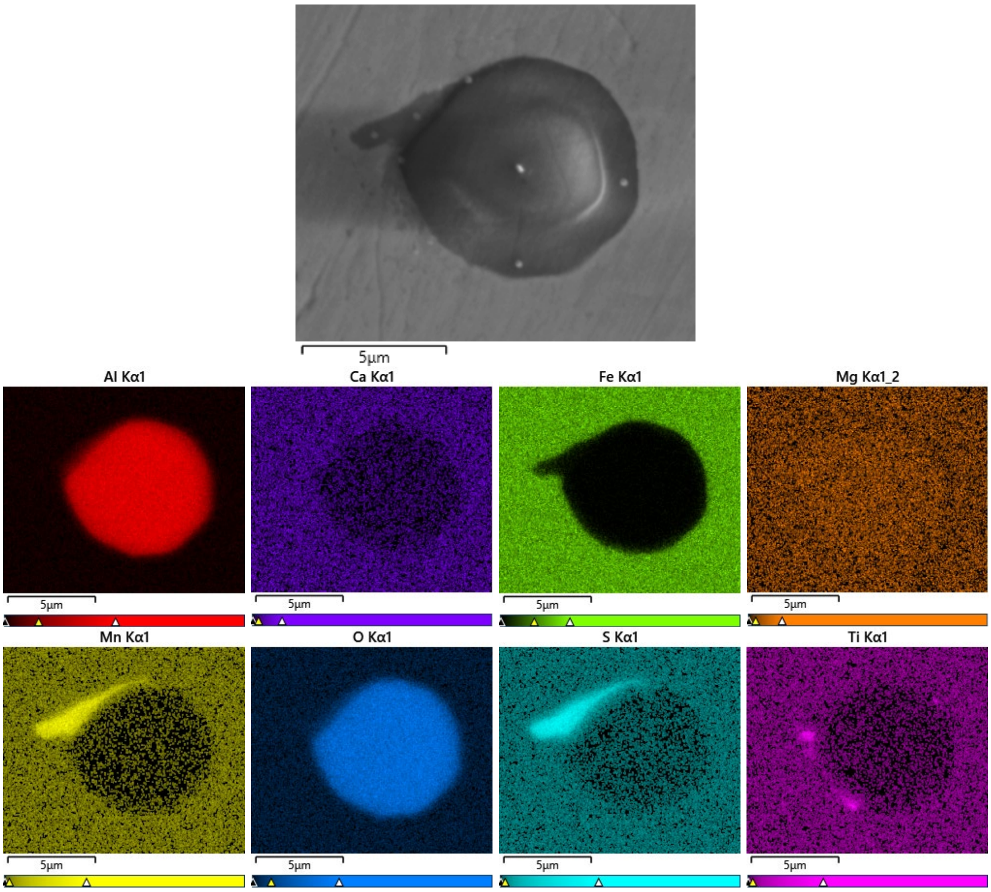

Figure 4-44. Example of a standard ‘Cored’ Globular Inclusion found in 11QS44/7L1

4.4. Discussion

4.4.1. Differences Between HR Dry and HR P&O

While Figure 4-2 shows that there is a general level of ductily across the entire sample range, the HR P&O samples are subject to necking earlier than the HR Dry samples suffering slightly lower average UE (Figure 4-2), UTS and 0.2% PS as a result (Table 4-1). As the only real difference between the samples is the fact that the HR P&O samples have undergone a pickling process to removes the scale from the surface of the steel, this is the most likely cause of this difference. During this process the steel is placed in an acid bath that has been reported to increase the average surface roughness of the steel [108, 109]. This increased surface roughness leads to the formation of stress concentrations which in turn could lead to the formation of localised strain. This would cause a greater decrease in cross-sectional area at these points and thus results in a further increase in localised strain and the onset of necking.

Whilst the results in Figure 4-10 only show an increase in surface roughness of 10.96% (2dp) between the HR Dry and HR P&O, they also show large standard deviations of error that would make this result difficult to accept completely. However, together with the fact that so many other things can influence surface roughness – i.e. pickling time [109], rolling temperature and how 'fresh' the roller used during rolling was [108] - it can be seen not all HR Dry samples have better surface roughness. This is demonstrated in Figure 4-2, where even though on average the HR P&O samples have lower properties than the HR Dry samples, they still sit within the overall range of results seen in HR Dry samples. Whilst it would be interesting to see how these other properties affected surface roughness, unfortunately this data was not available, especially for the HR P&O samples rolled in Tata Steels Llanwern Works. It would however be useful to look at in a further study.

While the surface roughness appears to cause the early onset of necking, it does not appear to have the stress raising effects necessary to cause ultimate failure of the material as the HR P&O samples have a slightly higher total elongation value on average. This is most likely due to the fact that the average surface roughness was still relatively small and overall failure likely due to other factors.

As seen in Figure 4-8, the normalised HEC values are unaffected by the surface roughness effects of pickling. This is due to the fact that the hole punching technique used to manufacture the testing sample, creates a rollover zone and a burr that dramatically changes the surface characteristics of the top and bottom of the cut edge position [106].This is highlighted by the fact that the highest overall HEC value was seen in a HR P&O sample that had an Ra value of 3.48 ± 0.44 μm (2dp).

4.4.2. Effect of Calcium Sulphur Ratio on Tensile Properties

As highlighted in Figure's 4-3 & 4-4, there is no change in UTS, 0.2% PS or UE that can be directly associated with a change in either Ca:S or S level respectively. This is even more evident in Figure 4-5 which, as they consist only of samples taken in the transverse direction, should be more influenced by a change in Ca:S. This is because if the Ca:S is too low, there will not be enough Ca to modify the S resulting in the formation of the elongated MnS inclusions [39] that reduce the isotropy of the steel. However, as seen in Figure 4-16, the entire range shows a significant level of globular inclusions, with this level not changing as the Ca:S increases. If anything, this percentage level of globular inclusions is below what is expected when compared to other studies [10, 63, 101].

This high percentage level of globular inclusions appears to be due to a variety of reasons. The chief being that across the entire Ca:S range, virtually all of the inclusions encountered – highlighted in Figure's 4-25 to 4-34 – show a certain level of CaS bonded to the MnS in a solid solution. This CaS is enough to distort the lattice of the MnS, preventing it from elongating upon rolling. This is supported by the work conducted by Leung and Van Vlack [52], as well as Nordgren and Melander [110].

The solid solutioning effect is then compounded by the fact that if the sample has a (Ca,Mn)S 'shell', it is normally seen to only be roughly 1μm thick, making it even more difficult to elongate. This is highlighted further by the inclusions that either have a larger 'shell' than 1μm (Figure 4-29) or are 'sulphide-based' (Figure 4-30), elongating significantly less than any of the purely MnS shells exhibited in either Ca treated (Figure 4-31) or non-Ca treated (Figure's 4-41 to 4-44) steel samples.

However, even with this high level of modification, there does appear to be quite a large range in the percentage amount of globular inclusions seen within the Ca treated samples, with results from roughly 50% to almost 90%. Whilst this could be due to the undermeasurement mentioned earlier, as highlighted by Figure 4-45, this level of percentage globular has no direct correlation with either UTS, 0.2% PS or UE.

It is even more surprising considering that, as shown in the literature review, an increase in the number of stringers within a sample should result in a subsequent drop in mechanical properties. This is further highlighted by the non-Ca treated sample exhibiting, not only 0.2% PS and UE values that were well within the range of results shown by the Ca treated samples, but also some of the highest UTS values seen amongst the entire sample range.

Because only 1 sample was obtained from a comparable non-Ca treated grade, it is impossible to draw any absolute conclusions, it is however still worth discussing further. As Kiessling [19] describes, at the elevated temperatures of hot rolling, the MnS inclusions deform more than the surrounding steel. This means that cracks are unlikely to form during the rolling process that can propagate under mechanical load. Also, as seen in Section 4.3.4.2, the MnS inclusions have the benefit of encapsulating the alumina 'cores' reducing the negative impact of their facetted structure.

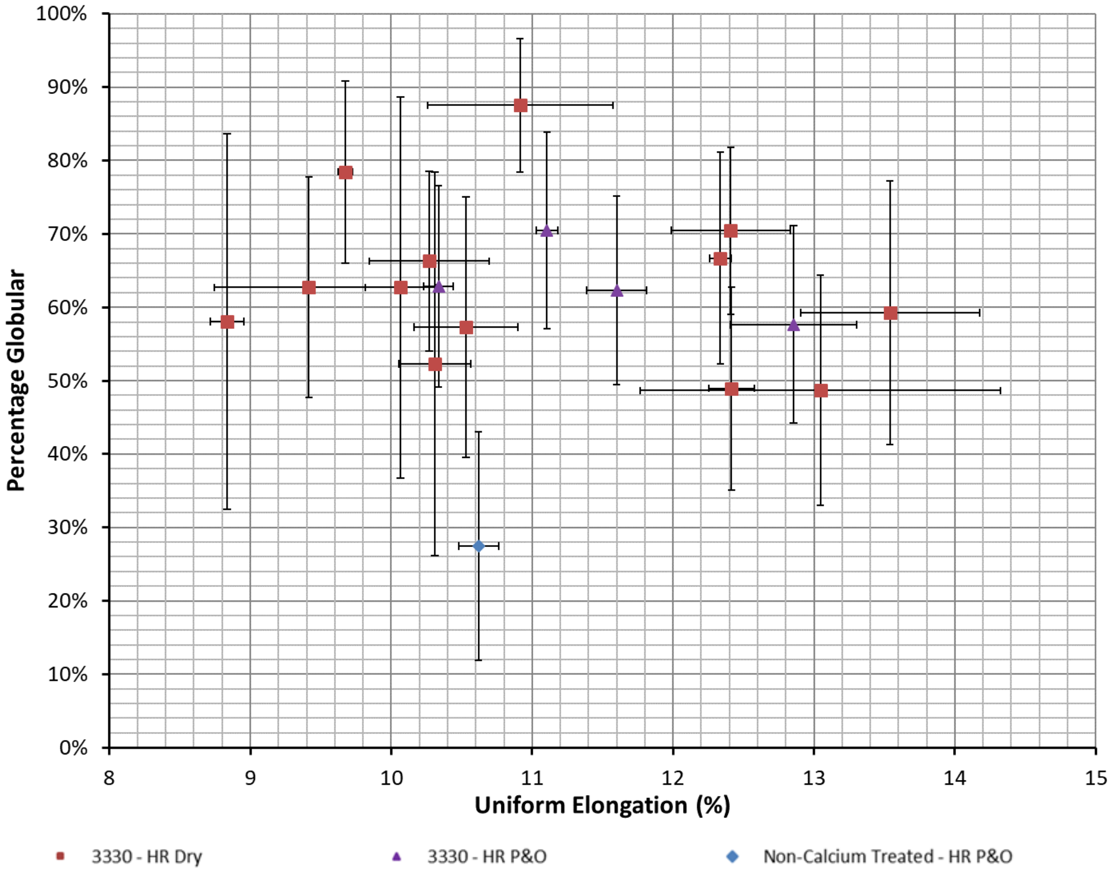

Figure 4-45. A Comparison of How the Percentage Amount of Globular Inclusions Affects UE in the Transverse Direction for the Calcium Treated and Non-Calcium Treated Samples.

Another explanation could be that, if the MnS inclusions which form were of the ‘type-C’ configuration observed by Wu et al [83], the poor cohesion between the inclusion and the surrounding steel means that under load, a void forms around the inclusion that, in effect, blunts or ‘rounds-off’ the crack. This stops the crack from propagating until the specimen fractures. However, this relies upon the fact that the inclusions are sufficiently far apart that the voids that form, cannot linkup though localised shear.

This is further highlighted by the fact that in Figure 4-6, the non-Ca treated sample does not suffer from a significantly higher percentage difference between the transverse and the longitudinal direction for UE, UTS or 0.2% PS than the equivalent Ca treated samples. In fact, as highlighted in Figure's 4-46 & 4-47, the amount of globular inclusions does not seem to have a direct correlation to this percentage difference. This leads to the assumption that any difference is caused by something other than the percentage of the population that is made up of globular inclusions.

One aspect that would influence it, as shown in Figure 4-14, is that all the samples have grains that are elongated in the rolling direction. Whilst, no sections were taken perpendicular to the rolling direction, work conducted by Shrama [111] on FB590 indicates that it can be expected to look similar to the direction observed in this study. Because of these elongated grains, dislocation movement would be impeded by an increase in grain boundaries in the transverse direction when compared to the longitudinal direction.

As such, more force would be required to plastically deform the material and the steel would undergo a higher level of stress before necking. This is highlighted both in Figure 4-7, where almost all the samples exhibit a higher UTS, and in the fact that most of the samples show a higher 0.2% PS in the transverse direction respectively. This impeding of the dislocation movement would also make slip increasingly difficult and therefore account for the sample have lower levels of UE in the transverse direction than in the longitudinal direction (Figure 4-47).

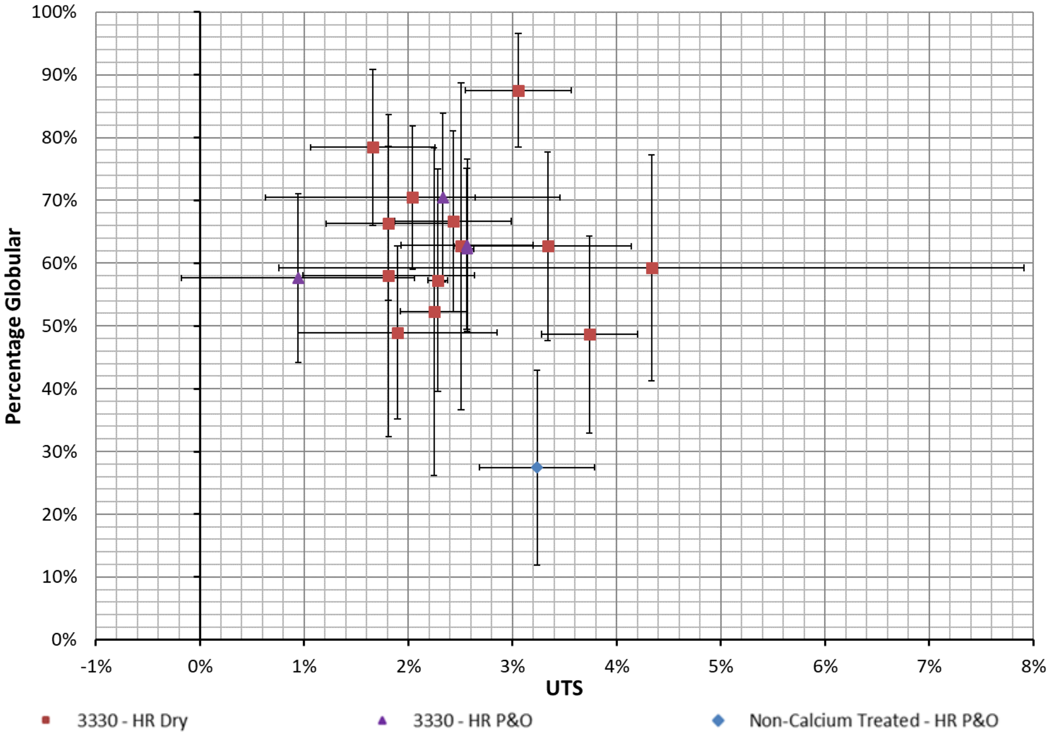

Figure 4-46. A Comparison of How the Percentage Amount of Globular Inclusions Affects Percentage Difference in UTS between the Transverse and Longitudinal Direction for the Calcium Treated and Non-Calcium Treated Samples.

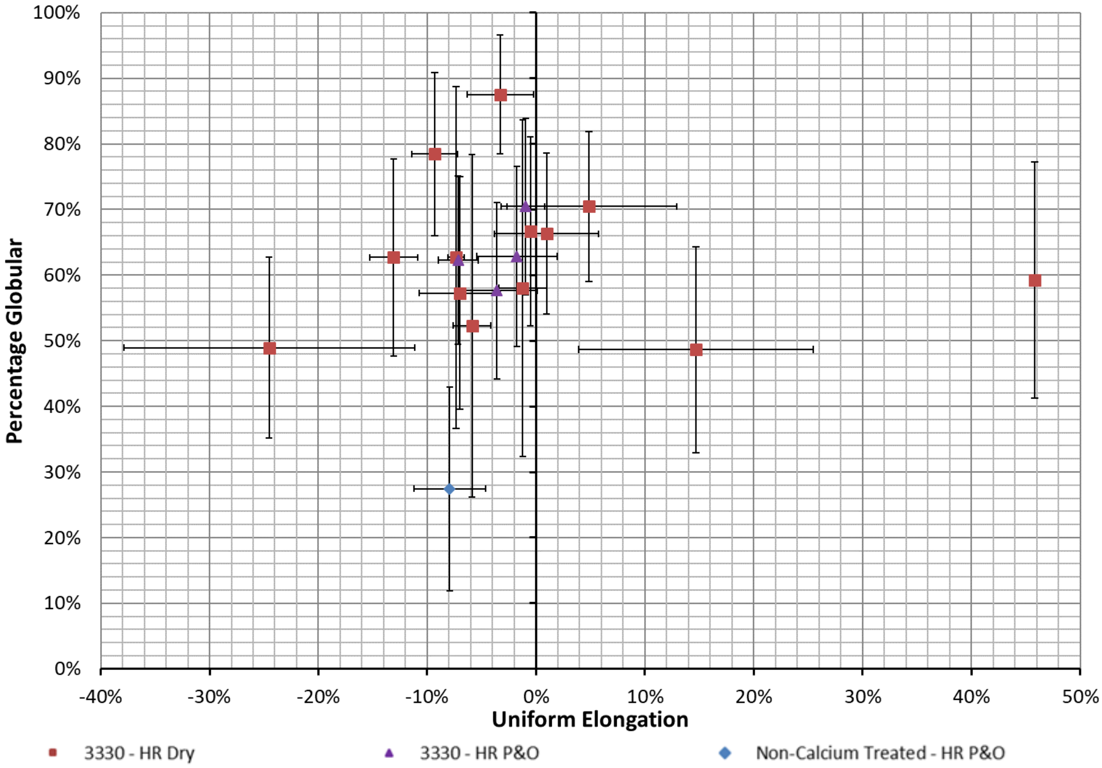

Figure 4-47. A Comparison of How the Percentage Amount of Globular Inclusions Affects Percentage Difference in UE between the Transverse and Longitudinal Direction for the Calcium Treated and Non-Calcium Treated Samples.

4.4.3. Effect of Sulphur Level on Tensile Properties

Of course, the percentage total of globular inclusions is not the only impact Ca treatment has upon steel and is not the only thing that can have an impact on the steel's mechanical properties.

As mentioned in the results section, even though the number of inclusions decreases as the Ca:S increases, Figure 4-36 which shows both a tighter trend of increasing number of inclusions as S level increases (R^2 of 0.41 compared to 0.35 for Ca:S) but also shows that the non-Ca treated samples, which you cannot compare directly through Ca:S, also fit this trend. This is further highlighted in the EDS spectra in Figure's 4-31 to 4-34 which show that the sulphide portion of the inclusion is normally roughly 1µm thick and does not increase in size if the samples are not Ca treated (Figure's 4-41 to 4-44). This means that the change in the total inclusion population is due to the general S level which, if it is low, tends to lead to a higher Ca:S since there is only a relatively small variation in Ca level.

This is unexpected because, as the literature shows, the non-Ca treated alumina remains solid in the ladle and tend to move together to form large agglomerated inclusions. However, this is likely to still be the case, except they have agglomerated to such a point that any large alumina inclusions that have formed readily float out from the steel and into the slag phase. This is highlighted further by Figure 4-38 which shows that the non-Ca sample have an average inclusion size of roughly 12µm^2 with a relatively small error range.

The increased number of inclusions with S level is then simply due to the fact that, because the inclusion is stoichiometric and there is always an excess of Manganese (Mn) in the melt, with an increase in S, more MnS inclusions are able to form, most likely as a 'classic' elongated inclusions (Figure 4-41) or a purely 'sulphide-based' inclusions as shown in Figure 4-43.

The Ca treated samples on the other hand exhibit not only larger numbers of inclusions at low Ca:S, but also larger inclusions in general. However, as with the average number of inclusions, this trend in size of inclusions is stronger with a change in S level, with increasing S showing a general increase in the inclusions size. This trend shows an R^2 of 0.30 (2dp) compared to 0.24 (2dp) for Ca:S.

Whilst there appears to be limited information on the direct impact of S level on the number and size of inclusions in Ca treated steels, Holappa *et al* [112] shows that Ca preferentially bonds with S forming CaS. The presence of this compound then means that less Ca is available to bond with the alumina, resulting in the stable phase of calcium aluminate being $CaO{\cdot}2Al_2O_3$ instead of $CaO{\cdot}Al_2O_3$. Because $CaO{\cdot}2Al_2O_3$ solidifies at a higher temperature ($\simeq$1750°C compared to $\simeq$1605°C for $CaO{\cdot}Al_2O_3$) it could lead to more inclusions forming out of the melt earlier in process. This, along with an increase in the number of sulphide inclusions, would mean the inclusions also have more time to agglomerate. While not directly linking to S content, Lis [9] did also experience an increase in both inclusion size and inclusion number as the Ca:S decreased.

However, this trend for the number of inclusions, and especially size of inclusions, is not very well defined and is likely due to fact that the analysis does not account for the impact of Oxygen (O) content. This unfortunately is not measured during the OES testing employed by the material producer. The obvious impact being that without the O content required to form alumina in the first place, less inclusions will nucleate and they will agglomerate to a lesser extent [63].

Also, as shown by Listhuber *et al* [113] and Wang *et al* [114], the inclusion distribution and size vary dramatically across the length of the strand. During these studies it is demonstrated that during ladle or tundish changes, slag inclusions are drawn into the melt, together with a risk of reoxidation of the melt due to contact with the air. This has the impact of increasing not only the number but also the size of inclusions within the steel.

As a result, this could cause the anomalous results shown in Figure's 4-48 and 4-49. This could mean that point (a) is the result of an increased level of oxygen due to the sample possibly being taken near/on a ladle/tundish change therefore leading to a higher number and size of inclusions. Point (b) could instead show an unusually low oxygen level leading to the opposite effect. As a result, further analysis should include the monitoring of the oxygen levels within the samples to help eliminate this as a cause of these anomalies.

However, as highlighted by Figure's 4-50 and 4-51, both the average number of inclusions and the average size of inclusions have little to no discernible impact on the final materials properties within this sample range. This is due to a combination of reasons:

1. Most of the inclusions are globular so do not have the resulting 'stress raisers' associated with stringer inclusions (Figure 4-16).
2. Any facetted edges in non-spherical alumina tend to be 'rounded-off' by an associated sulphide.
3. The average inclusion size is below the critical inclusion diameter of 10µm (~79µm^2 if you assume a perfectly spherical inclusion) [115].
4. As shown in Figure's 4-23 and 4-24, if there are larger inclusions than the critical size, they exist in far smaller numbers and tend to appear on the centreline of the material. This is significantly further away from the surface than the 100µm distance where the critical size increases to a diameter of 30µm (~707µm^2 assuming a perfectly spherical inclusion) [85]. This suggests that the critical size of inclusions would increase further when moving towards the actual depth of the centreline. This is critical because during the bending mode associated with forming (i.e. the key use of this material), the distribution of stress is not uniform over the whole surface area and is higher at the surface when compared to the centreline.

This relatively large number of inclusions at the surface seen in some samples, compared to their centres is due to the fact that this is the first region to cool and therefore the site of preferential inclusion nucleation. If the inclusions that form are then larger than the they are then encapsulated by the advancing solid front [116]. This is because larger inclusions exhibit a greater interfacial force with the solid front than the viscous drag force, because of their larger surface area [116].

However, the velocity of the advancing melt/solid interface has an impact on this critical size. The greater the cooling rate applied to the steel, the higher the velocity of the interface, the more likely it is for an inclusion to become entrapped [117]. As a result, this critical diameter (or 2R) – i.e. the diameter of which an inclusion will be engulfed - is determined by the critical growth velocity (µm/s) (Vc) of the advancing interface. This being Vc=60/R for solid alumina clusters and Vc=23/R for liquid globular inclusions. However, Shibata *et al* also observed that liquid globular inclusions with a diameter of <6µm (~28µm^2 for a perfectly spherical inclusion) are always pushed [116].

This explains why in Figure's 4-23 and 4-24, only samples with an average inclusion size larger than 20µm^2 show an increased number of inclusions near the surface of the sample. The other samples generally show a relatively even distribution of inclusions throughout the melt implying that these sub-critical diameter inclusions have been ‘pushed’ through the solidifying steel.

Luo *et al* [118] have shown that the size of alumina cored MnS inclusions tend to be larger in the centre of steel as the latent heat of the strand changes, leading to the local solidification time increasing. This results in larger inclusions in the centre of the steel and as both the MnS and the CaS/(Ca,Mn)S inclusions share a similar structure due to a majority alumina based ‘core’, it is reasonable to assume a similar phenomenon is occurring within the samples studied here.

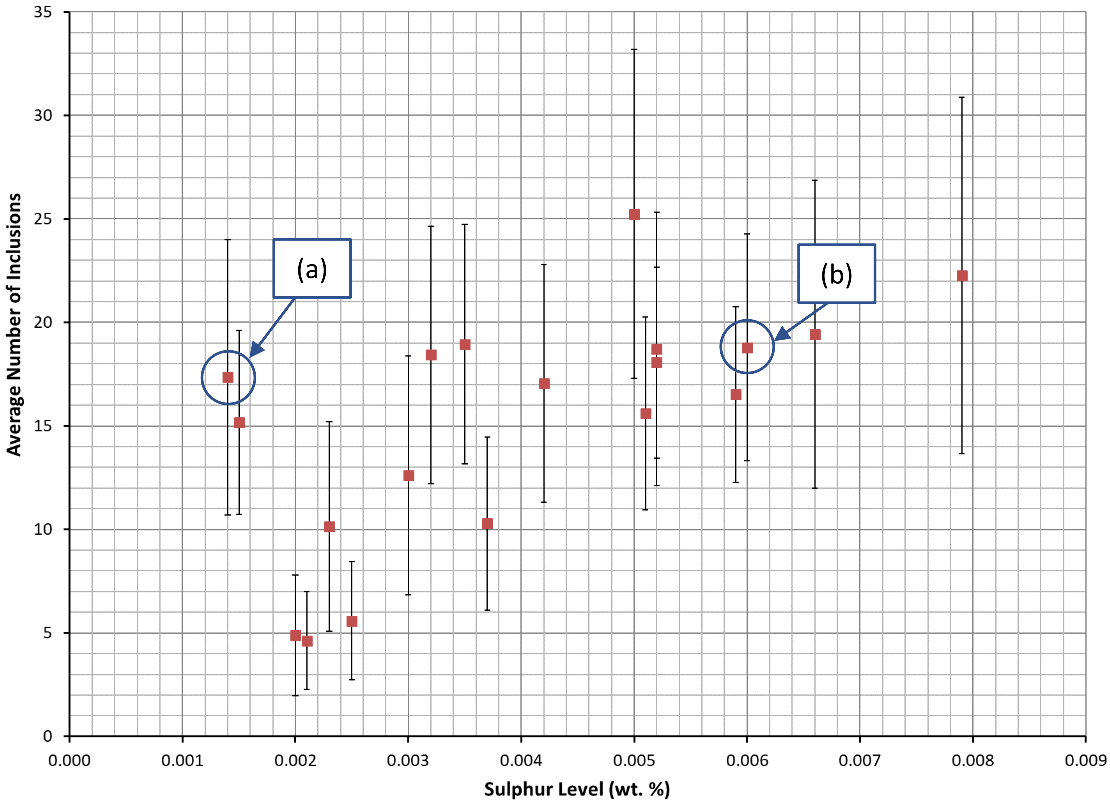

Figure 4-48. Average Number of Inclusions vs Sulphur Level for Calcium Treated FB590 Highlighting the 2 Samples That Do Not Fit the Trend for Size of Inclusion.

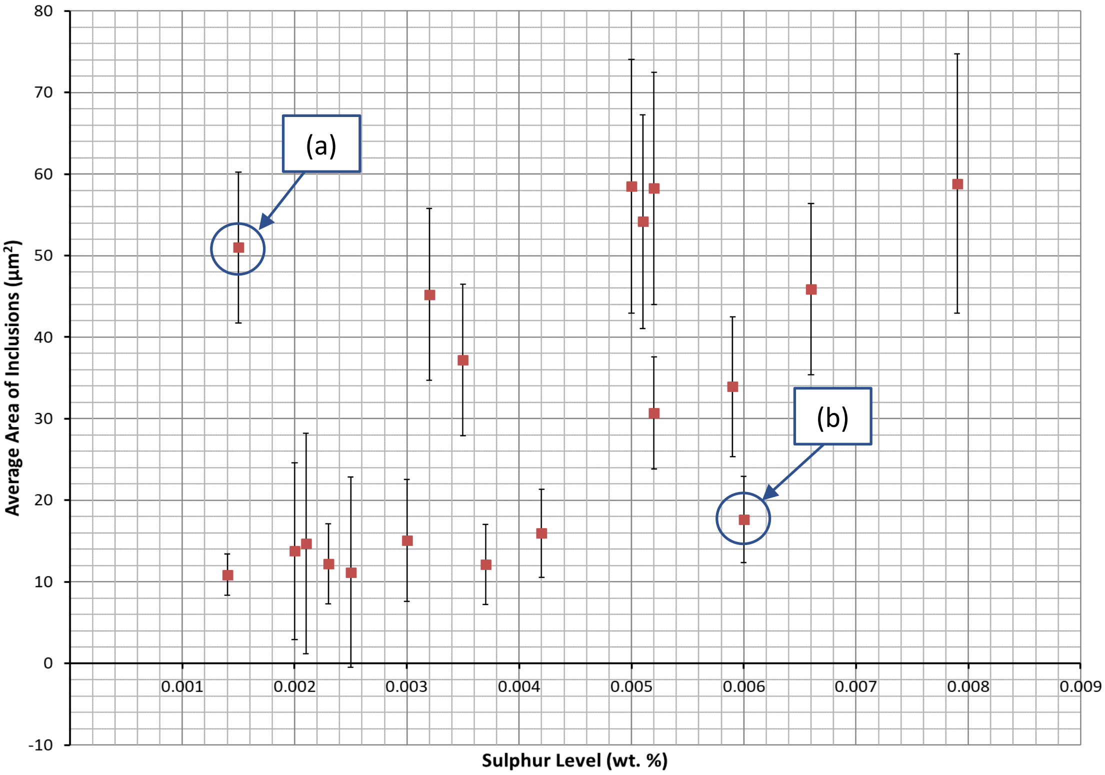

Figure 4-49. Average Area of Inclusions vs Sulphur Level for Calcium Treated FB590 Highlighting the 2 Samples That Do Not Fit the Trend.

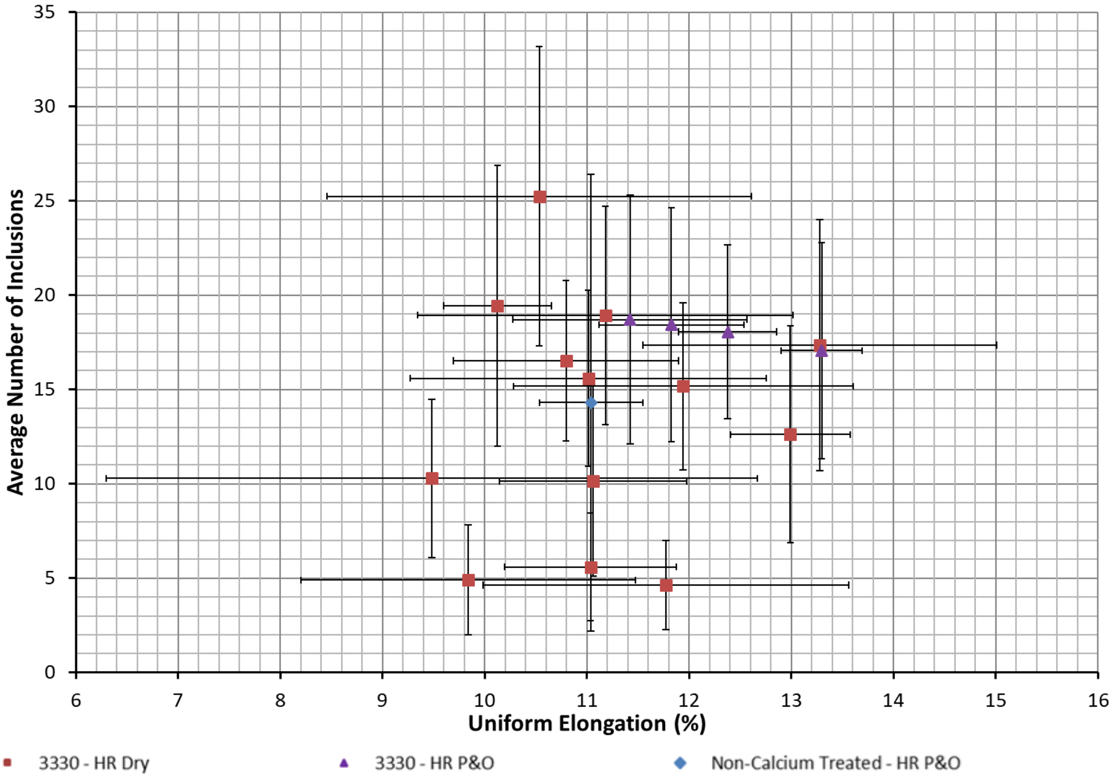

Figure 4-50. A Comparison of How the Average Number of Inclusions Affects the Uniform Elongation for the Calcium Treated and Non-Calcium Treated Samples.

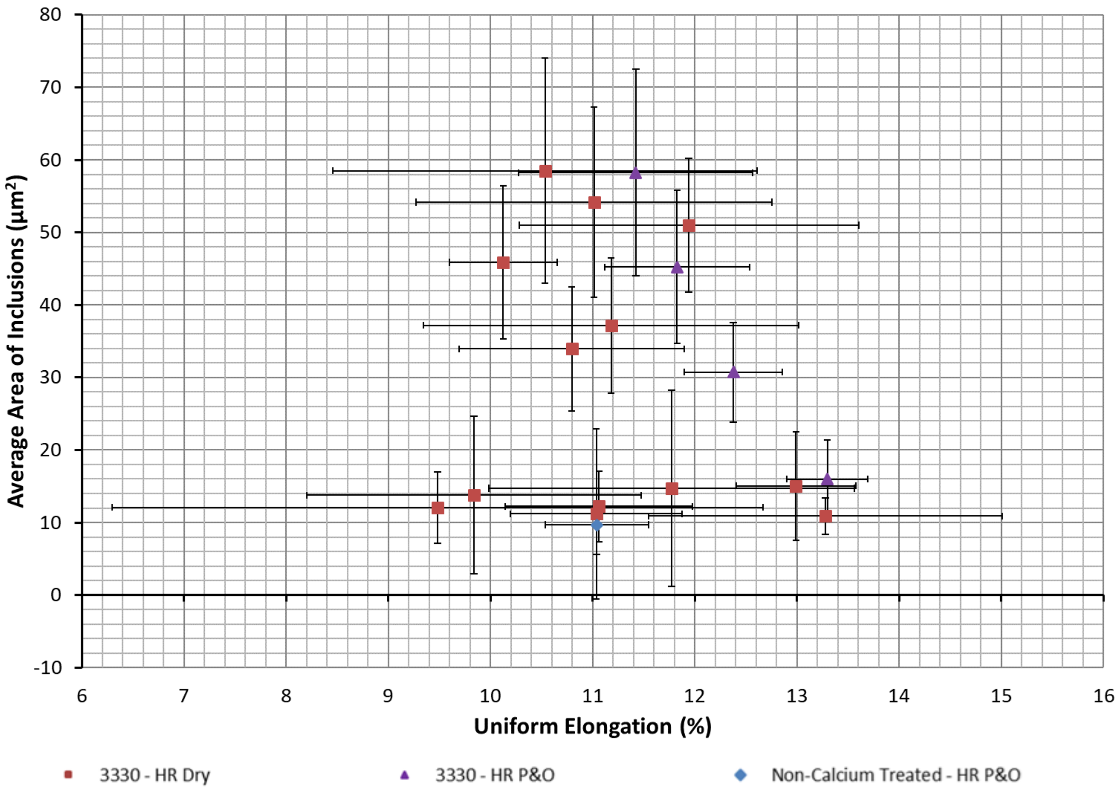

Figure 4-51. A Comparison of How the Average Size of Inclusions Affects the UE for the Calcium Treated and Non-Calcium Treated Samples.

4.4.4. Effect on Hole Expansion Coefficient

The hole expansion data tells a similar story to the tensile data in that, as can be seen in Figure's 4-52 to 4-54, the Ca treated grades experience very little direct impact from the percentage of globular, number of inclusions and size of inclusions on the HEC for the steel samples. This is likely to be due to the same reasons as discussed earlier, in that near complete modification limits the impact of the stringer inclusions and the fact that the inclusions were below the critical size to cause failure.

One thing that is different however, is that the non-Ca treated sample is now showing a significantly lower HEC value than almost all the Ca treated samples. This is most likely because, unlike tensile testing a transverse sample, the load is not applied on a single axis. This increases the effect of the stress raisers, which in turn makes it more likely for a crack to propagate from this point.

There is, however, one HR P&O sample that also shows a significantly lower HEC. As can be seen in Figure's 4-52 to 4-54, the sample does not suffer from significantly different levels of globular inclusions, number or size of inclusions. It also has a low average Ra value of 0.92µm, together with similar overall levels of ferrite and Feret ratio for its grains. The only difference that can be seen is that it has a larger grain size than the rest of the samples tested (Figure 4-55). While it is difficult to draw any direct conclusions from the graph, as only 8 samples were tested for both grain size and HEC, the HEC does appear to increase as the average diameter decreases.

A similar result was seen in Misra *et al*'s [119] study, which showed that the presence of unusually large ferrite grains in the steel correlate with the formation of large voids. Large grains could also be associated with larger than normal dislocation pileup, possibly initiating brittle fracture. The study also proposes that, because large dislocation-free ferrite grains would be comparatively soft, it would lead to a larger than normal hardness ratio between them and the surrounding bainite that has been suggested to be a key factor in crack initiation [120].

An important factor to note is that, while this sample exhibits a similar HEC results to the non-Ca treated sample, the non-Ca treated sample has an average grain size that is in line with the rest of the Ca-treated samples. This further emphasises that the low HEC seen in the non-Ca treated steel is caused by its MnS inclusions and not by any change in grain size.

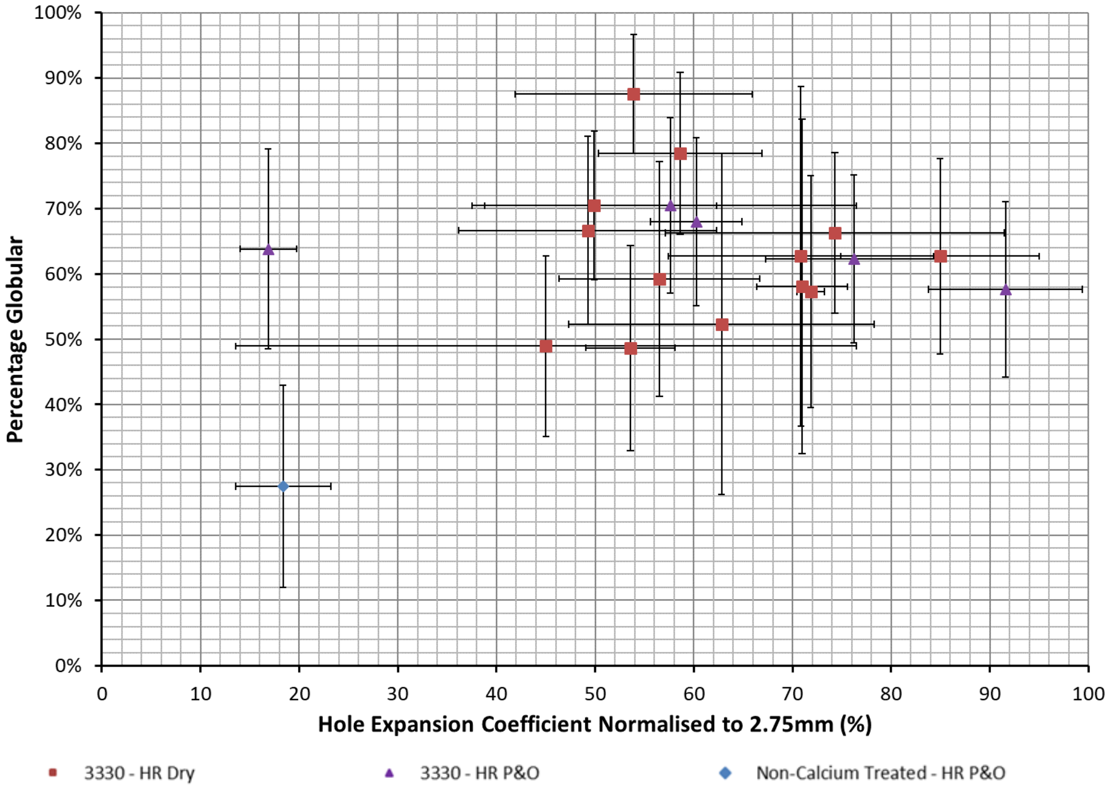

Figure 4-52. A Comparison of How the Percentage Amount of Globular Inclusions Affects the Hole Expansion Coefficient for the Calcium Treated and Non-Calcium Treated Samples.

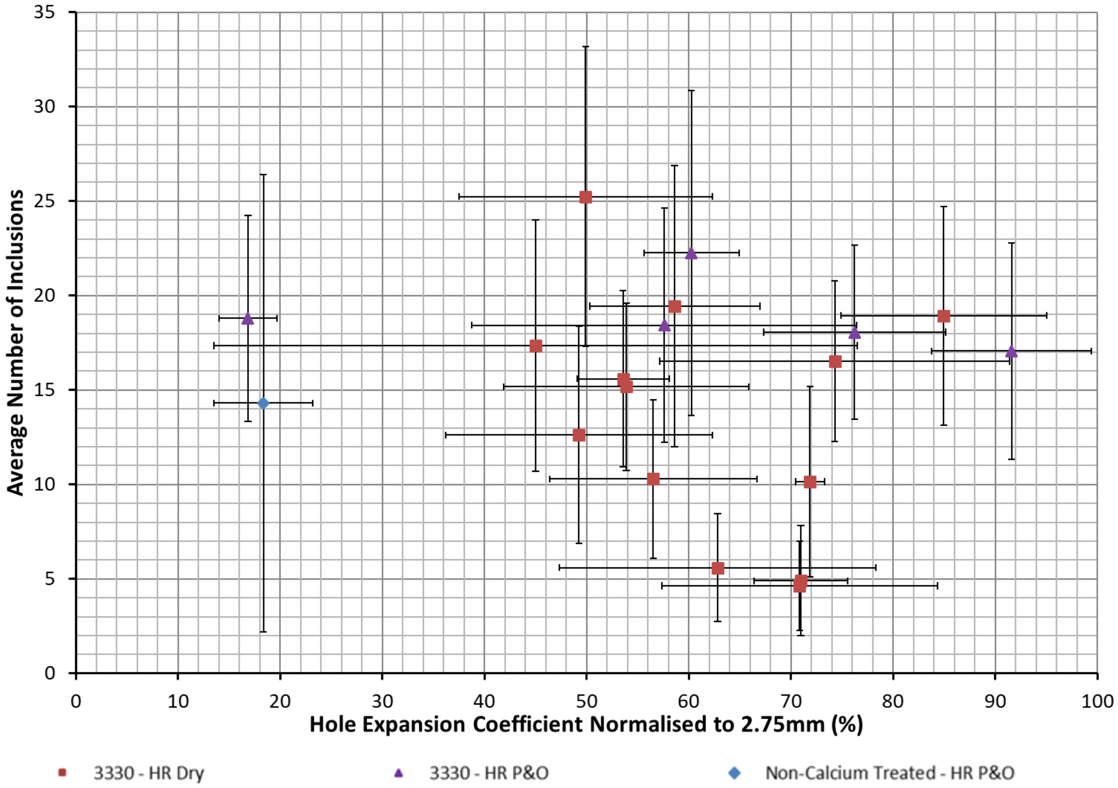

Figure 4-53. A Comparison of How the Number of Inclusions Affects the Hole Expansion Coefficient for the Calcium Treated and Non-Calcium Treated Samples.

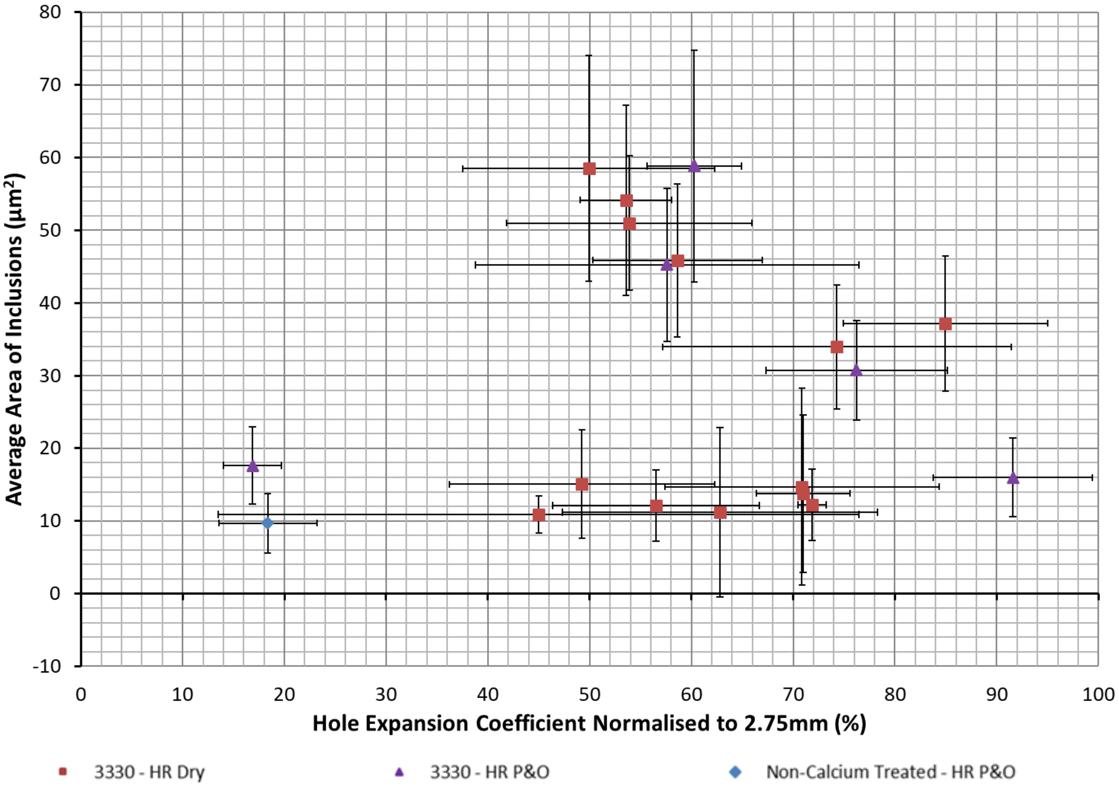

Figure 4-54. A Comparison of How the Size of Inclusions Affects the Hole Expansion Coefficient for the Calcium Treated and Non-Calcium Treated Samples.

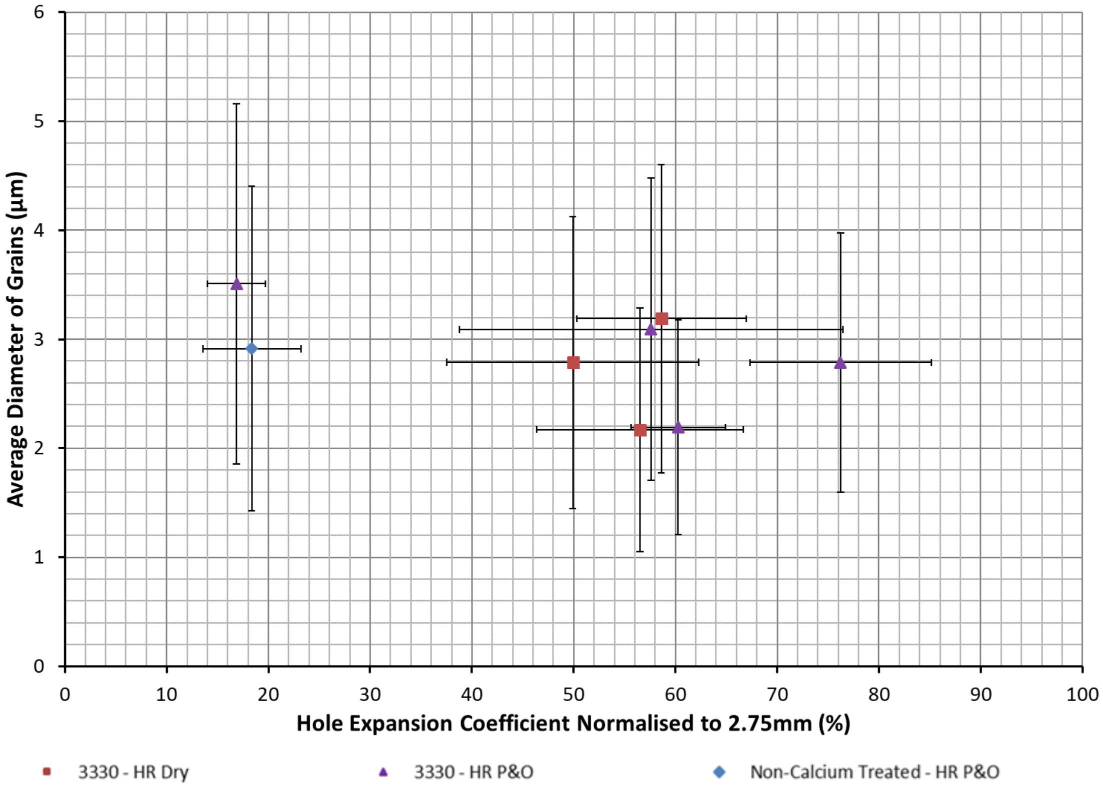

Figure 4-55. A Comparison of How the Average Grain Diameter Affects the Hole Expansion Coefficient for the Calcium Treated and Non-Calcium Treated Samples.

4.4.5. Types of Globular Inclusion

Figure's 4-31 to 4-34 also showed that there were 2 keys types of Ca treated inclusions formed:

1. **‘Cored’** Globular Inclusion (Figure's 4-25 & 4-26):
    - An alumina-based ‘core’ surrounded by a sulphide ‘shell’, consisting of either CaS or (Ca,Mn)S and forms via the nucleation of a sulphide on an already formed alumina inclusion.
    - As shown in Figure 4-56, this is by far the most common type with roughly 4 times as many seen during EDS compared to the “Ying-Yang” type.
2. **‘Ying-Yang’** Inclusion (Figure 4-27):
    - Forms from the collision of two or more inclusions in the melt [121].
    - This is most commonly a sulphide and alumina-based inclusion but has also been seen forming from the collision of a ‘cored’ inclusion and a sulphide/alumina-based inclusion.

However, unlike the literature suggests [38, 121], there were no inclusions encountered that homogenously distributed the CaS within the Calcium Aluminate. As a result, this indicates that the calcium aluminate ($12Ca\cdot 7A1_2O_3$) with the lowest melting temperature is not present.

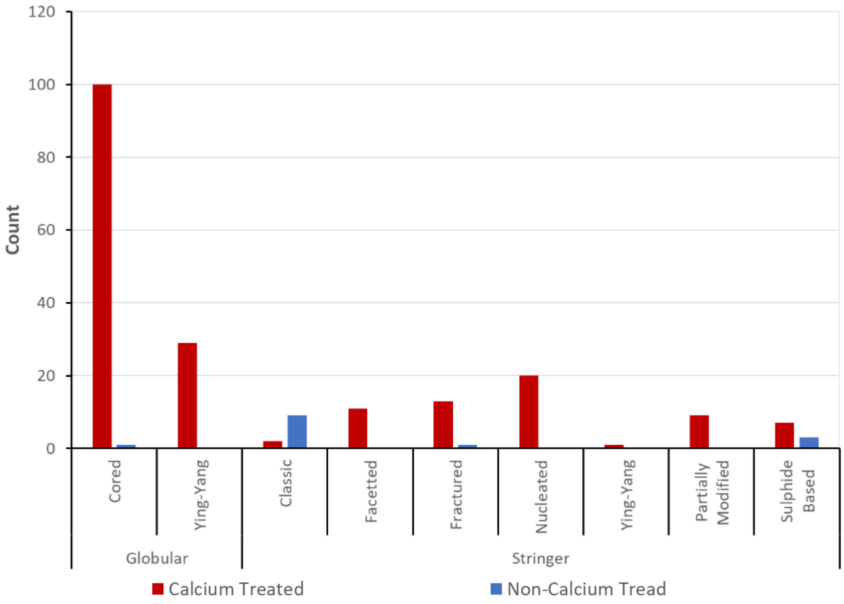

Figure 4-56. Number of Different Inclusion Types Seen During EDS Analysis.

4.4.6. Types of Stringer Inclusion

The value for percentage globular is never going to reach 100%, irrespective of the level of Ca treatment because of the 5 other stringer types that form which are not related to the ‘classic’ elongated stringer. While the general populations for these inclusions are shown in Figure 4-56, it should be noted that the Ca and non-Ca treated samples results cannot be directly compared as there was only 1 non-Ca treated sample analysed compared to 19 Ca treated. Some general statistics for the different types are seen in Table 4-3 with a breakdown of the different L/W ratios for each stringer inclusion type shown in Figure 4-57.

1. ‘**Classic’** Stringer Inclusion (Figure 4-28):
    - Alumina-based core with a MnS shell that elongates on rolling.
    - Most common amongst inclusions seen within non-Ca treated samples but the least common ‘type’ within the Ca treated samples (Figure 4-56).
    - Tends to have extremely high length/width ratios (L/W). The relatively low minimum L/W results are most likely the consequence of losing a portion of the inclusion during sectioning and polishing.
    - Also seen to have some of the lowest heights of all stringer inclusion types.
2. **‘Fractured’** inclusion type (Figure 4-32 & Figure 4-33):
    - Forms because inclusions, especially larger ones, have a tendency to fracture upon rolling, exposing the facetted edges of the inclusion’s ‘core’.
    - This results in, not only stress concentrations on the corners of the facetted structure, but also the proximity of the fractured inclusions means that if a crack were to form it would be able to propagate much more quickly.
    - Especially damaging considering this type exhibits some of highest L/W of all the stringer types and can reach lengths of over 100μm.
    - Even with this L/W, it is by far the tallest of the inclusion types on average due to it generally being a large inclusion with an average estimated diameter of 17.85μm^2 prior to fracture.

3. **'Facetted'** stringers (Figure 4-31):
    - Occur if the inclusion's 'core' is already 'stringer- shaped' before the sulphide 'shell' nucleates and is most prevalent in samples that have alumina-based 'cores' that have undergone none, or very little, Ca modification.
    - This is because the alumina core has bonded with MgO through reactions with either the refractory lining [122] or the slag [34]. The resulting $MgO \cdot Al_2O_3$ that forms, has the same facetted/dendritic structures as pure alumina (Figure 4-31).
    - However, once the Ca concentration has increased to a certain level, it reacts with the $MgO \cdot Al_2O_3$, forming either a multi-phase inclusion of $CaO\text{-}MgO\text{-}Al_2O_3$ or $CaO \cdot Al_2O_3$, reducing the MgO in the inclusion into Mg in the melt [36, 122]. Both these inclusion types have low melting points, so remain liquid in the melt, forming globular inclusions upon solidification.
    - While being relatively common, it has the lowest average L/W and therefore has a limited impact on mechanical properties in comparison to other stringer inclusion types.
4. **'Nucleated'** Stringer Inclusion (Figure 4-34)
    - Appear when 2 or more separate inclusions nucleate within 40μm in the *x*-direction and 10μm in the *y*-direction from each other, as determined the BS and ASTM standards.
    - These are the most common type of stringer seen within Ca treated steels and can exhibit large L/W but generally not to the same extent as the 'classic', 'fractured' or 'sulphide-based' types.
    - This is largely down to the fact that the separate inclusions can be up to 40μm apart in the rolling direction and still be classified as a stringer.
    - Can exhibit large heights simply down to the fact that it can contain very large 'cored' inclusions.
    - While these inclusions are still globular in nature and therefore do not have any of the usual stress raising effects of stringer inclusions, their

proximity to each other means that if a crack was to form on one of them, it would be able to propagate more easily.

5. **'Partially-Modified'** Inclusion (Figure 4-29)

    - This inclusion forms when the amount of CaS that bonds in solid solution to the MnS is not high enough to completely prevent elongation upon rolling.
    - As a result, they partially elongate but to a significantly lower degree than the 'Classic' stringer inclusion.
    - Second lowest average L/W of the stringer types, largely due to the solid solution strengthening effects of Ca still preventing the 'shell' elongating like a 'classic' stringer resulting in a lower impact on mechanical properties in comparison to other stringer types.

6. **'Sulphide-based'** Stringer Inclusion - (Ca,Mn)S-based - Figure 4-30
   MnS-Based - Figure 4-43

    - Forms via the nucleation of a purely sulphide inclusion.
    - While it can exist as a solid solution of (Ca,Mn)S inclusion in the Ca treated steel it is most commonly seen as a purely MnS inclusion.
    - As can be seen in the figures, the (Ca,Mn)S inclusion has very slightly elongated, whereas the MnS inclusion has elongated to a much larger extent (>50μm in length).
    - Both however tend to be <1μm in thickness with the slightly larger heights in Table 4-3 caused by the fact the height include several inclusions as they can form small clusters.
    - This type of inclusion has the largest L/W because of this thickness.
    - It should be noted that this inclusion is likely more common that shown in Figure 4-56 due to the fact that these inclusions were located using a LM image taken at 100x magnification and this inclusion type would be, for all intents and purposes, invisible at that level.

As highlighted in Table 4-3, only 3 of these types ('Classic', 'Fractured' and 'Sulphide-based') were encountered within the non-Ca treated grade. This is simply because a level of Ca modification is required for these types to form.

Table 4-3. Table of Statistics of Stringer Inclusions (1dp).

Stringer Type	Calcium Treated				Non-Calcium Tread			
	L/W			Height (µm) (1dp)	L/W			Height (µm) (1dp)
	Min.	Max.	Average	Average	Min.	Max.	Average	Average
Classic	9.1	9.1	9.1	5.0	2.7	17.8	7.7	3.8
Facetted	1.3	3.8	1.9	8.6				
Fractured	1.9	25.2	7.1	13.1	9.9	9.9	9.9	8.9
Nucleated	1.5	4.8	2.8	11.0				
Partially Modified	1.4	3.4	2.0	5.1				
Sulphide-Based	1.7	18.0	4.8	1.3	3.4	22.3	14.3	2.1
Ying-Yang*	1.4	1.4	1.4	13.4				

***Only one observed, included for general comparison.**

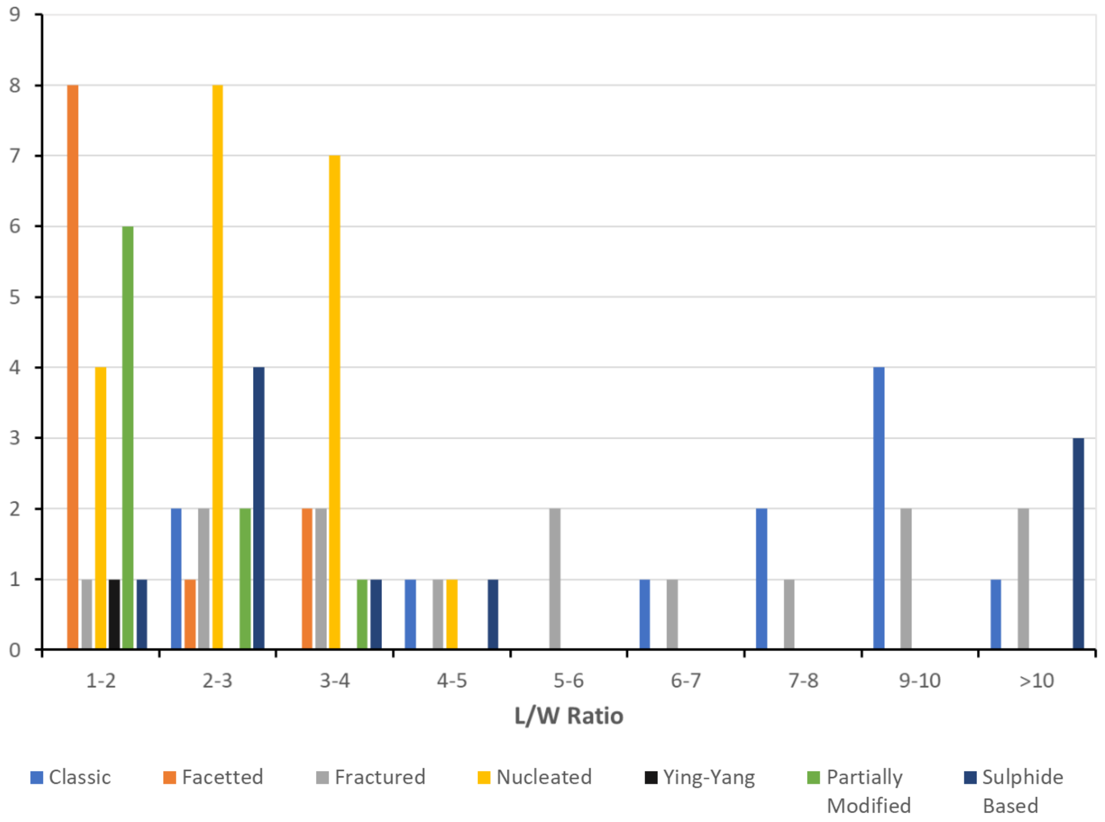

Figure 4-57. Count of Inclusion Type at Different L/W.

4.5. Conclusions

1. On average, the pickling process increases the surface roughness of the steel, possibly contributing to the early onset of plastic deformation and necking, which results in lower average mechanical properties for HR P&O samples.
2. Increase in surface roughness does not appear to be the cause of ultimate failure of the steel as HR P&O samples exhibit higher average TE.
3. Pickling is not the only factor to affect surface roughness, as shown by some HR Dry samples demonstrating increased levels of surface roughness.
4. Even at relatively high S levels, the Ca modification is enough to prevent the inclusion elongation upon rolling, with the inclusions generally solid solution strengthened sufficiently to remain globular. Therefore, no definitive Ca:S was observed, with all Ca treated samples achieving the required properties. When factoring in the light microscopy results, this implies that as long as a Ca:S of ≥ 0.23 is maintained, a significant enough level of modification of sulphide-based inclusions is achieved to obtain the required mechanical properties. This Ca:S level being accurate is also dependent on the steel having a Ca:Al of ≥ 0.039. This is to ensure modification of the alumina inclusions in order to prevent the formation of large agglomerated alumina-based inclusions and the formation of solid CaS inclusions that can cause further problems (e.g. nozzle blockage).
5. The percentage number of globular inclusions in unlikely to ever reach 100% due to a number of different stringer type inclusions forming.
6. Detrimental $MgO \cdot Al_2O_3$ forms through reactions with either the slag or the refractory lining, thus increasing the chances of stringers forming. However, through Ca treatment and the reduction of MgO into Mg in the melt by CaO, inclusions generally form complex globular inclusions of $CaO\text{-}MgO\text{-}Al_2O_3$.
7. Inclusion modification appears to have little to no effect on any differences between the longitudinal and transverse directions properties. Any difference is likely to be due to the grain elongation in the rolling direction.
8. Elevated S level is a key factor in the increased number and size of inclusions. This is due to the increased presence of S shifting the $CaO \cdot Al_2O_3$ to the higher

melting temperature phase $CaO \cdot 2Al_2O_3$. However, it is suggested that O content be included in future analysis to identify its impact.

9. The increase in the number and size of inclusions within the steel have been shown to have limited impact on final mechanical properties for the following reasons: -
    i. The average size of inclusions near the surface is below the critical inclusion diameter of 10μm for failure.
    ii. The high percentage of globular inclusions.
    iii. The facetted edges of alumina-based 'cores' being 'rounded-off' by the sulphide 'shell'.
    iv. Any inclusions larger than the critical inclusion diameter of 10 μm will most likely be in the centre of the sample in very low numbers, limiting its effects on mechanical properties.

10. As inclusions larger than a critical size of 6μm (~28μm^2) are enveloped and not 'pushed-in' towards the centre of the sample. This has resulted in build-up of inclusions at the sample surface in samples that exhibit these larger inclusions.

11. The MnS inclusions that form within the non-Ca treated steel, tend to be smaller in size (~12 μm^2) and appear to be dispersed sufficiently so that when the crack-tip blunting voids form under uniaxial tension, they cannot coalesce easily. However, as only one non-Ca treated sample was able to be obtained that had comparable mechanical properties, more analysis would need to be done to confirm this as a trend.

12. Large amount of MnS inclusions (i.e. non-Ca treated steels) appear to significantly lower the sheared edge flangeability.

13. Also alluded to is the fact that the grain size could have a dramatic impact on the sheared edge flangeability, since one sample that exhibited larger grains had a significantly lower HEC. This could be due to the possibility of dislocation pile-up, the formation of large voids, large hardness ratios between grains and less grain boundaries to impede grain growth.

14. 2 different types of globular inclusion form:
    1. **‘Cored’** Inclusion –
        - Sulphide shell nucleating on the surface of an already formed alumina-based inclusion.
        - Most common form of Globular Inclusion
    2. **‘Ying-Yang’** Inclusion –
        - Formed through the collision of 2 or more liquid inclusions.
15. No inclusions were encountered with a homogenous distribution of CaS within Calcium Aluminate, indicating that $12Ca{\cdot}7A1_2O_3$ is not present.
16. 6 different types of stringer inclusions form:
    1. ‘**Classic’** Stringer Inclusion: –
        - Alumina-based core with a MnS shell that elongates on rolling.
        - Most common inclusion type in non-Ca treated steels
        - Medium height, high L/W
    2. **‘Fractured’** Inclusion: –
        - Due to large inclusions (17.85μm^2 averaged estimated diameter) fracturing upon rolling and forming clusters in rolling direction.
        - High L/W considering it is the tallest of all the stringer types.
    3. **‘Facetted’** Inclusion: –
        - Forms when inclusion’s ‘core’ is ‘stringer- shaped’ prior to the sulphide ‘shell’ nucleating.
        - Lowest L/W
    4. **‘Nucleated’** Inclusion: –
        - Formed when 2 or more separate globular inclusions nucleate within distances determined by the standards.
        - Most common stringer in Ca treated steels.
        - Large range of heights and L/W due to containing variety of inclusions up to 40µm apart in the rolling direction
    5. **‘Partially-Modified’** Inclusion –
        - Not enough CaS bonded to the MnS to sufficiently solid solution strengthens the inclusion & totally prevent elongation.
        - Low L/W

vi. **‘Sulphide-based’** Inclusion –

  - Forms via the nucleation of a purely sulphide inclusion with 2 subtypes; (Ca,Mn)S which mildly elongates and pure MnS which significantly elongates.
  - Highest L/W, lowest height (<1µm in general).

17. Only the ‘Classic’, ‘Fractured’ and ‘Sulphide-based’ stringer inclusion types were found in the non-Ca treated steel grade because a level of Ca modification is required for the other stringer types to form.

Chapter 5

Assessment of Automated Inclusion Analysis

5.1. Introduction

3 different techniques were utilised to compare and contrast against the automated inclusion analysis technique that was developed for this study and utilised within Chapter 4. The first technique utilised was the Average Field Measurement: Method K from BS EN 10247 [100] that is used widely across the steel industry as a means of understanding the inclusion content of the steel. While there are other techniques, even within this standard, that take much less time to complete, they do not convey the same level of detail and are therefore not the best sources of comparison.

The second technique, that was used for comparison, was a procedure similar to that employed by Walker [101] and was the starting point to the automated technique utilised in this study. Because this analysis was conducted on a different microscope to the automated technique and therefore employed a different camera, this allowed a comparison based on the effect of pixel size.

The third technique employed was the use of automated EDS inclusion analysis, which is another standard technique of the steel industry. Because it uses a chemical analysis to generate results, it provided an alternative method to aspect ratio as a means to compare inclusion type and therefore the assumption that with Ca modification, comes sufficient inclusion shape modification.

Utilising 3 techniques that calculated similar result sets via a variety of different process routes, allowed for the strengths and weaknesses of, not only this automated technique, but also the established techniques to be assessed, leading to improvements to the automated technique for future analysis.

The final method that will be assessed during this chapter is the Pulse Discrimination Analysis (PDA) model that was developed by Whiteside *et al* [94] for use within Tata Steel. This method is relatively new however and, as such, Tata have requested it be included in this study so as to contribute towards this model's validity. This will therefore give an indication of its potential use as a means of testing the modification level of large amounts of steel samples very quickly.

As with Chapter 4, all the graphs presented in this chapter show averaged results, with any resulting error bars indicating ± 1σ from this average. Unlike Chapter

4 however, the results show a variety of different significant figures based on the technique that was used the calculate the inclusion data. The optical measurement results for the average size of inclusions were capped at 0dp, due to the pixel size used to calculate these results. Percentage modified/globular and average number of inclusions for manual and automated techniques were capped at 1dp, due to the fact that these techniques included data for well over 1000 inclusions, many more times than in the case of the automated technique. These results from the other methods were also capped at 0dp because they did not include such large quantities of inclusions in the analysis. This was consistently applied, unless otherwise stated.

5.2. Optical Measurement Comparison

5.2.1. Analysis Techniques

5.2.1.1. Manual Measurements

As mentioned previously, this technique is very time consuming and as it was only to be used as reference against the automated technique, only 5 out of the 19 Calcium treated samples were analysed. These samples were chosen to represent a full range of both Ca:S and S levels exhibited within the sample set, as well as coming from both the HR and HR P&O process routes. The samples that were chosen can be seen in Table 5-1.The study was conducted on a minimum of 80 710µm^2 fields, with the analysis conducted on the same images used for the automated analysis, giving a 90% confidence level according to the standard. To ensure a good representation of the samples in general, they were taken in rows containing a minimum of 27 fields from roughly the surface, 25% of the thickness from the surface and the middle of the sample.

Table 5-1. Samples for Manual Measurement.

Sample	Ca:S	S	Ca	Sol. Al.	Product
14S17-3MW	0.81	0.0032	0.0026	0.037	HR P&O
14S17-7MW	0.69	0.0035	0.0024	0.032	HR Dry
14S17-8MW	0.40	0.005	0.002	0.029	HR Dry
14S21-2L1	0.23	0.0079	0.0018	0.034	HR P&O
15S24/6L1	1.40	0.0015	0.0021	0.032	HR Dry

5.2.1.2. Semi-Automated Inclusion Assessment

During this analysis 13 Ca treated samples and the non-Ca treated sample that was mechanically tested, were imaged at 100x magnification in the manner described in Chapter 3. While these Ca treated samples exhibit a smaller Ca:S range than the full set due to only comprising of first 13 samples, they should still provide a good comparison to the validity of the automated technique.

5.2.2. Percentage Globular

The resulting average percentage globular inclusions for all 3 optical techniques are shown in Figure 5-1, along with their corresponding sample numbers. As can be seen in the majority of the samples, both the manual and the semi-automated techniques have significantly higher percentage globular values than the automated technique. The only exemption to this is 15S24/6L1 which shows a slightly higher result than the manual analysis – i.e. the only other technique this sample was analysed against.

The manual and semi-automated methods however showed either very similar results or the manual results were slightly lower. As a result, the manual measurements all show >75% globular whereas the semi-automated technique showed slightly higher with >80% globular. Also worth noting is that, as the error bars show, all of the samples show a similar spread of results. For the non-Ca treated steel (11QS44/7L1), the semi-automated procedure shows a higher percentage number of globular inclusions when compared to the results from the automated method (39% compared to 25.3%).

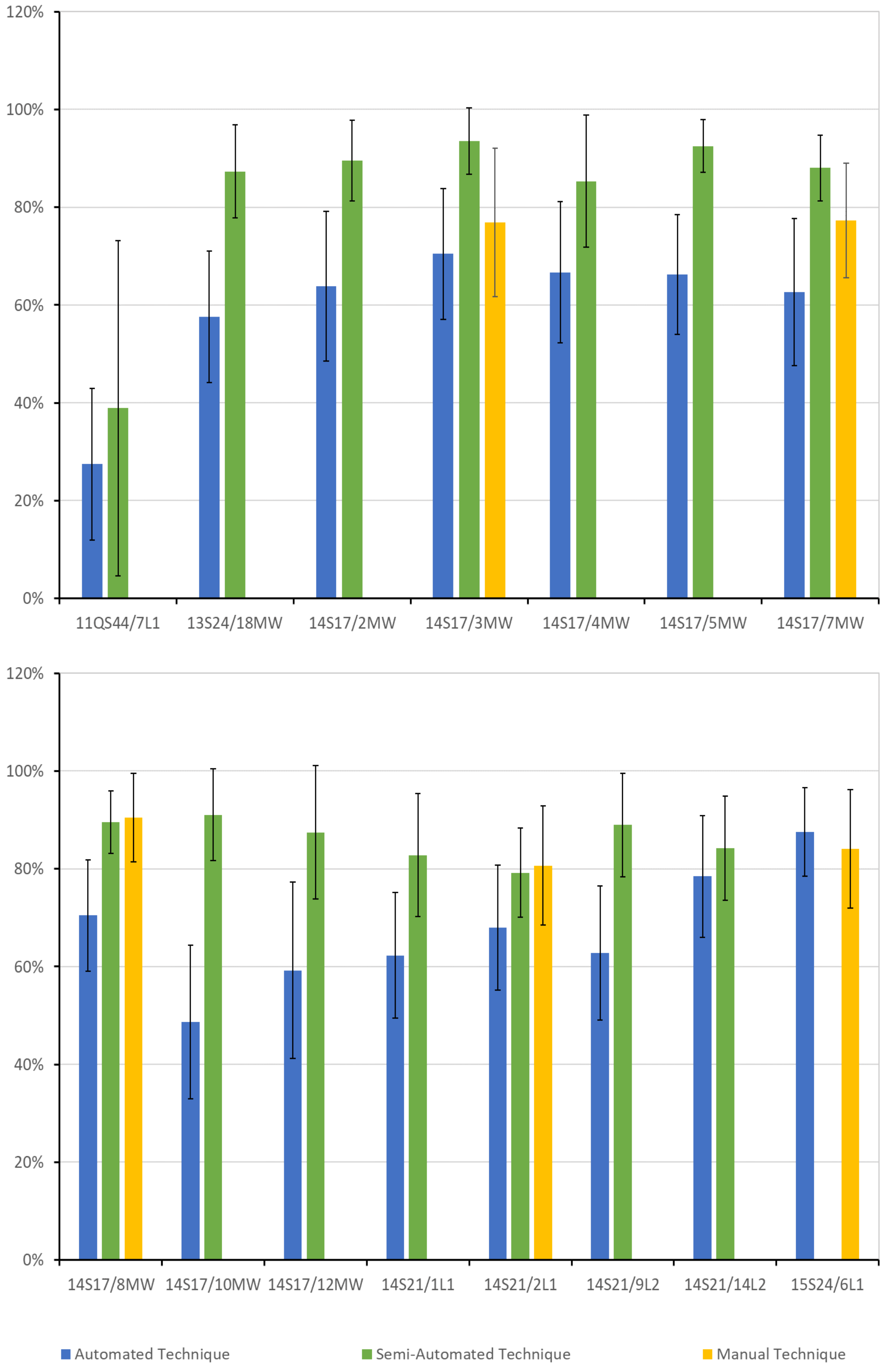

Figure 5-1. Comparison of the Optical Measurement Results for the Percentage Globular Taken from the Same Samples.

5.2.3. Inclusion Population Density

Figure 5-2 shows the average number of inclusions for each of the samples from the 3 different optical microscopy methods. As can be seen, a significant proportion of the samples have relatively similar levels of inclusion population results from the 3 different techniques, as well as similar levels of variation between those populations. While a few of the automated techniques show a large increase in the average number of inclusions compared to the other techniques, this could simply be due to the fact that this method calculates inclusions over a significantly larger area than either of the other 2 procedures. This is also shown in a large increase in the number of inclusions in the automated results for the non-Ca treated steel compared to the results from the semi-automated technique.

5.2.4. Size of Inclusions

Figure 5-3 shows instead the average size of inclusions calculated through the three different process routes. As can be seen, the manual method shows significantly greater average inclusion sizes when compared to the other two techniques, with most samples exhibiting an average inclusion size equal to or greater than 90μm^2. This technique also shows a greater range of results as shown by the much larger σ associated to them. In fact, in most cases the higher the average size of inclusions, the larger the range of inclusion sizes within the sample as shown by the larger error bar. Instead the sample showing the lowest average area have by far the smallest error bar.

Of the other two techniques, the automated technique also shows larger inclusion size results than the semi-automated method, but to nowhere near the same extent. As can be seen, most of the samples' results for the semi-automated method exhibit roughly a 20μm^2 area on average. If the samples exhibit larger than this, they also have much larger corresponding error bars.

The non-Ca treated sample results from the semi-automated method show both a large increase in average size and a significantly larger σ when compared to the automated technique. This is likely because it only measures 10 fields compared to the 390 for the automated technique, so will be more greatly affected by any large inclusions which do not represent the general population of inclusions.

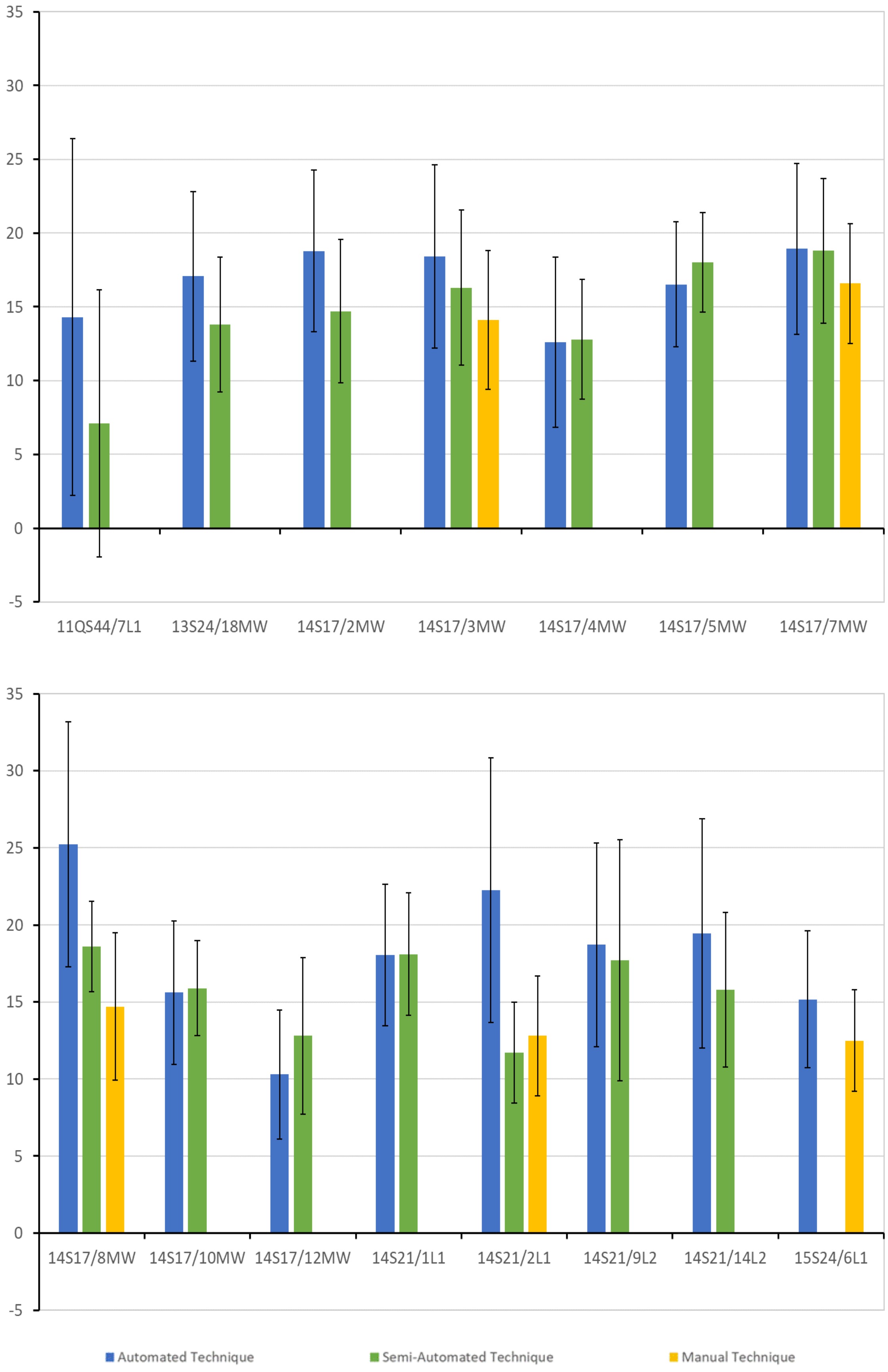

Figure 5-2. Comparison of the Optical Measurement Results for the Average Number of Inclusions Taken from the Same Samples.

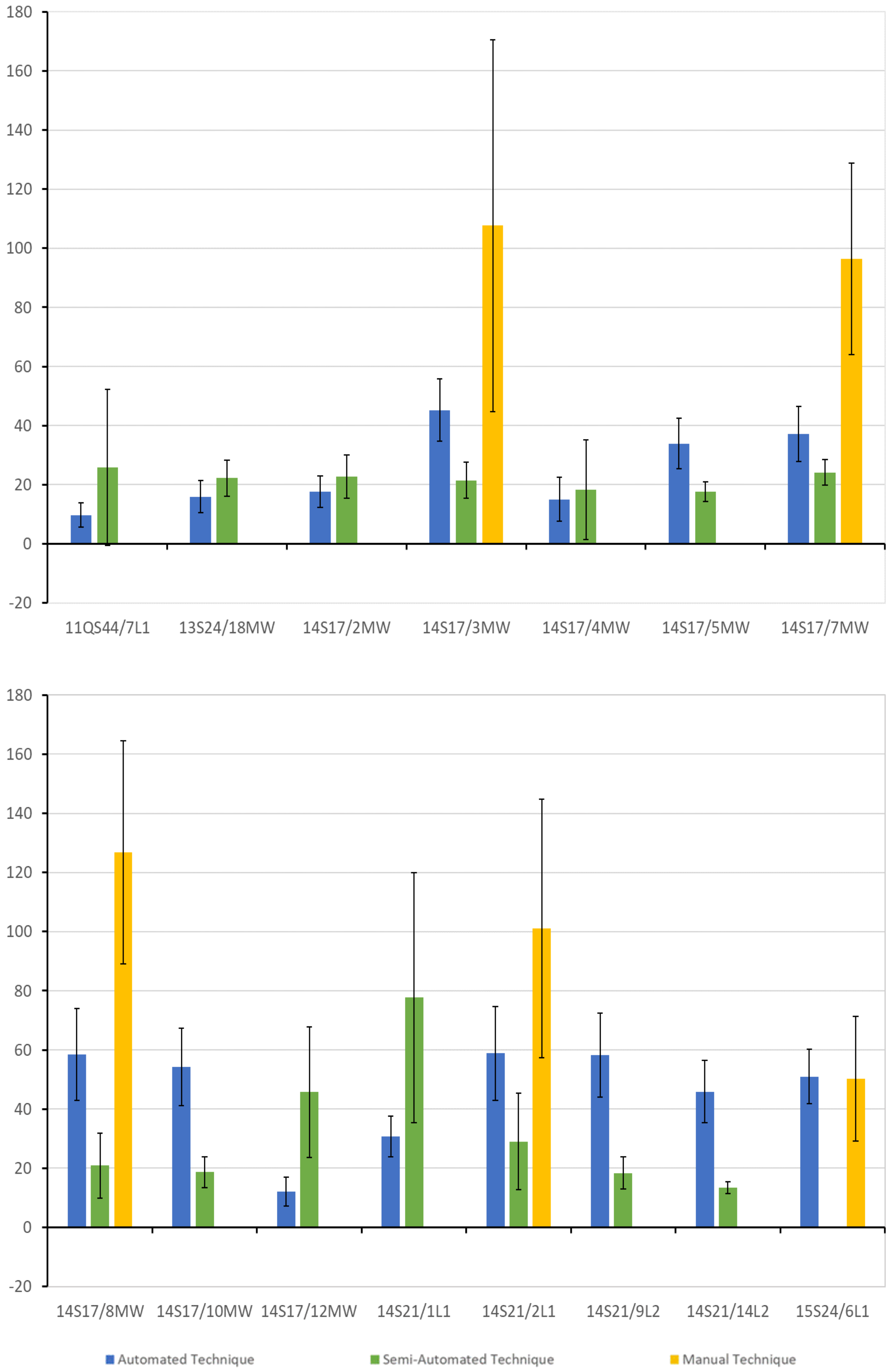

Figure 5-3. Comparison of the Optical Measurement Results for the Average Size of Inclusions Taken from the Same Samples.

5.3. Automated EDS Inclusion Analysis

The next technique used utilises the ‘Particle Analysis’ tool within the EDAX Genesis software. An area of roughly 19.6 mm^2 in the centre of each sample was analysed, as described in Chapter 3. The analysis was conducted on the same 14 samples analysed in the Semi-Automated study. However, this analysis was setup to analyse only the sulphide-based inclusions for modification levels.

5.3.1. Percentage Calcium Modified

The percentage of the total number of sulphide-based inclusions that were successfully modified with Ca is shown (either in combination with MnS – e.g. (Ca,Mn)S - or purely CaS) in Figure's 5-4 and 5-5. Figure 5-4 shows this value in relation to its associated Ca:S, while Figure 5-5 is instead graphed against its S level. As can be seen in Figure 5-4, all the Ca treated grades sulphide-based inclusions show a significant level of Ca modification, with the sample with the lowest Ca:S (0.23) showing 76% of its sulphide-based inclusions modified. This percentage increases until a Ca:S of roughly 0.45, after which the level of modification essentially hits 100%.

A similar trend appears in Figure 5-5 where the level of modification decreases as the S level increases. However, the trend indicated by the line is less defined, instead showing an R^2 value of 0.65 (2dp) compared to 0.73 (2dp) for the trend against Ca:S. This trendline was calculated as a second-degree polynomial regression but would ignore any decrease in percentage modified after it reaches 100%, as there is no data to support this. This specific trend line was chosen because it fit the trend the most accurately, whilst also not estimating the percentage modified would not exceed 100%, which would obviously not be possible.

As can be seen in both Figure's 5-4 and 5-5, the non-Ca treated grade shows a significantly lower level of modification, with only 19% of the sulphide-based inclusions successfully modified. It should be noted that there are no error bars because these values were calculated simply by how many inclusions were modified compared to the total inclusion number for the entire data set and was not an average of each individual field.

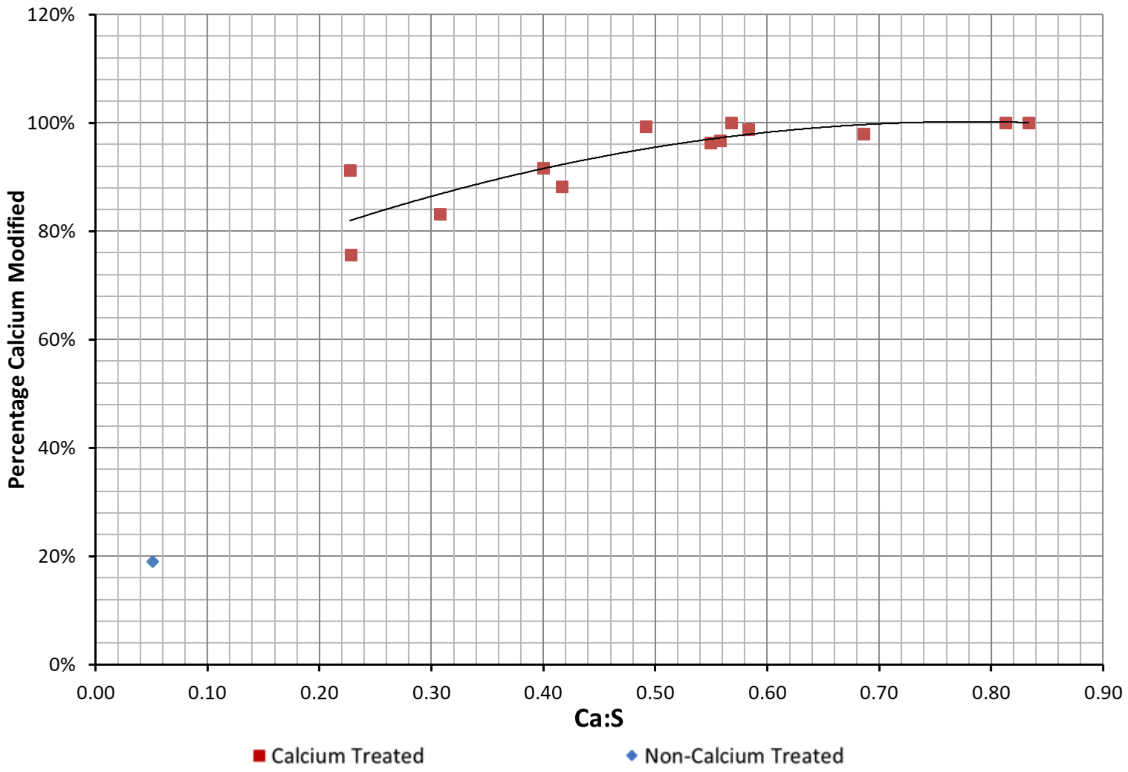

Figure 5-4. Calcium Sulphur Ratio Versus the Percentage of Sulphide Inclusions That Have Been Calcium Modified in FB590 and a Non-Calcium Treated Grade using Automated Inclusion Analysis on the FEI Quanta 600.

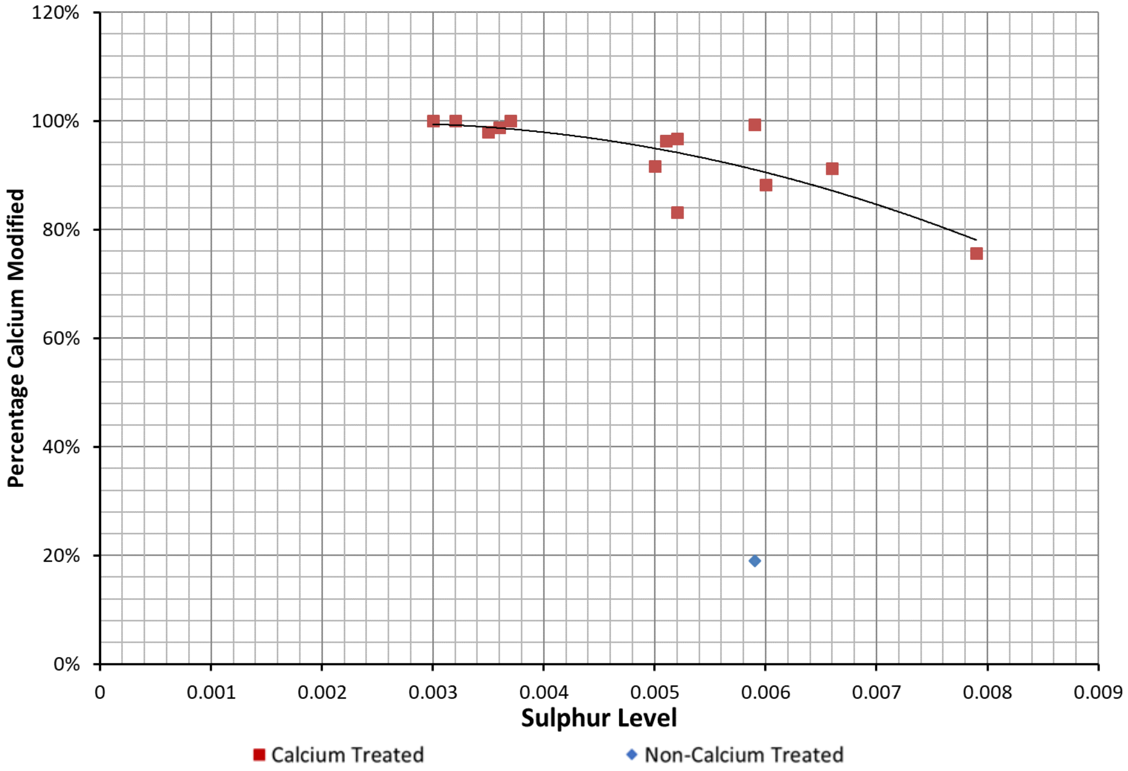

Figure 5-5. Sulphur Level Versus the Percentage of Sulphide Inclusions That Have Been Calcium Modified in FB590 and a Non-Calcium Treated Grade using Automated Inclusion Analysis on the FEI Quanta 600.

5.3.2. Average Inclusion Diameter

Because the automated inclusion analysis was set up to analyse sulphide-based inclusions, the most common inclusion types – i.e. 'cored', 'Ying-Yang' & 'classic' – overall area could not be measured. This is because these types of inclusions are made up of a significant amount of alumina which were not measured. Even if the alumina were also characterised, these specific inclusion portions would simply be classified as separate inclusions leading to no method of calculating overall inclusion size. What this technique did allow for was the calculation of the average diameter of these portions, plus the diameter of the also common 'sulphide-based' inclusions. These results can be seen in Figure 5-6, where it is plotted against the samples Ca:S ratio.

While there is no change in the diameter of these inclusions that can be attributed to a change in Ca:S, the graph does show that the average diameter for the 'sulphide-based' inclusions is ≤2µm. The non-Ca treated sample has an even lower average diameter of 0.8µm and even if you factor in the variation associated with 2σ, this value is still <1.6 µm.

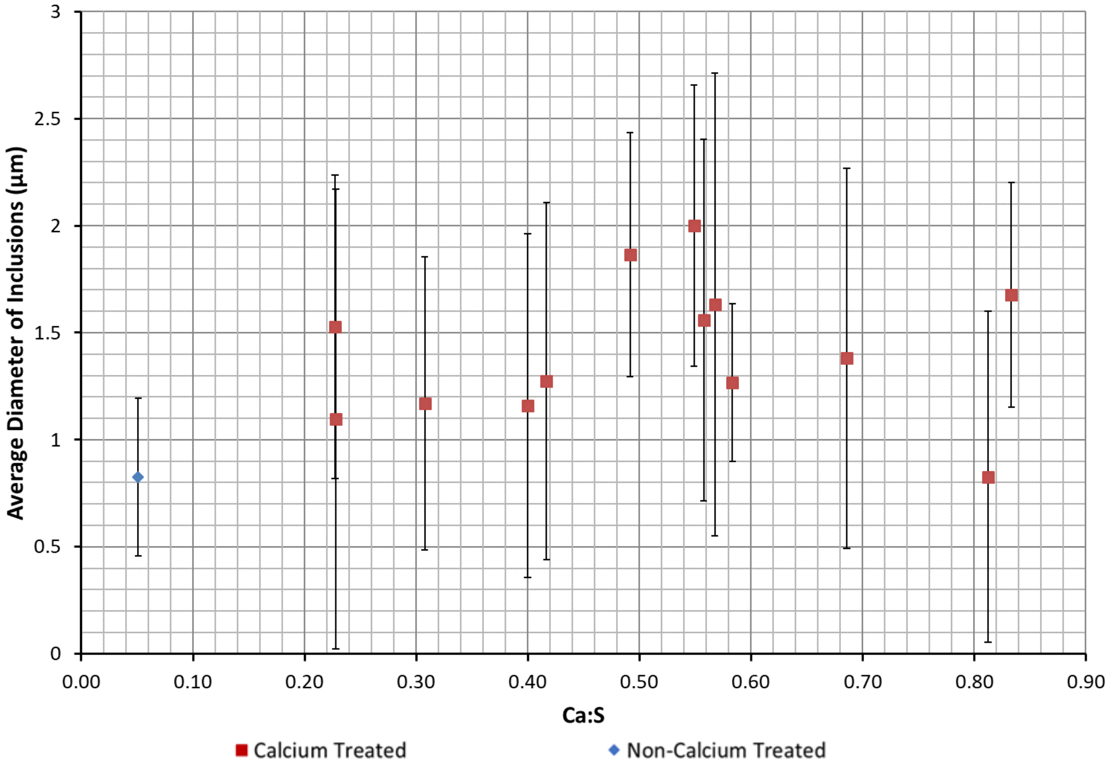

Figure 5-6. Calcium Sulphur Ratio Versus the Average Diameter of Sulphide Inclusions in FB590 and a Non-Calcium Treated Grade using Automated Inclusion Analysis on the FEI Quanta 600.

5.4. PDA Analysis

During OES analysis, a number of sparks will be generated from inclusions within the sample. These results were passed through Tata Steel’s in-house OES-PDA algorithm which classified the inclusions based on whether there was sufficient Ca to modify the sulphide and aluminates successfully. This analysis was run on all the samples available for re-analysis in the process described in Chapter 3. These samples covered the entire Ca:S range, as well as incorporating analysis on 11 non-Ca treated samples, including the non-Ca treated sample that was mechanically tested.

5.4.1. Percentage Calcium Modified Sulphides

Figure 5-7 and Figure 5-8 show the percentage number of the inclusions that contained enough Ca to be successfully modified against the Ca:S and S level respectively. As can be seen in Figure 5-7, the percentage modification increases dramatically from 65% at a Ca:S of roughly 0.2 until about 0.45, after which it stays at roughly 85% - 90% as the Ca:S increases further. One thing that is interesting is that the trend almost lines up with non-Ca treated samples however their spread in Figure 5-8 implies that they are simply two separate populations.

Figure 5-8 also shows a trend of decreasing percentage modification as the S level increases. However, this trend is not as well defined as the trend for Ca:S. The R^2 value for the indicated trends for Ca:S is 0.50 (2dp) while it is 0.42 (2dp) for S level. It should also be noted that the trend for the S level was calculated as a 2nd degree polynomial as it was the only ‘curved’ trendline model that followed the downward progression of the results. The Ca:S trendline was calculated instead using the Power model. While the 2nd degree polynomial modal showed a higher R^2 value (0.55 (2dp)), it also predicted a decrease in percentage modified which is not shown in the results, even if the initial trend appeared to fit slightly better.

Figure's 5-7 and 5-8 both show that the non-Ca treated samples undergo a significantly lower level of modification, with every non-Ca treated samples showing < 21% modification.

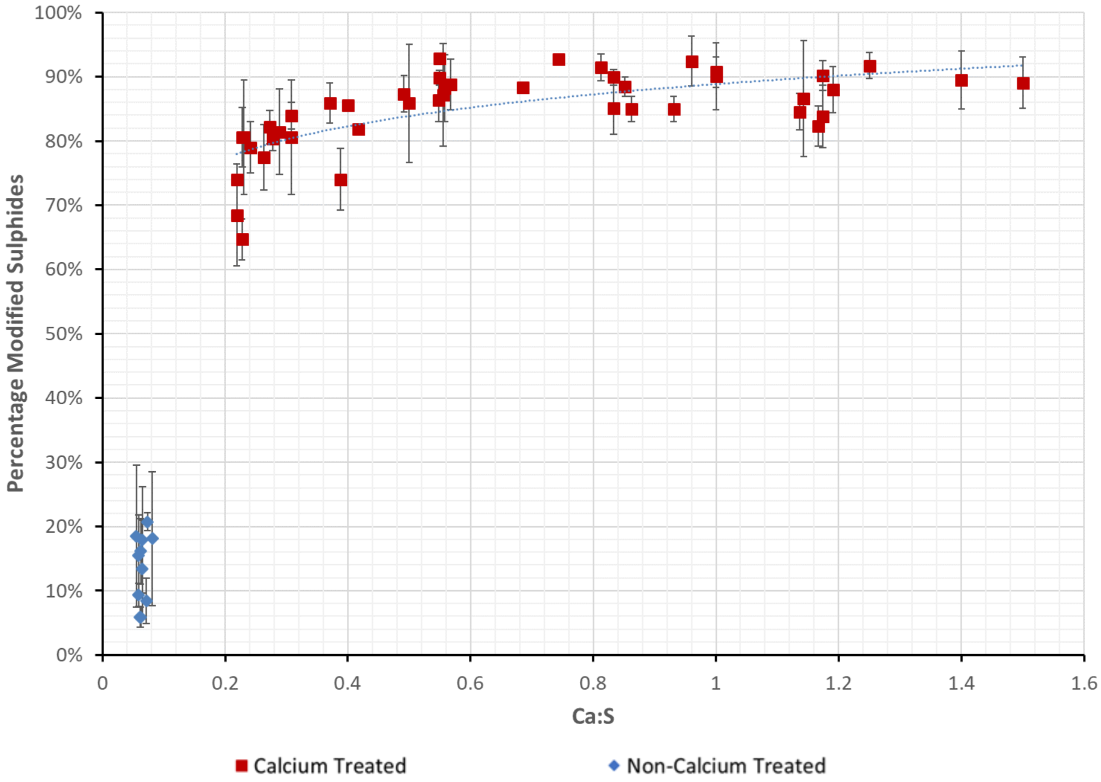

Figure 5-7. Calcium Sulphur Ratio Versus the Percentage of Sulphide Inclusions That Have Been Calcium Modified in FB590 and a Non-Calcium Treated Grade using PDA Analysis.

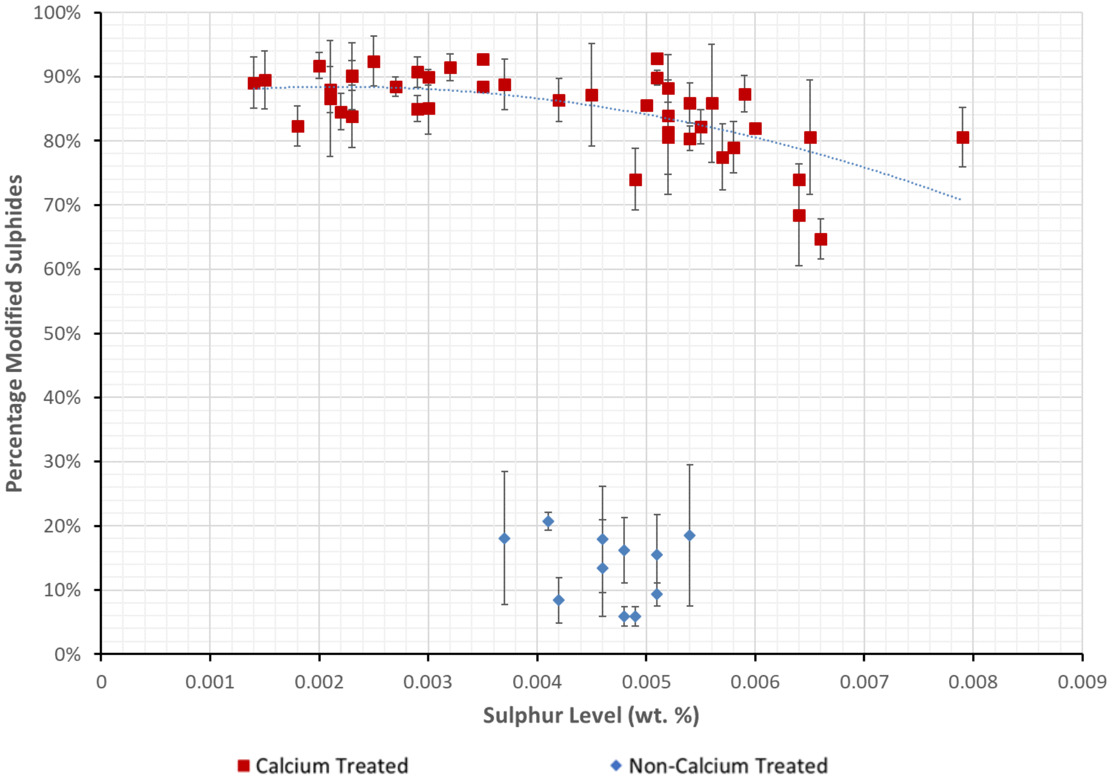

Figure 5-8. Sulphur Level Versus the Percentage of Sulphide Inclusions That Have Been Calcium Modified in FB590 and a Non-Calcium Treated Grade using PDA Analysis.

5.4.2. Percentage Calcium Modified Aluminates

The percentage number of aluminate inclusions that contain enough Ca to be successfully modified are graphed in Figure 5-9 and Figure 5-10 against Ca:S and S level respectively. As can be seen in both graphs, there is a significant level of modification across all the Ca treated samples with most samples showing a >85% level of modification and all samples showing a >72% level of modification. Even the non-Ca treated samples show a reasonable proportion of modified inclusions with most samples showing >45% and all above 31%. Figure's 5-9 and 5-10 also indicate there is no significant trend in the Ca or non-Ca treated samples that be associated to a change in either the Ca:S or S level.

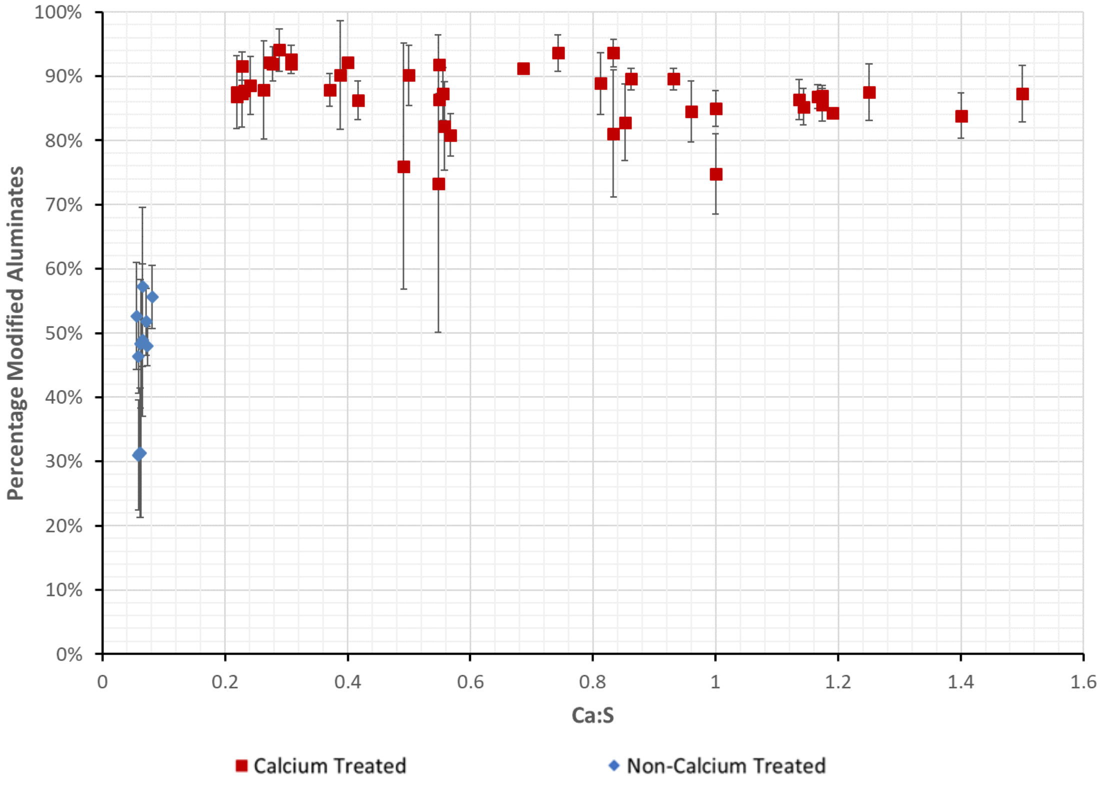

Figure 5-9. Calcium Sulphur Ratio Versus the Percentage of Aluminate Inclusions That Have Been Calcium Modified in FB590 and a Non-Calcium Treated Grade using PDA Analysis.

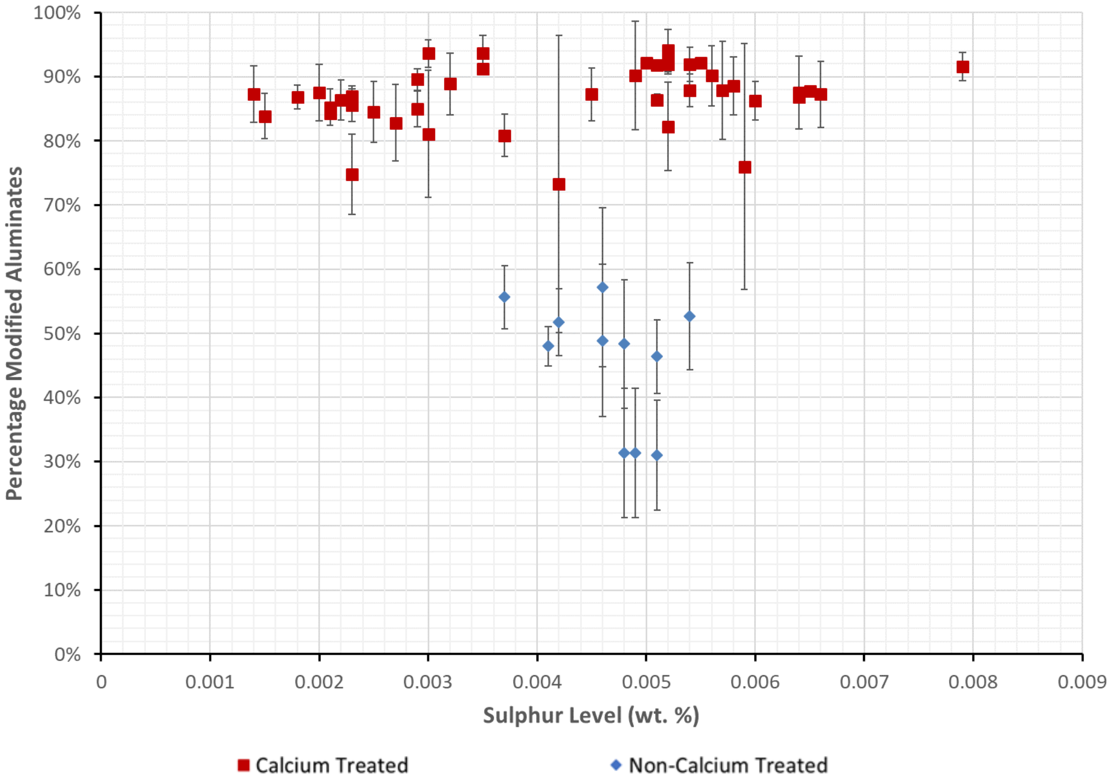

Figure 5-10. Sulphur Level Versus the Percentage of Aluminate Inclusions That Have Been Calcium Modified in FB590 and a Non-Calcium Treated Grade using PDA Analysis.

5.5. Discussion

5.5.1. Assessment of Results

To compare the results from the different types of analytical techniques employed within this study (i.e. inclusion shape vs chemistry), the assumption had to be made that any inclusion that was globular in nature was successfully modified by Ca. This successful modification was assumed to be the reason that the inclusion was globular and that it would have elongated into a stringer without it. As a result, the percentage globular and the percentage modified are treated as equivalent.

As can be seen in this chapter and highlighted further in Table 5-2, the biggest discrepancy between the automated technique and the other methods, is that the average percentage globular for the Ca treated samples is significantly reduced. The automated technique also shows the largest σ in terms of variability when compared to other techniques. However as shown by Table 5-3, its results for the percentage globular in the non-Ca treated are roughly in line with that shown by the chemical based analytical techniques, and is significantly lower than the Semi-Automated Inclusion method, even if this was conducted on only one sample.

One distinct advantage the imaging-based analysis has over the chemical-based analysis, and possibly the reason for some of the discrepancies between the two technique sets, is that it is the only technique that can possibly give you a true analysis of whether an inclusion is globular or stringer and thus its resulting impact on mechanical properties. This is because the chemical techniques only consider if the inclusion has been modified with Ca and do not account for how successful this modification has been in altering the shape of the inclusion. As a result, they do not account for stringer types that have some level of Ca modification – i.e. the 'fractured', 'facetted', 'nucleated' or 'partially-modified' types discussed in Chapter 4.

As can be seen in Figure 5-11 (a) – (f), the key reason for this difference however, is that while a significant proportion, if not the majority, of the inclusions are below the 1.3 Length/Width (L/W) ratio 'cut-off' as stipulated by the standards [99, 100]. It can also be seen that, of the rest of the inclusions, most have a L/W ratio of 1.4. In fact, unlike the non-Ca treated samples in Figure 5-12 (a) – (b), there are very few inclusions that have higher ratios.

Table 5-2. Average Percentage Globular /Modified for the Ca Treated Samples from Each Analysis Technique.

Technique	Average Percentage Globular/Modified
Automated Technique	63.4% ± 9.5%[†]
Manual Measurements	81.9% ± 5.6%[†]
Semi-Automated Inclusion Assessment	88% ± 4%[†]
Automated EDS Inclusion Analysis	94% ± 8%[‡]
PDA Analysis	85% ± 6%[‡]

[†] Percentage Globular **[‡] Percentage Modified**

Table 5-3. Average Percentage Globular for the non-Ca Treated Samples from Each Analysis Technique Used.

Technique	Average Percentage Globular/Modified (1dp)
Automated Technique	25.3% ± 2.9%[†]
Semi-Automated Inclusion Assessment	39%[†*]
Automated EDS Inclusion Analysis	19%[‡*]
PDA Analysis	14% ± 5%[‡]

[†] Percentage Globular **[‡] Percentage Modified**

*** Results Taken from 1 Sample – The Non-Ca Treated Sample That Was Mechanically Tested.**

The logical argument is that inclusions with a L/W ratio of 1.4 would have a similar impact on the steels properties as one of 1.3. Consequently, if you increase this ‘cut-off’ point to 1.4, it will give a more accurate representation of the true number of globular inclusions from the entire inclusion set. However, as can also be seen in Figure 5-12 (a) – (b), a significant proportion of the non-Ca treated inclusions also have a L/W ratio of 1.4. This means if you simply increased this ratio ‘cut-off’, you would also drastically increase their globular percentage. As a result, this value is no longer an accurate representation and because the final product needs to be a technique that can be applied uniformly to all steel types, this is not suitable.

One reason for the increase in inclusions with a L/W ratio of 1.4 could be due to the method by which the ‘Particle Analysis’ tool within ImageJ measures the length and width of inclusions. During this analysis, the software fits the smallest rectangle possible over the inclusion, even if this would mean it is not elongated in the rolling direction. While the argument could be made that this would provide a more accurate

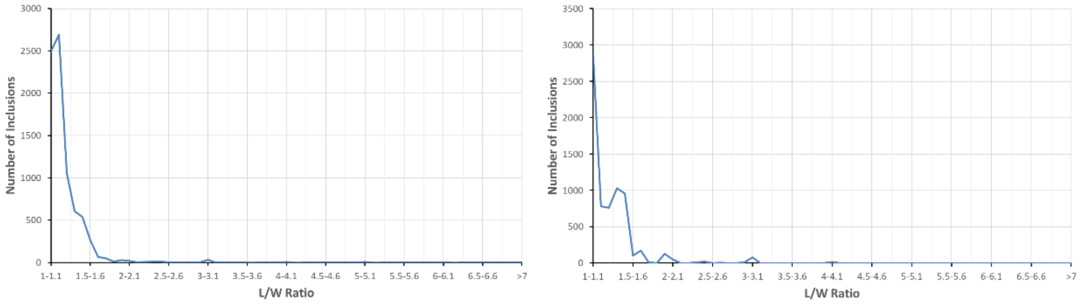

(a) 14S21/14L2 (Ca:S – 0.23, Glob. – 78.45%) **(b) 14S17/2MW (Ca:S – 0.42, Glob. – 63.82%)**

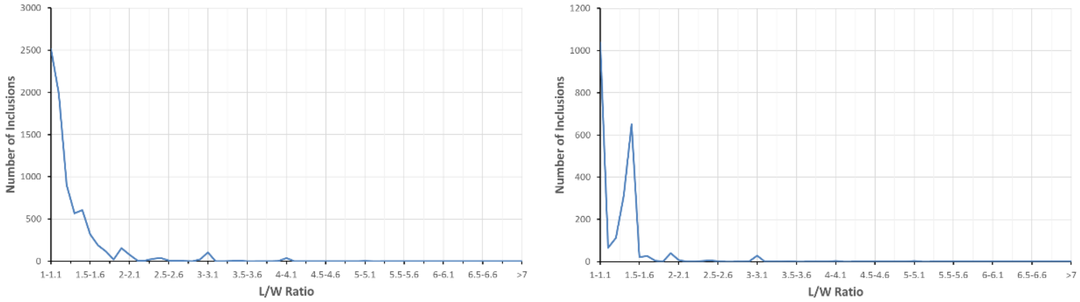

(c) 14S17/3MW (Ca:S – 0.81, Glob. – 70.47%) **(d) 15S24/14L1 (Ca:S – 0.96, Glob. – 52.30%)**

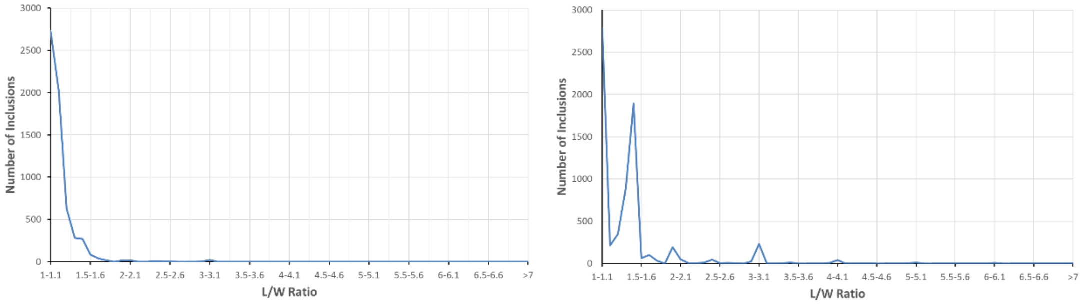

(e) 15S24/6L1 (Ca:S – 1.40, Glob. – 87.51%) **(f) 15S24/9L1 (Ca:S – 1.50, Glob. – 48.94%)**

Figure 5-11 (a) – (f). Number of Inclusions with Each Length/Width Ratio in the Labelled Calcium Treated Samples

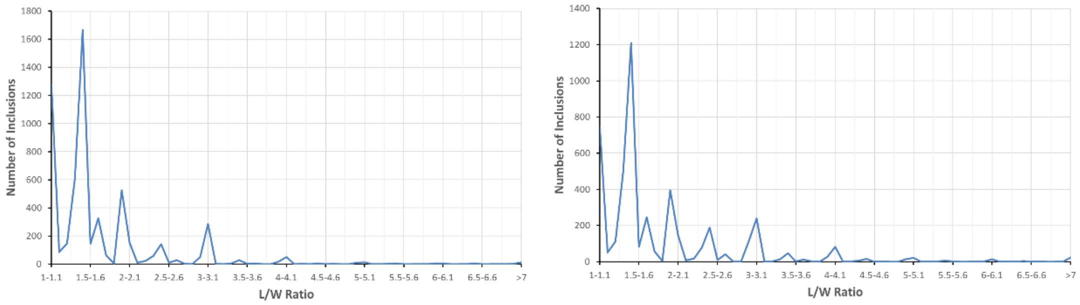

(a) 11QS44/7L1 (Ca:S – 0.06, Glob. – 27.46%) **(b) 16S18/26L1 (Ca:S – 0.06, Glob. – 20.41%)**

Figure 5-12 (a) – (b). Number of Inclusions with Each Length/Width Ratio in the Labelled Non-Calcium Treated Samples

assessment of the inclusion itself, none of the other techniques calculated it this way and with such fine lines between the globular or stringer classifications, it could be a factor in this increase of 1.4 ratioed inclusions.

Nevertheless, the most likely reason for this discrepancy is probably due to the effect of pixel size. This is highlighted by the fact that the Semi-Automated method has a significantly higher proportion of globular inclusions, which is much closer to the chemical analysis results. The reason for this is because the camera attached to the Reichart microscope captures images at a scale of 1.9 pixels/µm compared to 0.972 pixels/µm for the Zeiss Observer.

While this value is slightly below the 1 pixel/µm that is stipulated by the standards, the key reason it was chosen was the simple practicality of file size. The camera on the Observer does offer the option of using a 'Scanned' mode that uses 'pixel-shifting' to capture 3 images, taken 1/3 pixel apart, to create one image that can be either double or triple the resolution (1.98 pixels/µm or 2.955 pixels/µm). However, once this mode is used to create an image, it generates a proprietary file that is, at minimum, 4 times the size, ~10GB in size compared to ~2.5GB, which is impossible to convert into a TIFF due to the limitations of being a 32-bit format [123].

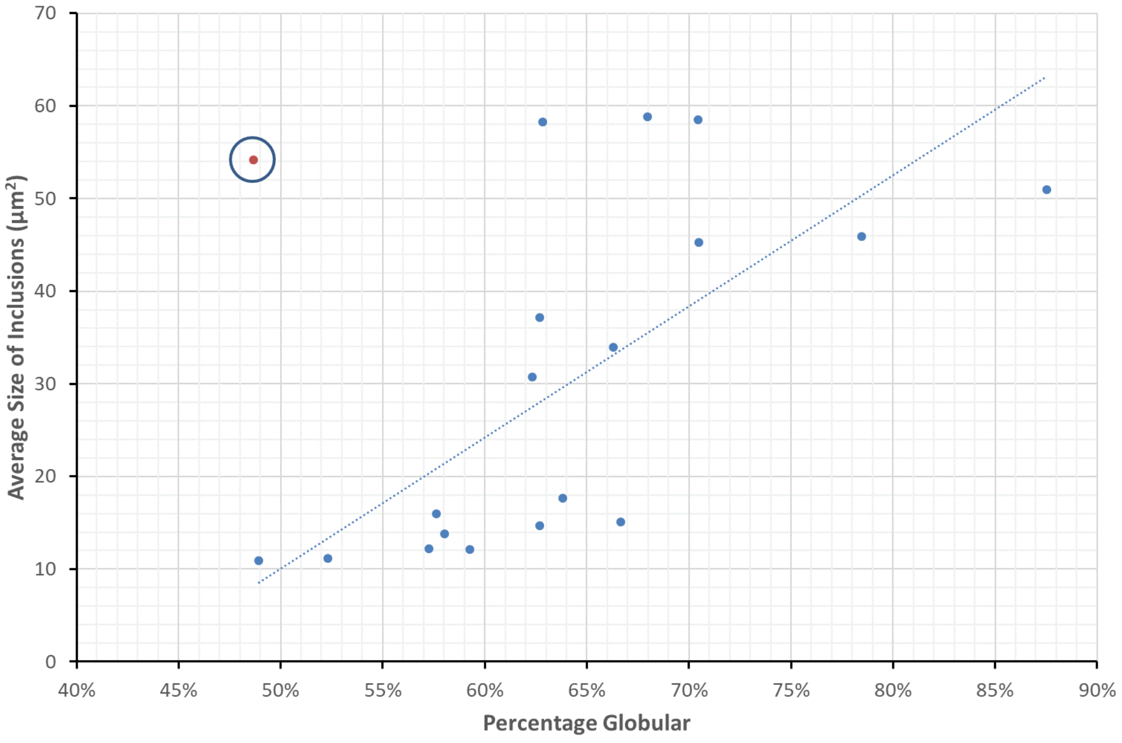

Figure 5-13. Percentage Globular versus Average Inclusions Size for Calcium Treated FB590.

This pixel size becomes vitally important as the size of the inclusions decreases, and is highlighted in Figure 5-13 where, other than the circled anomaly, there is a general trend of increasing percentage globular with increasing average inclusion size. This is because the small inclusions are more susceptible to changing inclusion type because of a slight variation in the number of pixels comprising an inclusion.

For example, Figure 5-14 shows that if the dark centre is classed as the inclusion region, it would be measured at 3 pixels by 3 pixels, giving it a L/W ratio of 1 and therefore would be classified as a globular inclusions. If, however, it is considered that top row of pixels is also part of the inclusion, the inclusion size would increase to 3 pixels by 4 pixels, therefore giving it a L/W ratio of 1.33 (2dp), therefore classing it as a stringer inclusion.

This fact could also lead to an increase in the number of globular inclusions that are measured in the non-Ca treated samples in the semi-automated inclusion assessment. Because, logically, with so many inclusions having a 1.4 L/W ratio in the non-Ca treated samples, an increase in resolution would result in some of those inclusions being incorrectly re-classified as globular. This is simply down to the fact that, even with the Reichart microscope's higher pixel count, the pixel size is still large due to the magnification used to capture the images.

The average sulphide inclusion/segment of the inclusion diameter seen in Figure 5-6 backs up what has been seen previously with the 'classic' and 'sulphide-based' stringer inclusions. This means that because the elongated regions of these inclusions are less than 1 μm in thickness, these regions are less than 1 pixel in diameter on the Observer and less than 2 pixels on the Reichart. Consequently, these elongated regions are impossible to determine accurately. As a result, the 2 most common stringers found in non-Ca treated steel are either only measured for the largely globular-shaped alumina-based cores – i.e. 'classic' stringer - (Figure 5-15), and therefore incorrectly classified as globular, or the inclusion is completely ignored in the case of the purely 'sulphide-based' stringers (Figure 5-16). Nevertheless, as 'sulphide-based' inclusions are less than 2 μm in thickness, they would not be included in the measurement due to stipulations in the standards anyway, unless they were grouped.

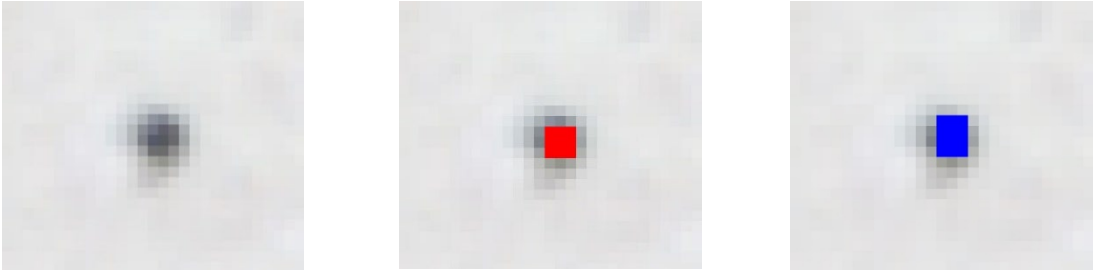

(a) Original Inclusion

(b) 3 Pixel x 3 Pixel Measurement

(c) 3 Pixel x 4 Pixel Measurement

Figure 5-14 (a) – (c). Pixel Measurement Discrepancies in Inclusion Taken From 15S24/6L1.

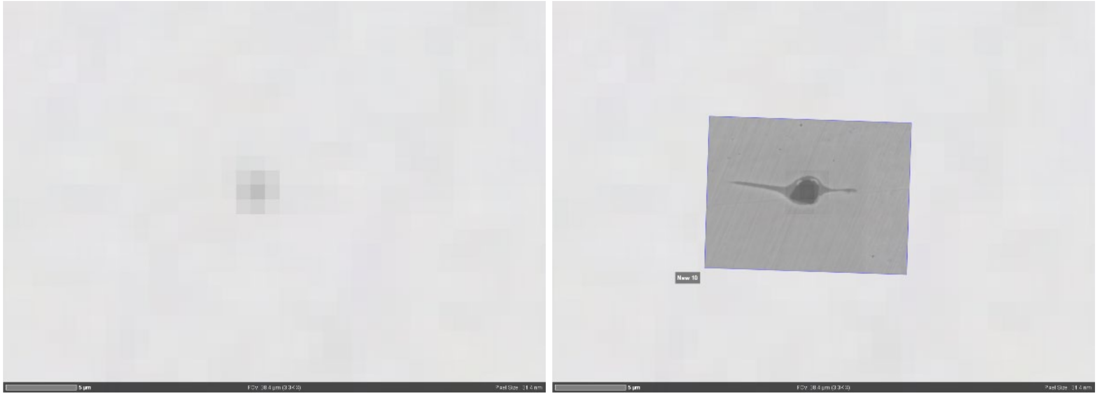

(a) 100x Magnification LM Image

(b) Overlaid with SEM Image

Figure 5-15. 'Classic' Stringer Inclusion with its Conventional Alumina Core from the Non-Calcium Treated 11QS44/7L1.

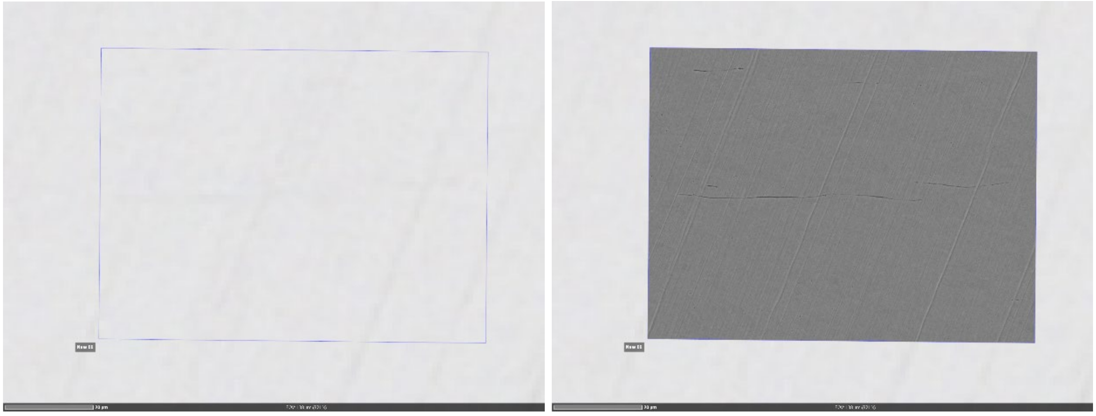

(a) 100x Magnification LM Image

(b) Overlaid with SEM Image

Figure 5-16. Purely 'Sulphide-based' Inclusion from the Non-Calcium Treated 11QS44/7L1.

The other effect of the large pixel size is that it becomes very difficult to define the edge of the inclusion accurately. This is because, as seen in Figure 5-17, the edge of the inclusion is blurred over several pixels with only the centre portion of the inclusion appearing dark. As a result, even manual measurements of the inclusions are difficult and with the pixel size being so large, slight variations in the pixel area of the inclusions, can lead to relatively drastic changes in inclusion size, especially for small inclusions.

This is then compounded through the greyscale-based segmentation that is the basis of the automated analysis technique. Consequently, a compromise had to be made between encapsulating as much of the greyscale for the inclusion as possible without also incorporating artifacts - e.g. scratches - or noise into the analysis.

The automated analysis could be improved via the use of commercially available machine learning segmentation software such as Zeiss's Intellesis Module. These pieces of software incorporate shape recognition and edge detection into the segmentation. However, these automated segmentation tools tend to be slow and expensive and as such may not provide value for money at this point in their development. This should, however, change as the product matures.

Figure 5-18 shows that on average the inclusions found via manual measurements are significantly larger than those from the automated technique. A key reason for this occurring is due to the automated technique not classifying inclusions that have $e \leq 40$ µm and $t \leq 10$ µm (Figure 3-10) as one inclusion. This is unless they are in close enough proximity to each other that the separate inclusions blur into each other. Limitations in the code simply prevented the 'grouping' of inclusions because the particle analysis tool within ImageJ, which was the basis for the assessment, did not allow for this.

As a result, inclusions that fall into this category are measured as being significantly larger than normal. This means a much fairer means of comparison between the techniques would be to compare the average areas of globular inclusions, as seen in Figure 5-19. While these inclusions are still larger on average than the ones taken using the automated method, there are a couple of reasons why this is the case. One reason is that there are still examples of inclusions that were classified as globular, but still consist of multiple aligned inclusions (Figure 5-21). However, these were significantly rarer than their elongated equivalents. Another reason could be the effect of greyscale and large pixel size, discussed earlier, resulting in any slight variation in the pixel area having a relatively large impact on the calculated inclusion area.

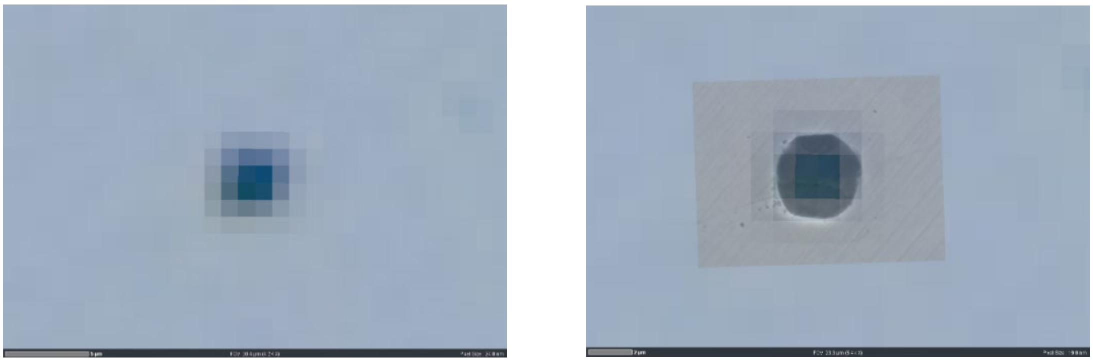

(a) 100x Magnification LM Image **(b) Overlaid with SEM Image**

Figure 5-17. Globular Inclusion from Calcium Treated 15S24-10L1.

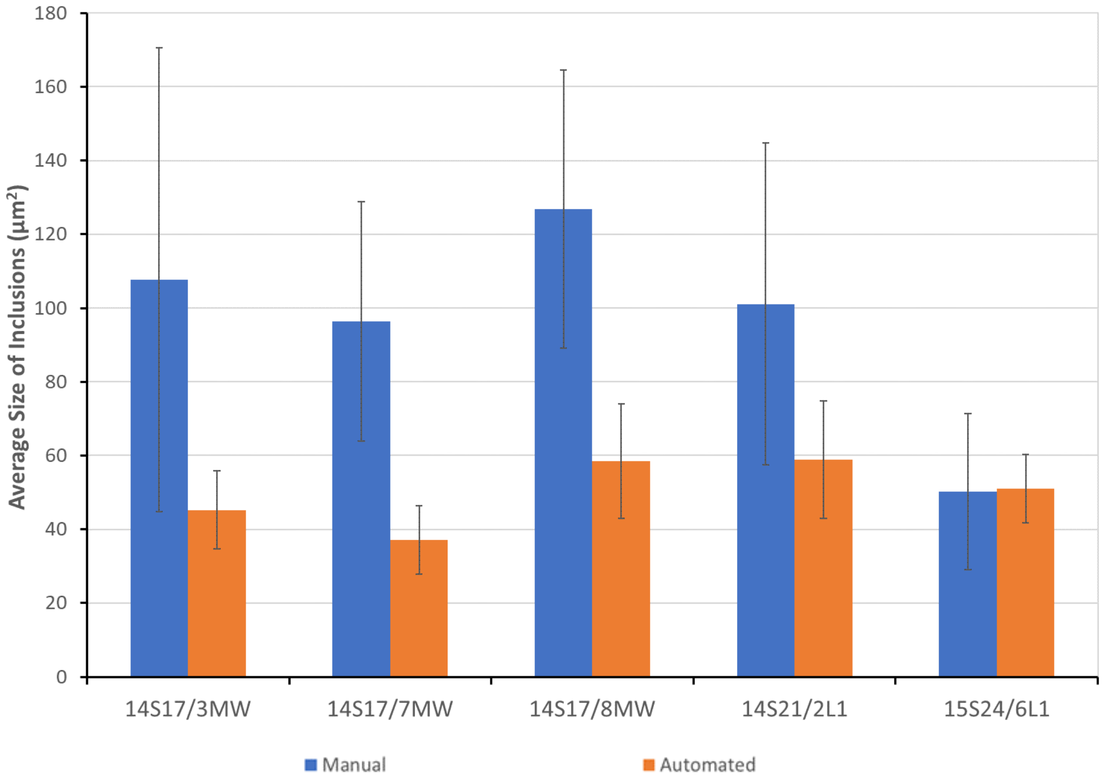

Figure 5-18. Comparison Between the Automated and Manual Techniques for the Average Size of Inclusions Results Taken from the Same Samples.

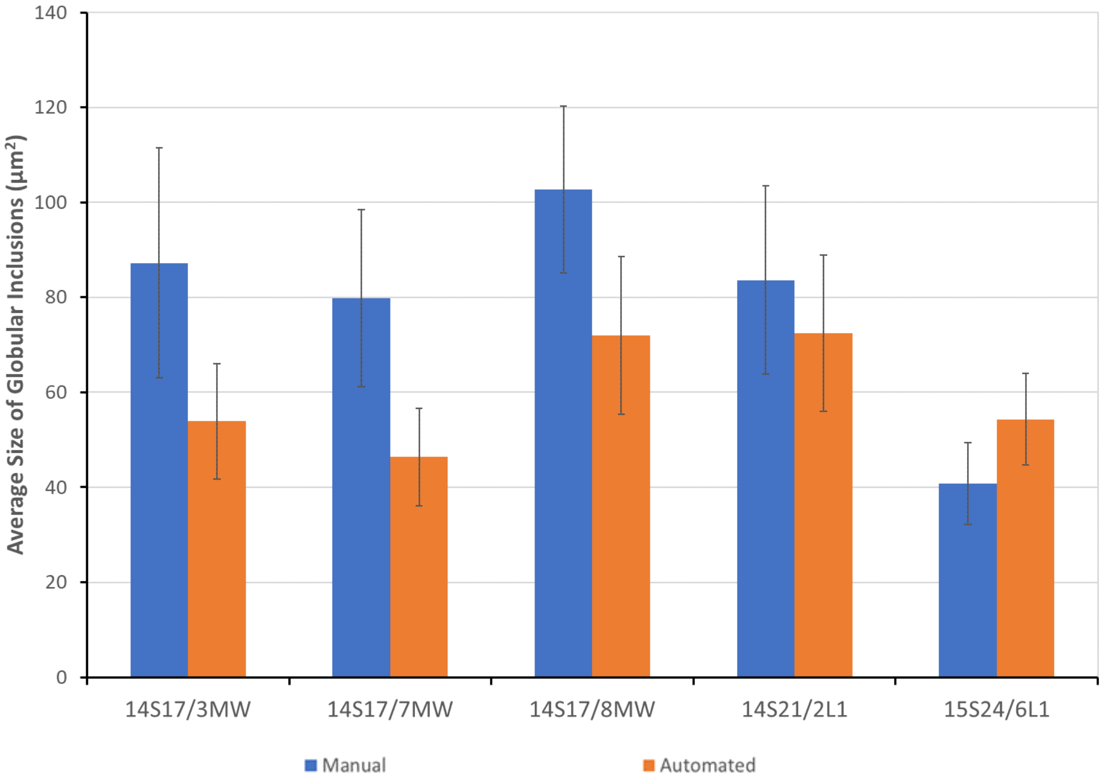

Figure 5-19. Comparison Between the Automated and Manual Techniques for the Average Size of Globular Inclusions Results Taken from the Same Samples.

However, the main reason for this difference in area is that the automated technique calculates the area of inclusion based on the number of pixels that make up the inclusion (Figure 5-22 (b)). This is unlike the manual method which instead calculates the area by multiplying the width and the height of the inclusion (Figure 5-22 (c)). This means that the area calculated for the inclusion by the manual method is significantly larger than the inclusion itself. For example, in Figure 5-22 the area calculated by the manual method is 165.12µm^2 (2dp) compared to 112.19µm^2 (2dp) by the automated method. As a result, the automated method will provide a much more accurate representation of the inclusions area.

This is further highlighted by the fact that, when you compare both techniques (Figure 5-20), the entire inclusion population has very similar average heights. Most samples also have a significant overlap in the range of results, as indicated by their σ, in addition to the average differences normally being less than 1 pixel.

The only other analysis approach that is capable of measuring the average size of inclusions is the Semi-Automated technique. As can be seen in Figure 5-3, the average inclusion size for this technique is significantly smaller than for the other 2

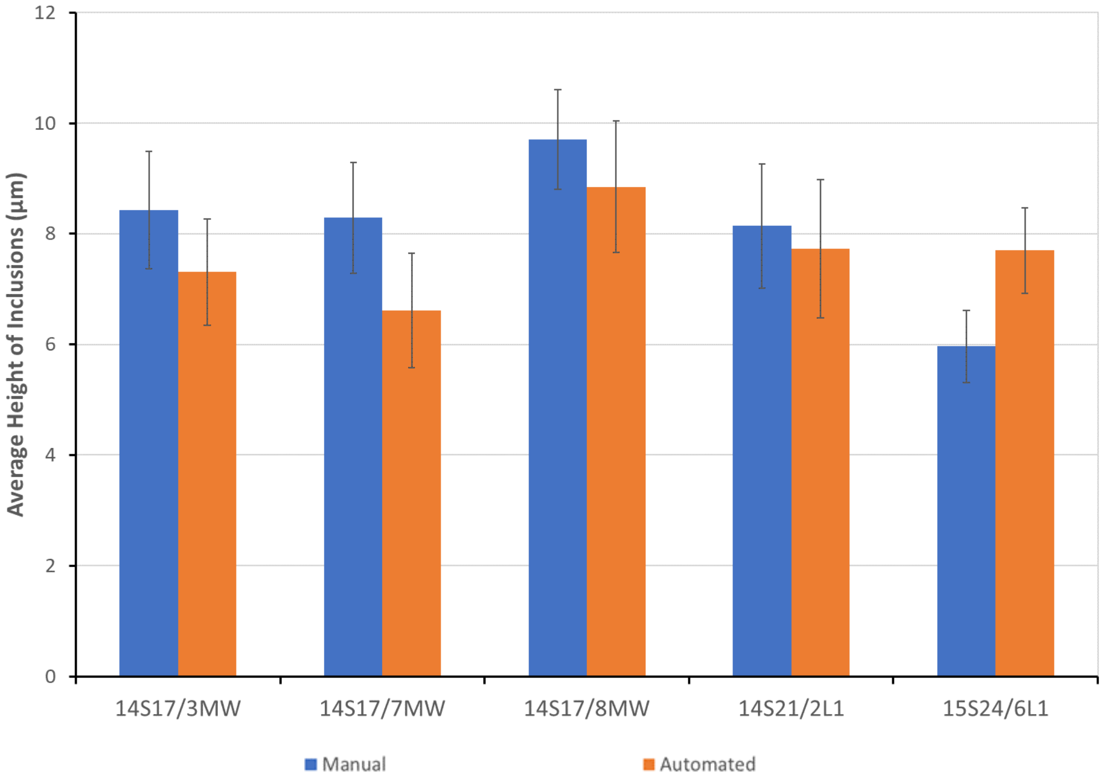

Figure 5-20. Comparison Between the Automated and Manual Techniques for the Average Height of Inclusions Results Taken from the Same Samples.

optical methods. This is likely to be because there were only 10 fields analysed per sample. As the SEM analysis has shown, a wider variety of inclusion sizes commonly exist, this implies that insufficient inclusions were included for the calculation to be accurate for the sample as a whole.

As can be seen in Figure 5-2, the other key difference between the automated and the manual methods is the average number of inclusions per 710µm^2 field. 3 of the samples have relatively similar numbers of inclusions for the 2 different analytical techniques, with any differences most likely influenced by the fact that the automated method does not include the ‘grouped’ elongated inclusions. This is further highlighted in Table 5-4 which shows that all the samples have at least one of these inclusions in over half of the fields, with some being significantly higher. These inclusions consist of at least 2 inclusions but can contain up to 6. Incorporating this into the measurement brings these 3 samples results well into the range of each other’s σ (Figure 5-23).

(a) Light Microscope Image **(b) Measured Inclusion**

Figure 5-21 (a) – (b). Globular Aligned Particle from 14S17/8MW

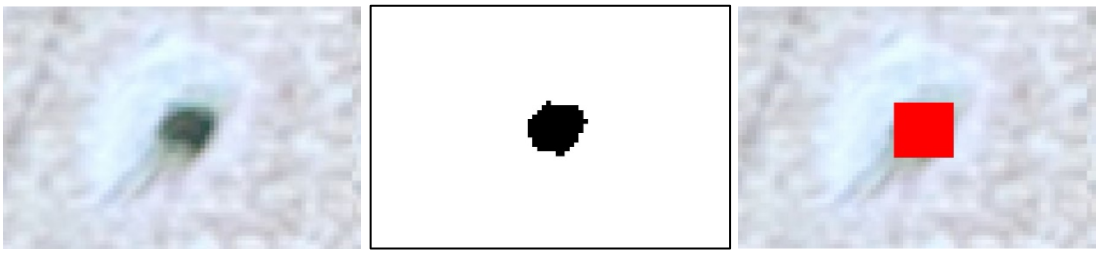

(a) Light Microscope Image **(b) Automated Inclusion Area** **(c) Manual Inclusion Area**

Figure 5-22 (a) – (c). Area Calculation Difference Between Automated and Manual Techniques.

However, 2 of the samples can be seen to have significantly less inclusions in the manual results compared to their automated counterparts. These samples have a significant amount of very small inclusions as seen in Figure 5-24 (a), which tend to only be made up a few pixels (Figure 5-24 (b)).

During manual measurements, a significant proportion of these inclusions were deemed to be too small to be included in the calculations, since they measured 2 pixels by 2 pixels (Figure 5-24 (c)) and were therefore below the 2μm by 3μm size ‘cut-off’ from the standards. However, due to a combination of the large pixel size and greyscale effects mentioned earlier, the automated inclusion analysis incorporated some of these ‘excluded’ inclusions as the minimum size stringer inclusions. This could also help account for some of the variation in percentage globular and the average size of inclusions seen in Figure 5-1 and Figure 5-3.

While the semi-automated method is also capable of calculating the inclusion population density, this suffers from the same problem as its assessment of inclusion size in that it does not measure enough fields over a wide enough area to obtain an accurate average. This can be seen more clearly in the change of both inclusion number and size through thickness in Figure’s 4-22 & 4-23.

Table 5-4. Table of Statistics on the 'Nucleated' Inclusions Found in the Manual Measurements

Sample	Row	Average Number of Elongated	Standard Deviation	Total Number of Elongated Inclusions	Average Number of Inclusions in Elongated 'Set'	Standard Deviation
14S17/3MW	1	0.81	1.11	22	2.18	0.39
	8	0.33	0.62	9	2.00	0.00
	12	0.85	0.99	23	2.16	0.50
	Total	0.67	0.95	54	2.14	0.40
14S17/7MW	1	1.00	0.96	27	2.23	0.51
	6	0.74	0.86	20	2.25	0.55
	9	1.07	1.14	29	2.10	0.31
	Total	0.94	0.99	76	2.19	0.46
14S17/8MW	1	1.63	1.67	44	2.11	0.39
	3	1.04	1.02	28	2.07	0.26
	9	0.41	0.57	11	2.09	0.30
	Total	1.02	1.26	83	2.10	0.34
14S21/2L1	1	0.71	0.90	20	2.10	0.45
	4	0.64	0.83	18	2.11	0.32
	7	1.00	1.02	28	2.11	0.31
	Total	0.79	0.92	66	2.11	0.36
15S24/6L1	1	0.74	0.81	20	2.05	0.22
	4	0.44	0.58	12	2.08	0.29
	8	0.52	0.89	14	2.07	0.27
	Total	0.57	0.77	46	2.07	0.25

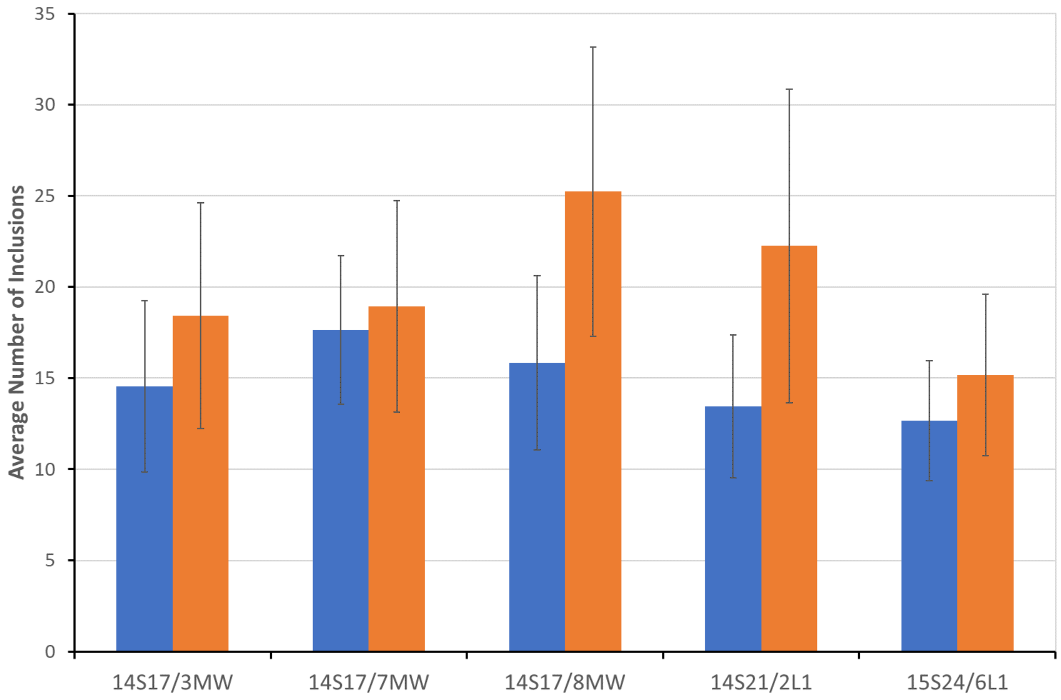

Figure 5-23. Average Number of Inclusions Including those Classified within Stringers.

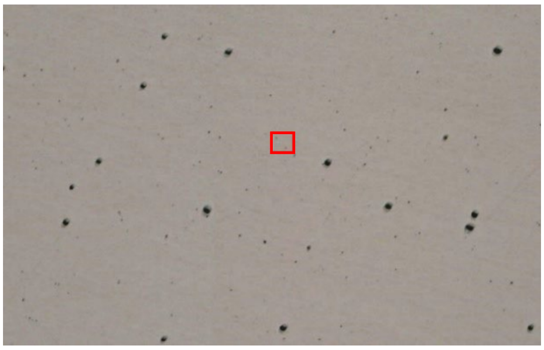

(a) Large Area Illustrating Quantity of Small Inclusions

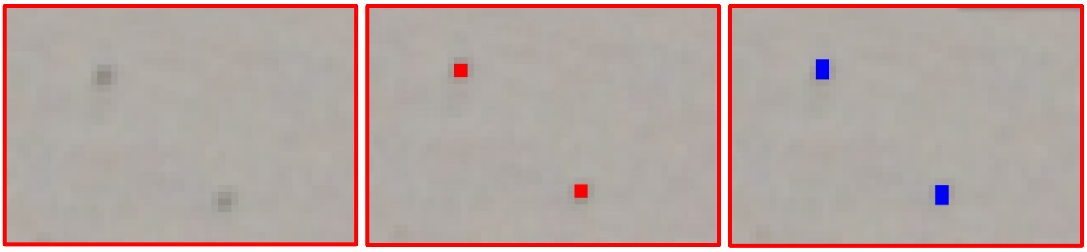

(b) Zoomed in LM Image (c) 2x2 Inclusions Too Small to Be Included (d) 2x3 Inclusions Included as Stringers

Figure 5-24 (a) – (d). Light Microscope Image Illustrating Small Inclusions in 14S21/2L1.

5.5.2. Advantages of Automated Analysis

1. **Large Data Set**

Unlike the chemical-based analysis techniques, this method is able to analyse inclusions over a significantly larger area, encompassing thousands of inclusions.

Another by-product of this is that you could use the information gained from the SEM analysis in Table 4-3 to determine how many of each inclusion type based of their L/W ratio height. Therefore, it would be possible to categorise the samples based the impact factor of these inclusion types instead of just a globular/stringer ratio.

2. **Positional Measurements**

Calculated both the number and size of inclusions and their positions through the thickness of sample. These results can be easily manipulated to calculate different statistics, such as the position of the worst inclusion etc. While this is possible with manual measurements, it would take such a long period of time that it is not feasible.

In continuation of categorising steels based on the impact factor of their inclusion types, this could be further refined to include location data further increasing the value of this categorisation technique.

3. **True Area Measurements**

Measures the true area of the inclusion based off the pixel count, instead of an estimate based of its length and width.

4. **Time Taken to Run Analysis.** For example: -

   i. Automated Inclusion Analysis - Once the sample has been prepared, it takes a maximum of 30 minutes to capture the stitched image, 30 minutes to adjust and format the image, 5 minutes to run the macro and 10 minutes to organise and move the data into excel. This results in analysis taking roughly 1¼ hours per sample.

   ii. Manual Method – Takes a minimum of 5 minutes per field to measure all the inclusions. However, this is normally closer to 10/15 minutes but can be significantly longer depending on number of inclusions and how many ‘grouped’ elongated inclusions there are. To the run the analysis included in this study, even at the most conservative estimate of 5 minutes per field puts this analysis at roughly 7½ hours per sample which does not include the time to capture the image in the first place or run any excel analysis. This increases up to several months to accomplish the full level of analysis if conducted entirely manually using a standard light microscope with an eyepiece graticule.

iii. Semi-Automated Inclusion Assessment – As stated in Chapter 3, it would take roughly 5 minutes to capture each image plus approximately 15 minutes to adjust and format the image to conduct the post processing. This is because essentially the same work is conducted on each individual image that would be conducted on the entire stitched image in the automated method. This meant that each sample was taking roughly 3½ hours to complete, and this was to only complete 10 fields.

iv. Automated EDS Inclusion Assessment – This can vary, but for these samples as a 400-field area was selected and if, conservatively, 5 minutes was spent scanning each field, this would result in roughly a 33½ hour scan time per sample and that is to only scan roughly a 19.6mm^2 area.

v. PDA Analysis – This is the only test that is faster with the standard OES analysis, taking roughly 5 minutes to run before inputting the data into the PDA algorithm. However, while these results look promising, this version of the algorithm is still in need of validation using a much larger data set.

5.5.3. Disadvantages of Automated Analysis

1. **Preparation**

To prepare a 200mm^2 area down to a completely ¼ µm^2 finish was difficult and very time consuming. However, after significant trial and error, the procedure described in Chapter 2 was relatively effective. If the sample was only prepped down to 1µm^2 (Figure 5-25), or any residual scratches that could not be manually removed, would be picked up during thresholding and classified as an inclusion.

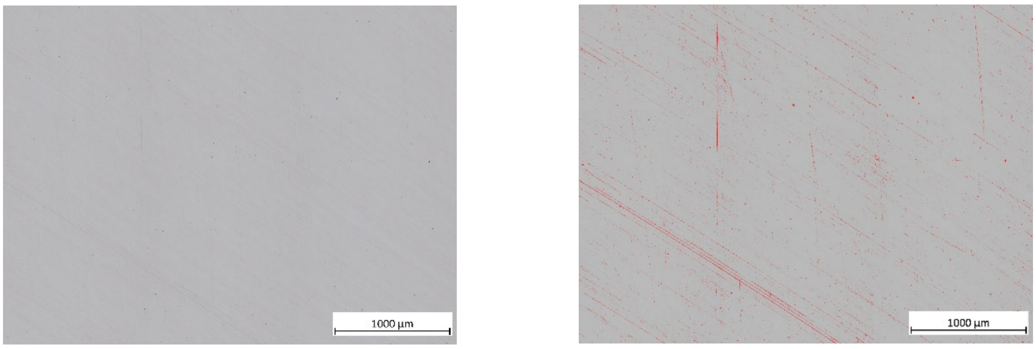

(a) 1µm Scratches **(b) After Greyscale Segmentation**

Figure 5-25. Effect of 1µm Scratches on the Ability to Segment Inclusions in 14S17/2MW

2. **Inclusion Pull-Out** (Figure 5-26 & Figure 5-27).

Normally inclusion pull-out was immediately obvious and resulted in the characteristic scratches that can be seen in Figure 5-27, thus making it easy to re-prepare the sample. However, on occasion these did not occur (Figure 5-26 (a)) and when this happened the manual and the automated technique treated it very differently.

During automated analysis, only the part of the inclusion 'crater' that can be seen in the SEM image (Figure 5-26 (d)) that it shadowed by the light is classed as the inclusion (Figure 5-26 (b)). It is therefore classified as a stringer with an incorrect volume. The manual method instead measures what can be assumed to be the whole 'crater' (Figure 5-26 (c)).

While both these methods would lead to an incorrect area measurement, the manual method should be more accurate as the 'crater' size would be relatively representative of the inclusions area. This is also the most likely cause for the anomaly seen in Figure 5-13. The inclusion population would not be affected in either case, however, as the inclusion would be counted in some shape or form.

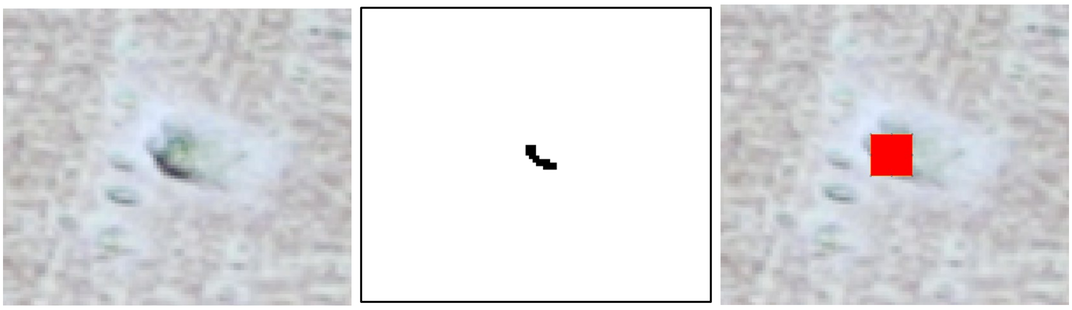

(a) LM Inclusion **(b) Greyscale Segmentation** **(c) Manual Measurement**

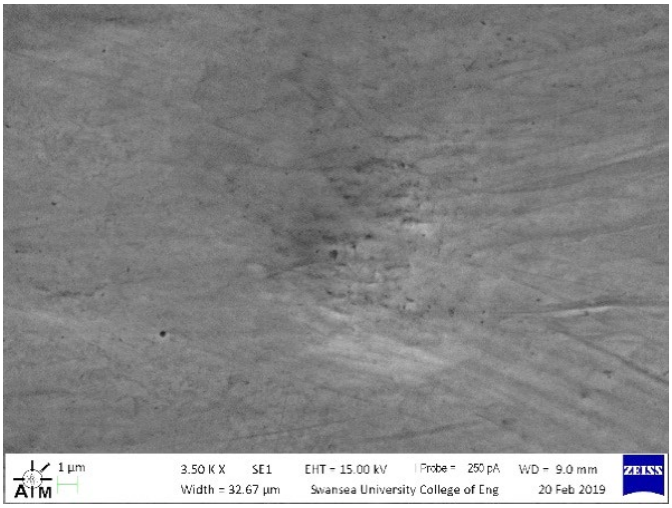

(d) Inclusion in SEM

Figure 5-26 (a)-(d). Inclusion Pull-Out Seen In 14S17/10MW

Figure 5-27. Typical Example of Inclusion Pull-out.

3. Image Stitching

The simplistic nature of the stitching process utilised within AxioVision meant the images were stitched together based on a combination of their stage positions and a 5% image overlap. This resulted in occasions where inclusions were either split in half (Figure 5-28 (a)) or multiplied (Figure 5-28 (c)). Consequently, inclusions would be classified as 2 stringers, with half the area, instead of 1 full globular inclusion. The effect of this would be limited by the fact that the macro could not group these incorrect inclusions into large elongated inclusions. But also, the fact that they were relatively rare, and with so many inclusions measured, the effects should be averaged out.

Manual measurements did have the advantage of being able to correct (Figure 5-28 (b)) or simply ignore these errors as they were found. It would however add a significant amount of time to correct for the Automated analysis. These errors occurred due to the lack of features on the sample surface, meaning that the 'stitching tool' would lead to significant errors (Figure 5-29). However, the new Zeiss ZEN software seems to have overcome these issues, leading to a significantly improved automated stitch.

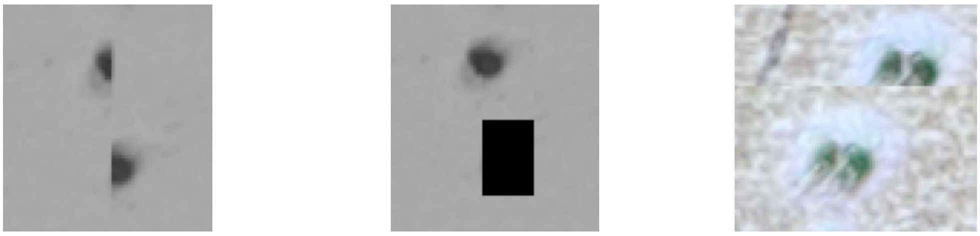

(a) Stitch Separated Inclusion **(b) Reconnected Inclusion** **(c) Duplicated Inclusion**

Figure 5-28 (a) – (c). Examples of Stitching Errors of Inclusions

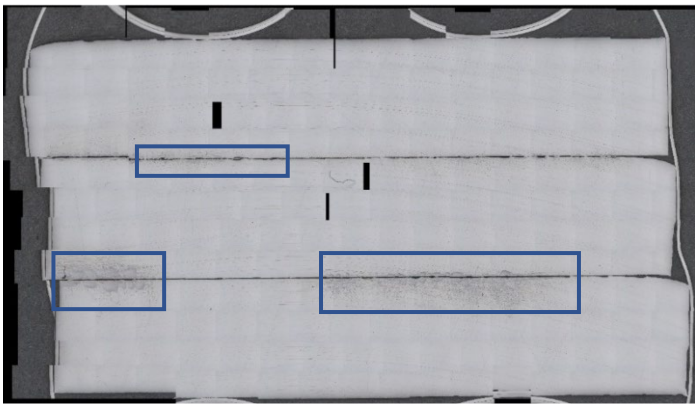

Figure 5-29. Example of Stitching Error with Some Regions of Oil Residue Highlighted.

4. **Surface Dirt** would also be included in the segmentation and therefore classed as an inclusion in the measurements. This dirt could be the result of: -

   i. Dust - Inevitably lands on the surface of the sample after cleaning (Figure 5-30). While the large and obvious dust particles are edited out during post-processing of the images, there are particles that would remain on the sample, but these were rare enough to be averaged out.

   ii. Ethanol Staining (Figure 5-31) – Mitigated by using IPA during polishing, before finally cleaning with Acetone before drying with compressed air while the sample was still wet. Any remnants were hopefully removed using the plasma cleaner.

   iii. Oil Residue (Figure 5-29) – Due to the water-free preparation process. Tended to be removed by cleaning with Acetone and Selvyt cleaning cloths but could be drawn out of cracks between the sample and the Bakelite by the vacuum during the plasma cleaning process. This can also be streaked over the sample surface during cleaning, making imaging impossible and being very difficult to remove.

(a) Surface Dirt Found on 14S17/7MW **(b) Surface Dirt Found on 14S21/2L1**

Figure 5-30 (a) – (b). Some Examples of Surface Dirt

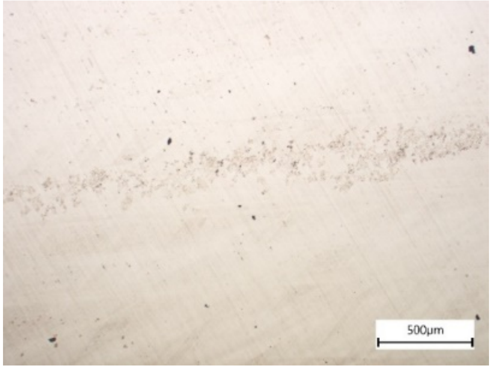

Figure 5-31. Example of Ethanol Staining.

5. Not Factoring 'Nucleated' Inclusions as 1 Inclusion

As mentioned previously, the biggest deviation from the standards is the fact that the automated technique does not classify 'nucleated' inclusions as a single inclusion. This is something that it shares with both the Semi-Automated and the Automated EDS Inclusion Analysis. As shown by the manual measurements (Table 5-4) there was, on average, one of these 'grouped' inclusions somewhere between every and every other field. However, the standard states that these inclusions are 'grouped' because they are assumed to be either traditional stringers, that have been separated during the preparation process, or that they are fractured inclusions that have formed clustered 'stringers.' The EDS analysis on the other hand, as highlighted in Section 4.3.3.5, shows that most of the inclusions are of the 'nucleated' type and therefore consist of complete globular inclusions, that just happen to of nucleated near each other.

The next logical argument is that due to 'nucleated' inclusions proximity to each other, once a void forms, it can coalesce more easily. This leads to the formation of large cracks with a higher stress raising intensity. Nevertheless, the standards contradict this as they state that inclusions should only be grouped if they are within 10µm of each other in the vertical direction - which would affect longitudinal samples as traditional stringers affect transverse sample.

A further point to this could be that the inclusions proximity to each other increases the stress raising effect meaning voids are more likely to form. Research by Courbon *et al* [124] on spherical inclusions in bearing steel shows that there is only an interaction between the Hertzian stress concentration of inclusions if they are separated by a distance that is less than 3 diameters. As the average height of the inclusions for all the samples combined is 5.6µm and all the samples individual average's under 9µm, they are both significantly under 40µm when multiplied by 3. The research does however make some assumptions that are unlikely to be relevant to these samples, due to the use of the Moschovidis extension of the Eshelby method. The key point one is that the inclusions and the matrix are perfectly bonded.

If instead this was treated as a 'worst case scenario', in that the interface between the inclusion and the steel had already broken and formed a void. Atleast for 2 circular holes in an infinitely thin piece of material under uniaxial tension, it has been found that when the distance between these holes is greater than 3 diameters, then the influence between the 2 holes is so weak, it is reasonable to treat them as individual holes [125].

To include either an inclusion diameter-based or the standard's distance-based metric in the automated analysis would however require a custom python-based script (or equivalent). This is because the 'particle analysis tool' in ImageJ that was employed in this study does not offer the flexibility to include this.

6. **Pixel size and magnification.**

5.5.4. Reducing the Effect of Pixel Size

As a result, a short study was carried out on 5 samples (Table 5-5) at 200x and 500x magnifications and compared back to the 100x magnification results. These results can be seen in Figure's 5-32 to 5-34. The key difference between these methods was the number of 710µm fields measured, resulting in increasingly reduced areas as the magnification increased. This was to keep the resulting stitched TIF images below a 2GB file size, so they could be opened by ImageJ.

As can be seen, both the 200x and the 500x magnifications showed significantly higher results for the percentage globular, with the 500x magnification showing results that were most similar to those seen in the chemical-based analysis (Figure 5-35), especially the PDA results.

The Ca treated samples have less inclusions on average, at both the 200x and 500x magnifications. This is because there would less noise etc. in the image that could be classified as inclusions. The non-Ca treated sample shows progressively more inclusions between 100x, 200x and 500x. This is because with each increasing magnification, more stringers are visible and, therefore, included in the calculation.

Table 5-5. Samples for 100x, 200x & 500x Comparative Measurements.

Sample	Ca:S	S	Ca	Sol. Al.	Product
11QS44/7L1	0.06	0.0054	0.0003	0.033	HR P&O
14S17/2MW	0.42	0.0060	0.0025	0.045	HR P&O
14S21/14L2	0.23	0.0066	0.0015	0.035	HR Dry
15S24/9L1	1.50	0.0014	0.0021	0.032	HR Dry
15S24/14L1	0.96	0.0024	0.0025	0.037	HR Dry

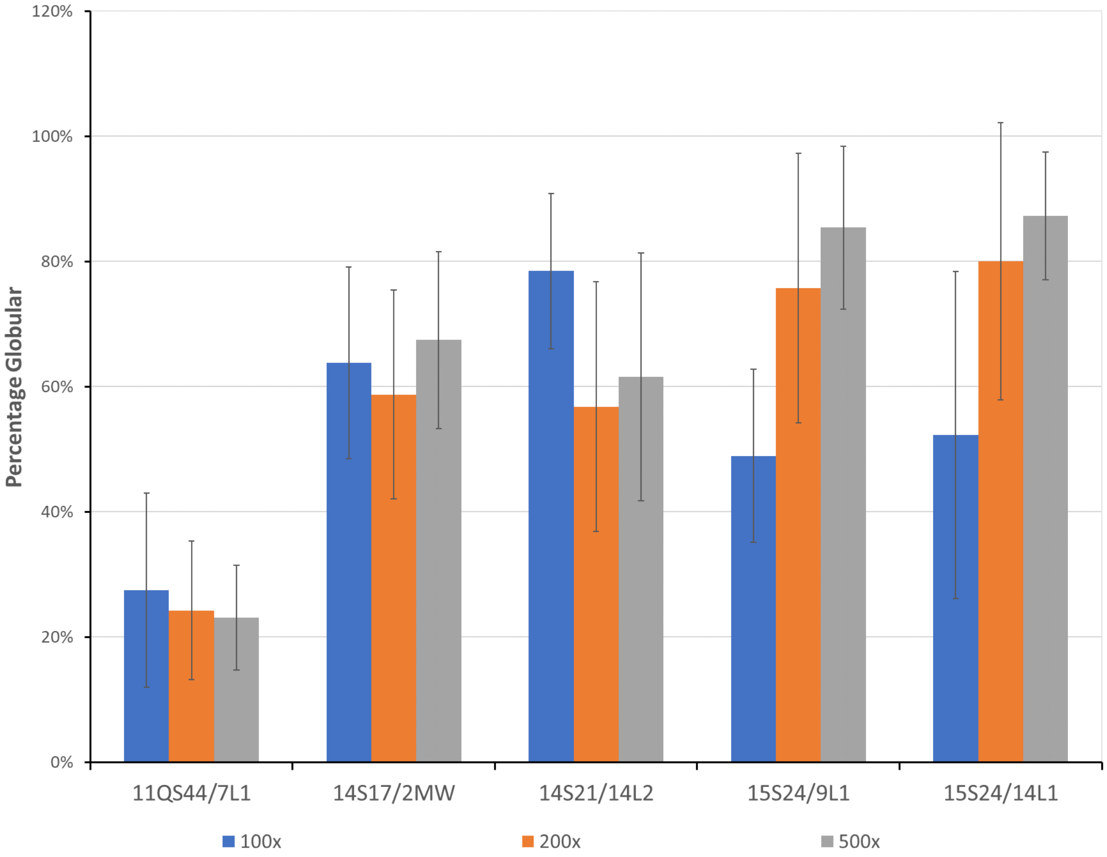

Figure 5-32. Comparison of the Globular Levels at Different Magnifications.

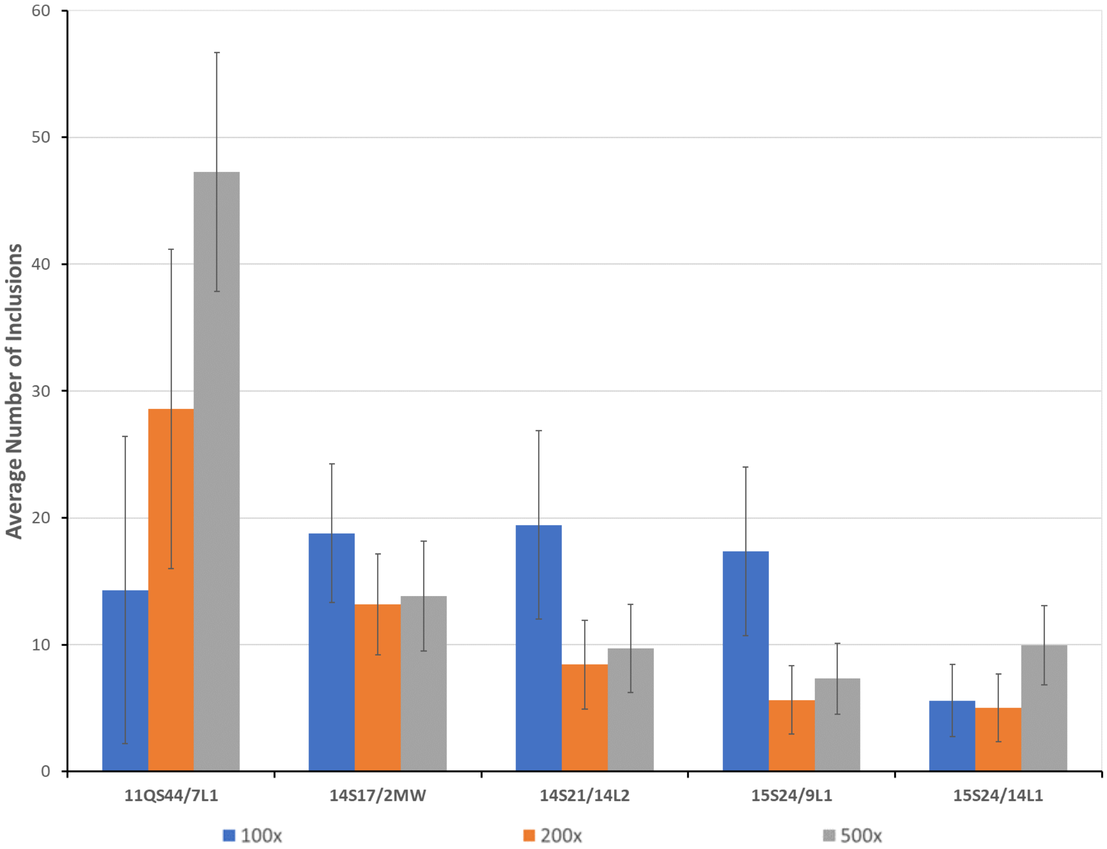

Figure 5-33. Comparison of the Average Number of Inclusions at Different Magnifications.

The decrease in pixel size would naturally lead to smaller average inclusion sizes at the higher magnifications since the calculated area ‘mask’ fits the inclusion more accurately. This effect would then increase as the inclusion size gets larger. While the ramifications of this can been seen in most of the results, the sample 14S21/14L2 in particular shows a dramatic decrease in average inclusion size between 100x and the higher magnifications. This could be the result of the key advantage of the 100x magnification since it images over a much larger area than even the 200x magnification and thus measures significantly more inclusions.

Consequently, it is suggested that future analysis be conducted at 500x magnification in order to limit the impact of pixel size. It is also suggested that when this analysis takes place, several stitched regions should be taken from different areas of the steel sample. This is to ensure that enough inclusions are measured to give accurate results. While this will take longer to capture the initial images, once the setup has been completed once, successive images will be much quicker to capture – e.g. 3 stitched images at 500x would take an hour, compared to roughly 30 minutes for one. The post-imaging analysis will also take less time, since a smaller area will need to be formatted. As a result, it may only take slightly longer than the normal analysis.

Alternatively, the BigTIFF file format could potentially be used since, as a 64-bit file format, it does not suffer the same drawbacks of the 32-bit TIFF format. This would result in larger areas being captured and analysed more quickly but would make the handling of these larger file sizes more resource intensive.

Another unintended advantage of the 500x magnification is that, as seen in Figure 5-36, the chemical structure for larger inclusions is visible. As a result, future analysis, possibly with the help of more advanced machine learning software, could classify inclusion type and structure accurately, without the need to run EDS analysis. Theoretically, as the sections of the inclusion generally have different crystal structures (Table 5-6), the contrast between the areas could be increased by using polarised light. This could potentially even allow for the classification of the different alumina-based systems within the inclusion. This is supported by work conducted by Safaie *et al* [126] using polarised light to determine the grain orientations of a titanium alloy based on the different crystal orientations of the hexagonal titanium.

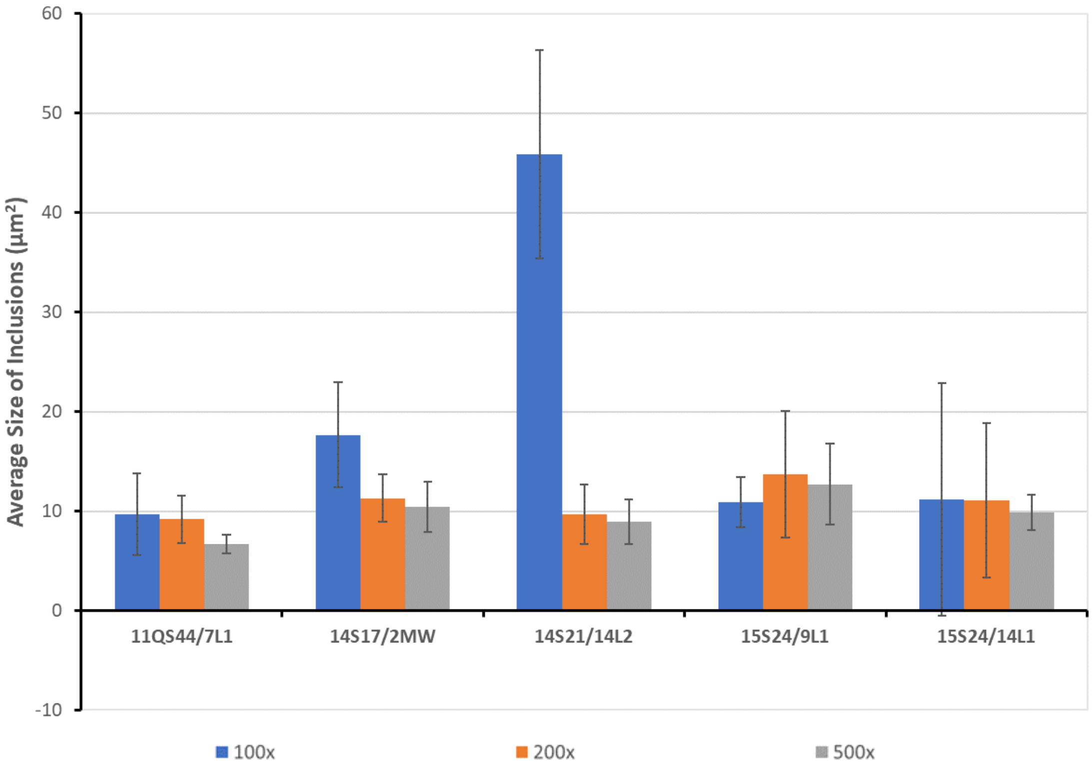

Figure 5-34. Comparison of the Average Size of Inclusions at Different Magnifications

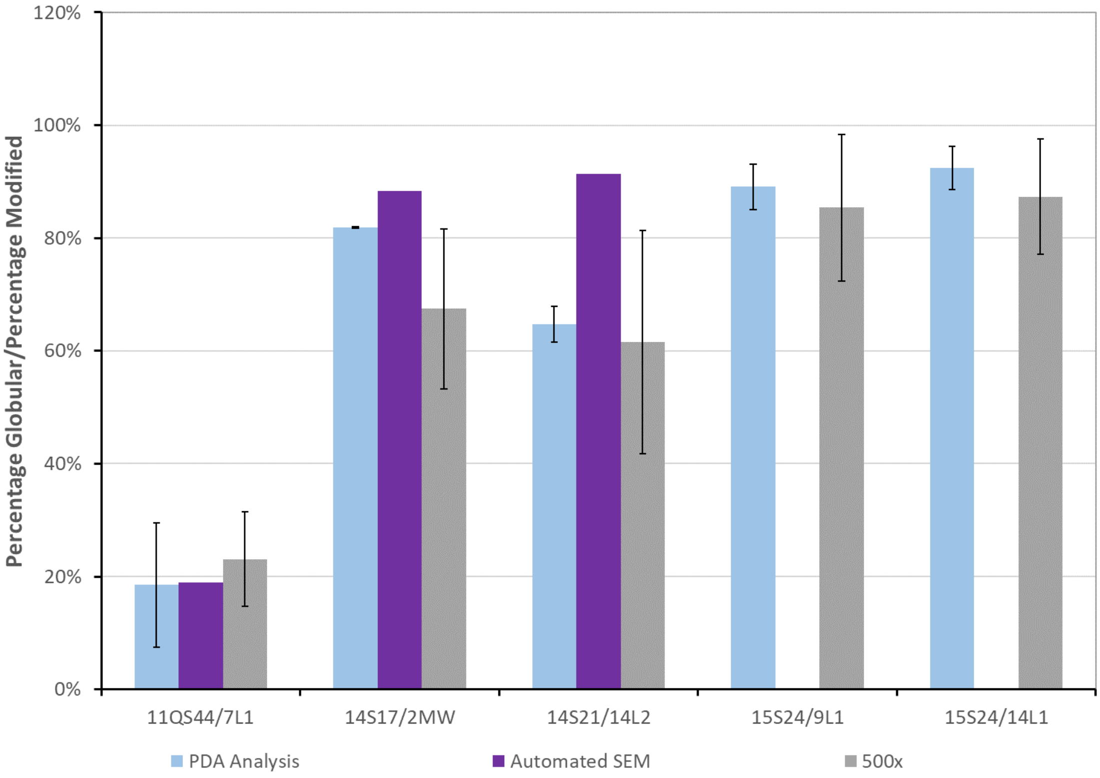

Figure 5-35. Comparison of Chemical Analysis Results to the 500x Magnification Results.

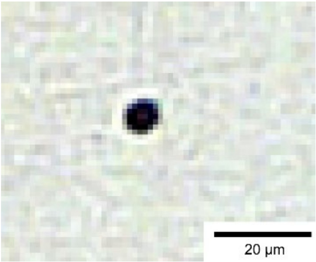

(a) 100x Magnification

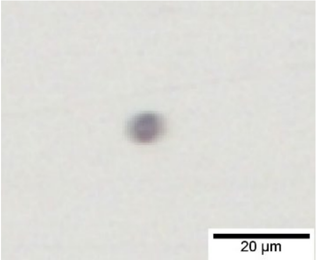

(b) 200x Magnification

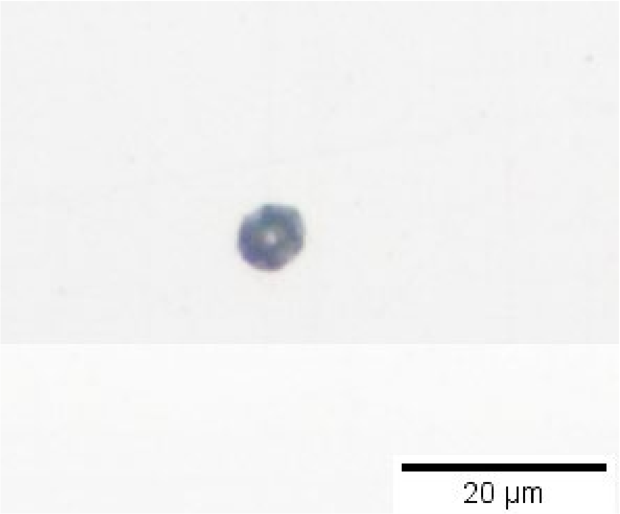

(c) 500x Magnification

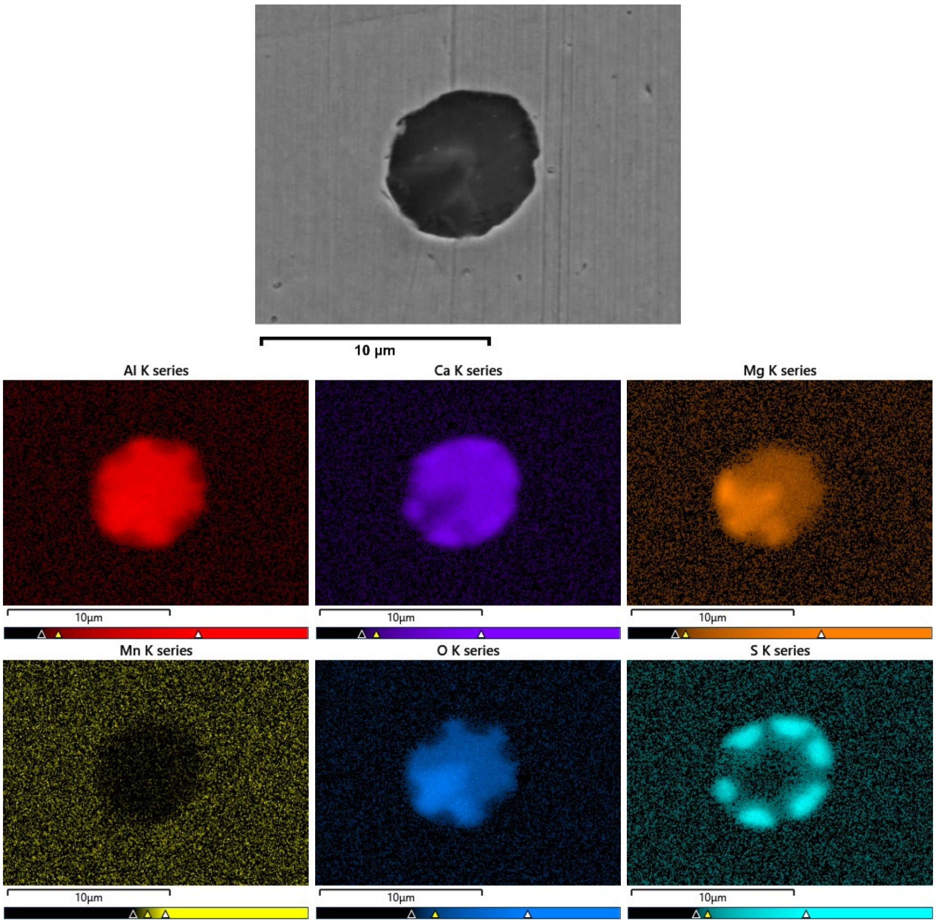

(d) EDS Analysis of Inclusion

Figure 5-36 (a) – (d) ‘Cored’ Inclusion at Different Magnifications and EDS Analysis

Table 5-6. Crystallographic Structures & Spacings for Inclusion Components [34, 127, 128].

System	Structure Type	
Al_2O_3	Hexagonal (Cr_2O_3-type)	
$MgO \cdot Al_2O_3$	Cubic (Spinel)	
$CaO \cdot Al_2O_3$	C_3A	Cubic
	$C_{12}A_7$	Cubic
	CA	Monoclinic
	CA_2	Monoclinic
	CA_6	Hexagonal
CaS	Cubic (NaCl-type)	
MnS	Cubic (NaCl-type)	

5.6. Conclusions

Key Advantages of Automated Inclusion Technique:

1. Measurements include thousands of inclusions over a large area.
2. Positional information on inclusions through the thickness of the material.
3. Measures actual inclusion area instead of an estimation from the length and width.
4. Results can easily be manipulated to show a wide variety of information e.g. worst inclusion size, number of inclusions with most damaging L/W's etc.
5. Significantly faster than most comparable technique and gives significantly more information. Could be easily used in addition to OES-PDA model to give a more comprehensive analysis once the model has been fully validated.
6. Refined technique at 500x magnification has the potential to classify based on their internal structure which is visible at this magnification in inclusions. This classification can theoretically be improved by using polarised light.

Key Disadvantages:

1. Difficult to prepare 200mm^2 area down to required 0.25μm finish.
2. Inclusion pull-out a problem but mitigated with refined preparation technique.
3. Simplistic stitching process can result in splitting/duplicating of inclusions. Effects appears to be lessened if using more up-to-date stitching software but should be average out due to number of inclusions measured.
4. Risk of surface dirt effecting results. Impact reduced by correct preparation, careful editing of images and averaging out.
5. Not including 'grouped' inclusions. However, the impact of these 'grouped' inclusions is likely less than the standard implies, as a significant proportion of the potential 'grouped' inclusions are neither fractured inclusion clusters nor elongated inclusions. Future work could be conducted on the impact of these inclusions and potentially incorporated into the analysis.

6. Large pixel size combined with relatively low magnification leading to lower than predicted percentage globular levels and can lead to incorrect inclusions identification. As result, it has been suggested that future studies are conducted at 500x magnification, via a revised macro designed to incorporate this. It would then include several stitched images taken at different positions in the steel sample, giving a greater representation of the full sample.

Chapter 6

Conclusions & Future Work

6.1. Introduction

The chapters within this project contain both data and analysis that should aid in the future development of Ca treated steels, both from a steel manufacturing and quality control standpoint. As a result, whilst not covering all the conclusions from the 2 results chapters, the most significant conclusions are highlighted in the following sections before focussing on their industrial impacts. This chapter also presents suggestions for further work for anyone wishing to continue this analysis.

6.2. Mechanical & Microstructural Analysis of AHSS Automotive Steel

1. Between Ca:S of 0.23 and 1.5 and Ca:Al of 0.039 and 0.074, the Ca treatment has been shown to be effective at producing the required mechanical properties in the steel by modifying a significant proportion of both the sulphide and alumina-based inclusions into 'globular' inclusions.

2. The percentage number of 'globular' inclusions in never likely to reach 100% due to a number of different Ca modified 'stringers' forming.

3. 2 key types of globular inclusion formed out of the melt:

   I. 'Cored' - Sulphide shell nucleating on pre-existing alumina-based inclusion.
   II. 'Ying-Yang' - Formed from the collision of 2 other inclusions.

4. 6 types of stringer inclusion form:

   I. 'Classic' – Alumina-based core with elongated MnS 'shell'
   II. 'Fractured' – Large inclusion that has fractured upon rolling
   III. 'Facetted' – Sulphide shell forms on stringer shaped core
   IV. 'Nucleated' – 2 or more globular inclusions nucleate within the distance defined by the standards
   V. 'Partially-Modified – Insufficient CaS has solid solution strengthened MnS to prevent partial elongation
   VI. 'Sulphide-based' – 2 subtypes: purely (Ca,Mn)S which partially elongates
   purely MnS which significantly elongates

5. Increasing the S level from 0.0014% wt. up to a maximum of 0.0079% wt. has led to an increase in both the size and number of inclusions within steel. This

increase however showed no impact on final mechanical properties that can be directly associated with S level due to the fact that the inclusions close to the surface were considerably smaller than the critical inclusion diameter of 10µm. If inclusions were observed that were any larger, they tended to be both globular in nature and positioned nearer the centre of the steel where they would be less detrimental to the steel's properties.

6. Possibility of non-Ca treated samples having similar tensile properties due to size and population density of elongated inclusions. It did, however, show significantly worse hole expansion properties than almost all the Ca treated samples. More analysis will be needed to confirm this as only 1 comparable sample was tested.
7. Grain orientation is the key parameter affecting change in properties in longitudinal and transverse directions instead of the inclusion population.

6.3. Assessment of Automated Inclusion Analysis

Main Advantages: -

1. Measures both inclusion population, actual size and position within sample.
2. Potential to categorise inclusions more thoroughly based of their L/W
3. Results can be easily engineered to user requirements.
4. Significantly faster than equivalent techniques.
5. 500x has the capability of categorising inclusions based off their chemical structure which could possibly be enhanced using polarised light.

Main Disadvantages: -

1. Difficult to prepare samples efficiently.
2. Not including 'grouped' inclusions.
3. Large pixel size and relatively low magnification. As a result, all future analysis of this grade should be conducted at 500x magnification and incorporate several stitched areas. In general, the magnification/resolution should be based off the number of pixels that make up the narrowest region of the inclusion and not based on the number of pixels that make up the inclusion as a whole.

6.4. Industrial Impact of Research

1. Deepens the understanding of the effect of Ca-treatment on sulphide-based inclusions, allowing for the production of steel grades that fulfil the customers mechanical property requirements even if a lower than expected Ca:S is achieved due to the volatile nature of the Ca addition process.
2. Potential indicator to industry on the amount of Ca to be added to the steel based off the steels S and Al levels (and resulting Ca:S and Ca:Al) to ensure that mechanical properties are achieved while also preventing the negative effects of adding an excessive amount of Ca. While theoretically possible, it must be treated on a case by case basis and depends on whether the steel has gone through any further processes (e.g. chemical reheating) after the final chemical analysis was taken prior to Ca treatment.
3. Created a reliable, reproducible, and auditable method of analysing inclusions that can be conducted in a much more time efficient manner. While not ideal, this method could also be applied to any traditional microscope with very little modification. The minimum modification that would be suggested is the installation of a micrometre to control the stage movement and therefore allow for a more accurate stitching of the final image.
4. The automated method is not limited to the analysis of successful Ca modification and can be applied to any analysis requiring the number, size, shape & position of features with a different greyscale (i.e. pores/inclusions etc.) potentially saving Tata Steel both time and money in the future.
5. Provides data that supports the analysis provided by the OES-PDA model developed by Whiteside *et al* and while not providing sufficient information to fully validate the model, the data produced within this study encourages Tata Steel to pursue this line of research.

6.5. Suggestions for Future Work

1. Conduct analysis on samples with more samples with a Ca:S < 0.23 to see lower limit of Ca:S where mechanical properties are still achieved.
2. Test samples with a Ca:S > 1.5 in order to determine upper limit of Ca additions.
3. Include O content in all future analysis to investigate how that affects inclusion population and size in combination with Ca:S.
4. Conduct mechanical testing on comparable non-Ca treated samples.
5. Analyse how grain size affects HEC.
6. Conduct analysis at 500x magnification to investigate whether effects of S content on inclusion size and population are still accurate.
7. Analyse proximity of inclusions and the resulting impact on stress concentrations, especially in comparison to a single large inclusion.
8. Incorporate the results from suggestion 6 & 7 into an updated macro/python-based script.
9. Conduct polarised light analysis to test the viability of its ability to categorise inclusions.

Chapter 7

References

[1] Millman MS. Secondary steelmaking developments in British Steel. Ironmak Steelmak. 1999; 26(3):169–75.

[2] Meyer K, Dings J. CO_2 Emissions from New Cars. European Federation for Transport and Environment. 2008.

[3] Llewellyn DT. Steels: Metallurgy and Applications. Second. Oxford: Butterworth-Heinemann Ltd.; 1994.

[4] Pielet HM, Tsai HT, Gass RT. Characterization of Inclusions in TiSULC Steels from Degasser to Mold. ISSTech. Indianapolis, IN: Iron & Steel Society; 2003.

[5] Tiekink WK. Al_2O_3 in Steel and Its Transformation With Calcium. . Technical University of Delft; 2012.

[6] Kiessling R, Nordberg H. Influence of Inclusions on Mechanical Properties of Steel. Prod Appl Clean Steels. Balatonfüred: The Iron and Steel Institute; 1970; 179–85.

[7] Brahma D, Boom R. Fundamentals of Steelmaking Metallurgy. Hertfordshire: Prentice Hall International (UK) Ltd.; 1993.

[8] Tähtinen K, Väinölä R, Sandholm R. Ladle Injection–A way to continuously cast aluminium-killed steels for billets at Ovako. Scaninject II. Luleå, Sweden; 1980.

[9] Lis T. Modification of Oxygen and Sulphur Inclusions in Steel by Calcium Treatment. Metalurgija. 2009; 48(2):95–8.

[10] Ototani T. Calcium Clean Steel. Berlin: Springer-Verlag; 1986.

[11] Tomita Y. Effect of desulphurization and calcium treatments on the inclusion morphology of 0.4C-Cr-Mo-Ni steel. J Mater Sci. 1994; 29(11):2873–8.

[12] Voort GF Vander. Results of Interlaboratory Test Programs to Assess the Precision of Inclusion Ratings by Methods A , C and D of ASTM E45. 2017; 22(May):2016–7.

[13] Sims CE. Iron and Steel Division - The Nonmetallic Constituents of Steel. Trans AIME. 1959; (215).

[14] Holappa L, Wijk O. Chapter 1.7 - Inclusion Engineering. In: Treatise on Process Metallurgy - Industrial Processes. Oxford: Elsevier; 2014; bk. 3, .

[15] Costa E Silva ALV Da. Non-metallic inclusions in steels - Origin and control. J Mater Res Technol. Brazilian Metallurgical, Materials and Mining Association; 2018; 7(3):283–99.

[16] Kazakov AA. Nonmetallic Inclusions in Steel – Origin, Estimation, Interpretation and Control. Microscopy & Microanalysis. Columbus, Ohio; 2016.

[17] Kohn A. The Use of Radioisotopes in Metallurgical Research and Industry. Metall Rev. 1958; 3(1):143–201.

[18] Poirier J. A review: influence of refractories on steel quality. Metall Res Technol. 2015; 112(4):410.

[19] Kiessling R. Non-Metallic Inclusions in Steel (Part III). The Origin and Behaviour of Inclusions and Their Influence on the Properties of Steels. London: The Iron and Steel Institute; 1968.

[20] Kaushik P, Pielet H, Yin H, Kaushik P, Pielet H, Yin H. Inclusion characterisation – tool for measurement of steel cleanliness and process control : Part 1. 2013; 9233.

[21] ISO. 4967-1979 (E). Determination of Content of Non-Metallic Inclusions - Micrographic Method Using Standard Diagrams. 1979.

[22] Holappa L. Chapter 1.6 - Secondary Steelmaking. In: Treatise on Process Metallurgy - Industrial Processes. Oxford: Elsevier; 2014; bk. 3, .

[23] Zhang L, Thomas BG. State of the Art in Evaluation and Control of Steel Cleanliness. ISIJ Int. 2003; 43(3):291–7.

[24] Wauby PE. Some Aspects of the Formation of Inclusions During Deoxidation. In: Pickering FB, editor. Inclusions. London: The Institute of Metallurgists; 1979; p. 13–28.

[25] Muan A, Osborn EF. Phase Equilibria Among Oxides in Steelmaking. Massachusetts: Addison-Wesley Publishing Company, Inc.; 1965.

[26] Zhang L, Pluschkell W, Thomas BG. Nucleation and Growth of Alumina Inclusions During Steel Deoxidation. 85th Steelmaking Conference. Nashville, TN: ISS; 2002.

[27] Tiekink WK, Pieters A, Hekkema J. Al_2O_3 in Steel: Morphology Dependent Treatment. Iron Steelmak. 1994; 39–41.

[28] Pickering FB. The Constitution of Non-Metallic Inclusions in Steel. In: Pickering FB, editor. Inclusions. London: The Institute of Metallurgists; 1979; p. 73–93.

[29] Zheng L, Malfliet A, Wollants P, Blanpain B, Guo M. Effect of Interfacial Properties on the Clustering of Alumina Inclusions in Molten Iron. 6th International Congress on the Science and Technology of Steelmaking. Beijing,China: The Chinese Society for Metals; 2015.

[30] Yin H, Shibata H, Emi T, Suzuki M. "In-situ" Observation of Collision, Agglomeration and Cluster Formation of Alumina Inclusion Particles on Steel Melts. ISIJ Int. 2008; 37(10):936–45.

[31] Sakalli E. Nozzle Blockage in Continuous Casting of Al-Killed SAE 1006 and SAE 1008 Steel Grades in Iskenderun Iron and Steel Works. The Department of Metallurgical and Materials Engineering. Ankara: The Middle East Technical University; 2004.

[32] Robinson SW, Martin IW, Pickering FB. Formation of alumina in steel and its dissemination during mechanical working. Met Technol [Internet]. 1979; 6(1):157–69.

[33] Carraro F, Vozniuk O, Calvillo L, Nodari L, Fontaine C La, Cavani F, et al. In operando XAS investigation of reduction and oxidation processes in cobalt and iron mixed spinels during the chemical loop reforming of ethanol. J Mater Chem A. 2017; 5(39):20808–17.

[34] Kiessling R, Lange N. Non-Metallic Inclusions in Steel (Part II). Inclusions Belonging To The Systems MgO-SiO_2-Al_2O_3, CaO-SiO_2-Al_2O_3 and Related Oxide Systems. Sulphide Inclusions. London: The Iron and Steel Institute; 1966.

[35] Mendez J, Gómez A, Capurro C, Donayo R, Cicutti C. Effect of Process Conditions on the Evolution of MgO Content of Inclusions During the Production of Calcium Treated, Aluminum Killed Steels. 8th Int Conf Clean Steel. 2012; (November 2015).

[36] Yang S, Li J, Zhang L, Peaslee K, Wang Z. Behaviour of $MgO \cdot Al_2O_3$ Based Inclusions in Alloy Steel During the Refining Process. Metall Min Ind. Central Iron and Steel Research Institute; 2010; 2(2):87–92.

[37] Deng Z, Zhu M, Zhong B, Sichen D. Attachment of Liquid Calcium Aluminate Inclusions on Inner Wall of Submerged Entry Nozzle during Continuous Casting of Calcium-Treated Steel. ISIJ Int [Internet]. 2014; 54(12):2813–20. Available from: https://www.jstage.jst.go.jp/article/isijinternational/54/12/54_2813/_article.

[38] Abraham S, Bodnar R, Raines J, Wang Y. Inclusion engineering and metallurgy of calcium treatment. J Iron Steel Res Int [Internet]. Springer Singapore; 2018; 25(2):133–45. Available from: https://doi.org/10.1007/s42243-018-0017-3.

[39] Turkdogan ET. Fundamentals of Steelmaking. Cambridge: The Institute of Materials; 1996.

[40] Hägg G, Sucksdorff I. Die Kristallstruktur von Troilit und Magnetkies. Zeitschrift für Phys Chemie. 1933; B(22):444–52.

[41] Mann GS, Vlack LH Van. FeS-MnS Phase Relationships in the Presence of Excess Iron. Metall Trans B. 1976; 7(3):469–75.

[42] Nayak H, Agrawal CM, Pandey KS. Effect of Manganese Addition and the Initial Aspect Ratios on the Densification Mechanism/S and Barrelling In Sintered Hyper Eutectoid P/M Steel Preforms During Hot Upset Forging . Am J Eng Res. 2014; 3(06):323–39.

[43] Goldbeck OK von. Iron - Binary Phase Diagrams. Berlin: Springer; 1982.

[44] Brimacombe JK. The challenge of quality in continuous casting processes. Metall Mater Trans B. 1999; 30(4):553–66.

[45] Shao X, Wang X, Ji C, Li H, Cui Y, Zhu G. Morphology, size and distribution of MnS inclusions in non-quenched and tempered steel during heat treatment. Int J Miner Metall Mater. 2015; 22(5):483–91.

[46] Sims CE, Dahle FB. The effect of aluminum on the properties of medium carbon cast steel. Trans. A.F.A. 1938; 46:65–132.

[47] Fujiwara J. Cutting Mechanism of Sulfurized Free-Machining Steel. In: Kazmiruk V, editor. Scanning Electron Microscopy [Internet]. InTechOpen; 2012. Available from: https://www.intechopen.com/books/scanning-electron-microscopy/cutting-mechanism-of-sulfurized-free-machining-steel.

[48] Yoshioka T, Shimamura Y, Karasev A, Ohba Y, Jönsson PG. Mechanism of a CaS Formation in an Al-Killed High-S Containing Steel during a Secondary Refining Process without a Ca-Treatment. Steel Res Int. 2017; 88(10):1700147.

[49] Verma N, Pistorius PC, Fruehan RJ, Potter MS, Oltmann HG, Pretorius EB. Calcium Modification of Spinel Inclusions in Aluminum-Killed Steel: Reaction Steps. Metall Mater Trans B. 2012; 43(4):830–40.

[50] Förster E, Klapdar W, Richter H, Rommerswinkel HW, Spetzler E, Wendorff J. Deoxidation and Desulphurisation by Blowing of Calcium Compounds into Molten Steel and Its Effects on the Mechanical Properties of Heavy Plates. Stahl und Eisen. 1974; 94(11):474–85.

[51] Leung C-H, Vlack LH Van. Solubility Limits in Binary (Ca,Mn) Chalcogenides. J Am Ceram Soc. 1979; 62(11–12):613–6.

[52] Leung CH, Vlack LH Van. Solution and Precipitation Hardening in (Ca, Mn) Sulphides and Selenides. Metall Trans A, Phys Metall Mater Sci. 1981; 12 A(6):987–91.

[53] Piao R, Lee H-G, Kang Y-B. Activity Measurement of the CaS–MnS Sulfide Solid Solution and Thermodynamic Modeling of the CaO–MnO–Al_2O_3–CaS–MnS–Al_2S_3 System. ISIJ Int [Internet]. 2013; 53(12):2132–41.Available from: http://jlc.jst.go.jp/DN/JST.JSTAGE/isijinternational/53.2132?lang=en&from=CrossRef&type=abstract.

[54] Faulring GM, Farrell JW, Hilty DC. Steel Flow Through Nozzles: Influence of calcium. In: Chemical and Physical Interactions During Transfer Operations. Warrendale: Iron & Steel Society of AIME; 1983; p. 57–66.

[55] Fruehan RJ. Future Steelmaking Technologies and the Role of Basic Research. Metall Mater Trans B. 1997; 28(5):743–53.

[56] Holappa L. Inclusion Control for Castability of Resulphurized Steels. ISS Steelmaking Conference. Warrendale, USA; 2001.

[57] Zhang LF, Thomas BG. Inclusions in Continuous Casting of Steel. XXIV Natl Steelmak Symp. Morelia, Mich, Mexico; 2003; 26–8.

[58] Janke D, Ma Z, Valentin P, Heinen A. Improvement of Castability and Quality of Continuously Cast Steel. ISIJ Int [Internet]. 2000; 40(1):31–9. Available from: http://joi.jlc.jst.go.jp/JST.Journalarchive/isijinternational1989/40.31?from=CrossRef.

[59] Holappa L, Hämäläinen M, Liukkonen M, Lind M. Thermodynamic Examination of Inclusion Modification and Precipitation from Calcium Treatment to Solidified Steel. Ironmak Steelmak [Internet]. 2003; 30(2):111–5. Available from: http://www.tandfonline.com/doi/full/10.1179/030192303225001748.

[60] Kumar B, Mishra S, Rao MB V, Roy GG. Experimental investigation of recovery and efficiency of calcium addition through cored wire in steel melt at Visakhapatnam Steel Plant. Ironmak Steelmak [Internet]. 2017; 1–9. Available from: https://www.tandfonline.com/doi/full/10.1080/03019233.2017.1405147.

[61] Maciejewski J. The Effects of Sulfide Inclusions on Mechanical Properties and Failures of Steel Components. J Fail Anal Prev. 2015; 15(2):169–78.

[62] Barbaro FJ, Jones CA, Edwards PD, Williams JG, Wilson PR. Sulphide Inclusions in Low Manganese Steels. 3rd International Conference on Thermomechanical Processing of Steels. Padua, Italy: Italian Association for Metallurgy; 2008.

[63] Kiessling R. Non-Metallic Inclusions in Steel (Part V). London: The Institute of Metals; 1989.

[64] Boussard P, Szezesny R, Pellicani F, Gueussier A. Resulfurized Steels for Improved Machinability with Calcium Treatment. First International Calcium Treatment Symposium. Glasgow, Scotland: The Institute of Metals; 1988.

[65] Joyant M, Gatellier C. IRSID Report, PCM-RE, 1108. Maizières-lès-Metz, France; 1984.

[66] Gaye H, Gatellier C, Nadif M, Riboud PV, Saleil J, Faral MM. Slags and Inclusions Control in Secondary Steelmaking. Clean Steel Conference. Balatonfüred, Hungary; 1986.

[67] Gaye H. Chapter 3, Inclusion Formation in Steels. In: Cramb A, editor. The Making, Shaping and Treating of Steel, Casting Volume. 11th Ed. Pittsbrugh, PA: AISE; 2003.

[68] Gaye H, Lehmann J, Rocabois P, Ruby-Meyer F. Slag modelling and Industrial applications. Proceedings 6th International Conference on Molten Slags, Fluxes and Salts; 12-17th June 2000. Stockholm-Helsinki: High Temperature Materials and Processes, Vol. 20, No. 3-4; 2001.

[69] Harvey DS. Rev Metall. 1986; 83(5):433–40.

[70] Gatellier C, Gaye H, Lehmann J, Pontoire JN, Riboud PV. Physico-chemical aspects of the behaviour of inclusions in steels. Steel Res. 1993; 64(1):87–92.

[71] Wang Y, Sridhar S, Valdez M. Formation of CaS on Al_2O_3-CaO inclusions during solidification of steels. Metall Mater Trans B Process Metall Mater Process Sci. 2002; 33(4):625–32.

[72] Jehan M. Calcium Metal Granules Injection in Steel Ladles - Advantages, Technological and Metallurgical Conditions and Results in Free Silicon and Special Steels. Scaninject IV - Part 2. Luleå, Sweden; 1986.

[73] Herbert A, Notman GK, Morris D, Knowles S, Jemson C. Experiences with Powder and Wire Injection at British Steel Corporation, Lackenby Works, Basic Oxygen Steelmaking Plant. Scaninject IV - Part 2. Luleå, Sweden; 1986.

[74] Tomita Y. Effect of Desulphurization and Calcium Treatments on the Inclusion Morphology of 0.4C-Cr-Mo-Ni Steel. J Mater Sci. 1994; 29(11):2873–8.

[75] Sponseller DL, Flinn RA. Iron and Steel Division - The Solubility of Calcium in Liquid Iron and Third-Element Interaction Effects. Trans Met Soc AIME. 1964; 230:876–88.

[76] Bannenburg N, Harste K, Bode O. Melting Behaviour of Cored Wire During Injection. Scaninject VI. Luleå, Sweden: MEFOS; 1992.

[77] Arreola-Herrera R, Cruz-Ramírez A, Rivera-Salinas JE, Romero-Serrano JA, Sánchez-Alvarado RG. The effect of non-metallic inclusions on the mechanical properties of 32 CDV 13 steel and their mechanical stress analysis by numerical simulation. Theor Appl Fract Mech [Internet]. Elsevier; 2018; 94(January):134–46. Available from: https://doi.org/10.1016/j.tafmec.2018.01.013.

[78] Costa E Silva ALV Da. The effects of non-metallic inclusions on properties relevant to the performance of steel in structural and mechanical applications. J Mater Res Technol [Internet]. Brazilian Metallurgical, Materials and Mining Association; 2019; 8(2):2408–22. Available from: https://doi.org/10.1016/j.jmrt.2019.01.009.

[79] Knott J. Fundamentals of Fracture Mechanics. London: Butherworths; 1973.

[80] Srivastava A, Ponson L, Osovski S, Bouchaud E, Tvergaard V, Needleman A. Effect of inclusion density on ductile fracture toughness and roughness. J Mech Phys Solids [Internet]. Elsevier; 2014; 63(1):62–79. Available from: http://dx.doi.org/10.1016/j.jmps.2013.10.003.

[81] Kiessling R. The Influence of Non-Metallic Inclusions of the Properties of Steel. J Met. 1969; 21:47–54.

[82] Roesch L, Henry G, Endier M, Plateau J. Mem Sci Rev Met. 1966; 63:927–40.

[83] Wu M, Fang W, Chen R, Jiang B, Wang H, Liu Y, et al. Mechanical anisotropy and local ductility in transverse tensile deformation in hot rolled steels: The role of MnS inclusions. Mater Sci Eng A Struct Mater Prop Microstruct Process [Internet]. Elsevier B.V.; 2019; 744(September 2018):324–34. Available from: https://www.sciencedirect.com/science/article/pii/S0921509318317052?dgcid=rss_sd_all.

[84] Bartosiaki BG, Pereira JAM, Bielefeldt WV, Vilela ACF, Aníbal J, Pereira M, et al. Assessment of inclusion analysis via manual and automated SEM and total oxygen content of steel. J Mater Res Technol [Internet]. Korea Institute of Oriental Medicine; 2015; 4(3):235–40. Available from: http://dx.doi.org/10.1016/j.jmrt.2015.01.008.

[85] Atkinson H V., Shi G. Characterization of inclusions in clean steels: A review including the statistics of extremes methods. Prog Mater Sci. 2003; 48(5):457–520.

[86] Auclair G, Daguier P. Appropriate Techniques for Internal Cleanliness Assessment. Bear Steel Technol. 2002; ASTM STP 1:101–12.

[87] Irving B. Methods for Assessment of Nonmetallic Inclusions in Steel. Ironmak Steelmak. 1994; 21(3):174–81.

[88] Alatarvas T. Evolution of inclusion population in calcium treated ultra-high strength steels : novel applications of sample data treatment. University of Oulo; 2018.

[89] Net VB, Activex A. Method of Automatic Characterization of Inclusion Population by a SEM-FEG / EDS / Image. 2006; 41(1):1–3.

[90] Kurtuldu H, Durkaya G, Kaplan H, Çelebi T, Dikilitaş F, Yazaroğlu O. Fully Automated Analysis of Non-Metallic Inclusions in Steel According to EN10247 and Focus Effect. 2016; 428–30.

[91] Pande MM, Guo M, Dumarey R, Devisscher S, Blanpain B. Determination of Steel Cleanliness in Ultra Low Carbon Steel by Pulse Discrimination Analysis-Optical Emission Spectroscopy Technique. 2011; 51(11):1778–87.

[92] Meilland R, Irsid LD. Rapid characterization of inclusionnary cleanliness in steels by PDA-OES mapping. 2002.

[93] Nastasi G, Wester R, Colla V, Noll R. Determining inclusion size distributions from OES / PDA data. 2013; (March).

[94] Whiteside IRC, Meilland R, Ruby-Meyer F, Tusset V, Didriksson R, Bengtson A, et al. Fast characterisation of steel cleanness by advanced mathematical analysis of spark and laser source optical emission data. European Commission - Technical Steel Research. 2006.

[95] Whiteside I, Bryce R. Secondary Steelmaking Clean Steel Developments. Internal Communication. Tata Steel. 2011.

[96] Zhang L. Indirect Methods of Detecting and Evaluating Inclusions in Steel-A Review.pdf. J Iron Steel Res Int. 2006; 13(4):1–8.

[97] BS. EN 10002-1:2001. Metallic Materials - Tensile Testing - Part 1: Method of Test at Ambient Temperature. British Standards Institute; 2001.

[98] ISO. 16630:2009. Metallic Materials - Sheet and Strip - Hole Expanding Test. International Organisation for Standardisation; 2009.

[99] ASTM. E45-87. Standard Practice for Determining the Inclusion Content of Steel. American Society for Testing and Materials; 1987.

[100] BS. EN 10247:2007. Micrographic Examination of the Non-Metallic Inclusion Content of Steels Using Standard Pictures. British Standards Institute; 2007.

[101] Walker J. Effects of Cleanliness and Additions on the Tensile and Fatigue Performance of AHSS & UHSS Steels for Automotive Under Body Applications. Engineering. Swansea: Swansea University; 2013.

[102] BS. EN ISO 643-2003. Steels — Micrographic Determination of the Apparent Grain Size. British Standards Institute; 2003.

[103] Surface Roughness Profile [Internet]. [cited 31 Jan 2019]. Available from: https://static4.olympus-ims.com/data/Image/knowledge/roughness/ols4100_roughness_parameter_ra.en.jpg?rev=89AD.

[104] Pande MM, Guo M, Dumarey R, Devisscher S, Blanpain B. Determination of Steel Cleanliness in Ultra Low Carbon Steel by Pulse Discrimination Analysis-Optical Emission Spectroscopy Technique. ISIJ Int [Internet]. 2011; 51(11):1778–87. Available from: http://joi.jlc.jst.go.jp/JST.JSTAGE/isijinternational/51.1778?from=CrossRef.

[105] Evans P. Hole Expansion Overview. Internal Communication. Tata Steel. 2010.

[106] McCulloch JA. Microstructural and Product Performance Assessment of Advanced High Strength Steels. Swansea University; 2018.

[107] Nolze G. Image distortions in SEM and their influences on EBSD measurements. 2007; 107:172–83.

[108] Chang YN, Lin SN, Liou HY, Chang CW, Wu CC, Wang YC. Improving the surface roughness of pickled steel strip by control of rolling temperature. J Mater Eng Perform. 2013; 22(1):322–9.

[109] Izzati R, Asri M. Effect of Acid Pickling on Microstructure and Surface Roughness of 316L Stainless Steel. 2016; 20–2.

[110] Nordgren A, Melander A. Tool wear and inclusion behaviour during turning of a calcium-treated quenched and tempered steel using coated cemented carbide tools. Wear [Internet]. 1990; 139(2):209–23. Available from: https://linkinghub.elsevier.com/retrieve/pii/004316489090046D.

[111] Shrama KM. Fatigue of welded high strength steels for automotive chassis and suspension applications School of Engineering Cardiff University UK Supervisors : [Internet]. Cardiff University; 2016. Available from: http://orca.cf.ac.uk/92903/2/2016ShramaKMPhD.pdf.

[112] Holappa L, Hämäläinen M, Liukkonen M, Lind M. Thermodynamic examination of inclusion modification and precipitation from calcium treatment to solidified steel. Ironmak Steelmak [Internet]. 2003; 30(2):111–5. Available from: http://www.tandfonline.com/doi/full/10.1179/030192303225001748.

[113] Listhuber FE, Ecker K, Fastner T. Sheets and Plates of High Quality Made from Continuously Cast Slabs. Iron Steel Eng. 1971; 51(4):92–8.

[114] Wang Y, Zuo X, Zhang L, Li S, Group S, Province H, et al. Entrapment of Inclusions in Continuous Casting Billet: Industrial Observation and Modeling. Lecture. 2010; II(January):793–806.

[115] Holappa LEK, Helle AS. Inclusion Control in High-Performance Steels. J Mater Process Technol. 1995; 53:177–86.

[116] Shibata H, Yin H, Yoshinaga S, Emi T, Suzuki M. In Situ Observation of Engulfment and Pushing of Nonmetallic Inclusions in Steel Melt by Advancing Melt/Solid Interface. ISIJ Int. 1998; 38(0):49–56.

[117] Zhang LF, Thomas BG. Inclusions in Continuous Casting of Steel. XXIV Natl Steelmak Symp. 2003; 26–8.

[118] Luo S, Wang B, Wang Z, Jiang D, Wang W, Zhu M. Morphology of Solidification Structure and MnS Inclusion in High Carbon Steel Continuously Cast Bloom. ISIJ Int [Internet]. 2017; 57(11):2000–9. Available from: https://www.jstage.jst.go.jp/article/isijinternational/57/11/57_ISIJINT-2017-294/_article.

[119] Misra RDK, Thompson SW, Hylton TA, Boucek AJ. Microstructures of hot-rolled high-strength steels with significant differences in edge formability. Metall Mater Trans A Phys Metall Mater Sci. 2001; 32(13):745–60.

[120] Sudo M, Kokubo I. Microstructure-Mechanical Property Relationships in Multi-Phase Steel Sheet. Scand J Metall. 1984; 13:329–42.

[121] Yang W, Zhang L, Wang X, Ren Y, Liu X, Shan Q. Characteristics of Inclusions in Low Carbon Al-Killed Steel during Ladle Furnace Refining and Calcium Treatment. ISIJ Int [Internet]. 2013; 53(8):1401–10.

[122] Zhang L, Liu Y, Zhang Y, Yang W, Chen W. Transient Evolution of Nonmetallic Inclusions During Calcium Treatment of Molten Steel. Metall Mater Trans B Process Metall Mater Process Sci [Internet]. Springer US; 2018; 49(4):1841–59. Available from: https://doi.org/10.1007/s11663-018-1289-5.

[123] Aware (Systems) [Internet]. [cited 15 Feb 2019]. Available from: https://www.awaresystems.be/imaging/tiff/faq.html#q6.

[124] Influence of inclusion pairs, clusters and stringers on the lower bound of the endurance limit of bearing steels - Inclusion Proximity From Each Other.pdf. [date unknown].

[125] Pilkey WD, Pilkey DF. Peterson's Stress Concentration Factors. Hoboken, New Jersey, New Jersey: John Wiley & Sons, Inc.; 2008.

[126] Safaie H, Mitchell RL, Johnston R, Russell J, Pleydell-Pearce C. An Assessment of Polarized Light Microscopy for the Quantification of Grain Size and Orientation in Titanium Alloys via Microanalytical Correlative Light to Electron Microscopy (CLEM). Proceedings of Microscopy & Microanalysis 2018. Baltimore, MD: Microscopy Society of America; 2018.

[127] Kiessling R, Lange N. Non-Metallic Inclusions in Steel. The Institute of Metals. London: The Iron and Steel Institute; 1964.

[128] Hussain A, Mehmood S, Rasool MN, Aryal S, Rulis P, Ching WY. Electronic structure, mechanical, and optical properties of CaO·Al_2O_3 system: a first principles approach. Indian J Phys [Internet]. 2016 [cited 26 Mar 2019]; 90(8):917–29. Available from: https://info.umkc.edu/cpg/wp-content/uploads/2018/09/Hussain-et-al.-2016-Electronic-structure-mechanical-and-optical-prop.pdf.

Appendix A

Automated Inclusion Analysis Macro Code

```
requires("1.37");
run("Set Measurements...", "area mean standard perimeter bounding fit shape feret's area_fraction redirect=None decimal=9"); //sets all the measurements to be recorded

A=690; //Size of local area (690 pixels x 690 pixels) (690 pxls = 709.88µm)*;

w = getWidth();
h = getHeight();
dir = "Insert File Directory"; //sets file directory;
setForegroundColor(0, 54, 255); //Sets grid colour
for (j=1;j<=nSlices;j++){ //Sets number of slices so when j=2 (2nd slice) it stops as there's no second slice;
	setSlice(j);
	for (ii=0;ii<h/A;ii++){ //sets ii value to correct row value
		for (i=0;i<w/A;i++){ //set i value to correct column value
			run("Clear Results");
			x=i*A;
			y=ii*A;
			makeRectangle(x, y, A, A); //creates ROI at location x,y of a size A,A;
			w1 = x+A; //Measuring the end point of the ROI, if it is greater than the full width then it has gone off the edge and will not be included;
			h1 = y+A;
			if (h1<=h && w1<=w){ //Makes sure ROI is 690 pxls x 690 pxls;
				run("Analyze Particles...", "size=0-Infinity circularity=0.00-1.00 show=Nothing display exclude clear include slice"); //runs the analyse particle function while selecting to display results, exclude any inclusions that touch the edge of the ROI, clear any previous results, include any holes in inclusions and summarise the data (cannot show masks as it analyses the new masked image that has nothing in the new ROI);
				n=nResults;
				for(z=0;z<n;z++){ //Applies Column and Row Values;
					setResult("Row",z,ii);
					setResult("Column",z,i);
				}
				name = getTitle;
				index = lastIndexOf(name, "."); //removes .tif from image name;
				if (index!=-1) {
					name = substring(name, 0, index);
				}
				saveAs("Results",dir+"\\"+name+"\\Individual\\"+name+" (Grid "+ii+"-"+i+").csv"); //Saves results as sample  name plus grid position;
				print("Grid: "+ii+"-"+i+" Count: "+nResults); //Created summary results of whats been calculated so far;
			}
		}
	}
}
```

* 690 pixels by 690 pixels if for analysis in line with the standard at 100x magnification. The following alterations are made to the code for different magnifications:

200x Magnification

1. Used if wanting to directly compare to 100x Magnification: -

```
A=1400; //Size of local area (1400 pxls x 1400 pxls) (1400 pxls = 710.14µm);
```

2. Used to conduct analysis in line with standard.

```
A=690; //Size of local area (690 pxls x 690 pxls) (690 pxls = 350µm);
```

500x Magnification

1. Used if wanting to directly compare to 100x Magnification: -

```
A=3500; //Size of local area (3500 pxls x 3500 pxls) (3500 pxls = 710.23um);
```

2. Used to conduct analysis in line with assumed continuing reduction if field size in accordance to how the standard's field size halves from 50x – 100x – 200x magnification as 500x magnification is not addressed.

```
A=862; //Size of local area (862 pxls x 862 pxls) (862 pxls = 174.92um);
```

It should however be noted that while reduces the field size increases the accuracy of the positions of inclusions through the thickness of the steel plate, it also increases the chance of inclusions crossing between fields and therefore being ignored from the analysis.

Appendix B

Calculations of Estimated FB590 Chemistries

As stated previously, during retesting it was discovered that some of the original chemistries were inaccurate and some of the samples were unavailable for retesting. In order to the still utilise the tensile data associated with these samples; the remaining samples were split into 2 groups to calculate their updated chemistries: -

1. Samples that had other coils tested from the same heat.
2. Samples taken from coils with untested sample heats.

The samples taken from a coil that had other coils tested from the same heat, simply had their updated chemistries calculated from an average of the chemistry's other samples from the same heat. The resulting chemistries can be seen in Table 3-4.

The samples from heats that were not available for retesting were calculated by first calculating the percentage difference in chemistries between the original data set and the updated data set. The resulting percentage differences from each sample were then averaged, creating an average percentage difference for each individual element. These results are shown in Figure B-1, with error bars indicating ± 1σ. As can be seen, for most of the relevant elements the range of results indicated by their error bars were relatively small, however the errors bars for S were quite large, with the sample showing a σ of 22.19% (2dp). These average percentage differences were then multiplied against the original chemistries to provide the updated chemistry that can be seen in Table 3-5.

It should be noted that all the samples with these 'averaged' and 'estimated' chemistries are highlighted in the resulting comparisons with mechanical properties, as to not confuse them with samples with measured chemistries.

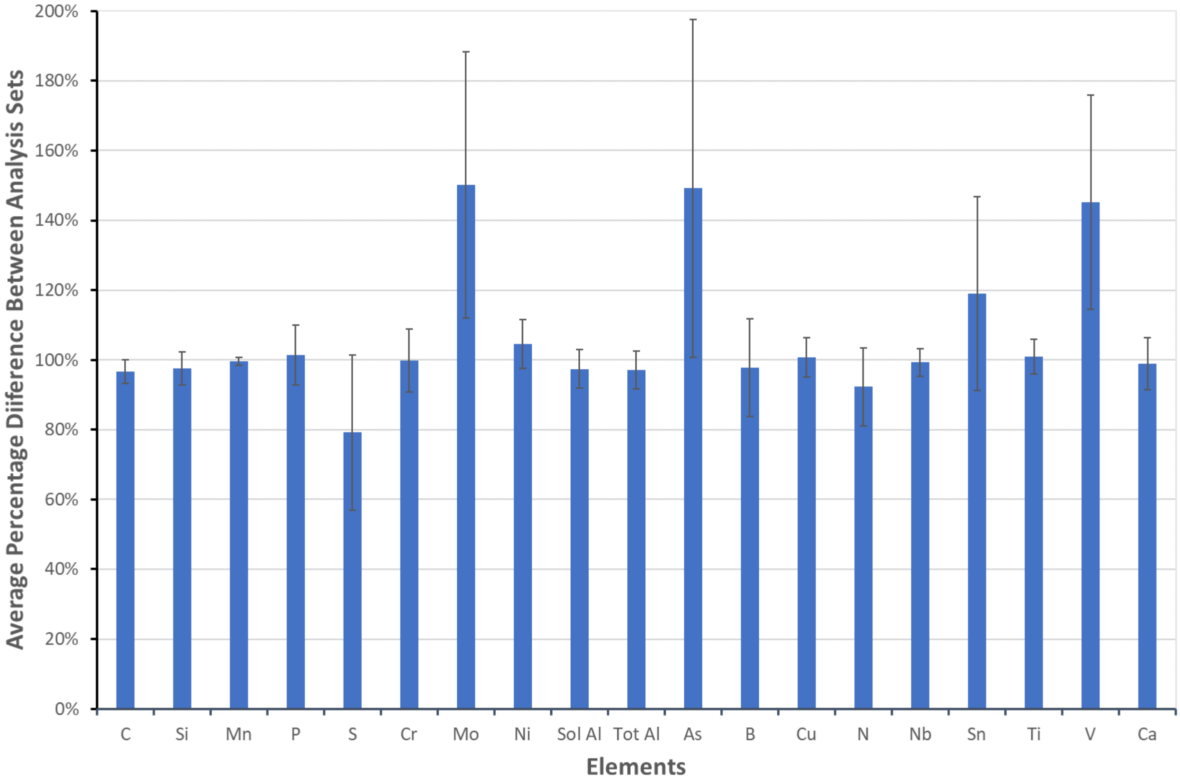

Figure B-1. Average Percentage Difference Between the Original OES Chemistries and the Updated Analysis.

Appendix C

Supplementary Results Supporting Assertions Made in Chapter 4

4.2.1.1. Entire Sample Range

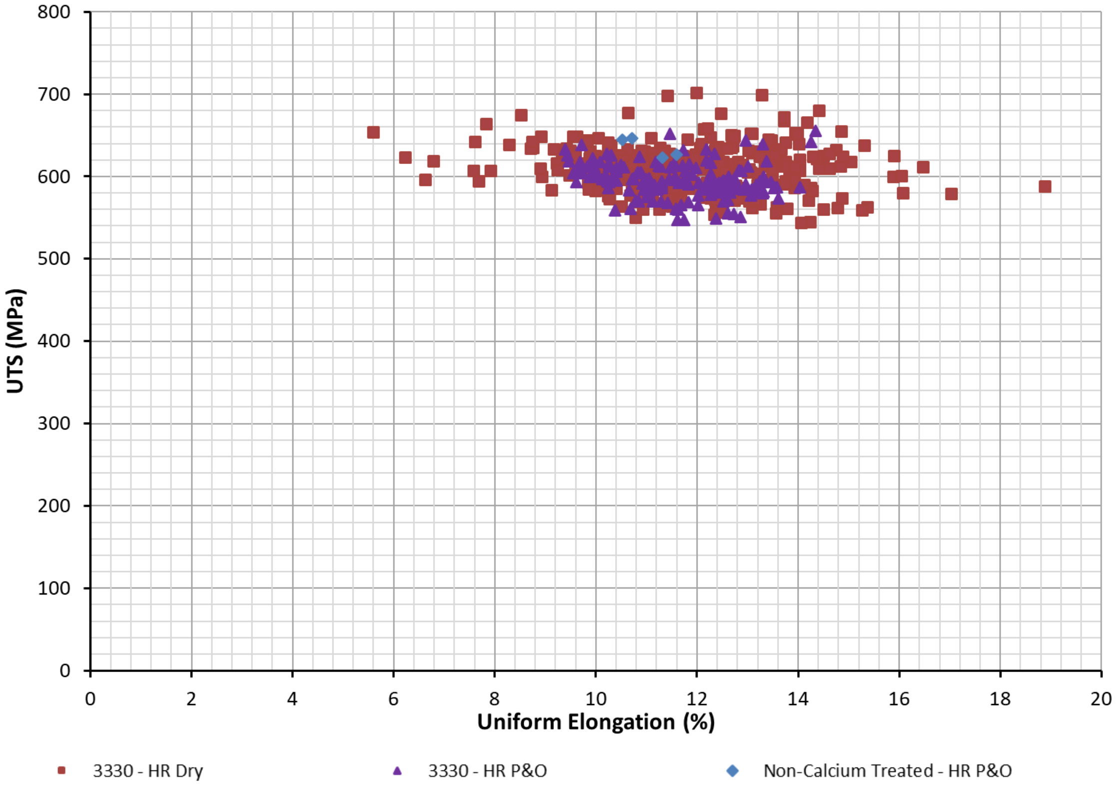

Figure C-1. Comparison of UE and UTS in FB590 and a Non-Calcium treated grade.

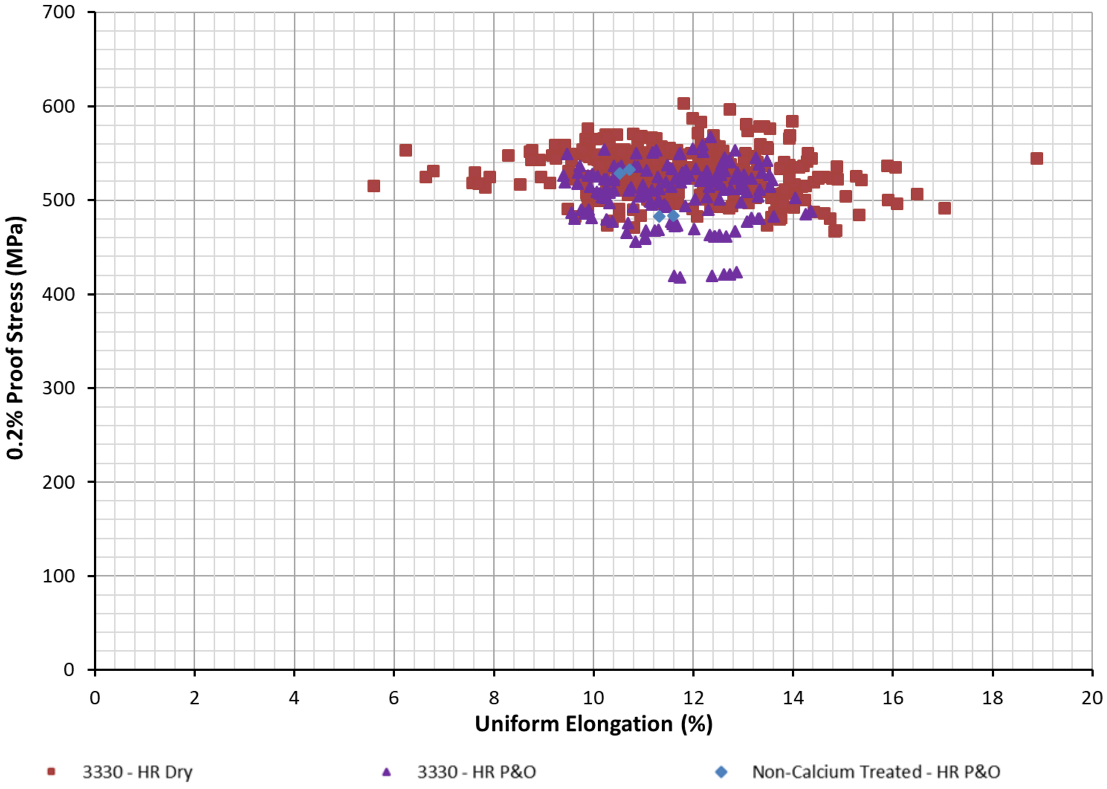

Figure C-2. Comparison of UE and 0.2% PS in FB590 and a Non-Calcium treated grade.

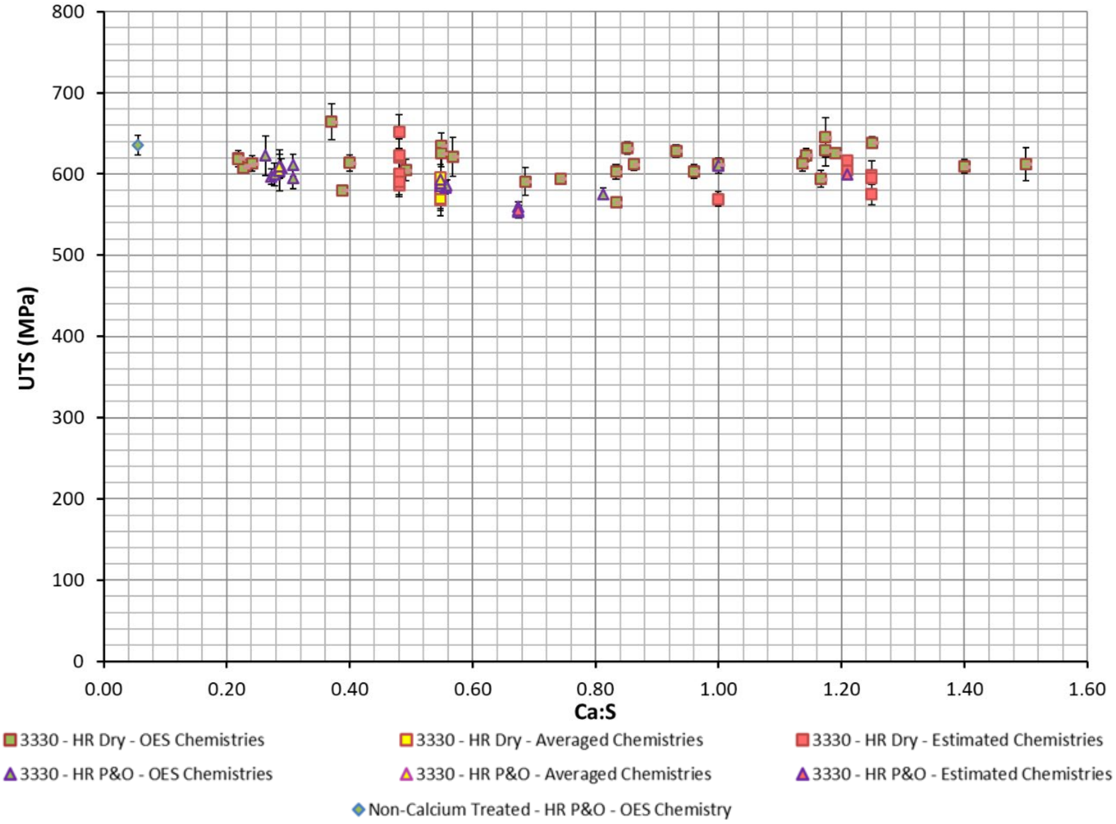

Figure C-3. Comparison of UTS and Ca:S in FB590 and a Non-Calcium treated grade.

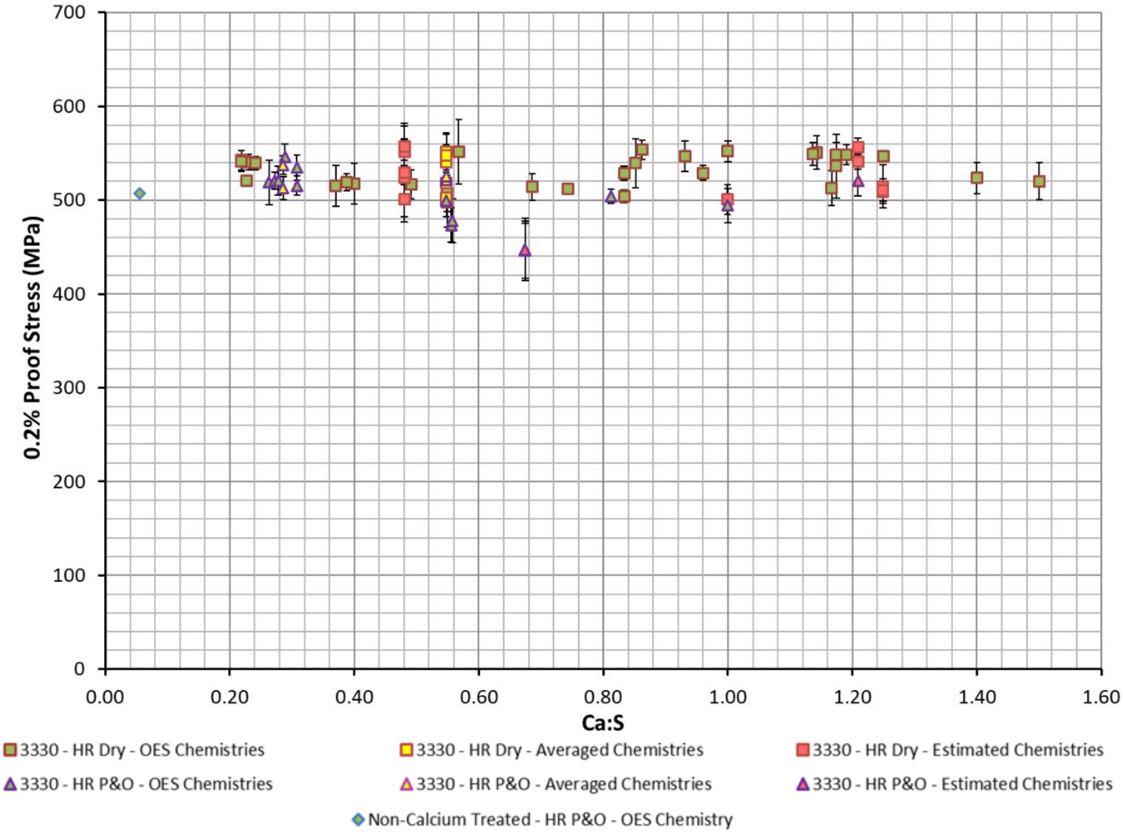

Figure C-4. Comparison of 0.2% PS and Ca:S in FB590 and a Non-Calcium treated grade.

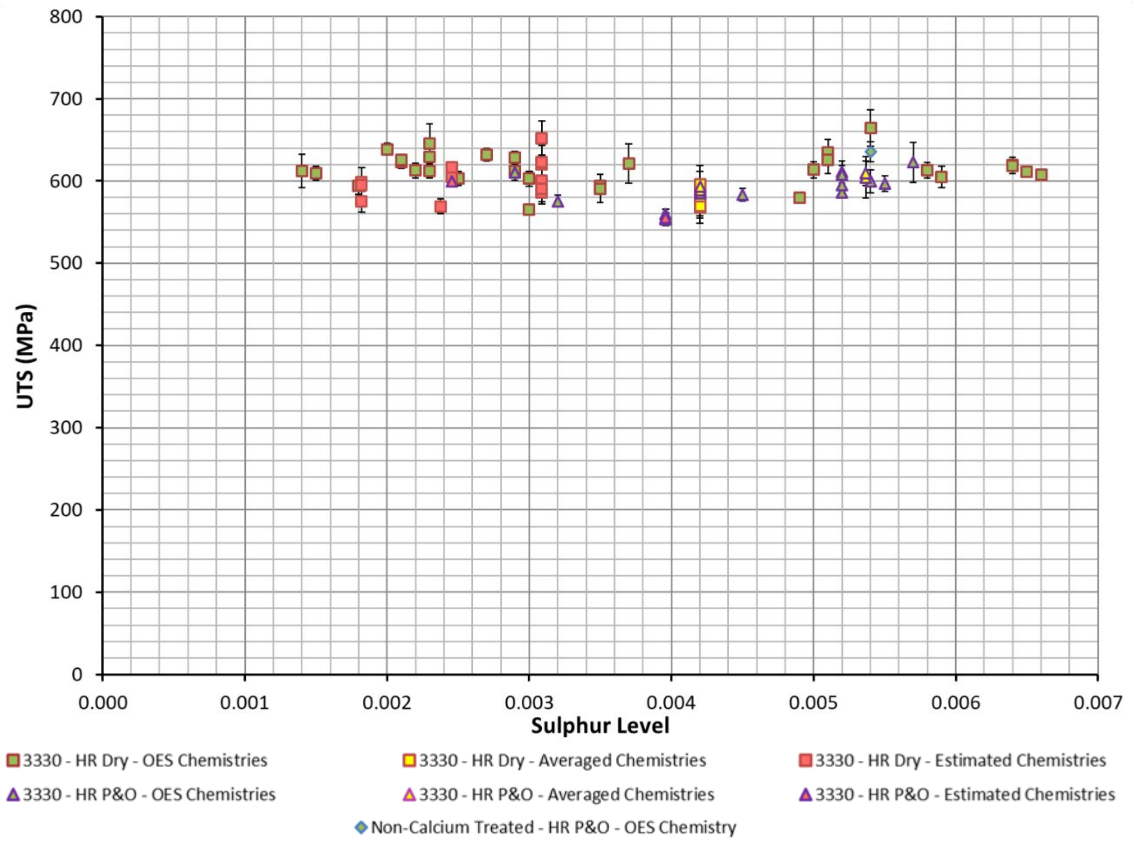

Figure C-5. Comparison of UTS and Sulphur Level in FB590 and a Non-Calcium treated grade.

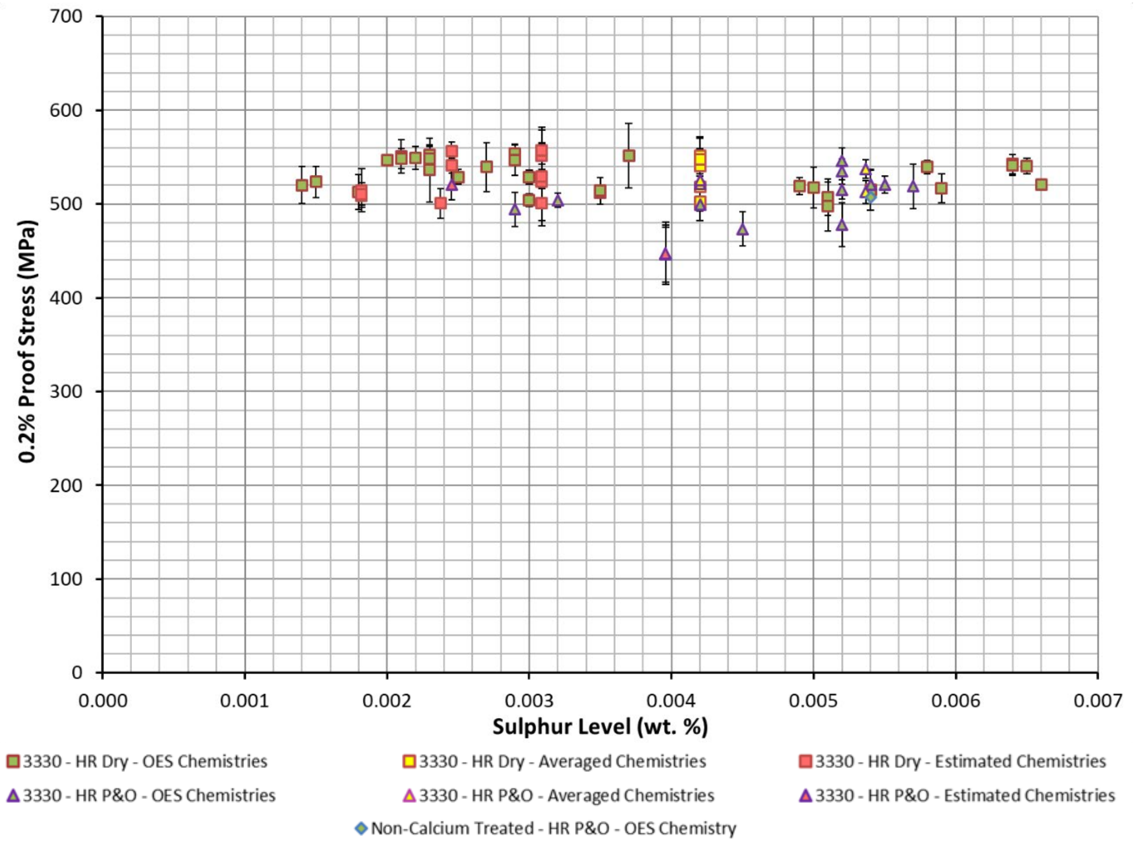

Figure C-6. Comparison of 0.2% PS and Sulphur Level in FB590 and a Non-Calcium treated grade.

4.2.1.2. Transverse Samples Only

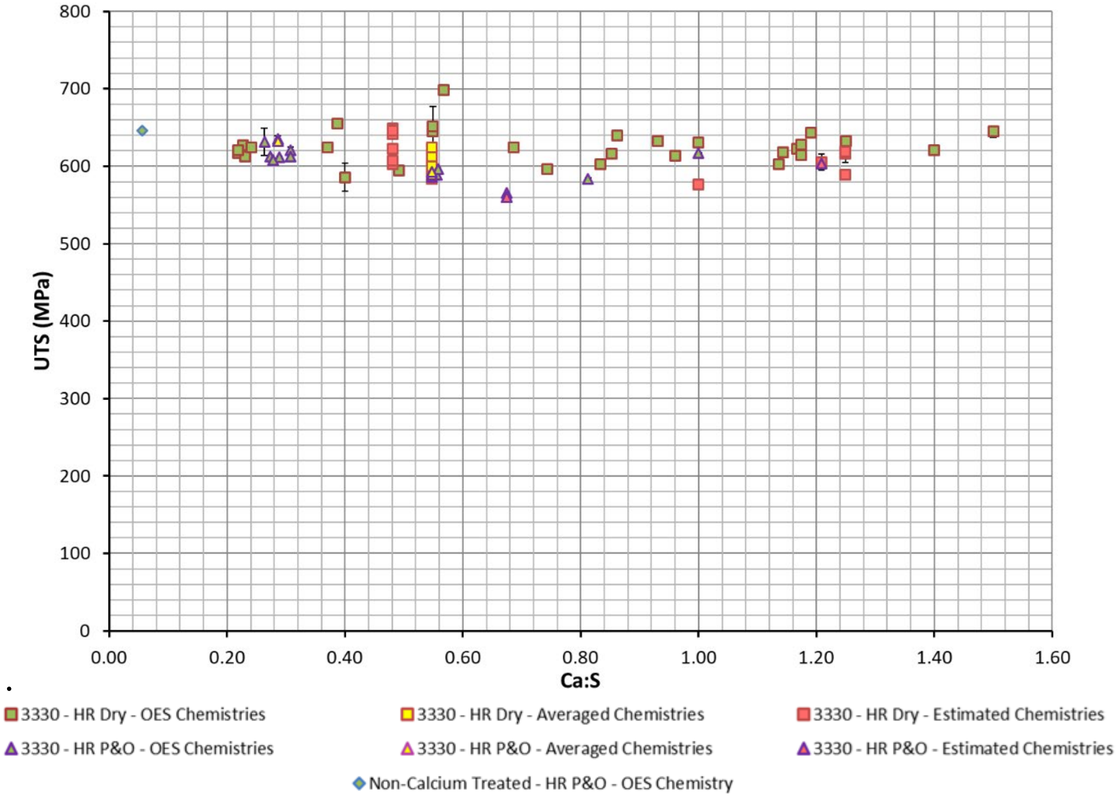

Figure C-7. Comparison of UTS and Ca:S in FB590 and a Non-Calcium treated grade in the transverse direction.

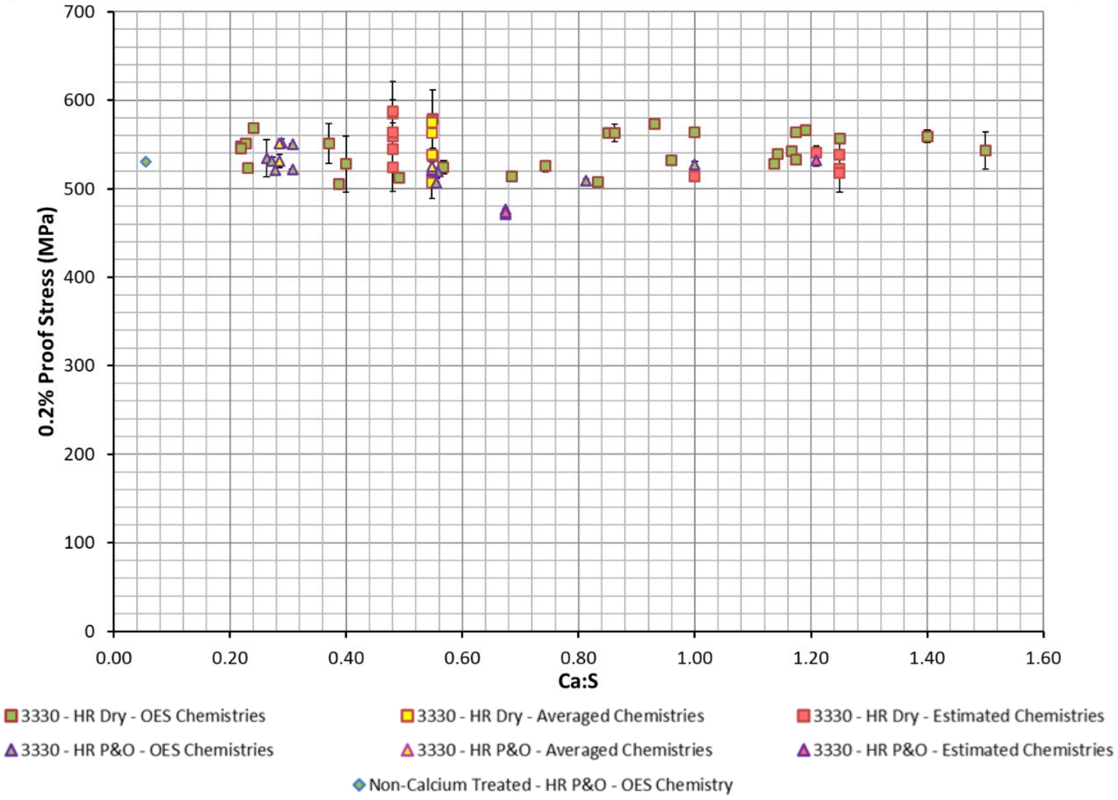

Figure C-8. Comparison of 0.2% PS and Ca:S in FB590 and a Non-Calcium treated grade in the transverse direction.

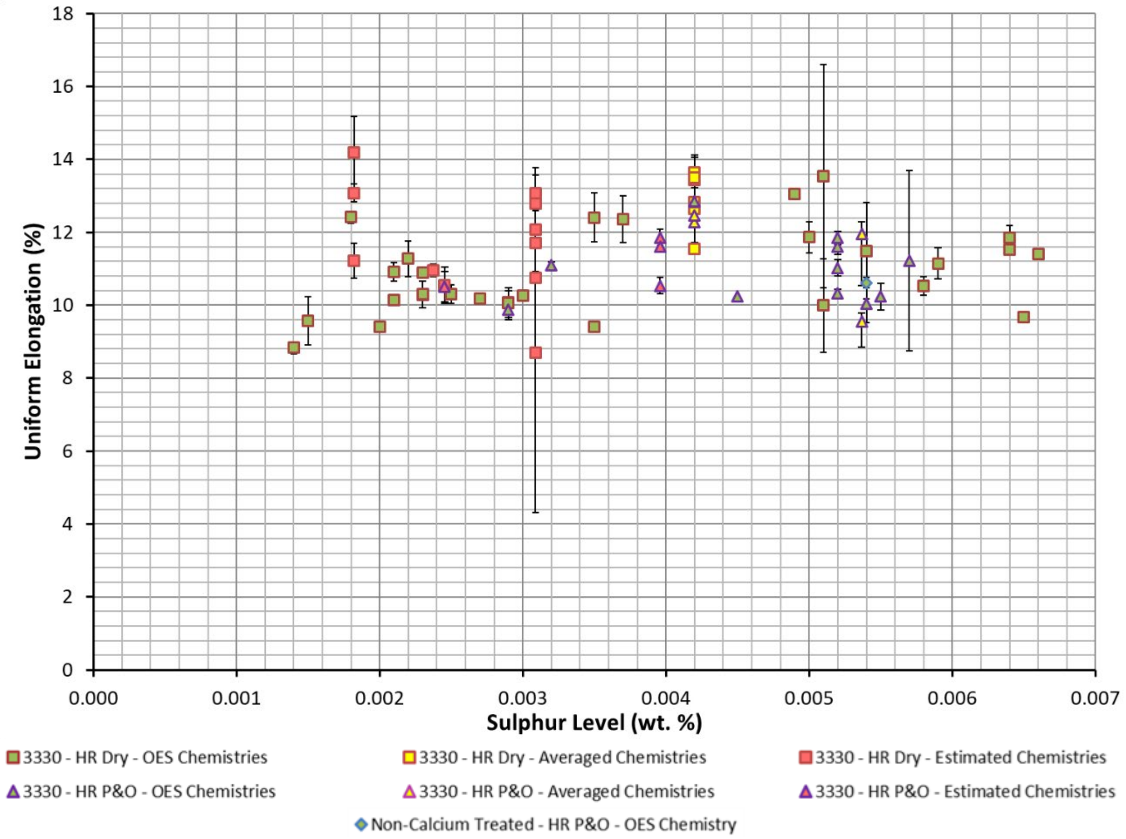

Figure C-9. Comparison of UE and Sulphur Level in FB590 and a Non-Calcium treated grade in the transverse direction.

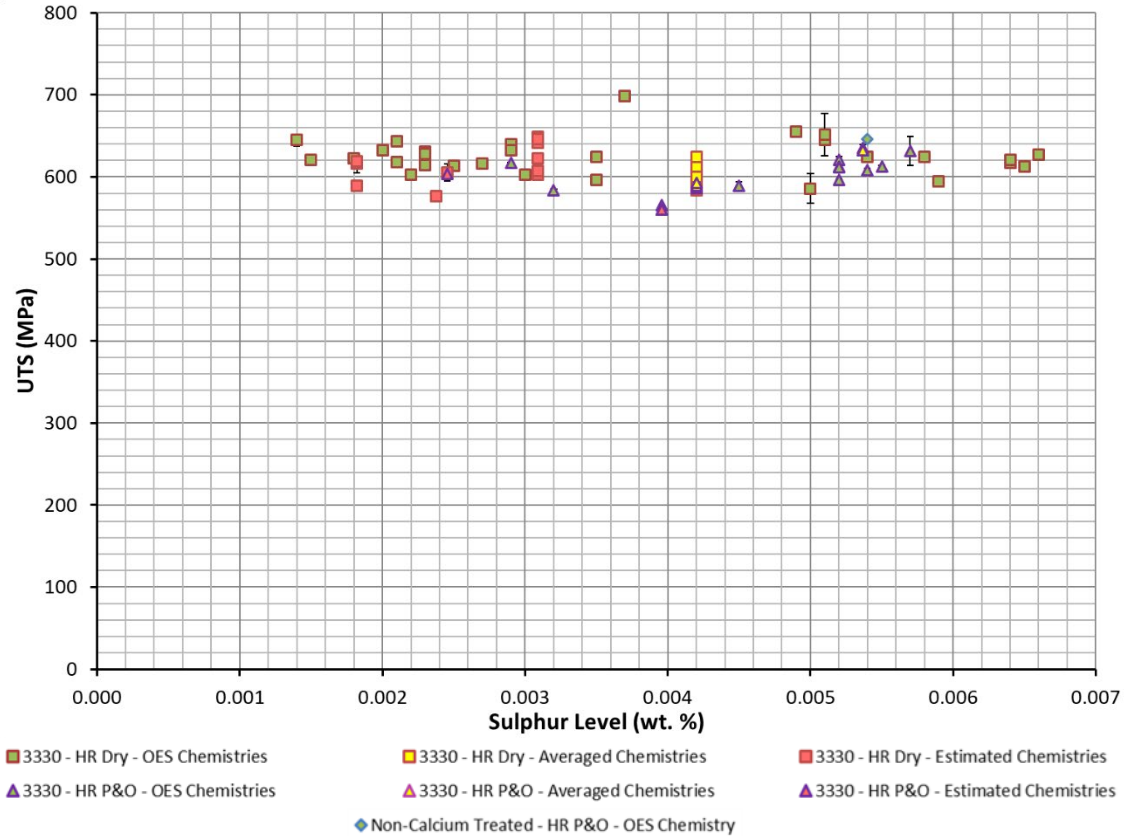

Figure C-10. Comparison of UTS and Sulphur Level in FB590 and a Non-Calcium treated grade in the transverse direction.

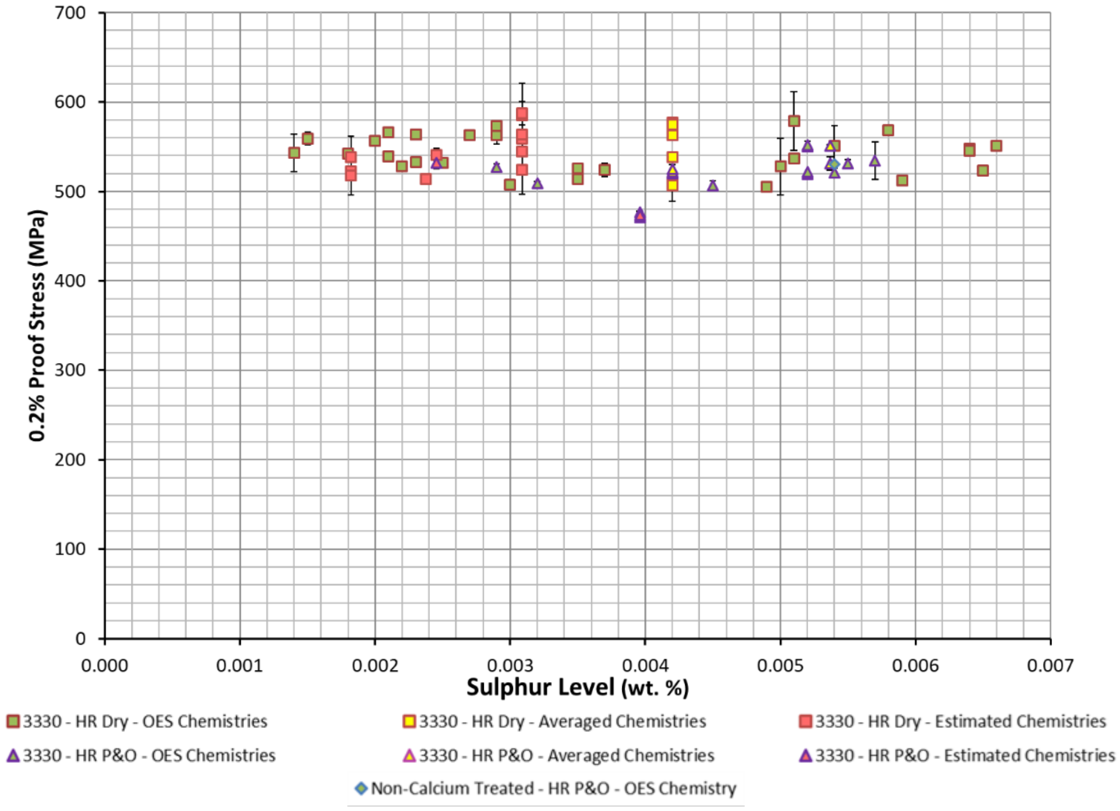

Figure C-11. Comparison of 0.2% Proof Stress and Sulphur Level in FB590 and a Non-Calcium treated grade only in the transverse direction.

4.2.1.3. Transverse vs Longitudinal Direction

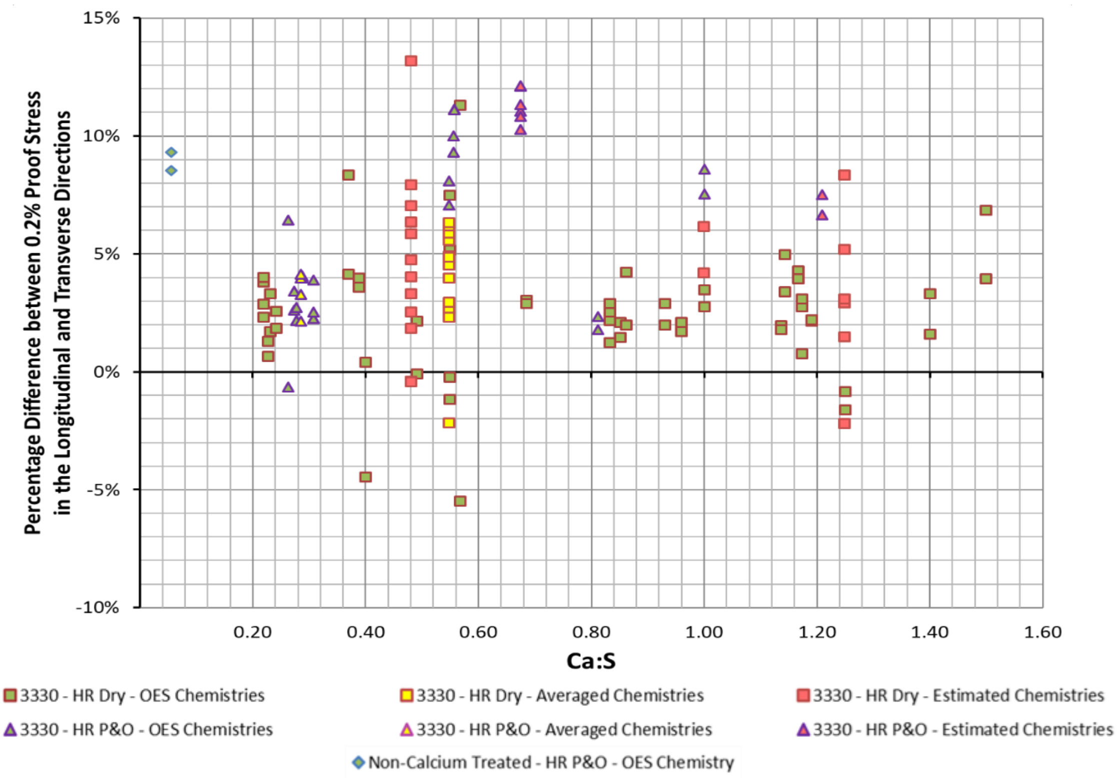

Figure C-12. Comparison of 0.2% Proof Stress and Ca:S in FB590 and a Non-calcium treated grade showing the percentage differences between the transverse and longitudinal directions.

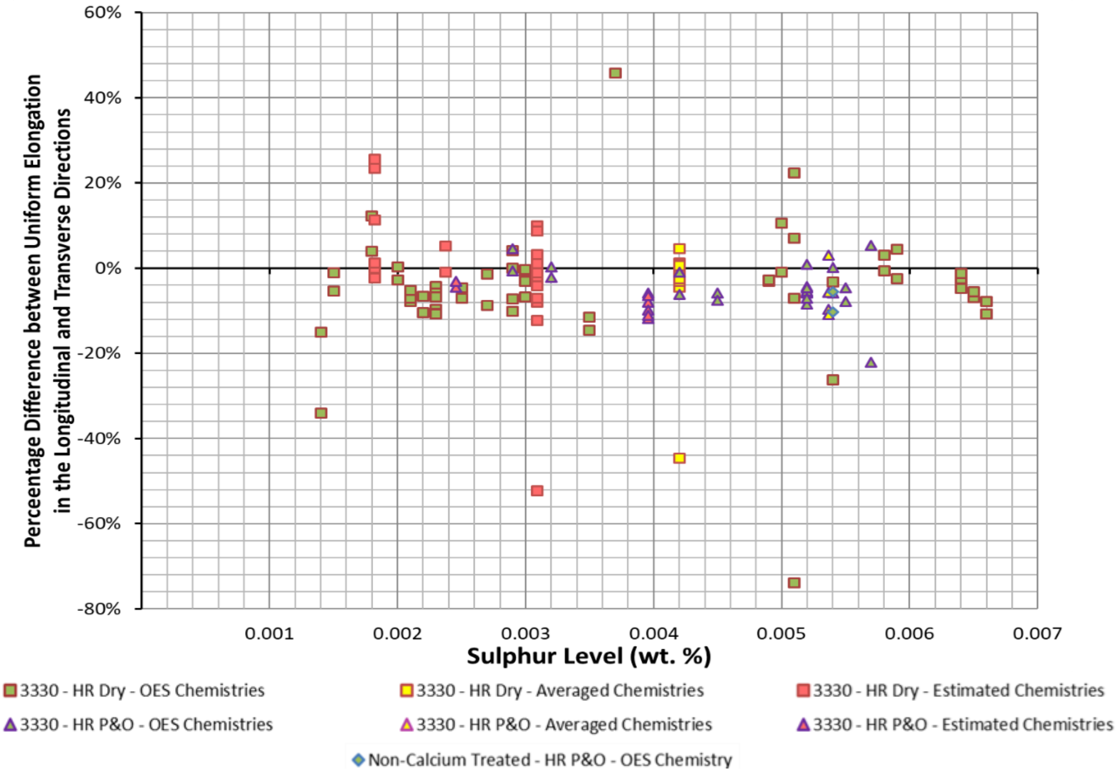

Figure C-13. Comparison of the Uniform Elongation and Sulphur Level in FB590 and a Non-Calcium treated grade showing the percentage differences between the transverse and longitudinal directions.

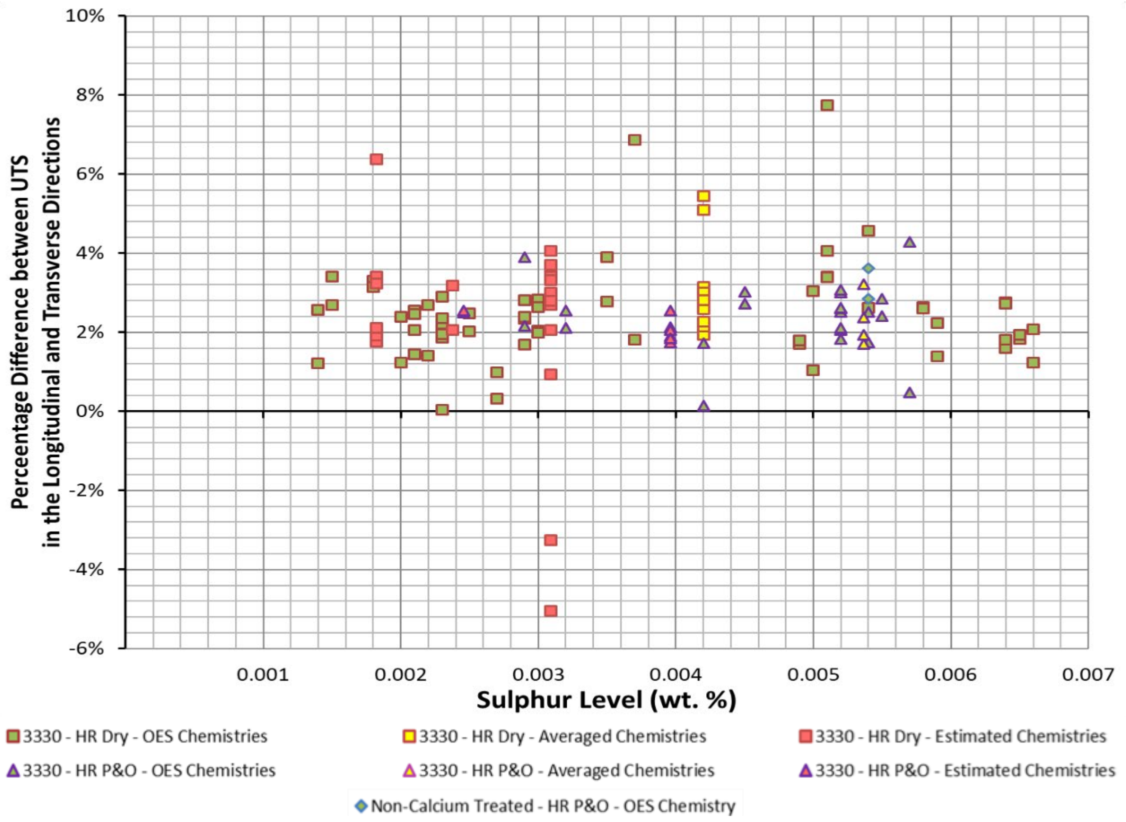

Figure C-14. Comparison of UTS and Sulphur Level in FB590 and a Non-Calcium treated grade showing the differences between the transverse and longitudinal directions.

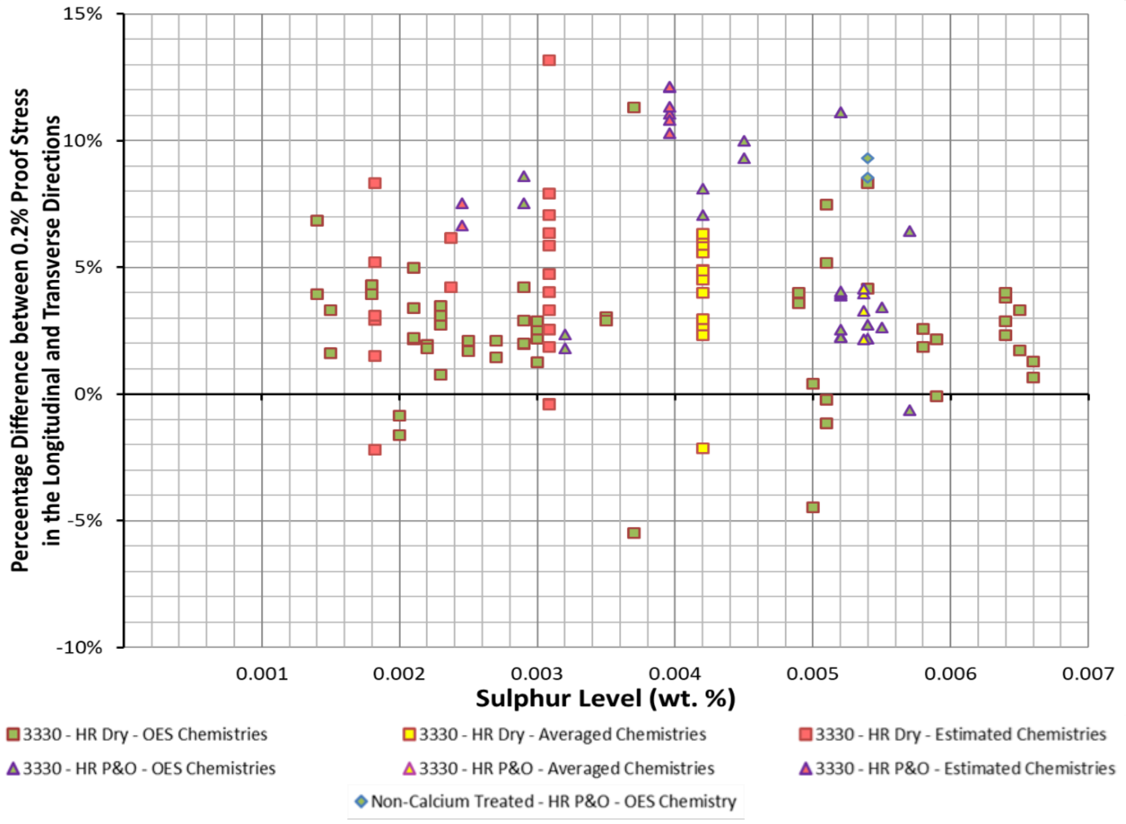

Figure C-15. Comparison of 0.2% Proof Stress and Sulphur Level in FB590 and a Non-Calcium treated grade showing the differences between the transverse and longitudinal directions.

4.3.3.1.2. Inclusion Population Density

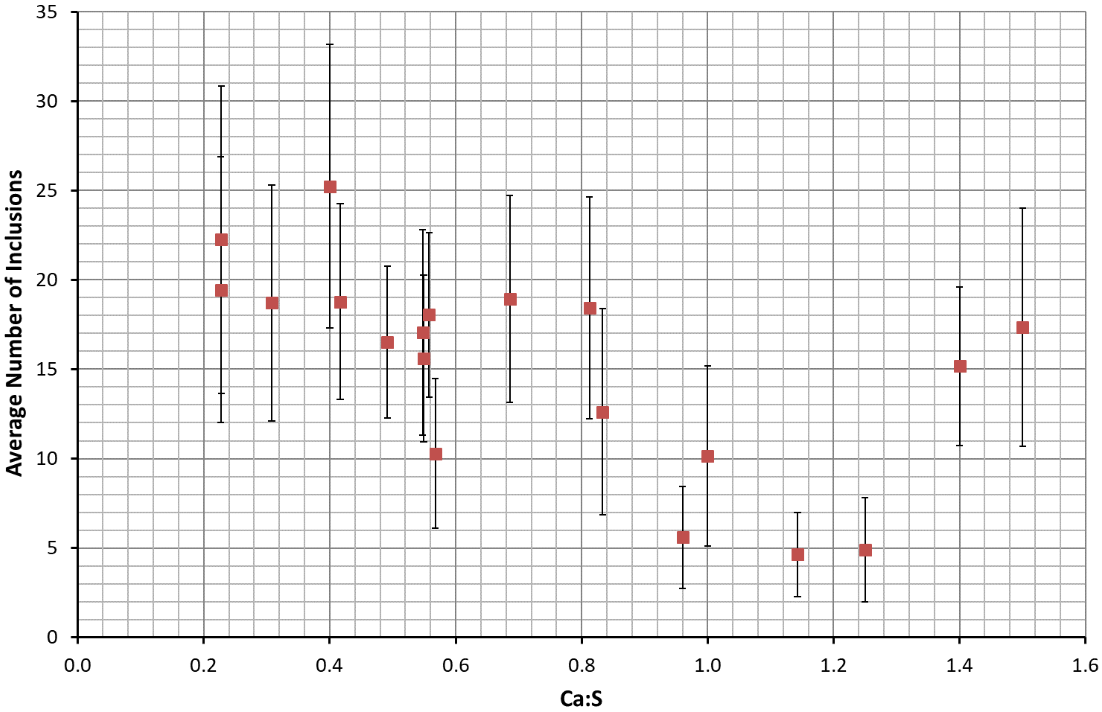

Figure C-16. Average Number of Inclusions vs Calcium Sulphur Ratio for the Calcium Treated FB590.

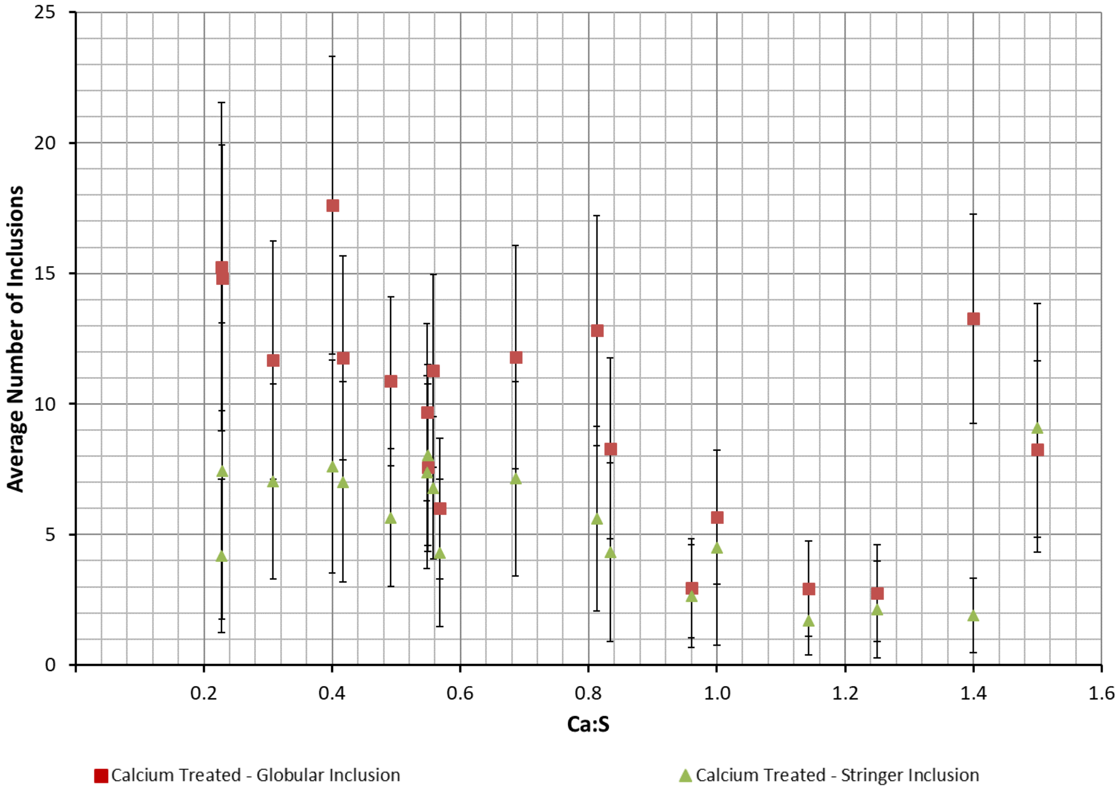

Figure C-17. Average Number of Globular and Stringer Inclusions vs Calcium Sulphur Ratio for the Calcium Treated FB590.

4.3.3.1.3. Size of Inclusions

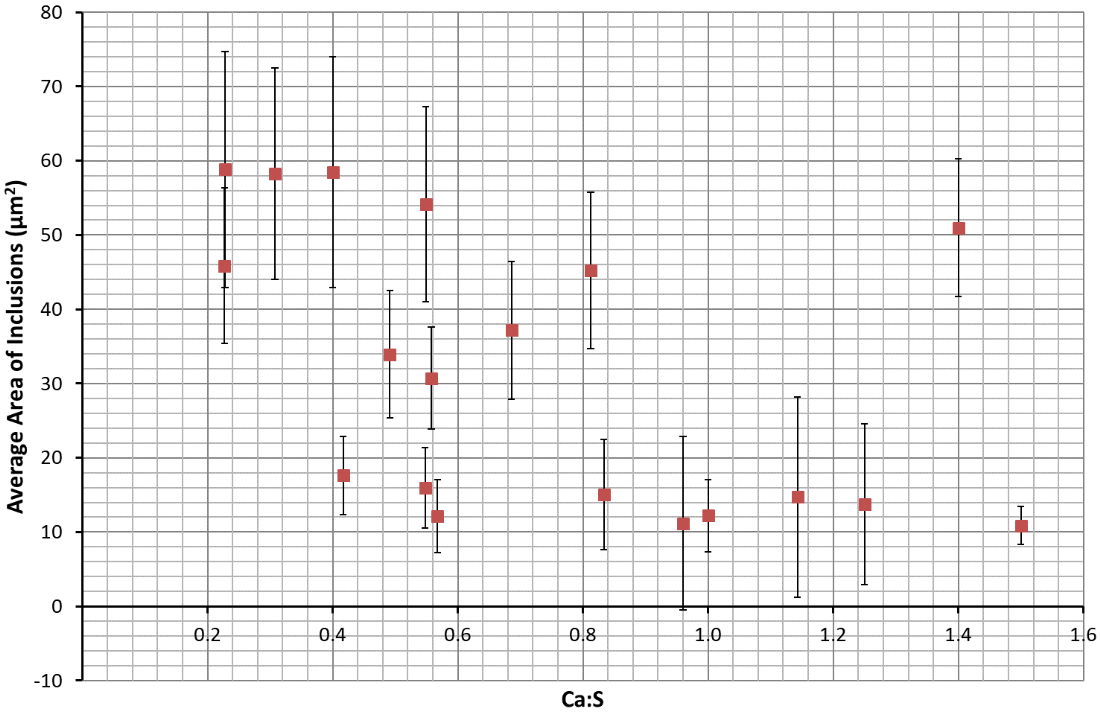

Figure C-18. Average Area of Inclusions vs Calcium Sulphur Ratio for Calcium Treated FB590.

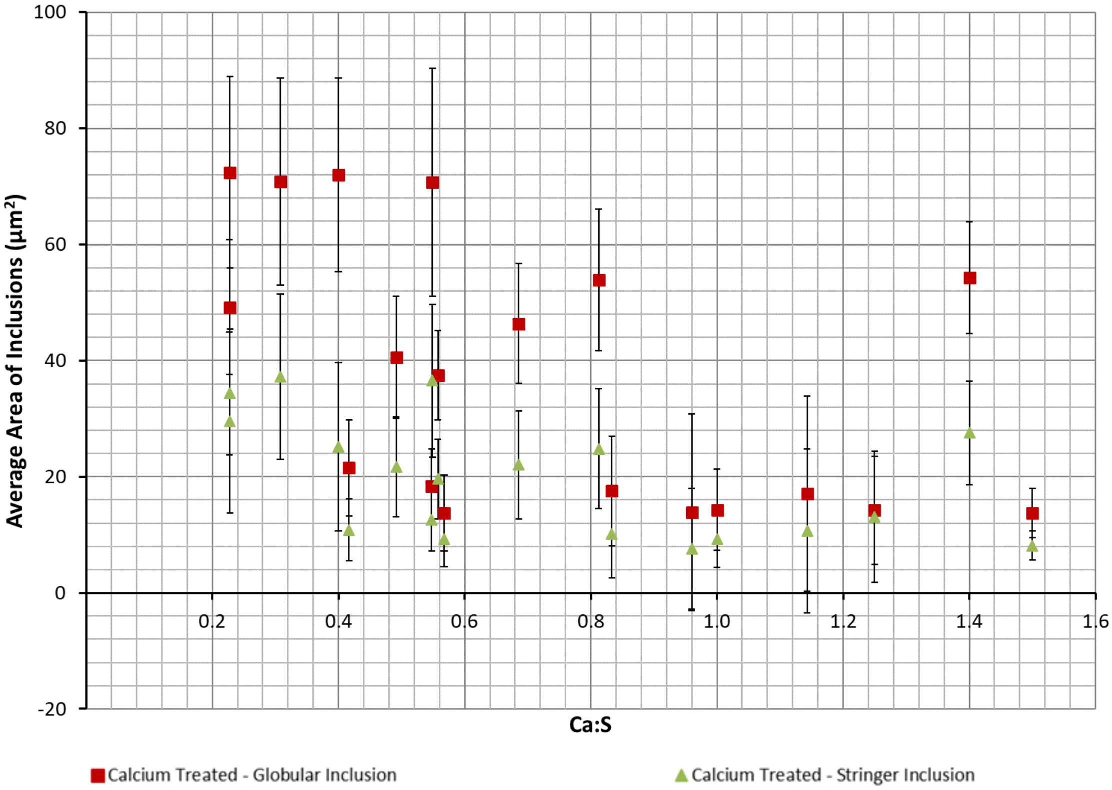

Figure C-19. Average Area of Globular and Stringer Inclusions vs Calcium Sulphur Ratio for Calcium Treated FB590.

4.3.3.2. Scanning Electron Microscopy (EDS Analysis) – Ca Treated

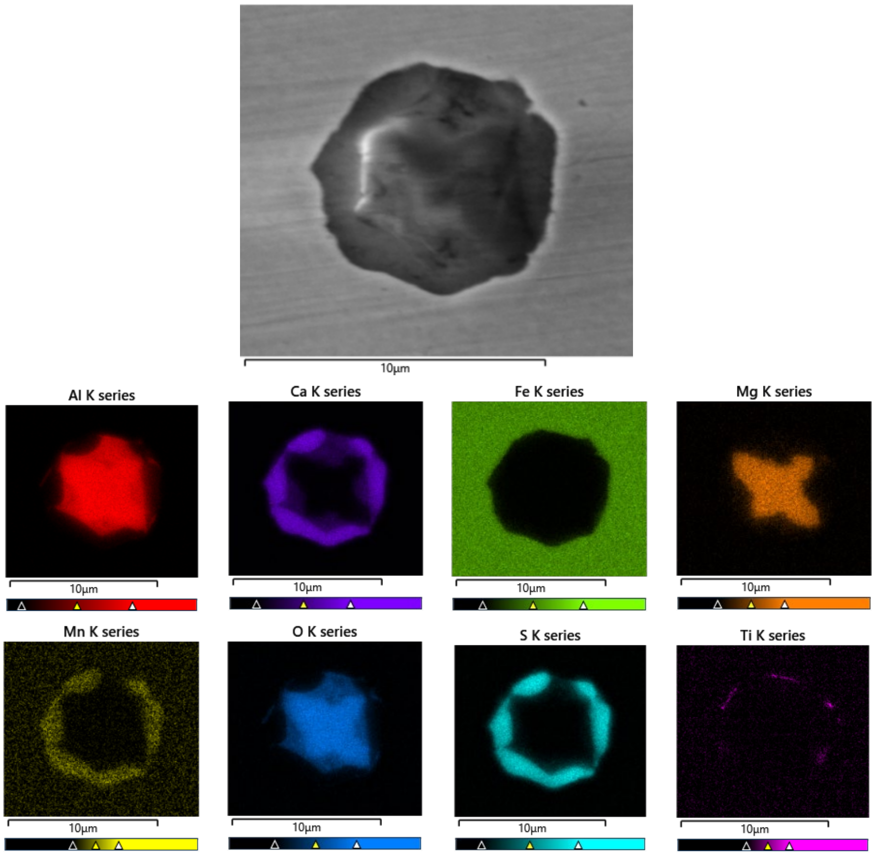

Figure C-20. ‘Globular’ Inclusion from 13S24/18MW

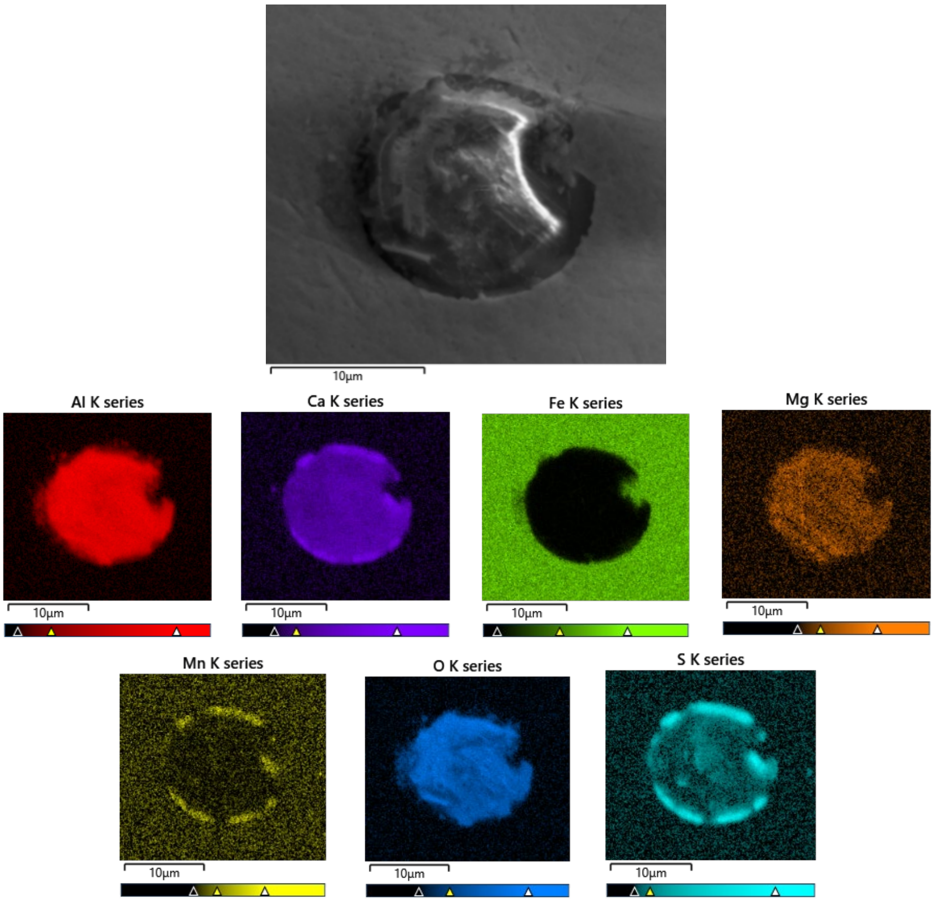

Figure C-21. ‘Globular’ Inclusion from 14S21/2L1 (Ca:S – 0.23, S – 0.0079 wt.%)

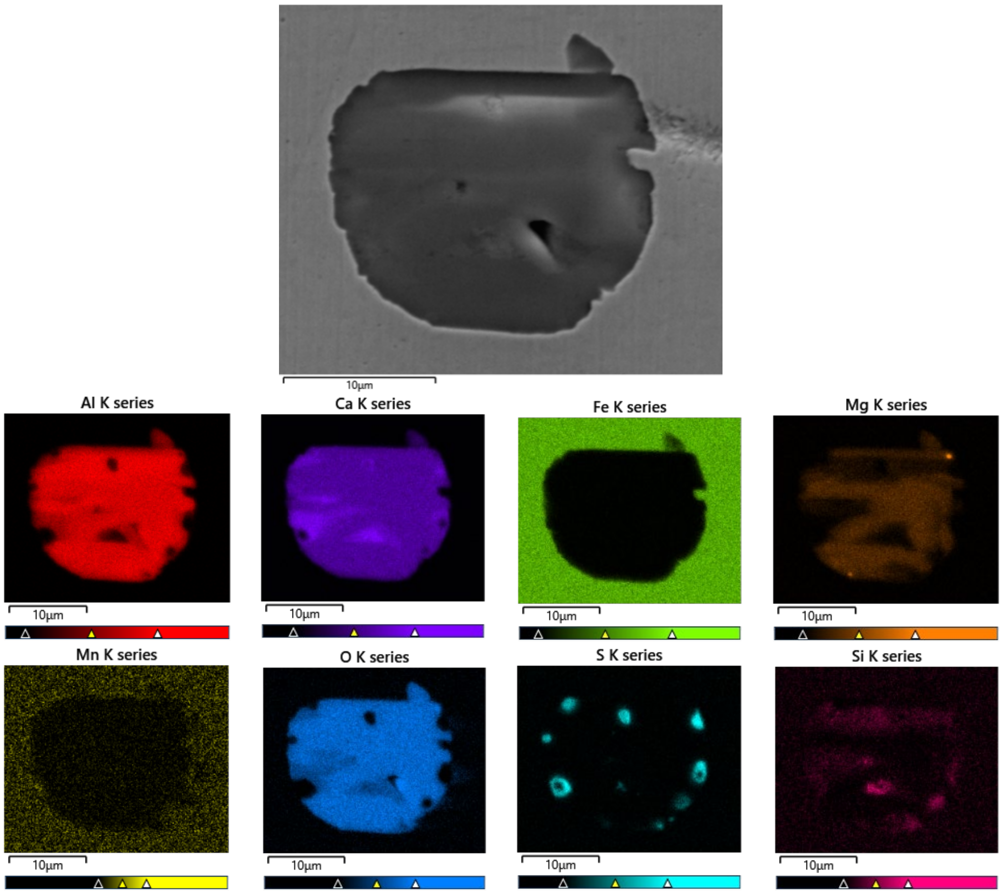

Figure C-22. ‘Globular’ Inclusions from 15S24/9L1.

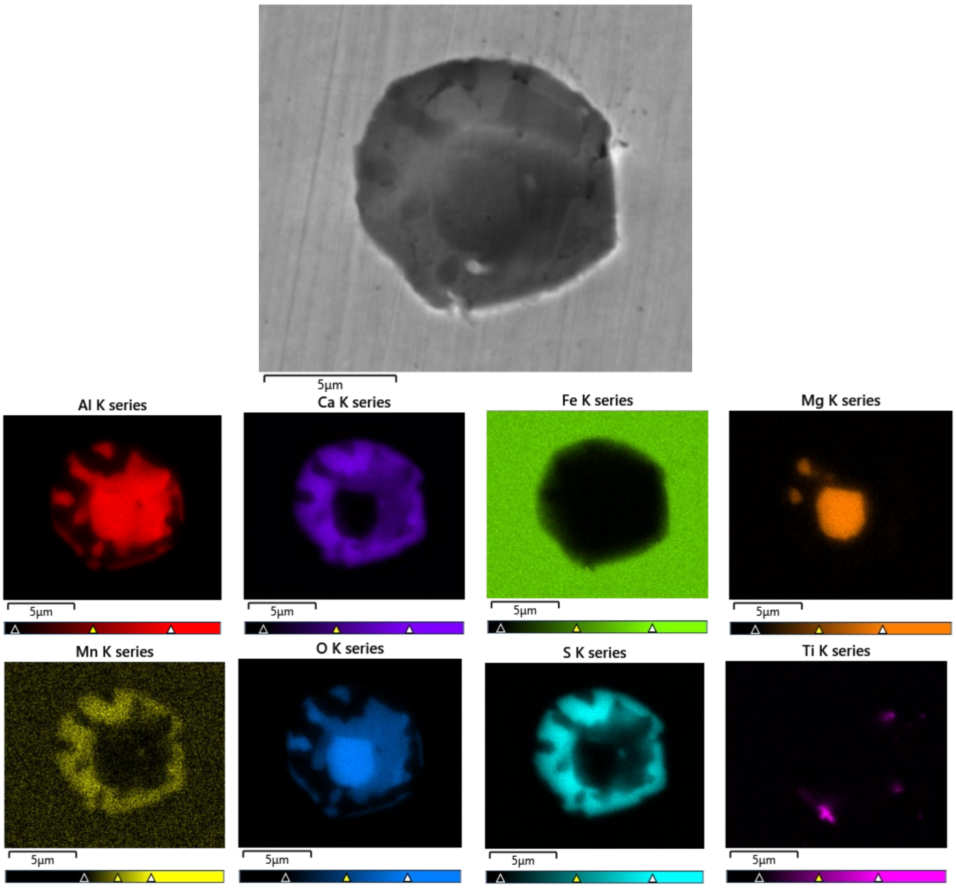

Figure C-23. Example of ‘Ying-Yang’ Globular Inclusion from 14S17/12MW

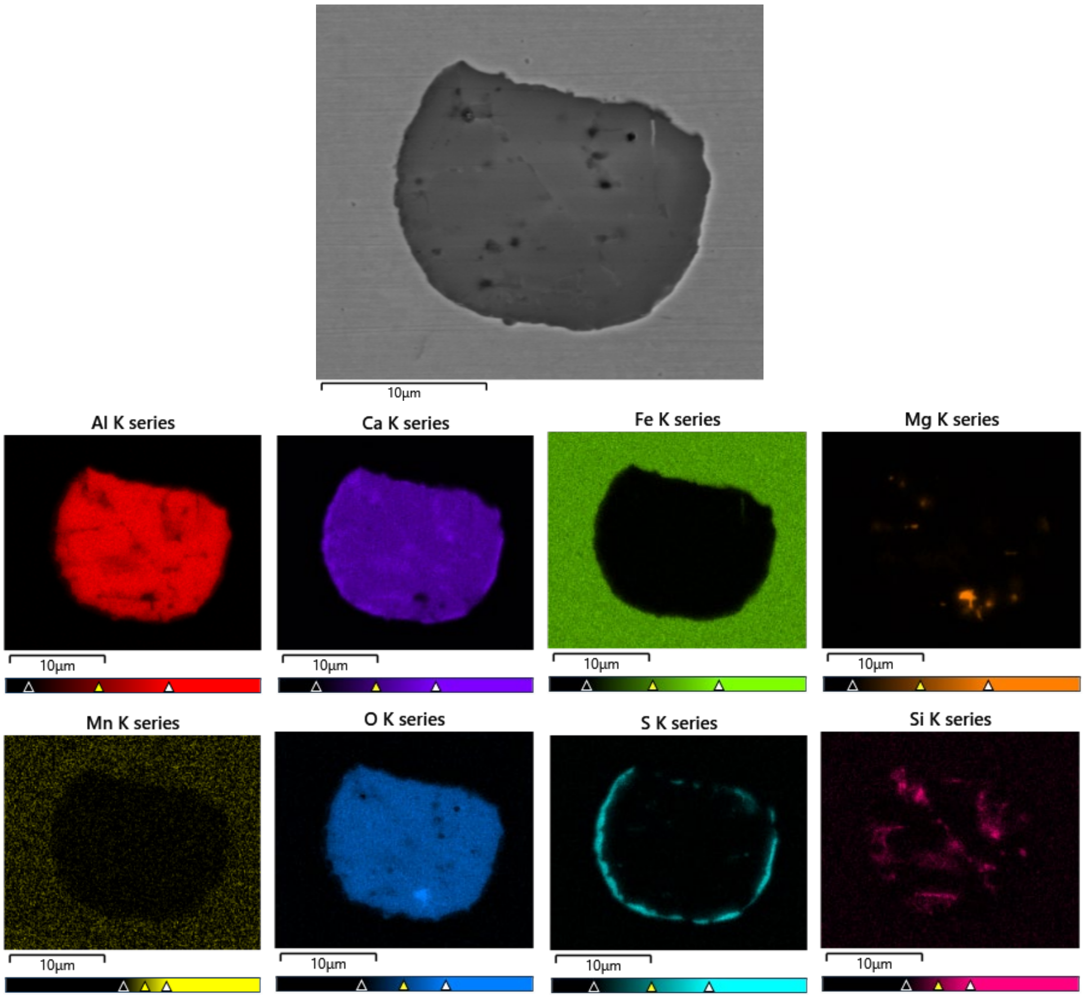

Figure C-24. 'Stringer' Inclusion from 13S24/18MW.

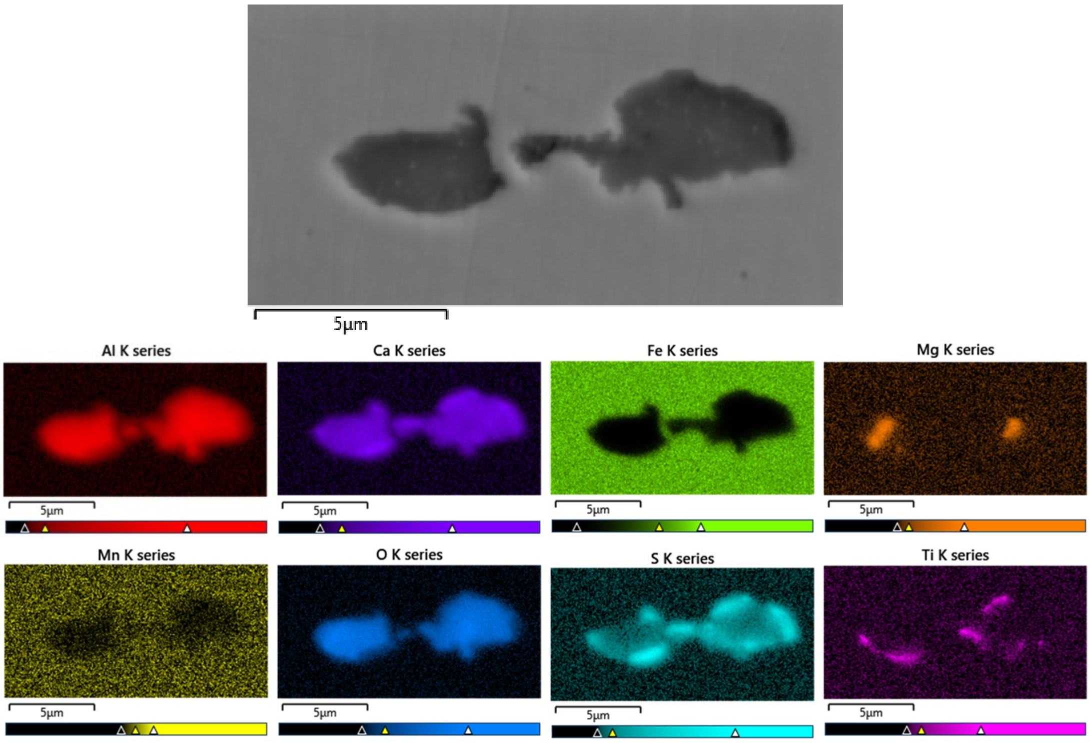

Figure C-25. Example of a Partially 'Fractured' Stringer Inclusion from 14S17/4MW.

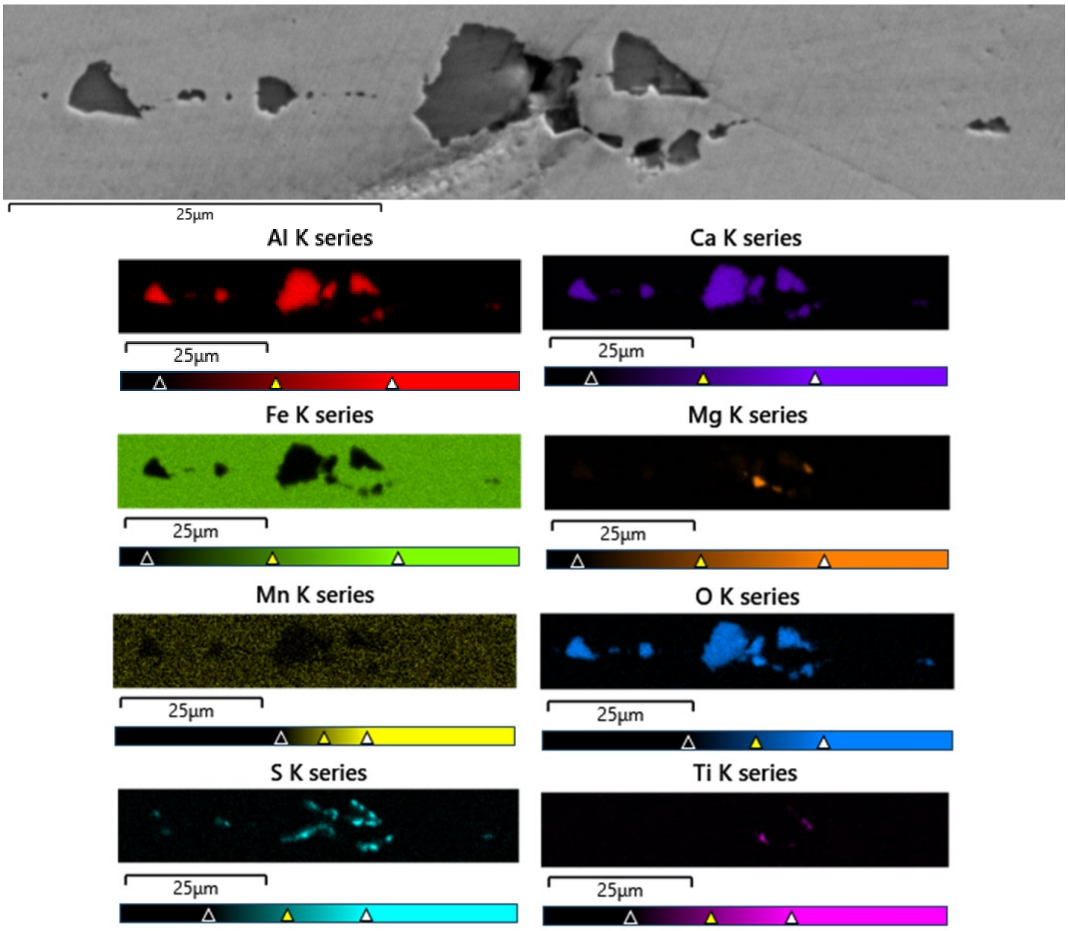

Figure C-26. Example of a Completely ‘Fractured’ Stringer Inclusions from 15S24/1L1

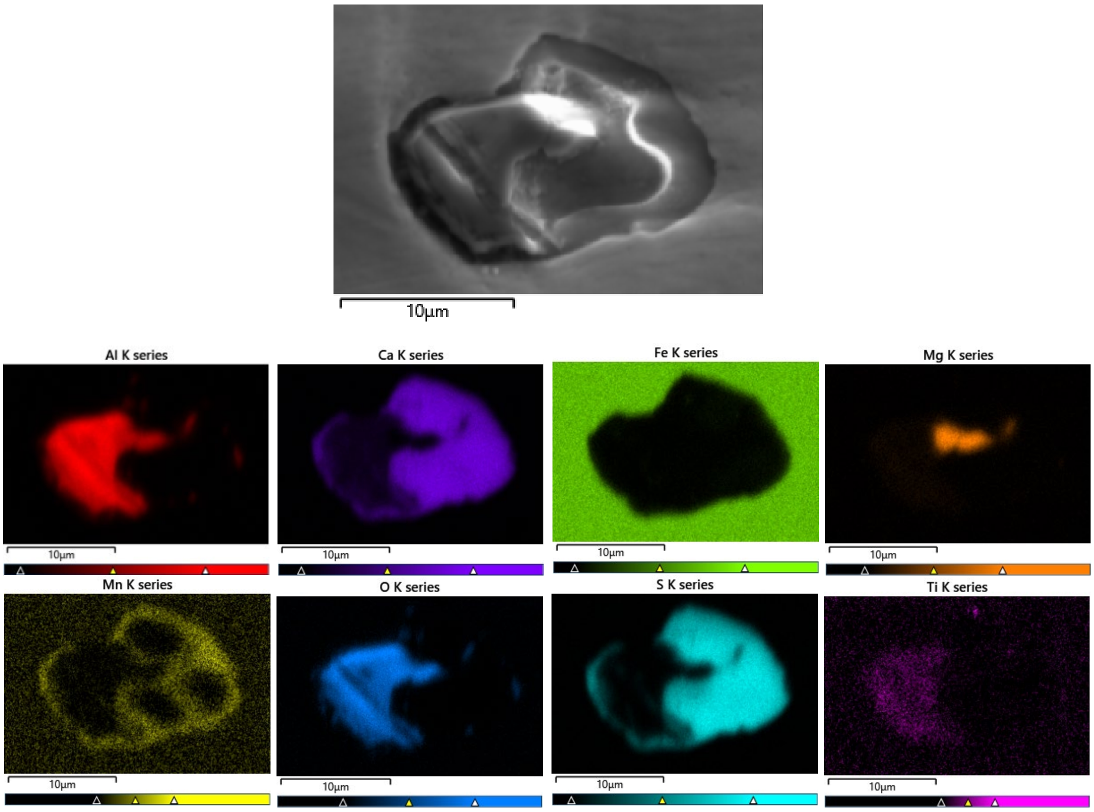

Figure C-27. Example of a ‘Ying-Yang’ Stringer Inclusion from 14S21/1L2.

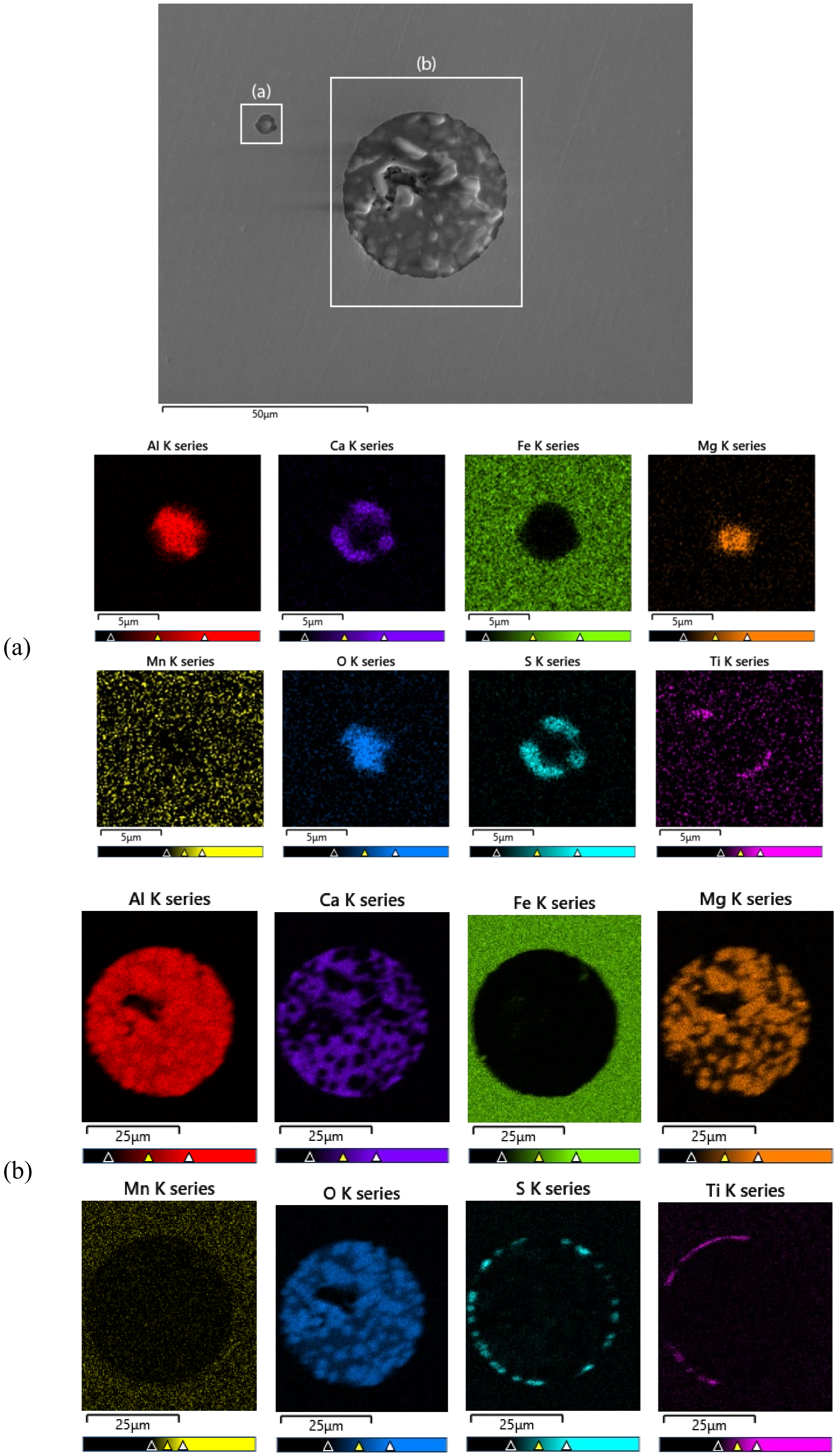

Figure C-28. Example of a 'Nucleated' Stringer Inclusions from 15S24/5L1.

4.3.4.2. Scanning Electron Microscopy (EDS Analysis) – Non-Ca Treated

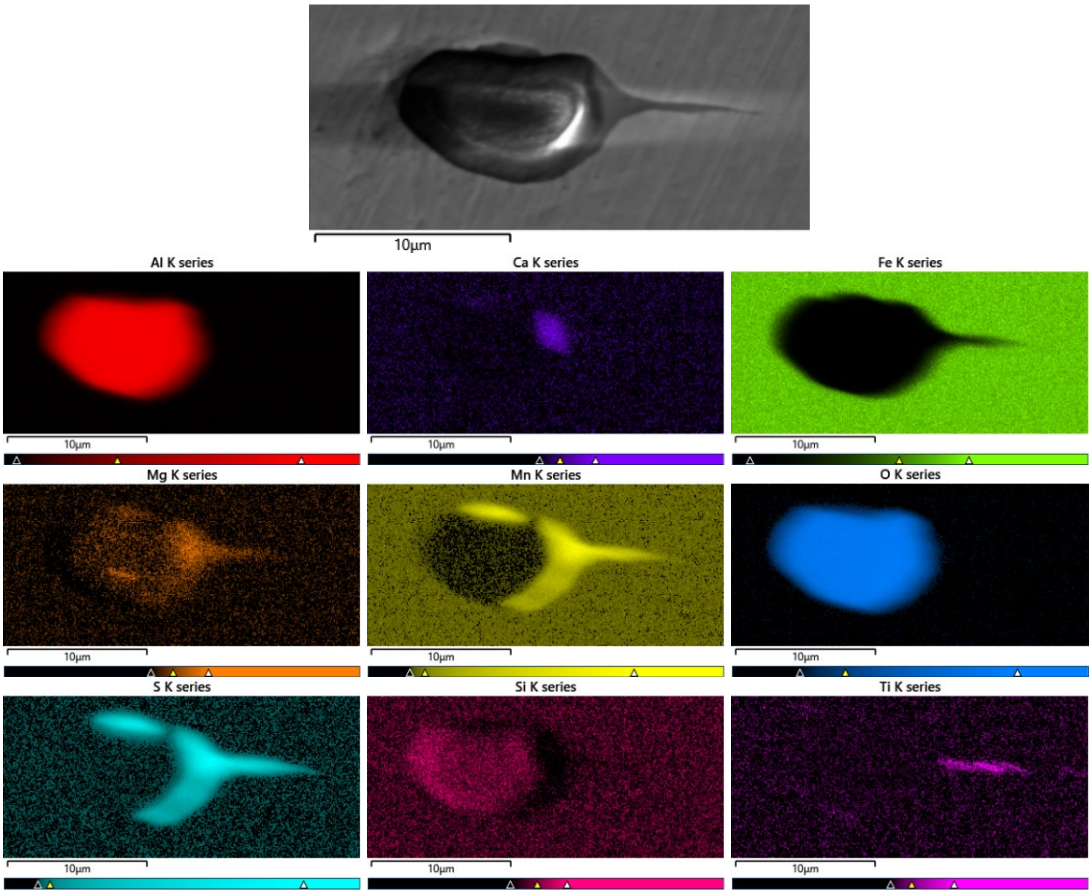

Figure C-29. Example of a ‘Classic’ Stringer Inclusion found in 11QS44-7L1.

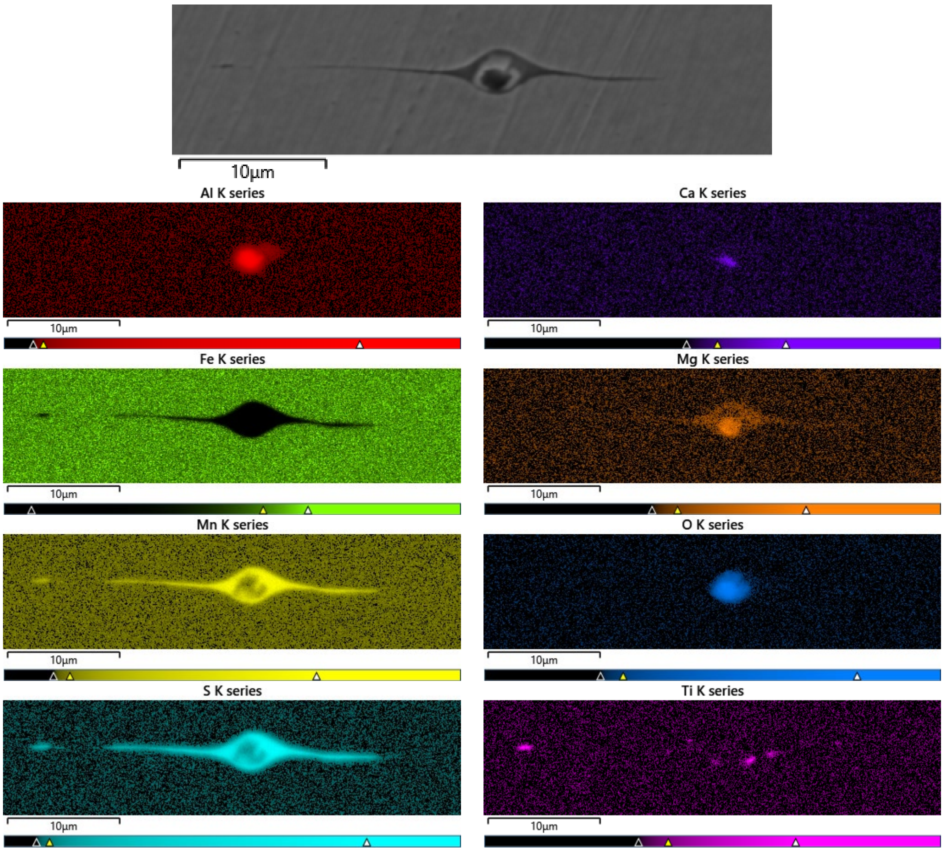

Figure C-30. Example of a ‘Classic’ Stringer Inclusion found in 11QS44-7L1

4.4.2. Effect of Calcium Treatment on Mechanical Properties

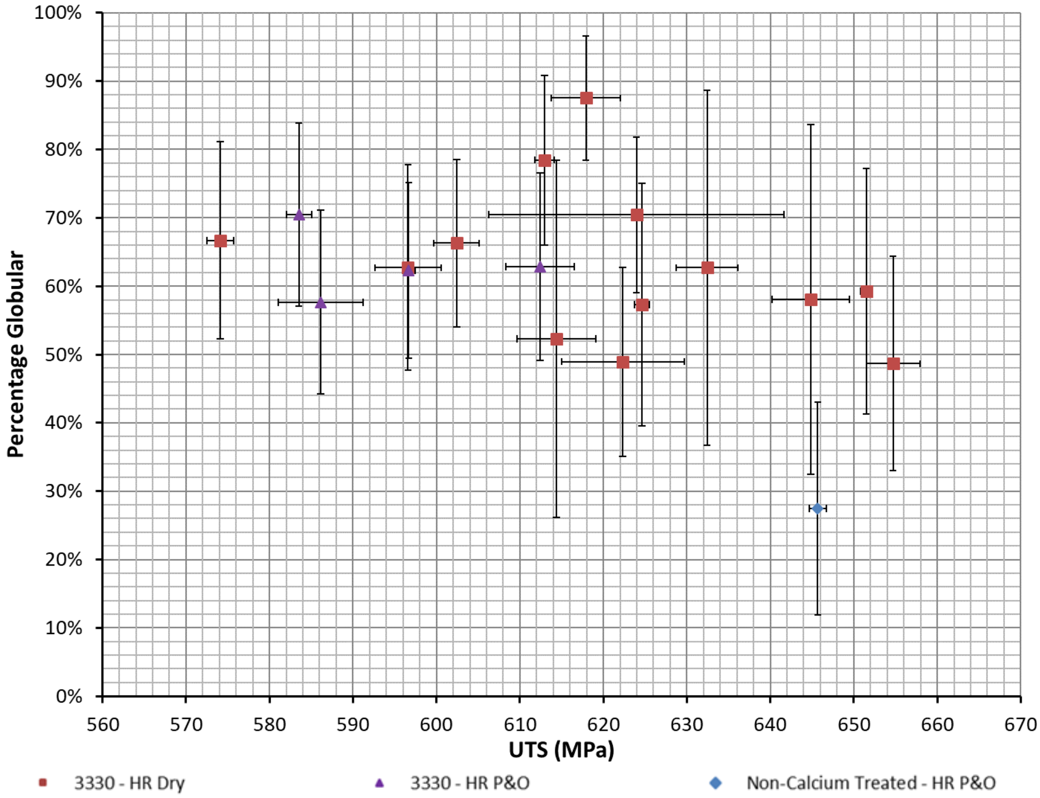

Figure C-31. A Comparison of How the Percentage Amount of Globular Inclusions Affects UTS in the Transverse Direction for the Ca Treated and Non-Ca Treated Samples.

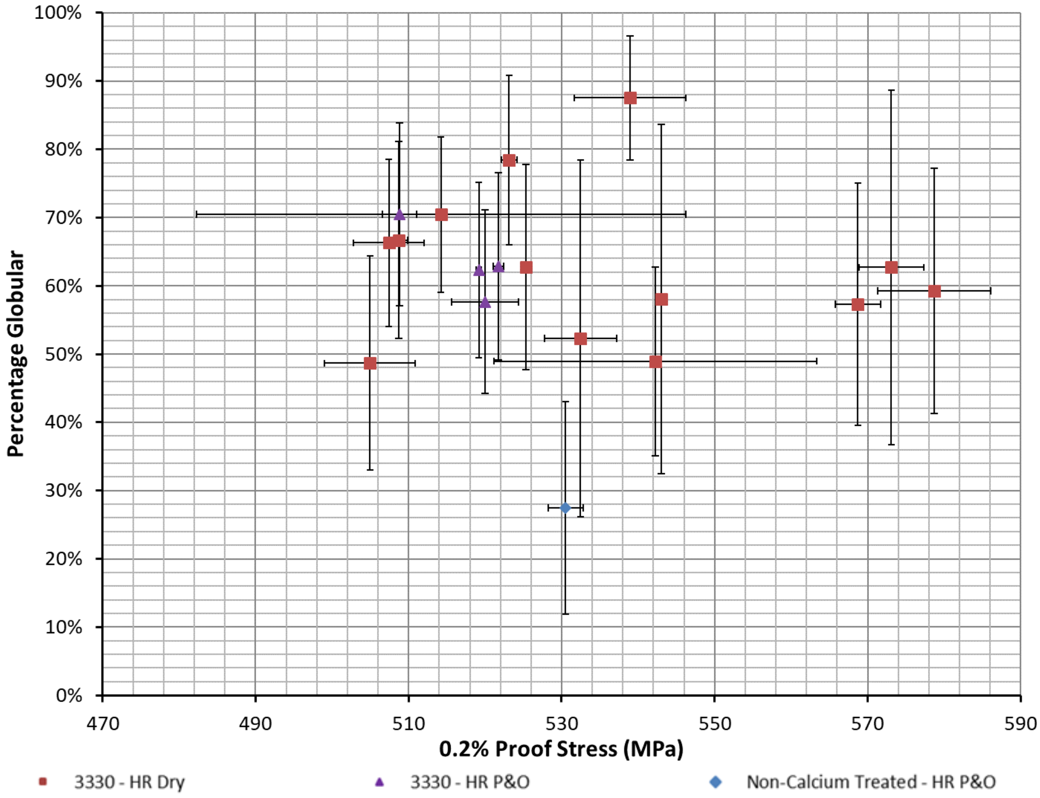

Figure C-32. A Comparison of How the Percentage Amount of Globular Inclusions Affects 0.2% PS in the Transverse Direction for the Ca Treated and Non-Ca Treated Samples.

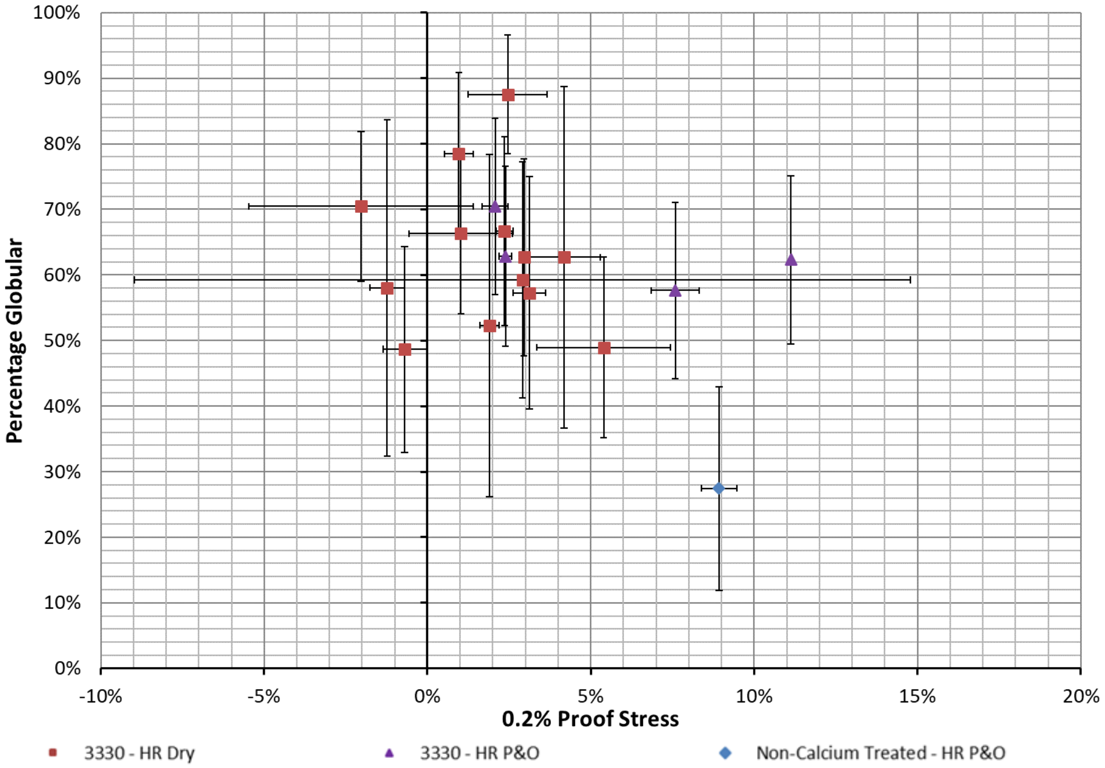

Figure C-33. A Comparison of How the Percentage Amount of Globular Inclusions Affects Percentage Difference in 0.2% PS between the Transverse and Longitudinal Direction for the Ca Treated and Non-Ca Treated Samples.

4.4.3. Effect of Sulphur Level on Tensile Properties

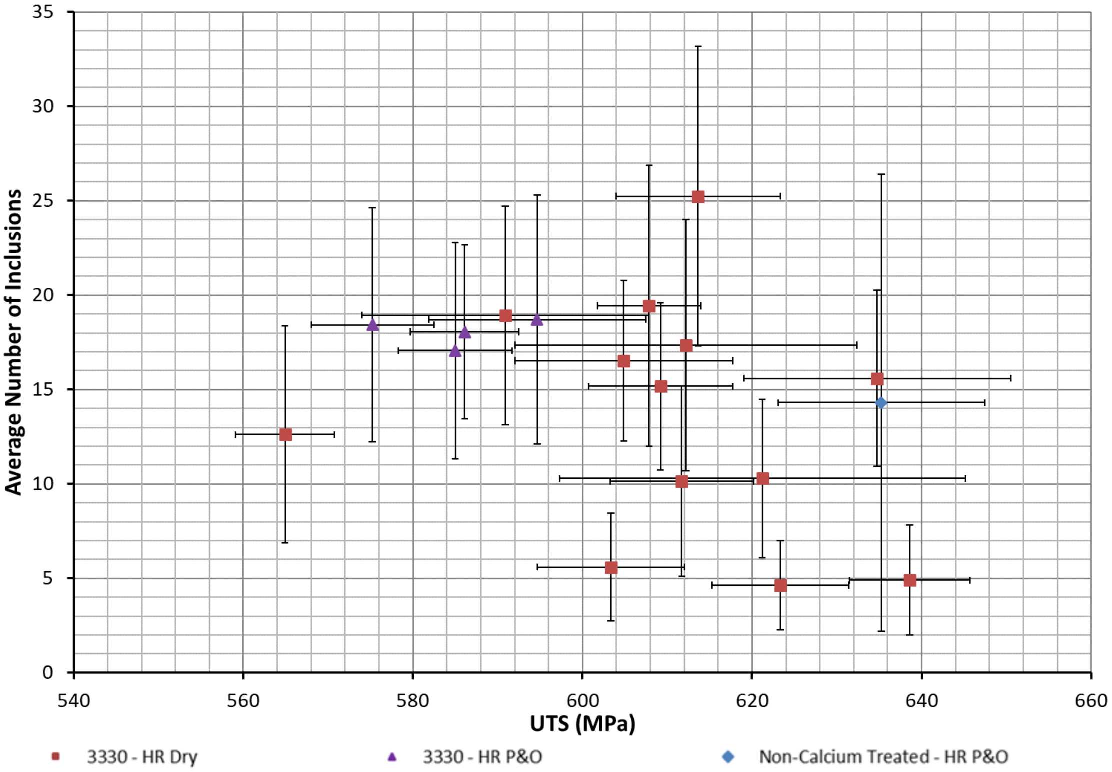

Figure C-34. A Comparison of How the Average Number of Inclusions Affects the UTS for the Calcium Treated and Non-Calcium Treated Samples.

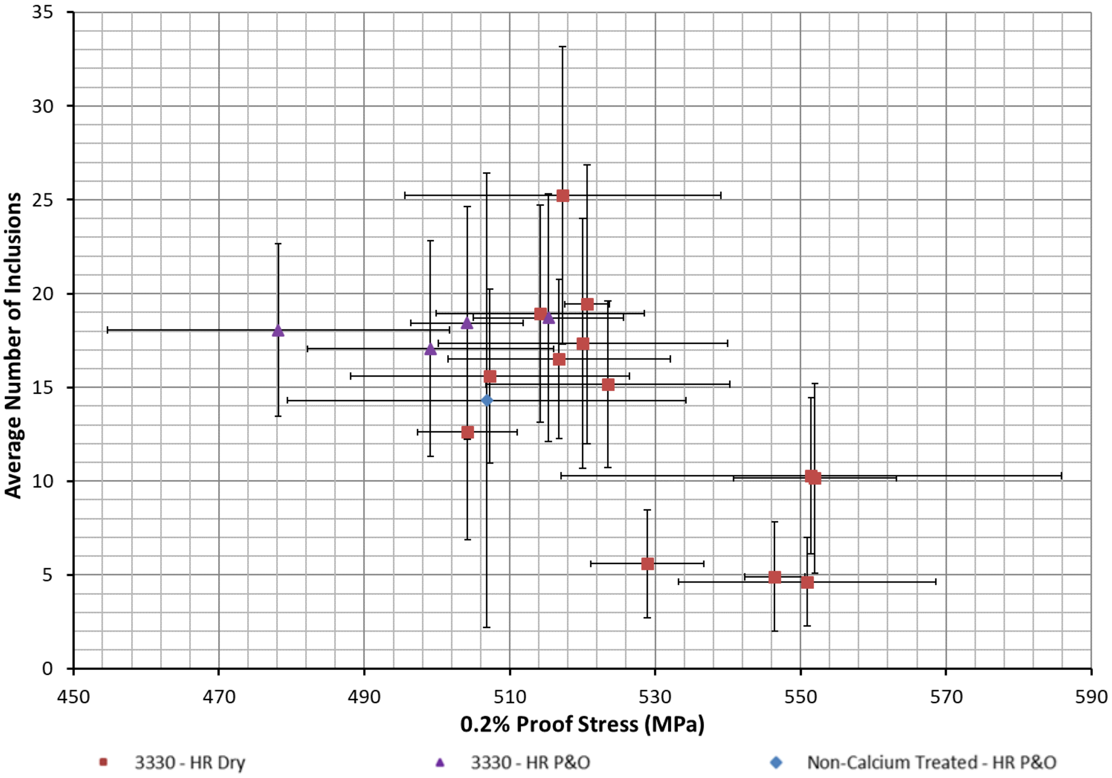

Figure C-35. A Comparison of How the Average Number of Inclusions Affects the 0.2% Proof Stress for the Calcium Treated and Non-Calcium Treated Samples.

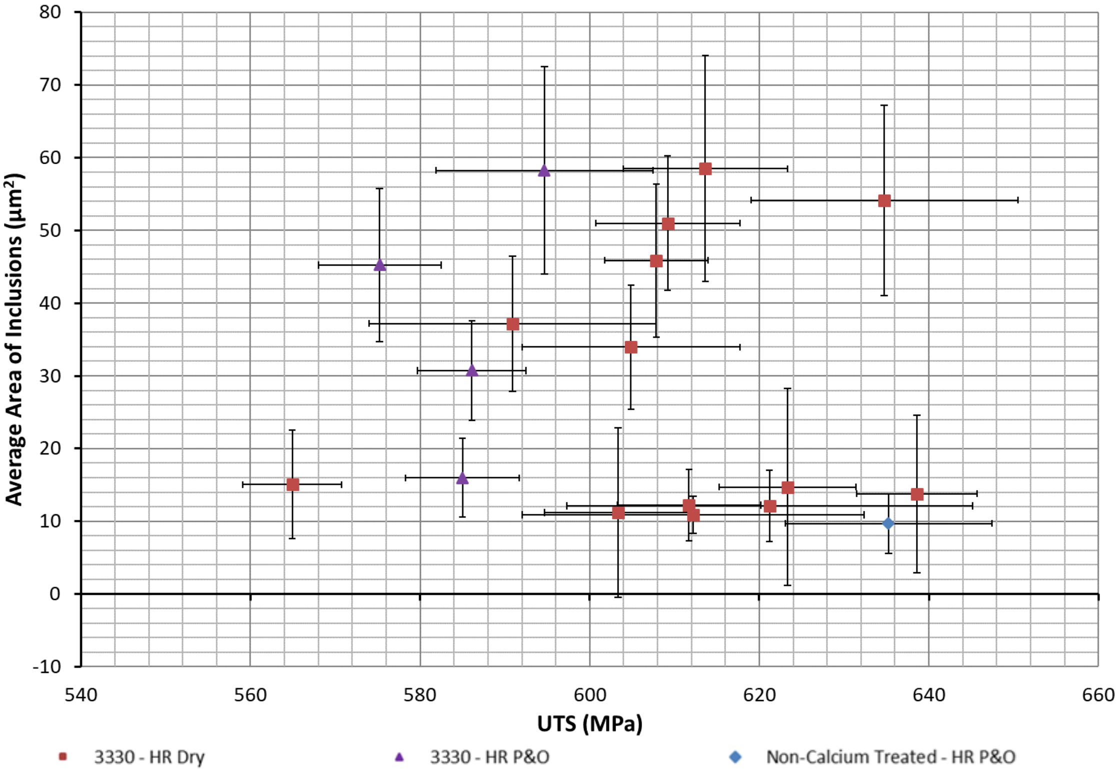

Figure C-36. A Comparison of How the Average Size of Inclusions Affects the UTS for the Calcium Treated and Non-Calcium Treated Samples.

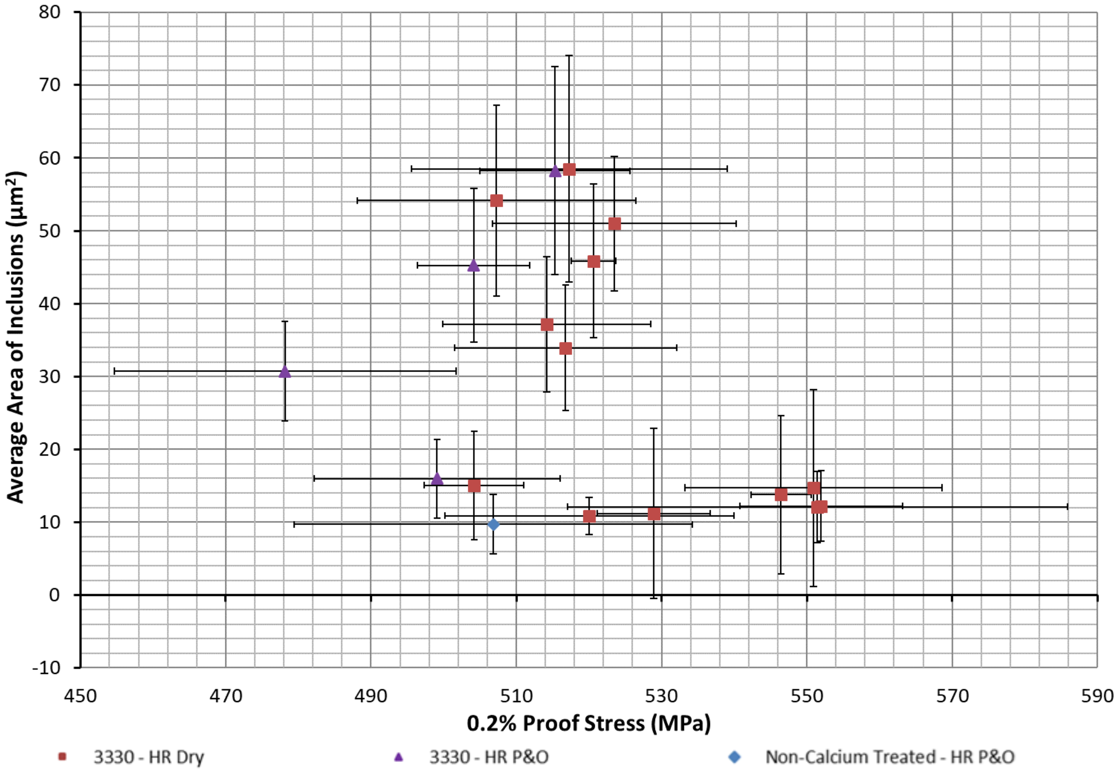

Figure C-37. A Comparison of How the Average Size of Inclusions Affects the 0.2% Proof Stress for the Calcium Treated and Non-Calcium Treated Samples.